**Atomic Scale Modeling of Fundamental Characteristics of Metal Anodes and Solid Electrolytes: Overpotentials, Elastic Properties, and Grain Boundary Transport**

by

Kyle S. Nagy

A dissertation submitted in partial fulfillment
of the requirements for the degree of
Doctor of Philosophy
(Mechanical Engineering)
in the University of Michigan
2020

Doctoral Committee:

Professor Donald J. Siegel, Chair
Professor Wei Lu
Associate Professor Jeff Sakamoto
Professor Katsuyo Thornton

Kyle S. Nagy

nagyky@umich.edu

ORCID iD:  0000-0002-5860-0725

## Dedication

I dedicate this work to my lovely wife, Regina, for her inspiration, love and support, and to our two wonderful children, Aiden and Aria.

**Acknowledgements**

First, I would like to express my sincere thanks to my advisor, Professor Don Siegel, for his patience and guidance throughout my Ph.D studies. This work would not have been possible without his wisdom and support.

I am also grateful to Dr. Saeed Kazemiabnavi and Professor Katsuyo Thornton for their efforts in developing and implementing the DFT-informed nucleation model, which predicted the steady-state nucleation rates presented in Chapter 3.

I would like to thank Professor Wei Lu and Professor Jeff Sakamoto for their valuable advice and service as members of my dissertation committee.

Finally, I would like to thank the Joint Center for Energy Storage Research (JCESR), an Energy Innovation Hub funded by the U.S. Department of Energy, Office of Science, Basic Energy Sciences, as well as the U.S. National Science Foundation, grant CBET-1351482, for their generous financial contribution.

## Table of Contents

## List of Tables

## List of Figures

## List of Appendices

## Abstract

A rechargeable battery with a metallic anode offers the possibility of significant improvement in energy density. However, commercialization of this technology has been hampered by several issues, including safety concerns posed by the formation and growth of dendrites during cycling. Use of a solid electrolyte can potentially address these concerns. Specifically, the solid electrolyte with composition $Li_7La_3Zr_2O_{12}$ (LLZO) has shown promise in conjunction with a Li metal anode due to its favorable combination of high conductivity and chemical stability. The present work characterizes several important properties of metallic anodes and LLZO at the atomic scale using Density Functional Theory (DFT) and molecular dynamics (MD) simulations.

First, thermodynamic deposition/dissolution efficiencies and nucleation rates for seven metals were assessed. Thermodynamic overpotentials were evaluated via DFT at terraces and steps on several low-energy surfaces. In general, overpotentials were observed to be smallest for plating/stripping at steps, and largest at terraces. Differences in coordination numbers between the surface and bulk were found to correlate with overpotential magnitude. Due to their low bulk coordination, body-centered alkali metals were predicted to be thermodynamically efficient for plating/stripping. In contrast, metals with larger bulk coordination, such as Al, Zn, and alkaline earths, exhibited higher thermodynamic overpotentials. The nucleation rate during electrodeposition was estimated using a classical nucleation model informed by the present DFT calculations. Nucleation rates were predicted to be several orders of magnitude larger on alkali

metal surfaces than on other metals. This multi-scale model highlights the sensitivity of nucleation behavior on the morphology and composition of the electrode surface.

Next, DFT calculations were employed to assess the elastic properties of eight candidate anode materials. These properties were predicted as a function of temperature within the quasi-harmonic approximation. Anisotropy was assessed by resolving the moduli as a function of crystallographic direction. The alkali metals were predicted to have the smallest elastic moduli overall, which decreased with increasing atomic number. Al and Mg were predicted to exhibit highly isotropic elastic properties, while the alkali metals were highly anisotropic. In cubic systems, crystallographic directions exhibiting extrema in the elastic properties were diametrically opposed: under axial loading, the stiffest (most compliant) orientation was <111> (<100>), while in shear <100> (<111>) was the stiffest (most compliant). Importantly, the maximum anisotropic shear modulus of some metals was observed to be more than twice as large as their respective polycrystalline values.

Finally, to better understand the impact of grain boundaries (GB's) on the performance of LLZO, the structure of a wide range of tilt and twist axis GB's, including amorphous GB's, were predicted via classical MD and Monte Carlo simulations. Their energetics, composition, and Li transport properties were assessed. Little to no change was observed in the concentration of the four constituent elements across GB's, with the exception of amorphous $\Sigma 9(221)/[1\bar{1}0]$, which showed a significant decrease in the density. Modeled Li trajectories and quantitative estimates of the diffusivity indicate that Li mobility is slowed (relative to bulk) in all GBs examined. The activation energy ($\Delta E_a$) for GB diffusion was comparable to or higher than the bulk. Interestingly, diffusivity and $\Delta E_a$ both decreased with increasing grain boundary energy. A relationship between the pre-exponential factor ($D_0$) and $\Delta E_a$ was observed, which suggested

significant variation of $D_0$ within the grain boundaries examined. Li diffusivity exhibited greater sensitivity to temperature within crystalline GB's than in amorphous GB's. Diffusivity at the GB's demonstrated anisotropy, with diffusion generally slower parallel to the GB plane, and faster normal to the plane.

# Chapter 1 Introduction

## 1.1 Motivation

The lithium-ion battery (LIB) is one of the great technological achievements of recent generations, earning the 2019 Nobel Prize in Chemistry for its inventors. The global energy demand for the LIB is projected to exceed 120 GWh by the end of 2020, driven largely by consumer electronics, but increasingly by automotive and grid storage applications. By the end of the decade, it is estimated that nearly 10% of light duty vehicles sold will possess a LIB.[1] The current energy storage goals specified by the US Department of Energy Vehicle Technologies Office list the required useable cell-level specific energy at 350 Wh/kg,[2] exceeding the highest available LIB specific energy (265 Wh/kg).[3] Indeed, due to the intrinsic energy density limitations of Li-ion batteries,[4] it is generally accepted that battery chemistries "beyond Li-ion" are highly desirable,[5-8] requiring the development of materials to meet these challenges. This dissertation presents atomistic computational studies of metallic anodes and the solid-state electrode $Li_7La_3Zr_2O_{12}$ (LLZO), both of which show promise as components of future rechargeable batteries.

Metals are promising candidates for future battery anodes because they have higher theoretical gravimetric and volumetric charge capacities than the graphite-based, intercalation anodes used in current LIB, as shown in Table 1.1. In some cases, the gains are by an order of magnitude, such as Li and Al in the case of gravimetric capacity, and Al in the case of

**Table 1.1** Properties of candidate negative electrode metals for use in battery applications.

| Anode | Abundance (ppm)[9] | Gravimetric Capacity (mAh/g) | Volumetric Capacity (mAh/cc) | Potential vs SHE (V)[10] |
|---|---|---|---|---|
| Al | 83,176 | 2980 | 8046 | -1.66 |
| Ca | 52,481 | 1337 | 2046 | -2.87 |
| Mg | 32,359 | 2205 | 3837 | -2.37 |
| Na | 22,909 | 1166 | 1181 | -2.71 |
| K | 9,120 | 685 | 624 | -2.93 |
| Zn | 79 | 820 | 5846 | -0.76 |
| Li | 13 | 3862 | 2093 | -3.04 |
| Graphite[11] | - | 300–350 | 790 | -2.79 to -2.94 |

volumetric capacity. Furthermore, the higher abundance of non-Li metals may result in reduced costs.

As shown in Figure 1.1, numerous solid electrolytes have been explored as components in rechargeable batteries.[12] The highest ionic conductivities belong to the sulfides; this is likely a result of the high polarizability of the sulfide ion.[13] However, sulfides are sensitive to moisture in the air, and can form toxic $H_2S$.[14] Alternatively, oxides are generally stable to air exposure, allowing for greater ease of handling.

Among the oxides, the NASICON-like solid electrolytes exhibit high Li-ion conductivities (~1 mS/cm), but they tend to be unstable when in contact with Li metal.[15-17] Perovskites show high Li-ion conductivities (0.1 – 1 mS/cm), but in addition to being unstable when in contact with Li metal, they exhibit high grain boundary resistances.[12, 17-18] Perhaps the most promising solid electrolyte class is the garnets, among which is $Li_7La_3Zr_2O_{12}$ (LLZO).[19-20] In addition to high Li-ion conductivity, the garnet oxides demonstrate chemical stability with Li metal.[21-24]

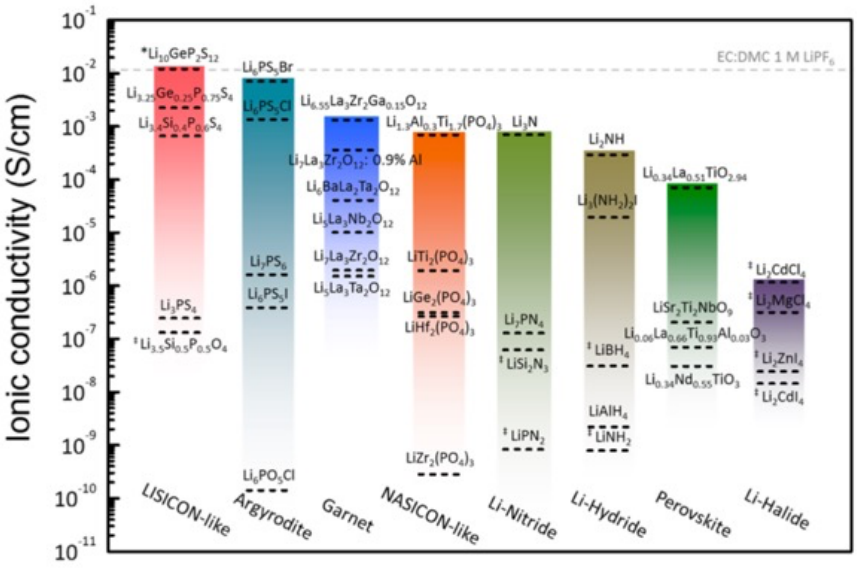


**Figure 1.1** Ionic conductivities for classes of Li-ion conducting solid electrolytes. Adapted from Bachman *et* al.[12]

## 1.2 Metal Anodes and Dendrites

### 1.2.1 Lithium

The earliest iterations of the LIB incorporated Li metal as the anode, but attempts to commercialize a Li metal-based cell were unsuccessful mainly because of dendrite growth during charging.[25-26] Today, Sion Power manufactures and sells a rechargeable battery with a ceramic-coated metallic anode, but it is currently relegated to niche markets, such as unmanned aerial vehicles.[27] Implementation of a Li metal anode for mass commercialization is extremely desirable, but so far unsuccessful due to a number of problems, including dendrite formation.

The problem of dendrites has proven a major obstacle toward the implementation of metallic Li anodes.[28-29] Past strategies to control dendrite growth have included the addition of additives to the electrolyte;[6, 28-31] applying an artificial protective layer to the anode surface[32] to 1) serve as a stiff barrier to dendrite growth,[6, 28, 30] 2) modify the solid electrolyte interphase (SEI) and 3) accommodate volume changes,[28] and 4) control surface morphology;[28, 30-31] using

ionic liquids as electrolytes;[31] and implementing 3D current collectors to increase surface area and reduce current density.[28-29] An additional challenge associated with the implementation of Li metal in rechargeable batteries, as well as metallic anodes more broadly, is the drastic volume change that occurs during cycling. This can fracture the SEI,[28, 33] which is essential for stable operation. Strategies to address this issue include the use of block copolymers[29, 33] and application of external pressure.[33]

### 1.2.2 Zinc

Primary Zn-air batteries are currently on the market, usually providing power for small devices such as hearing aids. Rechargeable batteries incorporating a Zn metal anode are still largely in development, although Fluidic Energy has commercialized a rechargeable Zn−air battery as an energy storage option for solar power installations.[34] The Zn-air battery is one of the most widely studied rechargeable Zn metal batteries, and is often composed of a Zn metal anode, alkaline electrolyte, separator, and a porous carbon air cathode with catalyst to facilitate oxygen reduction.[35-36] Although the open circuit voltage is 1.65 V, actual operating voltages are much lower due in large part to the overpotential associated with oxygen reduction, and recharging is inefficient due to the overpotential associated with the oxygen evolution reaction.[35-36] Other Zn metal rechargeable battery chemistries that have been investigated include a non-aqueous electrolyte with manganese oxide,[37-38] and cathodes composed of vanadium-based oxide, Prussian blue analogs, olivine-based phosphates, various Chevrel phase compounds, or organic quinones.[37]

As is common with other metallic electrodes, dendrite formation is problematic during cycling, with Zn providing the basis for early efforts to model dendrite formation.[39] Efforts to suppress Zn dendrites include alloying with other metals,[40-41] coating the surface with aluminum

oxide or lithium boron oxide,[41] and adding polymers to the electrolyte.[40-41] Ionic liquids have been attempted to mitigate dendrite formation with limited success,[42-43] although Liu et al. demonstrated 50 cycles by adding $Ni(TfO)_2$ to $Zn(TfO)_2$ in [EMIm]TfO.[44] Additionally, the previously mentioned rechargeable Zn-air battery developed by Fluidic incorporates ionic liquids as electrolyte.[34]

### 1.2.3 Aluminum

While the Al-air battery with a metallic Al anode has proven to be a successful primary energy storage device,[45] the utilization of an aqueous electrolyte frustrates its use as a rechargeable battery due to the irreversibility of the $Al_2O_3$ discharge product.[46] Rechargeable batteries using organic solvents with an Al metal anode have been attempted, including electrolytes composed of $AlCl_3$ dissolved in tetrahydrofuran (THF), propylene carbonate (PC), and formamide (FA),[47] and combinations of the salts $(C_2H_5)_4NCl$ (TEA), $AlCl_3$, and KCl in a variety of organic solvents.[48] These have demonstrated the ability to strip the Al anode, but not plate due to the persistence of the passivating oxide layer. Ionic liquids have plated and stripped reversibly at room temperature,[31, 49-51] but the corrosion of passive elements by the highly concentrated chlorides is problematic. Nakayama *et* al. studied the reversibility of Al using $AlCl_3$ in a variety of sulfones, and showed evidence of reversibility at room temperature when the electrolytes were diluted with solvents with small dielectric constants, such as benzene ($\varepsilon_r$ = 2.27) or toluene ($\varepsilon_r$ = 2.38). Furthermore, there was reduced corrosion of stainless steel because of lower chloride concentrations, and no dendrites were observed.[52]

This lack of dendrites is inconsistent with the prevailing literature on Al deposition morphology, which consistently shows dendritic growth except at very low current densities.[46] Chen et al. recently studied Al metal anodes in cells with graphite cathodes and the ionic liquid

1-ethyl-3 methylimidazolium chloride ([EMIm]Cl) as electrolyte, which demonstrated stable cycling over 45000 cycles at current densities of 5 mA/cm$^2$.[53] They attribute this performance to the native oxide layer on the as-received foil protecting the Al surface, allowing the electrolyte to come into contact with the Al metal only at locations where defects in the $Al_2O_3$ have occurred. These limited reaction sites allow cycling while at the same time confining the dendrites, limiting their growth, and eliminating the creation of "dead Al," dendrites which no longer maintain contact with the substrate and no longer contribute to charge transfer. This surprising mechanism suggests a possible route to an operable battery with Al metal as anode.

### 1.2.4 Magnesium

Mg metal anodes have been successfully implemented in primary batteries, but a secondary battery is still in research and development stages. Early electrochemical studies of Grignard reagents in ether,[54] and later in THF,[55] showed that Mg metal could be reversibly plated and stripped. Unfortunately, these solutions yielded a narrow anodic stability window and very low ionic conductivity.[56] Gregory et al. systematically tested various organic electrolytes with Mg metal anodes, and found that magnesium organoborates could both efficiently plate and strip Mg.[57] Unfortunately, these electrolytes also provided a narrow anodic stability window. Aurbach et al. developed the first, reliable, rechargeable Mg battery with a Chevrel phase $Mo_3S_4$ cathode, an electrolyte with organohaloaluminate salts in THF, and a Mg anode.[58] The device showed an impressive cycling efficiency, a high $Mg^{2+}$ conductivity (1 – 1.4 mS/cm), and a charge capacity loss of <15% after 2000 cycles at various current densities (0.1 – 1 mAh) and temperatures (-20°C – 80°C). However, a small nominal voltage of 1.1 V at current densities up to 2 mAh/cm$^2$ was reported, as well as a 100 Wh/kg energy density.[59]

Reports have suggested that Mg may deposit granularly, both in Grignard-based electrolytes,[60] as well as $Mg(TFSI)_2$.[61] Such reports led to widespread speculation that Mg could electrodeposit "dendrite-free," perhaps due to reduced surface diffusion barriers,[62] and spurred a significant amount of interest in Mg as a metal anode since it seemed to side-step the dendrite issue which plagued other metallic anodes.[63-66] More recently, Davidson et al. showed that Mg will form highly anisotropic, stiff, dendritic fractal deposits when the rate of nucleation significantly exceeds the rate of surface self-diffusion.[67] This most commonly occurs when high currents are applied to regions of local inhomogeneity and high reactivity, such as at electrode edges and at defect sites, which can be further exacerbated by operation at low temperatures. Therefore, while the danger from dendrites is less than in chemistries involving other metals, it is still an important factor that should not be neglected.

### 1.2.5 Sodium

There are currently rechargeable battery systems on the market utilizing molten Na electrodes, such as Na-S and ZEBRA batteries. These are large, stationary systems for load-levelling and emergency power applications.[68-69] However, a battery incorporating a solid Na anode would be preferable for applications requiring high energy density, such as electric vehicles. There is considerable interest in Na metal anode batteries, as evidenced by numerous studies mainly focused on Na-$O_2$ and Na-S systems.[68, 70-71]

Dendrites have been a problem for Na metal batteries, but recent advances have made significant headway toward safe implementation. Wu et. al. was able to achieve over 300 cycles at 1 C cycling rate with a concentrated electrolyte consisting of 2 M NaTFSI in a 7:3 mixture of trimethyl phosphate and fluoroethylene carbonate.[72] This cycling performance was attributed to the solid electrolyte interphase (SEI) composed primarily of NaF, which suppressed dendrite

growth. Choudhary et. al., after determining that NaBr had low surface diffusion energy barriers via a density functional theory study, applied an artificial SEI of NaBr and achieved over 250 stable cycles.[73] Gao et. al. compared the performance of the NASICON solid electrolyte with stoichiometry $Na_3Zr_2Si_2PO_{12}$ at 60°C with a liquid electrolyte containing 1 M $NaClO_4$ dissolved in a mixture of propylene carbonate and fluoroethylene carbonate.[74] The all-solid-state battery prevented dissolution of the Prussian blue cathode which plagued batteries with liquid electrolytes, showed higher charge capacity and lower total resistance, and demonstrated a lack of dendritic growth after 200 cycles. Other attempts at mitigating dendrites have included the use of novel carbon structures, such as microspheres[75] and sheets of carbon nanotubes.[76-77]

### 1.2.6 Potassium

The study of metallic potassium as a rechargeable battery anode is in relatively nascent stages. In 2013, Ren et al. reported a K-$O_2$ battery which showed a discharge/charge potential gap of less than 50 mV during the initial cycle, with rapid capacity decay caused by side reactions between the K and the ether solvent, as well as $O_2$ crossing over to the K anode to form a passivating layer on the anode surface.[78-79] Zhao et al. reported a K-S battery with very high initial charge capacity (513 mAh/g), but which faded to 202 mAh/g after 50 cycles due to irreversible polysulfide dissolution.[80] By coating the cathode surface with polyaniline, they were able to improve the charge capacity to 329 mAh/g after 50 cycles.

Potassium, like other metals, forms dendrites upon cycling, but strategies to mitigate this issue have met with some success. Xiao et al. developed a cell using an electrolyte consisting of KFSI in DME at room temperature without any surface coating or modification to the Celgard separator, demonstrating cycling of the K metal anode for over 200 cycles at ~99% Coulombic efficiency.[81] The relative stability was attributed to the formation of a stable and uniform SEI.

### 1.2.7 Calcium

Earlier investigations of Ca metal as a possible battery anode were performed in thionyl chloride solutions, where passivating layers composed primarily of $CaCl_2$ were formed, producing high resistivity which effectively insulated the metal and inhibited further deposition.[82] This insulating effect in the Ca/$SOCl_2$ system was further corroborated by studies utilizing a variety of salts.[83-84] Organic-based electrolytes for Ca systems showed similar results.[85] A recent study showed reversible Ca plating and stripping in various concentrations of $Ca(BF_4)_2$ in a 50/50 wt% mixture of EC:PC, with 0.45 M $Ca(BF_4)_2$ yielding the best performance at 100°C. However, small quantities of Ca were deposited, corresponding to 0.165 mAh/cm$^2$.[86] This was later improved with the use of $Ca(BF_4)_2$ in THF, where $CaH_2$, instead of the usual passivating products of calcium oxidation, formed and created a protection layer, yielding 1 mAh/cm$^2$ of charge.[87] However, the Coulombic efficiency of 96% was too low to be practical, and only 10 cycles were reported.

## 1.3 $Li_7La_3Zr_2O_{12}$ (LLZO)

Fast Li-ion conductors with cubic garnet structure and nominal composition $Li_5La_3M_2O_{12}$ (M = Nb, Ta) showed excellent stability against molten Li,[88] as well as a high bulk ionic conductivity of ~1 mS/cm. However, the total ionic conductivity was ~$7x10^{-5}$ S/cm, making it impractical for use in a battery. With the substitution of Zr to form the cubic garnet phase $Li_7La_3Zr_2O_{12}$ (LLZO),[20] the new material exhibited total Li-ion conductivities of ~0.1 mS/cm for 1 cm thick pellets, chemical stability with both air and molten Li, and thermal stability over a

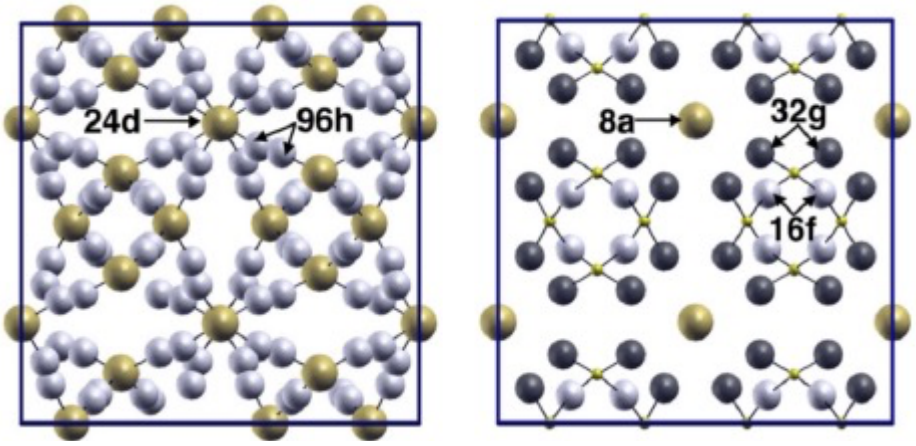


**Figure 1.2** Li sub-lattice for the cubic (left) and tetragonal (right) phases of LLZO. Adapted from Bernstein *et* al.[89]

wide range of temperatures (20°C – 900°C); subsequent theoretical predictions and experimental measurements confirmed the electrochemical stability and wide electrochemical window of LLZO,[90] making it a very promising candidate as an electrolyte for an all-solid-state rechargeable battery incorporating Li metal as an anode.

LLZO is known to exist as one of two polymorphs, either cubic or tetragonal. In cubic LLZO, Li migrates along a path consisting of tetrahedral sites bridged by octahedral sites, with 56.8% of the tetrahedral 24d sites occupied, and 44.2% of the octahedral 96h sites occupied.[91] In tetragonal LLZO, the 24d sites are transformed into fully-occupied tetrahedral 8a and unoccupied tetrahedral 16e sites, while the 96h sites are transformed into fully-occupied octahedral 16f and 32g sites.[89, 92-93] The lower Li-ion conductivity of the tetragonal phase (~$10^{-6}$ S $cm^{-1}$) is attributable to the fully-ordered Li distribution, whereas the higher conductivity of the cubic phase is attributable to the partial occupancy of the Li sublattice.[92, 94-95]

A distinctive chain process arises due to the arrangement of polyhedral interstitial Li sites within the cubic polymorph, as well as the conditions under which the 24d tetrahedral sites and the 96h octahedral sites may be occupied.[91, 95] If the 96h site is occupied, then one of the

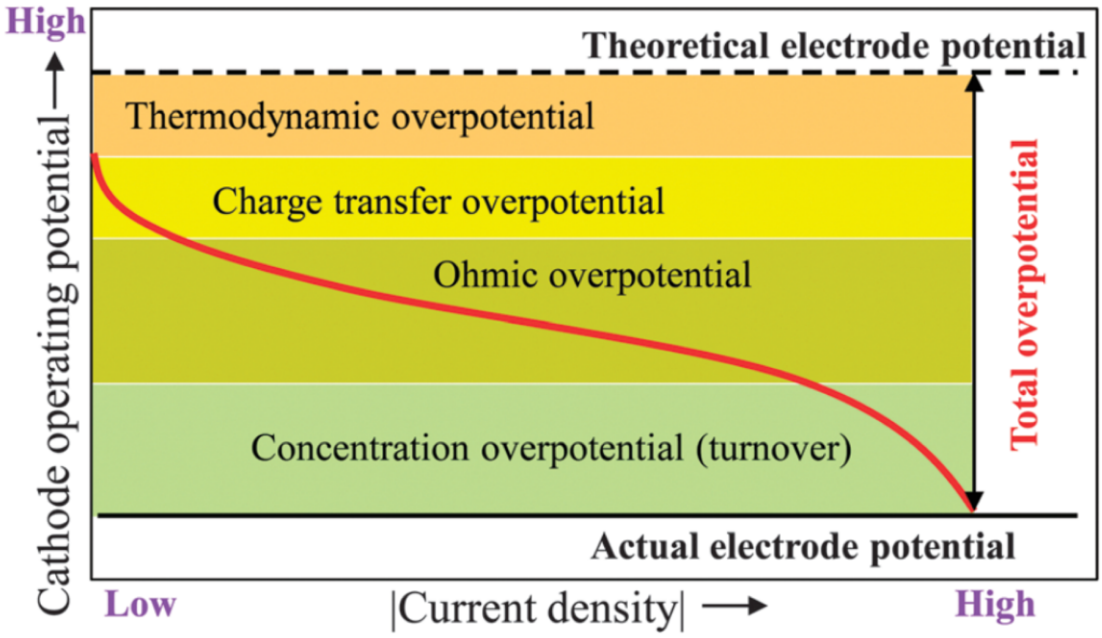


**Figure 1.3** Schematic illustration of overpotential dependence on current density. Adapted from Liu *et al.*[98]

neighboring 24d sites must be unoccupied and the other occupied; or, if both of the tetrahedral sites are occupied, then the intermediate 96h site must be unoccupied. *Ab initio* nudged elastic band calculations comparing diffusion in various cubic garnet structures ($Li_3La_3Te_2O_{12}$, $Li_5La_3Nb_2O_{12}$, and $Li_7Li_3Zr_2O_{12}$) showed that the distinctive Li diffusion process in LLZO yielded a much lower activation energy barrier compared to LLNO and LLTO.[96]

## 1.4 Thermodynamic Overpotentials

The deposition of metal adatoms onto a metal substrate, and the subsequent dissolution of the metal substrate, are the charge and discharge half-reactions in a rechargeable battery that utilizes a metal anode. Anodic cycling efficiencies are determined by the overpotentials associated with these deposition/dissolution reactions. In general, various mechanisms contribute to the overpotential: charge transfer across the electrochemical double-layer, transfer of mass across the cell, solvation/desolvation at the electrode/electrolyte interface, and

incorporation of the metal adatom into the substrate (removal from the substrate in the case of dissolution).[97] Figure 1.3 shows these overpotential contributions in alternate forms, with different mechanisms dominating as the current density is varied, as might be observed in an electrochemical cell utilizing a liquid electrolyte. Here, the thermodynamic overpotential, which is defined by the deposition/dissolution reaction energies at specific sites on the substrate surface, is the dominant mechanism only at low current densities, and thus at potentials near to the metal redox potential. However, in all-solid-state batteries, this might not be the case. For example, with adequate surface conditioning, and under a strictly controlled environment, LLZO is known to exhibit negligible interfacial resistance,[99-100] suggesting that the kinetic overpotential contributors in Figure 1.3 (charge transfer, ohmic, concentration) are significantly lessened.

Diverse deposition sites exist on a metal substrate surface, including kink sites, step-edge sites, and terrace sites,[97] It is expected that the heterogeneity of these sites will yield a variety of deposition reaction energies, and thus site-specific thermodynamic overpotentials. If, in certain electrochemical cells, kinetic overpotential contributions are significantly lessened, then the thermodynamic contribution can be expected to play an important role over a wide range of charge densities. While it may be difficult to decouple individual factors giving rise to the overpotential, Density Functional Theory is a powerful computational method by which the thermodynamic overpotential may be evaluated.

## 1.5 Anisotropic Elastic Properties

Dendrite formation during cycling of a metal anode is a problem which has long hampered their implementation in rechargeable batteries. Incorporation of a solid electrolyte, and application of adequate pressure, is expected to prevent non-uniform metal deposition and the propagation of dendrites.[101] To better understand the interplay between mechanical

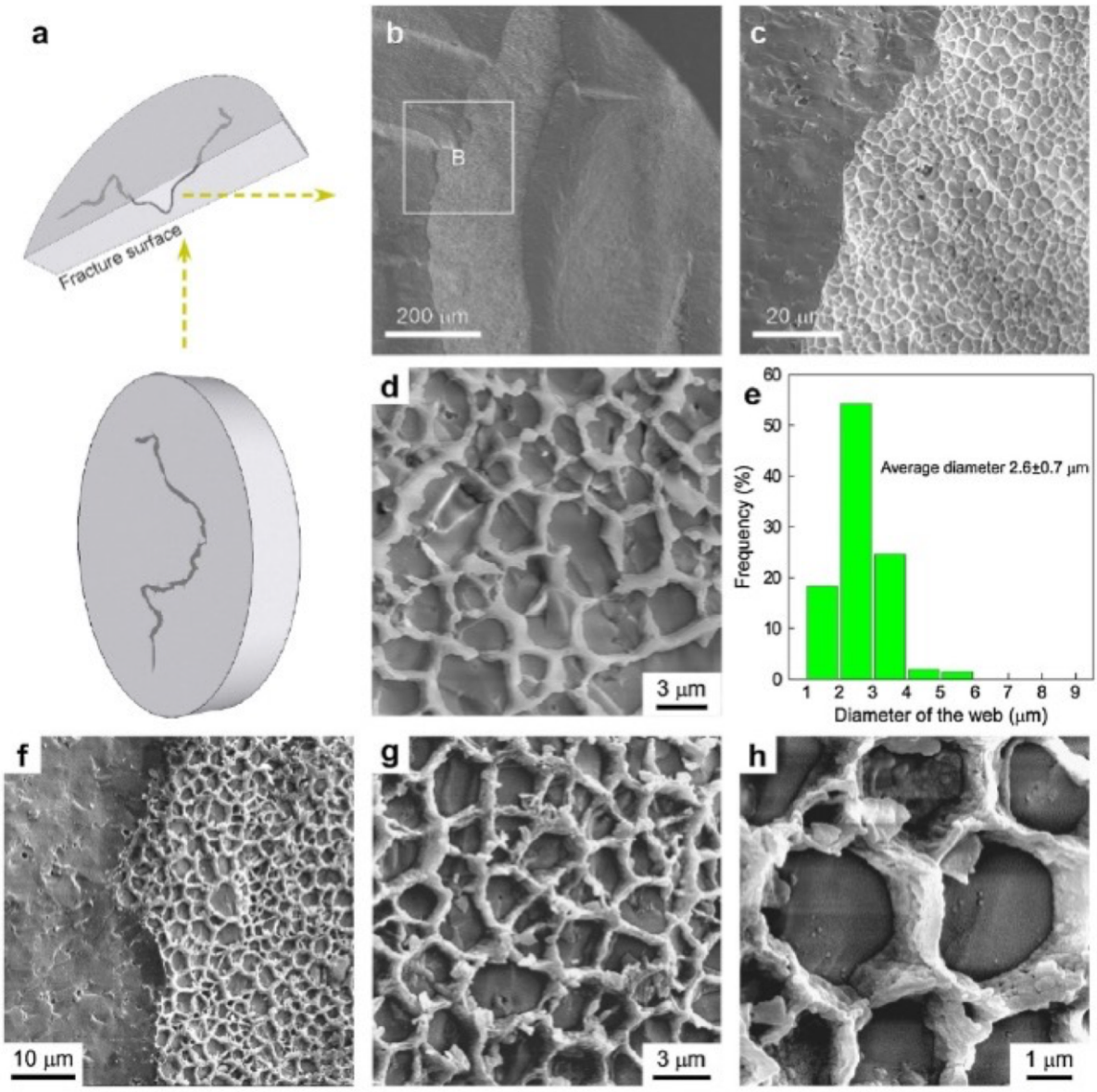


**Figure 1.4** SEM micrographs of the web structure in cycled LLZO. a) Illustration of a fractured surface through a black linear feature, b) SEM image of a fracture surface, c) enlarged SEM micrograph of boxed area B in b), d) higher magnification of web structure in c), e) statistical distribution of the average hexagon-like diameters defined by the web structure. f), g), and h) are successively amplified SEM images of the web structure after exposure to air. Adapted from Cheng *et al.*[103]

properties and dendrite formation, Monroe and Newman incorporated mechanical properties into an electrochemical model.[102] A major conclusion of their work was the suggestion that the ratio

of the shear modulus of the solid electrolyte to that of the anode should be greater than approximately two.

Nevertheless, numerous examples exist of lithium metal-based cells undergoing failure due to dendrite formation.[103-110] One example is shown in Figure 1.4, where Li metal appears to traverse the LLZO solid electrolyte along grain boundaries, despite LLZO possessing a polycrystalline shear modulus (54.8 – 68.9 GPa)[111] far greater than twice that of Li (~4.25 GPa). It is likely that other factors are important in understanding these failures. One possibility lies in anisotropies within the elastic moduli. The Monroe/Newman model, as well as subsequent mechano-electrochemical models, have assumed polycrystalline elastic properties at the solid electrolyte/electrode interface, which may not be appropriate when the formation of dendrite nuclei occur at the nanoscale. Accurate calculations of elastic properties would be an important step toward understanding failure modes associated with solid electrolytes.

## 1.6 Grain Boundary Transport

The solid electrolyte LLZO is attractive due to its high bulk ionic conductivity, but to be practical in a rechargeable, all-solid-state battery, it should also possess low grain boundary resistance. It is not clear, however, to what extent the grain boundaries will impact diffusivity in LLZO. For example, in perovskite solid electrolytes, the observation that grain boundaries severely impact diffusivity as compared to bulk has been attributed to the fact that ions travel along 2D pathways. However, the 3D pathways present in LLZO may result in less disruption.

Experimental studies have examined the impact of grain boundaries on the performance of LLZO, and in general, greater relative density has resulted in greater Li mobility.[112-113] Computational studies which have been performed have been limited to a few selected grain boundaries, but it is not certain if they are representative of all grain boundaries which may be

present in a sample. While experimental measurements may indicate the performance of an aggregation of grain boundaries, they cannot distinguish between various grain boundary geometries. Therefore, a study of Li transport within a broad set of grain boundaries expected to be present within a sample of LLZO would be helpful in revealing the role of grain boundaries in LLZO and in other solid electrolytes.

## 1.7 Scope and Goals of Dissertation

The goal of this dissertation is to examine fundamental properties of metal anodes and solid electrolytes. Understanding these properties is a prerequisite to establishing design principles for their incorporation into next generation rechargeable batteries. Cycling efficiency on surfaces of the metals Al, Ca, Li, Na, K, Mg, and Zn is predicted using first-principles calculations to evaluate "thermodynamic overpotentials"[114] associated with plating and stripping at terraces, step edges, and kinks. These data are used to inform a continuum-scale nucleation model, provided by collaborators from the Thornton group, to predict nucleation rates and observe trends across a variety of anode substrates. Additionally, calculations based on Density Functional Theory are used to evaluate the elastic constants, the aggregated, polycrystalline elastic properties, and the orientation-dependent elastic properties of these metals and Si at various temperatures. These data will be useful for future mechano-electrochemical models which seek to predict the conditions under which metal dendrites form, and should guide strategies for their prevention. Finally, classical molecular dynamics and Monte Carlo techniques are utilized to comprehensively characterize the structure of grain boundaries in the solid electrolyte LLZO. Diffusion characteristics are quantified at grain boundaries, and trends in Li transport across a broad selection of grain boundary systems are explored.

# Chapter 2 Methodology

## 2.1 First Principles Calculations

### 2.1.1 Density Functional Theory

The Schrödinger equation, given by

$$i\hbar \frac{d\Psi}{dt} = \widehat{H}\Psi \tag{2.1}$$

where $\hbar$ is the reduced Planck's constant, Ψ is the many-body wavefunction, and $\widehat{H}$ is the Hamiltonian operator, describes the fundamental physics of systems of atoms. Due to the complexity of the many-body interactions, certain simplifications are required. One is the assumption of time-independence, which yields the more familiar eigenvalue problem, given by

$$\widehat{H}\Psi = E\Psi \tag{2.2}$$

where $E$ are the energy eigenvalues of the system. Another simplification is the Born-Oppenheimer approximation, which treats the atomic nuclei as static. This is reasonable given that the masses of protons and neutrons are many times larger than those of electrons.

Unfortunately, even with these simplifications, Eqn. (2.2) is too complex for any computer to solve in a reasonable amount of time for all but the simplest systems of atoms. Fortunately, Density Functional Theory (DFT), proposed by Hohenberg and Kohn in 1964 and formalized by Kohn and Sham in 1965,[115-116] simplifies the problem even further by mapping the coordinate systems for many electrons onto a single coordinate system for a system-wide electron density. The total energy of the system of atoms is described as a functional of the electron density,

$$E[n(\boldsymbol{r})] = \int V_{ion}(\boldsymbol{r})n(\boldsymbol{r})d\boldsymbol{r} + E_C[n(\boldsymbol{r})] + T[n(\boldsymbol{r})] + E_{xc}[n(\boldsymbol{r})] \tag{2.3}$$

where $n(\boldsymbol{r})$ is the electron density, $V_{ion}(\mathbf{r})$ is the electron-ion interaction potential, $E_C[n(\mathbf{r})]$ is the Coulomb energy, $T[n(\mathbf{r})]$ is the kinetic energy, and $E_{xc}[n(\mathbf{r})]$ is the energy of electron correlation and exchange. The electron density

$$n(\boldsymbol{r}) = 2\sum|\psi_i(\boldsymbol{r})|^2 \tag{2.4}$$

is written in terms of non-interacting electronic wavefunctions, $\psi_i$. The set of wavefunctions that minimize Eqn. (2.3) are determined by self-consistently solving the single-particle Kohn-Sham equations

$$\left[\frac{-\hbar^2}{2m}\nabla^2 + V_{ion}(\boldsymbol{r}) + V_H(\boldsymbol{r}) + V_{xc}(\boldsymbol{r})\right]\psi_i = \varepsilon_i\psi_i \tag{2.5}$$

where $\varepsilon_i$ are the Kohn-Sham eigenvalues, and $V_H$ is the Hartree potential,

$$V_H(\boldsymbol{r}) = e^2\int\frac{n(\boldsymbol{r'})}{|\boldsymbol{r}-\boldsymbol{r'}|}d\boldsymbol{r'} \tag{2.6}$$

which describes the interaction between an electron and the electron density. Finally, the last term in the brackets in Eqn. (2.5) is the exchange-correlation potential, written formally as

$$V_{xc}[n(\boldsymbol{r})] = \frac{\delta E_{xc}[n(\boldsymbol{r})]}{\delta n(\boldsymbol{r})} \tag{2.7}$$

The treatment of wavefunctions varies depending on the system being analyzed. While a system composed of individual atoms or molecules might be treated by localized orbitals, a larger system may be more conveniently described with periodic potentials. In this case, as a result of Bloch's theorem, electronic wavefunctions may be treated as plane waves propagating through a potential field generated by cores of ions. A large number of plane waves are needed to expand the orbitals of core electrons near the ionic nuclei, as well as the valence electrons. Fortunately, further simplification can be achieved with the implementation of pseudopotentials, which replace the strong ion-electron interactions within a designated cut-off radius around the core with a much smoother potential.

### 2.1.2 Exchange-Correlation Functionals

The exact form of the exchange-correlation functional in Eqn. (2.3) is impossible to know exactly, so it must be treated with an appropriate approximation in order to solve the Kohn-Sham equations. Among the most commonly used are the local density approximation (LDA)-type functionals and the generalized gradient approximation (GGA)-type functionals. The LDA-type functionals treat the electrons as a homogeneous gas,[117] where data from quantum Monte Carlo calculations are used to interpolate over a wide range of densities.[118] However, LDA-type functionals typically overestimate the exchange energy and underestimate the correlation energy. The GGA-type functionals improve upon accuracy by incorporating the gradient of the electron density as an additional parameter.[119] Among the various formulations of the GGA-type functional, the PBE functional[120] is widely used for its computational efficiency and accuracy among a variety of systems.

### 2.1.3 Implementation

First-principles calculations were performed using the Vienna *Ab-initio* Simulation Package (VASP).[121-123] Charge densities and wavefunctions were expanded in a plane wave basis set, while core-valence electron interactions were treated using the projector augmented wave (PAW) method.[124-125] Occupancies were determined by a Gaussian smearing of width 0.1 eV, and the Brillouin zone was sampled with Monkhorst-Pack grids.[126]

## 2.2 Classical Molecular Dynamics

Molecular dynamics is a method of simulation that predicts the evolution of a system of particles over time. This is achieved by iteratively solving Newton's second law

$$\frac{d^2\boldsymbol{r}}{dt^2} = \frac{\boldsymbol{F}}{m} = \boldsymbol{f} \tag{2.8}$$

The force **F** acting on each atom is the negative gradient of the potential generated by the simulated system

$$F = -\nabla U(\boldsymbol{r}, t) \tag{2.9}$$

Taking the time derivative of **r**,

$$\frac{d\boldsymbol{r}}{dt} = \boldsymbol{v} \tag{2.10}$$

equations (2.8) and (2.10) form a system of coupled, first-order differential equations. A common method for solving such a system of equations is the velocity Verlet algorithm,[127] which updates positions and accelerations at each timestep $t + \Delta t$ and the velocity at each half timestep $t + \frac{1}{2}\Delta t$, by first performing a half step calculation on the initial atom positions,

$$\boldsymbol{v}\left(t + \frac{1}{2}\Delta t\right) = \boldsymbol{v}(t) + \frac{1}{2}\Delta t \boldsymbol{f}[\boldsymbol{r}(t), t] \tag{2.11}$$

and then repeatedly applying the following equations:

$$\boldsymbol{r}(t + \Delta t) = \boldsymbol{r}(t) + \Delta t \boldsymbol{v}\left(t + \frac{1}{2}\Delta t\right) \tag{2.12}$$

$$\boldsymbol{a}(t + \Delta t) = \Delta t \boldsymbol{f}[\boldsymbol{r}(t + \Delta t), t + \Delta t] \tag{2.13}$$

Finally, to calculate velocity at an integer timestep,

$$\boldsymbol{v}(t + \Delta t) = \boldsymbol{v}(t) + \frac{1}{2}[\boldsymbol{a}(t) + \boldsymbol{a}(t + \Delta t)]\Delta t = \boldsymbol{v}\left(t + \frac{1}{2}\Delta t\right) + \frac{1}{2}\boldsymbol{a}(t + \Delta t)\Delta t \tag{2.14}$$

Over the course of the simulation, atomic positions, forces, and energies can be used to examine system configuration, thermodynamic properties, and mass transport properties.

## 2.3 Metropolis Monte Carlo Method

In a given system of particles at temperature $T$, the probability that the system will occupy a state $i$ with energy $E_i$ is given as

$$P(E_i) = \frac{e^{-\beta(E_i)}}{Z} \quad with \quad Z = \sum_i e^{-\beta(E_i)} \tag{2.15}$$

where $\beta = \frac{1}{k_B T}$, $k_B$ is the Boltzmann constant, and $Z$ is the partition function. The expectation value of some quantity $X$ that takes the value $X_i$ at state $i$ is given as

$$\langle X \rangle = \sum_i X_i P(E_i) \tag{2.16}$$

Systems of particles are typically far too large, with far too many possible states, for the direct calculation of such quantities to be practical. Therefore, Monte Carlo methods seek to adequately sample a given random physical process in order to estimate the outcome of that process, and arrive at estimated expectation values for these quantities of interest. The Metropolis algorithm is one of the most commonly used Markov chain Monte Carlo methods.[127]

A Markov chain is a series of states through which the system evolves, changing from state $i$ to state $j$ with transition probability $T_{ij}$. Transition probabilities in a Markov chain must satisfy the following condition:

$$\frac{T_{ij}}{T_{ji}} = \frac{P(E_j)}{P(E_i)} = \frac{e^{-\beta(E_j)}/Z}{e^{-\beta(E_i)}/Z} = e^{-\beta(E_j - E_i)} \tag{2.17}$$

which the Metropolis algorithm satisfies by implementing the following acceptance probability:

$$P_a = \begin{cases} 1 & if \quad E_j \leq E_i \\ e^{-\beta(E_j - E_i)} & if \quad E_j > E_i \end{cases} \tag{2.18}$$

Following a sufficient number of iterations $N$, the ensemble average of quantity $X$ is estimated as

$$\langle X \rangle \cong \frac{1}{N} \sum_{i=1}^{N} X_i \tag{2.19}$$

# Chapter 3

## Thermodynamic Overpotentials and Nucleation Rates for Electrodeposition on Metal Anodes

### 3.1 Introduction

Metals are promising candidates for future battery anodes because they have higher theoretical capacities than the graphite-based, intercalation anodes used in lithium ion batteries, Table 1.1. Furthermore, the higher abundance of non-Li metals may result in reduced costs. However, to be viable, metal electrodes should undergo electrodeposition and -dissolution with low overpotentials. For some metals these processes are highly efficient, yet for others achieving efficient cycling is a greater challenge. For example, Table A.1 lists overpotentials extracted from cyclic voltammograms reported in the literature. These data suggest the existence of trends across the various metals. Electrodeposition involving Group I metals, Li, Na, and K, is the most efficient, whereas electrodeposition of Ca is much less so. Mg, Al, and Zn tend to fall between these extremes, with their performance dependent on electrolyte composition, scan rate, and temperature. (For example, Zn plating/stripping is typically efficient in aqueous electrolytes, but is less efficient in non-aqueous systems.)[44, 128]

These observations beg the question: Why are some metals able to plate and strip more easily than others? The overpotentials associated with electrodeposition and -dissolution provide a measure of the efficiency of these processes. In general, these overpotentials can be traced to four contributing processes: charge transfer, mass transport, chemical reaction, and crystallization.[97] As a step towards understanding efficiency differences between different metal electrodes, the present study uses first-principles calculations to evaluate 'thermodynamic overpotentials'[114] associated with plating and stripping on several low-energy surfaces of 7

metals relevant for battery applications: Li, Na, K, Mg, Ca, Al, and Zn. Reactions at terraces and step edges are considered. The thermodynamic factors probed here contribute to the reaction and crystallization components of overpotentials, and reflect heterogeneity in the adsorption/desorption energy of ions arising from inequivalent reaction sites on the electrode surface.

We find that the magnitude of the calculated overpotentials are in many cases similar to measured values, and range from tens to hundreds of mV. These calculations also capture the inefficiencies (i.e., large overpotentials) associated with ED of Ca and Mg: the calculated thermodynamic overpotentials for these metals are amongst the largest overall, which is consistent with measurements (summarized in Table A.1). We observe that the metal's crystal structure correlates with plating and stripping efficiency: the body-centered cubic alkali metals are predicted to be among the most efficient, whereas the remaining metals, all of which possess face-centered cubic or hexagonal close-packed crystal structures, are predicted to have higher thermodynamic overpotentials. As expected, electrodeposition/dissolution is most efficient at kink sites on steps,[129] while terrace sites yield the largest thermodynamic overpotentials. Quantitative differences between the calculated and experimentally measured overpotentials point towards the importance of kinetic factors, such as ohmic resistance in electrolytes, diffusion through solid electrolyte interphases, surface diffusion, electron transfer, etc. These factors are not accounted for in the thermodynamic analysis presented here.

Recognizing that the rate and density of nucleation can affect the evolution of electrodeposits,[130-133] steady-state nucleation rates are estimated using a multi-scale approach wherein a classical nucleation model is informed by the present DFT calculations.[134-136] These simulations allow for a comparison of nucleation rates during electrodeposition on different

metallic surfaces and surface features (e.g., terraces vs. step edges). The small thermodynamic overpotentials predicted for plating at step edges results in higher nucleation rates at these features, suggesting that a large population of kink sites will promote efficient cycling. Nucleation rates on terraces differ by several orders of magnitude across the metals, with rates on the body-centered cubic metals predicted to be fastest. In contrast, nucleation rates at step edges are within a few orders of magnitude of each other, indicating a relatively weak dependence on metal composition.

### 3.2 Methodology

Density functional theory calculations[116] were performed using the Vienna *ab-initio* Simulation Package (VASP).[121-123, 125] The Perdew-Burke-Ernzerhof formulation of the generalized gradient approximation[120] (GGA-PBE) was used for exchange-correlation effects, and Blöchl's projector augmented wave method[124] (PAW) was used to describe interactions between core and valence electrons. The plane-wave energy cutoff was set to 350 eV for all systems; convergence testing revealed that this cutoff was sufficient to achieve energy convergence to within 1 meV per atom. The electronic self-consistent iterations were discontinued when the change in total energy and the change in energy eigenvalues were both within $10^{-6}$ eV. Hellmann-Feynman forces were converged to within 0.02 eV/Å.

Convergence testing was performed on the primitive cells of the bulk metallic crystals to determine the optimal sizes of the Γ-centered k-point meshes. Energy convergence to within 1 meV per atom was achieved for k-point grids of density $34^3$ for Al, $16^3$ for Ca, $16^3$ for K, $28^3$ for Li, $20^3$ for Mg, $16^3$ for Na, and $27^3$ for Zn. For surface cells used in surface energy calculations and for expanded surface super-cells used in the adsorption energy calculations, Γ-centered k-point meshes of round $\left(\frac{k_0 a_0}{a}\right)$ × round $\left(\frac{k_0 a_0}{b}\right)$ × 1 were used, where $k_0$ is the k-point grid dimension

for the primitive cell, $a_0$ is the primitive cell lattice parameter (the basal plane lattice parameter in the case of the HCP metals), and a, b represent the in-plane lattice parameters of the surface cell.

During electrodeposition, atoms absorbed onto the electrode surface may subsequently diffuse to join other atoms, forming both stable and unstable clusters; some of these clusters then grow and ultimately form an electrodeposited film. The growth of a cluster is described as the sequential addition of individual atoms. The critical nucleus size is defined as the minimum size above which nuclei will spontaneously grow. Below the critical nucleus size, clusters dissolve with high probability.[97]

According to classical nucleation theory,[137-138] the time-dependent nucleation rate, J(t), can be expressed in terms of an induction time, $\tau$, and the steady-state nucleation rate, $J_0$, using Eq. (3.1):[138]

$$J(t) = J_0 \left[1 + 2\sum_{n=1}^{\infty}(-1)^n \exp\left(\frac{-n^2 t}{\tau}\right)\right] \tag{3.1}$$

where $J_0$ is expressed as:[137]

$$J_0 = N\left(\frac{S_c \omega}{g_c}\right)\left(\frac{\Delta G_c}{3\pi k_B T}\right)^{1/2} \exp\left(\frac{-\Delta G_c}{k_B T}\right) \tag{3.2}$$

Here, $N$ is the total number of atoms in the system that can contribute to the formation of nuclei, $\Delta G_c$ is the formation energy of the critical nucleus, $g_c$ is the number of atoms in the critical nucleus, $S_c$ is the surface area of the critical nucleus, and $\omega$ is the frequency of collision of the atoms with the surface.

In classical nucleation theory the formation energy of the cluster is assumed to be separable into bulk free energy and surface free energy terms. This assumption holds as long as the cluster is large enough to distinguish between its surface and bulk regions. However, very small clusters do not satisfy these criteria; the cluster does not necessarily take the crystal structure of the bulk phase, and no clear differentiation between the bulk and surface energy

contributions can be made. Therefore, an atomistic approach is necessary to determine the formation energies of clusters that are on the nanoscale. We define the critical cluster size for this study to be a single atom, and we define $\Delta G_c$ in equation 3.2 to be the reaction energy of the deposition of the initial adatom at either a terrace or step.

## 3.3 Results and Discussion

### 3.3.1 Bulk Properties

The lattice constants and bulk moduli for Al, Ca, K, Li, Mg, Na, and Zn were calculated and compared with experimental and computational values reported in the literature. Primitive cells of the metals were relaxed until the structure that minimized the total energy was achieved. The bulk moduli were calculated using a series of fixed-volume cells, allowing the lattice and basis vectors of each to relax, and fitting the total energy vs. volume data to the Murnaghan equation of state.[139] Table 3.1 lists the resulting lattice constants and bulk moduli, along with experimental values and other calculated values. There is excellent agreement between our calculated lattice vectors, experimental measurements, and those reported from other calculations which used the GGA-PBE exchange-correlation functional; in all cases the disagreement is ~2% or less. Similarly, less than 10% disagreement is observed between the calculated and measured bulk moduli. (One exception is Zn, which as noted in Ledbetter's compilation of Zn properties,[140] could be due to its relatively high anisotropy.)

To avoid spurious errors resulting from the differences in k-point sampling sets between surface and bulk simulation cells, the energies of the atoms in the bulk were calculated according to the method of Fiorentini and Methfessel.[141] Following this method, slab models of varying thicknesses were constructed for the surfaces under consideration. The in-plane surface dimensions were obtained from the bulk lattice parameters calculated previously, while the

**Table 3.1** Comparison of Calculated and Experimental Bulk Properties

| | Crystal Structure | This Work | | | Expt.[122-123,126] | | | Calc.[124-125] | |
|---|---|---|---|---|---|---|---|---|---|
| | | a (Å) | c (Å) | B (GPa) | a (Å) | c (Å) | B (GPa) | a (Å) | c (Å) |
| Li | BCC | 3.43 | | 13.9 | 3.49 | | 13.3 | 3.44 | |
| Na | BCC | 4.19 | | 7.9 | 4.23 | | 7.3 | 4.20 | |
| K | BCC | 5.29 | | 3.6 | 5.23 | | 3.7 | 5.28 | |
| Mg | HCP | 3.18 | 5.22 | 36.3 | 3.21 | 5.21 | 36.9 | 3.19 | 5.12 |
| Ca | FCC | 5.52 | | 17.8 | 5.58 | | 18.4 | 5.53 | |
| Al | FCC | 4.04 | | 77.3 | 4.05 | | 83.3 | 4.04 | |
| Zn | HCP | 2.67 | 4.97 | 60.9 | 2.66 | 4.95 | 73.3 | 2.65 | 5.12 |

thicknesses of the slabs were increased sequentially from 10 to 20 layers, maintaining 15 Å of vacuum separation between the surfaces. The total energies from the relaxed cell calculations were plotted vs. the number of layers, and the slopes of the linear portions yielded the bulk energies.

### 3.3.2 Surface Energies and Wulff Plots

In order to identify the most likely surfaces of the metal electrodes to be present during electrodeposition, equilibrium crystallite shapes were predicted by constructing Wulff plots from the calculated surface energies of several plausible facets. Surfaces with the largest areal packing densities are typically expected to exhibit the lowest surface energies; thus our surface energy calculations emphasize these surfaces. Supercells contained slabs of 10 to 22 layers in thickness, with the free surfaces separated by 20 Å of vacuum. All atoms were relaxed to their minimum force positions. The surface energy was calculated as:

$$\sigma = \frac{1}{2A}\left(E^{slab} - \frac{n_{slab}}{n_{bulk}}\mu^0\right) \tag{3.3}$$

where the surface area of the cell is given by $A = |\mathbf{a} \times \mathbf{b}|$, with **a** and **b** the surface lattice vectors, $E^{slab}$ is the total energy of the slab cell, $n_{slab}$ and $n_{bulk}$ are the number of atoms in the slab

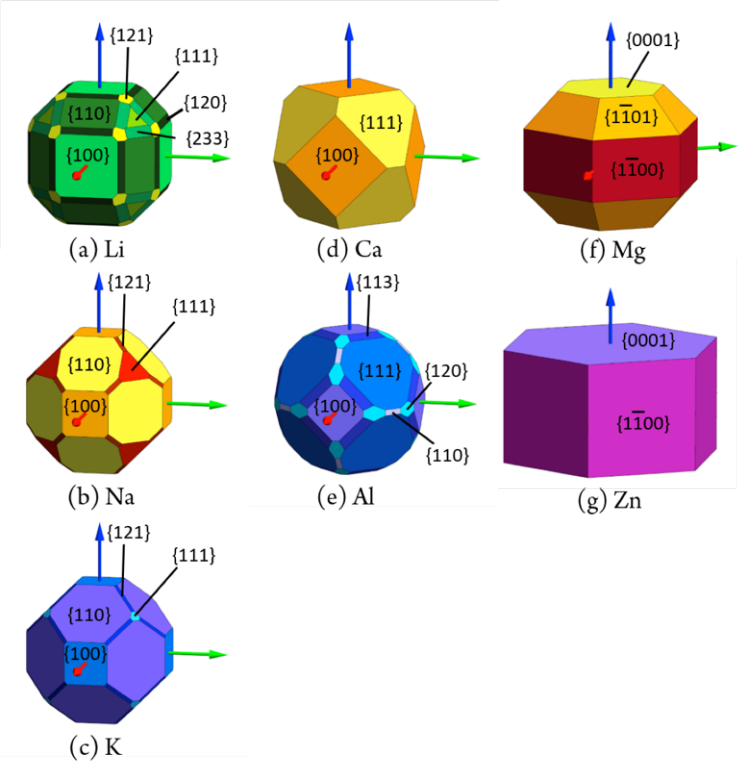


**Figure 3.1** Wulff Plots for (a) Li, (b) Na, (c) K, (d) Ca, (e) Al, (f) Mg, and (g) Zn. At ambient conditions (a) – (c) adopt the BCC crystal structure, (d) – (e) adopt the FCC structure, and (f) – (g) are HCP.

and bulk cells, respectively, and $\mu^0$ is the total energy per atom of the bulk cell, calculated using the method described above. The factor of 2 in the denominator accounts for the presence of two surfaces in the slab calculations.

Mattsson and co-workers have discussed an error present in local (LDA) and semi-local (GGA) DFT calculations on surfaces. This error arises from the rapidly decaying nature of the electron density at the solid-vacuum interface.[147-148] A simple scheme was developed to account for this error,[149-150] which in practice involves adding a correction to the surface energy as calculated with LDA, PBE, or PW91 functionals. We have applied this correction in our GGA-PBE-based surface energy calculations, which are summarized in Table 3.2. To facilitate comparisons with earlier, non-corrected calculations, our uncorrected surface energies are also

reported. As shown in the table, the present (uncorrected) surface energies are in good agreement with earlier calculations.

With these corrected surface energies, equilibrium crystallite shapes (i.e., Wulff plots) were constructed using the Wulffmaker program,[151] Figure 3.1. In addition to listing the corrected surface energies, Table 3.2 tabulates the respective fraction of the crystallite surface area of each facet. Based on the surface energies and areas, $\sigma_{weighted}$ represents the area-weighted average of the surface energy. This value is expected to be the property most closely resembling experimental measurements of the surface energy in cases where the *hkl* index of the surface is not known. Indeed, less than 12% disagreement was observed between $\sigma_{weighted}$ and the average of the experimental values for each of Al, Ca, Li, Na, and Mg. The discrepancy between theory and experiment is larger for potassium (~20%) and Zn (>40%). The absolute values for the surface energy of K are smaller than the other metals considered here, so a small variation yields a greater percentage error. It should also be noted that other calculated surface energies agree well with our calculated surface energies, including those of Zn.

There are several possible explanations for the discrepancies between the experimental and calculated surface energy of Zn, one of which is the experimental method used to obtain the surface energies. For example, Tyson[152] established a linear correlation between cohesive energy at 0 K and surface energy, while de Boer et al.[153] established a linear trend between enthalpy of vaporization and surface energy. It has been noted[154-155] that these methods use observables which are referenced to elements in the gas phase, which in the case of the divalent metals Hg, Cd, Mg, and Zn, leads to significant errors in the resulting surface energies. Furthermore, the experimental values use surface tensions measured at high temperatures, but then extrapolate to 0 K.[152, 154-155] Additionally, several authors[156-157] have noted that

**Table 3.2** Calculated surface energies (σ) for a given hkl surface facet with and without corrections (described in Refs. 129 - 130), the equilibrium area fraction of each facet as determined by the Wulff construction, and the area-weighted surface energy, $\sigma_{weighted}$.

| Metal | {hkl} | σ Uncorrected ($J/m^2$) | σ Corrected ($J/m^2$) | Other Calculations ($J/m^2$) **Refs. 61,138-141** | Area Fraction | $\sigma_{weighted}$ ($J/m^2$) | Expt. Values ($J/m^2$) **Refs. 132-133,142** |
|---|---|---|---|---|---|---|---|
| Al | {100} | 0.92 | 1.05 | 0.93, 0.92 | 0.17 | 1.01 | 1.14, 1.16, 1.14 |
| | {110} | 1.01 | 1.14 | 1.03, 0.98 | 0.02 | | |
| | {111} | 0.82 | 0.96 | 0.83, 0.80 | 0.57 | | |
| | {120} | 0.99 | 1.13 | 1.02 | 0.09 | | |
| | {113} | 0.96 | 1.09 | 0.98 | 0.15 | | |
| | {133} | 0.99 | 1.12 | 0.96 | - | | |
| Ca | {100} | 0.46 | 0.49 | 0.53, 0.44, 0.46 | 0.43 | 0.50 | 0.50, 0.49, 0.37 |
| | {110} | 0.55 | 0.58 | 0.64, 0.52, 0.54 | - | | |
| | {111} | 0.47 | 0.50 | 0.55, 0.44, 0.46 | 0.57 | | |
| | {120} | 0.55 | 0.59 | 0.55 | - | | |
| | {113} | 0.54 | 0.57 | 0.53 | - | | |
| | {133} | 0.53 | 0.56 | 0.53 | - | | |
| Li | {100} | 0.45 | 0.49 | 0.54, 0.46, 0.46 | 0.33 | 0.52 | 0.52, 0.53, 0.53 |
| | {110} | 0.49 | 0.53 | 0.59, 0.49, 0.50 | 0.33 | | |
| | {111} | 0.53 | 0.56 | 0.60, 0.53, 0.54 | 0.04 | | |
| | {114} | 0.52 | 0.55 | - | - | | |
| | {120} | 0.51 | 0.54 | 0.51 | 0.13 | | |
| | {121} | 0.54 | 0.57 | 0.54 | 0.06 | | |
| | {233} | 0.53 | 0.57 | 0.52 | 0.10 | | |
| Na | {100} | 0.23 | 0.24 | 0.26, 0.22, 0.22 | 0.20 | 0.24 | 0.26, 0.26, 0.24 |
| | {110} | 0.21 | 0.23 | 0.25, 0.22, 0.22 | 0.67 | | |
| | {111} | 0.23 | 0.25 | 0.30, 0.26, 0.25 | 0.09 | | |
| | {114} | 0.25 | 0.26 | - | - | | |
| | {120} | 0.29 | 0.30 | 0.23 | - | | |
| | {121} | 0.24 | 0.26 | 0.27 | 0.04 | | |
| | {233} | 0.25 | 0.26 | 0.25 | - | | |
| K | {100} | 0.12 | 0.12 | 0.15, 0.12 | 0.17 | 0.11 | 0.15, 0.13, 0.13 |
| | {110} | 0.11 | 0.11 | 0.14, 0.11 | 0.77 | | |
| | {111} | 0.13 | 0.13 | 0.17, 0.13 | 0.01 | | |
| | {114} | 0.13 | 0.13 | - | - | | |
| | {120} | 0.12 | 0.13 | 0.12 | - | | |
| | {121} | 0.12 | 0.13 | 0.13 | 0.05 | | |
| | {233} | 0.13 | 0.13 | 0.13 | - | | |
| Mg | {001} | 0.53 | 0.59 | 0.52, 0.54 | 0.17 | 0.69 | 0.79, 0.76, 0.47 |
| | {1$\bar{1}$0} | 0.63 | 0.70 | 0.60 | 0.37 | | |
| | {1$\bar{1}$1} | 0.65 | 0.71 | 0.63 | 0.46 | | |
| | {110} | 0.78 | 0.85 | 0.72 | - | | |
| | {111} | 0.78 | 0.84 | 0.76 | - | | |
| Zn | {001} | 0.32 | 0.41 | 0.35 | 0.46 | 0.57 | 0.99, 0.99, 0.92 |
| | {1$\bar{1}$0} | 0.61 | 0.71 | 0.53 | 0.54 | | |
| | {1$\bar{1}$1} | 0.71 | 0.80 | 0.70 | - | | |

experimentally determined surface energies are generally larger than those predicted by calculations. This results from the presence of surface defects, and the experimental surfaces being a mixture of several crystallographic planes.

### 3.3.3 Overview of Thermodynamic Overpotential Calculations

The calculation of thermodynamic overpotentials (TO) has been used extensively to examine electrocatalysts[163-171] and metal-air batteries.[114, 157, 172-180] The calculated overpotentials from these studies generally agree well with experimentally observed overpotentials. The present study adopts this methodology to explore overpotential contributions during the electrodeposition and -dissolution of metal ions at metallic negative electrodes in batteries. The goal is to examine trends in the TO as a function of anode composition and surface structure, the latter including various surface facets and adsorption/desorption sites.

Our calculations consider terrace and step sites on the electrode surface. In prior studies[114, 174] it was observed that application of the TO method at terrace sites alone led to an overestimation of the overpotential; electrochemical reactions at step and kink sites yielded predictions more in line with experimental data. Nevertheless, it has also been suggested[175, 179] that at high current densities the overpotentials resulting from charge transfer at terrace sites can contribute to the overpotential when a large number of terrace sites are available. Additionally, the limited time available for surface diffusion under high current densities implies that not all electrodeposited ions will have sufficient time to migrate to low-energy step/kink sites. Thus, it is reasonable to examine behavior at both terrace and kink sites.

Thermodynamic overpotentials for electrodeposition were calculated for a series of atomic deposition events on several low-energy surfaces of the seven metals shown in Figure 3.1. Deposition on terrace sites was simulated on 2×2 expansions of the surface unit cells. These

slabs comprised 5 – 12 layers, yielding slab thicknesses of 9 – 12 Å. All surfaces were constructed using the calculated lattice parameters of the bulk cells. The facets examined for TO's were those with the largest areal fractions: {111} and {100} for Al and Ca; {110} and {100} for Li, Na, and K; {001}, {1$\bar{1}$0}, and {1$\bar{1}$1} for Mg; {001} and {1$\bar{1}$0} for Zn. Additionally, deposition was simulated on stepped surfaces comprising 11 to 20 layers, yielding slabs 9 – 12 Å thick. Step morphologies were approximated using {210} surfaces for BCC metals, {212} for FCC metals, and {10$\bar{1}$7} for HCP metals. To limit image interactions between kink defects, 5-6 surface unit cells were used in the direction parallel to the step edge.

The energetically preferred adsorption sites were determined by a search over possible sites on each surface. This energy was recorded, and subsequent deposition reactions were evaluated in the presence of the adsorbate(s) produced in earlier steps. Each configuration was allowed to relax until it met the force convergence criterion, excluding the bottom two layers, which were fixed to maintain a bulk-like structure. This sequential adsorption-relaxation process was continued until a complete monolayer was deposited. Thermodynamic overpotentials for electro-dissolution (i.e., the reverse of electrodeposition) were calculated starting from a complete adsorbed monolayer, and running the deposition procedure in reverse.

Following earlier applications of the TO method, each deposition or stripping event, inclusively referred to here as a 'step,' is described by the equilibrium reaction: $\left(M^{z+}+ze^{-}\right) + * \leftrightarrows M^{0}*$ where $M^{z+}$ represents the metal cation incident upon the metal surface during deposition, the lone asterisk (*) represents an adsorption site on the surface, z is the oxidation number of the cation, $e^{-}$ represents an electron, and $M^{0}*$ is the adsorbed metal adatom after adsorption and reduction.

At equilibrium, the reaction energy associated with each deposition step *i* in the adsorption sequence is calculated as $\Delta E_{rxn,i}^{dep} = E_i - E_{i-1} - \mu^0$. Here, $E_i$ is the total energy of the surface cell with $i$ metal atoms adsorbed on the surface, $E_{i-1}$ is the energy of the same cell with $i - 1$ adatoms (i.e., from the previous deposition event), and $\mu^0$ is the chemical potential of the bulk metal. Equivalent reaction energies can be defined for the dissolution process, $\Delta E_{rxn,i}^{diss}$. The Nernst equation allows a reaction energy to be expressed in terms of a potential, U, as:

$$U = -\frac{\Delta E_{rxn,i}}{ze}. \tag{3.4}$$

At the equilibrium potential for each metal, the reaction free energy change will in principle vanish, $\Delta E_{rxn,i}^{dep} = \Delta E_{rxn,j}^{diss} = 0$, as there is no net reaction. However, as a result of surface heterogeneity, and differences between bonding of adatoms on the surface and within the bulk, $\Delta E_{rxn,i}^{dep}$ and $\Delta E_{rxn,i}^{diss}$ will in general not equal zero for each deposition/dissolution event. (Nevertheless, the sum of $\Delta E_{rxn,i}$ over all deposition/dissolution events that replicate the initial surface structure will be approximately zero. This can be seen by noting that such a sum corresponds to the addition/subtraction of a full monolayer to/from the surface, which is equivalent to increasing/decreasing the thickness of the slab by one bulk-like layer.)

Deviations of $\Delta E_{rxn,i}^{dep}$ and $\Delta E_{rxn,j}^{diss}$ from zero are interpreted via Eq. 3.4 as thermodynamic contributions to the overpotentials associated with plating or stripping. The most endothermic of these reaction energy changes encountered during the deposition or dissolution process is identified as its respective TO

$$\eta_{dep} = -\left(\frac{\max_i\left[\Delta E_{rxn,i}^{dep}\right]}{ze}\right); \quad \eta_{diss} = \left(\frac{\max_i\left[\Delta E_{rxn,i}^{diss}\right]}{ze}\right) \tag{3.5}$$

The sign difference between these two expressions maintains the convention such that plating potentials are negative and stripping potentials are positive.

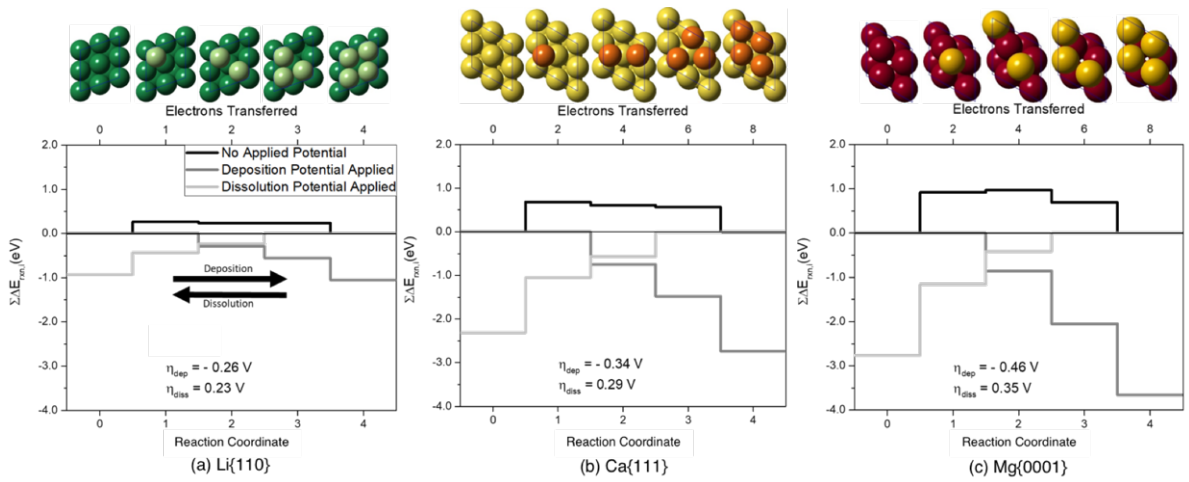


**Figure 3.2** Calculated deposition/dissolution reaction energies on the terraces of three representative metallic anodes: (a) Li{110}, (b) Ca{111}, and (c) Mg{0001}. Deposition energies are read left-to-right, and dissolution energies are read right-to-left. Reaction energies are plotted for three scenarios of applied potential, V: V = $E^0$, represented with the black line, corresponds to the equilibrium potential for a given metal; V = $\eta_{dep}$, dark grey line, where $\eta_{dep}$ is the thermodynamic overpotential for deposition; V = $\eta_{des}$, light grey line, where $\eta_{des}$ is the thermodynamic overpotential for desorption. Images above the plots show the state of the simulation cells at each reaction step. Dark green, yellow, and red represent the Li, Ca, and Mg electrode surface atoms, respectively, while light green, orange, and yellow represent Li, Ca, and Mg adatoms, respectively.

### 3.3.4 Deposition/Dissolution on Terraces

Taking the Li{110}, Ca{111}, and Mg{0001} surfaces as examples, Figure 3.2 plots the partial sums of the reaction energies, $\sum_i \Delta E_{rxn,i}$, for deposition and dissolution as a function of reaction step. Reading the plots from left to right represents the deposition reaction, whereas reading the plots from right to left represents dissolution. The thick black lines represent the equilibrium condition (i.e., operation at each metal's standard potential). Ideally, and as described above, $\Delta E_{rxn,i}^{dep} = \Delta E_{rxn,j}^{diss} = 0$ for all steps when in equilibrium. This is consistent with a scenario where the local structure of the deposited atom is similar to an atom in the bulk. However, heterogeneity in the surface structure gives rise to non-zero reaction energies. An endothermic reaction step contributes a thermodynamic barrier to the reaction.

Taking deposition on Li{110} as an example, reaction step 1, which represents depositing a single atom onto the pristine surface, has a reaction energy, $\Delta E_{rxn,1}^{dep}$ = 0.26 eV. The

reaction energy changes for the second, third, and fourth deposition steps are -0.03 eV, 0 eV, and -0.23 eV, respectively. The first deposition step is the most endothermic, and represents the limiting step. This step therefore determines the TO for deposition, $\eta_{dep}$ = -0.26 V, Eq. 3.5. Application of this potential results in all deposition steps being exothermic, $\Delta E_{rxn,i}^{dep}(V = \eta_{dep}) \leq 0$, dark grey curve; thus, deposition will occur spontaneously under these voltage conditions. Similarly, reading from right to left for dissolution, the first dissolution step $\Delta E_{rxn,1}^{diss}$ =0.23 eV is limiting, thus, $\eta_{diss}$ = 0.23 V. Application of a potential equal to 0.23 V results in all dissolution steps being exothermic, $\Delta E_{rxn,j}^{diss}(V = -\eta_{diss}) \leq 0$. This behavior is shown with the light grey curves in Fig. 3.2.

Figures 3.2a–c show that the initial deposition step onto an empty terrace is consistently the most endergonic step, independent of surface composition. This results from the initial deposition site presenting the least number of nearest neighbors for bonding; this step nucleates a new, single-atom island on top of an existing terrace. Similarly, the final deposition step, 3 → 4, is consistently the most exergonic. This behavior can be explained by the adsorbed species forming a pit in step 3, which subsequently becomes filled upon deposition (step 4). This geometry provides the maximum number of nearest neighbors available to an arriving atom. The reaction energy summed over the entire deposition process is approximately zero, as expected. The reaction energy profile between the initial and final reaction steps exhibits a plateau-like shape with nearly constant reaction energies. These energetic similarities suggest that the plateau reaction steps are structurally similar: indeed, these steps all correspond to deposition/stripping from sites at the edge of the island.

Figure 3.3 summarizes the TOs across all of the metal surfaces examined. The data are grouped by metal and arranged for a given metal according to increasing surface energy. We first

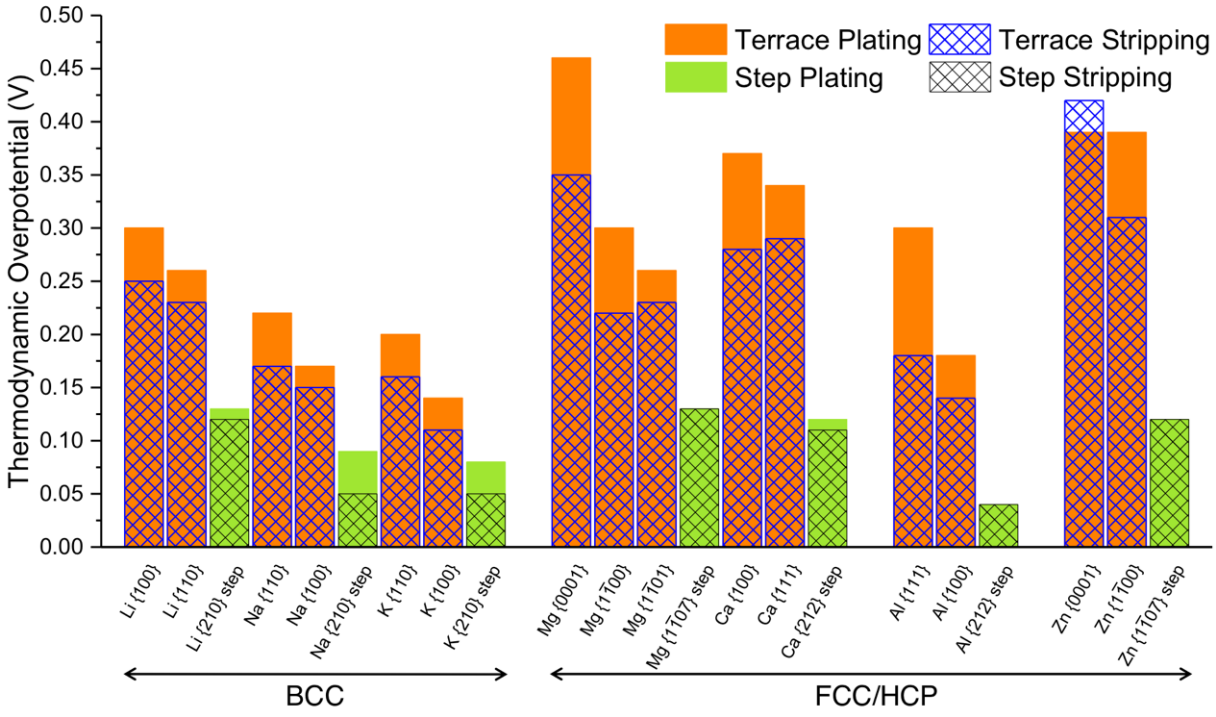


**Figure 3.3** Calculated thermodynamic overpotentials for electrodeposition and -dissolution on 7 metals as a function of surface facet and surface morphology (terraces vs. steps). Facets of a given metal are arranged according to ascending surface energy, and metals are grouped by column of the periodic table. Solid orange/green bars represent plating overpotentials on terraces/steps; cross-hatched bars represent stripping overpotentials on terraces and steps. For simplicity, only the absolute value of the overpotential is plotted.

discuss trends in the TO for terrace reactions, represented in Fig. 3.3 by the orange bars (deposition) and overlaid blue cross-hatching (dissolution). Broadly speaking, the calculated TOs on terraces are generally large, ranging from 100 to 500 mV. These values are somewhat larger than those typically observed experimentally at low current densities; see Table A.1. As discussed above, this overestimation may be due to the assumption of a terrace-based mechanism, which may not be the preferred experimental adsorption/dissolution site at low rates.

A second trend in the data pertains to the Group I metals, Li, Na, and K, which generally exhibit lower TOs compared to the Group II metals (Ca and Mg), Group III metal (Al), and the transition metal (Zn). This trend is in rough agreement with the experimental overpotentials in Table A.1, especially considering that the scan rates for the alkali metals reported there are, on

the whole, at least twice those of the Group II and Group III metals. This trend of less efficient plating in the di- and tri-valent metals would be further evident if the reaction energies, $\Delta E_{rxn,i}$, rather than the TOs, were plotted in Figure 3.3, as this would result in a doubling of the plotted values for the divalent metals, and a tripling for trivalent Al.

To explain the lower overpotentials observed for the alkali metals, we recall that they crystallize in the BCC structure, while the other metals adopt FCC or HCP lattices. BCC bulk atoms have a coordination number (CN) of 8, while the close-packed FCC and HCP systems the atoms have CN = 12. Focusing on deposition, we recall that the TO is determined by the initial deposition event. Therefore, the origin of the relatively lower overpotential for the alkali metals should be tied to the bonding environment of these initially deposited adatoms. These adatoms are coordinated by 4 or 5 nearest neighbors on the {110} and {100} surfaces, respectively. In contrast, the CNs for adatoms on the FCC and HCP metals (Mg, Ca, Al, Zn) are at best similar to the BCC surfaces, and are often smaller: CN = 3 on the close-packed {111} and {0001} surfaces; CN = 4 on the FCC {100} surfaces and on Mg $\{1\bar{1}00\}$ and $\{1\bar{1}01\}$; CN = 2 on Zn$\{1\bar{1}00\}$. Comparing the bulk CNs to the CNs of the initially deposited adatoms, we note that the BCC alkali metals have the smallest surface-to-bulk CN difference. In other words, the surface bonding environment experienced by the alkali metal adatoms is more similar to their bulk-like coordination than in the FCC or HCP systems, as illustrated in Figure A.1. We postulate that this similarity results in relatively lower TOs for the alkali metals. A similar argument based on CN has been invoked to explain differences in dendrite formation tendencies during electrodeposition of metals.[62]

Additional trends apparent in Figure 3.3 relate to the surface energy and the asymmetry between deposition and dissolution. Regarding surface energy effects, we note that the TO

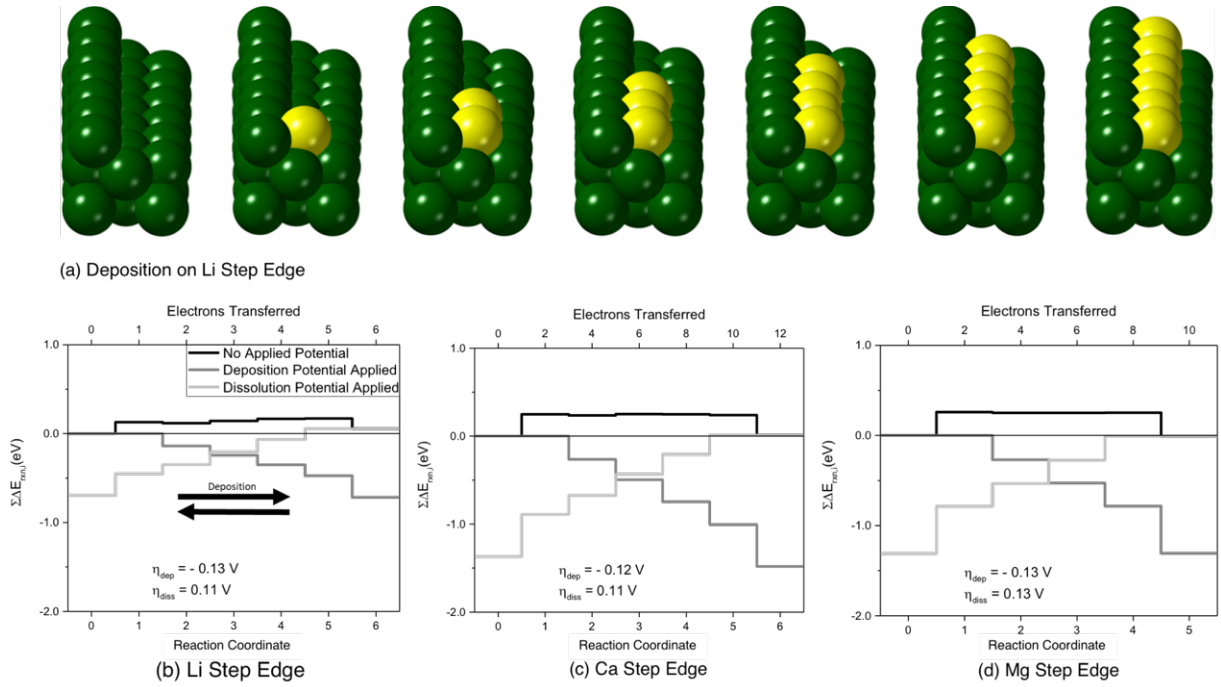


**Figure 3.4** Calculated deposition/dissolution reaction geometries (a) and energies on stepped surfaces of three representative metallic anodes: (b) Li{210}, (c) Ca{212}, and (d) Mg{10$\bar{1}$7}. In panel (a), dark green spheres represent the substrate Li atoms, and yellow represents the deposited Li atoms. Atoms are deposited along the step edge until a full row has been completed. (b-d) Reaction energies as a function of reaction step for three scenarios of applied potential, V: V = $E^0$, represented with the black line, corresponds to the equilibrium potential for a given metal; V = $\eta_{dep}$, dark grey line, corresponds to the potential needed to overcome the thermodynamic overpotential for deposition; V = -$\eta_{diss}$, light grey line, corresponds to the potential needed to overcome the thermodynamic overpotential for desorption.

generally decreases with increasing surface energy. In the case of deposition, this trend can be rationalized by recognizing that the atoms comprising a high-energy facet are more reactive to (i.e., more readily bond with) adatoms. In the case of stripping, and assuming a simple picture of surface energetics that depends only on bond counting, it will be energetically easier to remove an atom (step 4 → 3) from a high surface energy facet due to the fewer bonds that must be broken (relative to a more stable surface). This qualitatively explains the reduction in TO for stripping on higher surface energy facets.

### 3.3.5 Deposition/Dissolution on Step Edges

Figure 3.4 shows the calculated reaction energies for deposition and dissolution on selected stepped surfaces for Li, Ca, and Mg. Data for the other 4 metals are given in Figures A.2 – A.4. Similar to the energy profile for plating/stripping on terraces, Fig. 3.2, the limiting reaction on stepped surfaces is always the first deposition or stripping event, which corresponds to the nucleation of a kink. An additional similarity with the terraced surfaces is the plateau-like shape of the reaction profile. The reactions comprising the plateau region exhibit similar energies because they all correspond to the same process, i.e., propagation of a kink along the step edge.

An important difference between the stepped and terraced surfaces is the magnitude of the TO. For the systems depicted in Fig. 3.4, the TO ranges from -0.13 to 0.13 V. These values are roughly 2-3 times smaller than those for terraces reported in Fig. 3.2. The trend of the stepped surfaces exhibiting significantly smaller TO's is maintained across the other metals, as shown in Fig. 3.3. This trend can be understood using a simple bond-counting argument: adsorption at a step-edge or kink presents a larger number of coordinating atoms compared to adsorption on a terrace.

### 3.3.6 Steady-State Nucleation Rate

In the case of nucleation during the electrodeposition process, the frequency of collision of the atoms with the surface, $\omega$ in Eq. 3.2, is defined as $i_0/ze$, in which $i_0$ is the exchange current density.[97] Moreover, under an applied potential, $U_{app}$, the formation energy of the critical nucleus, $\Delta G_c$, can be written as:[97]

$$\Delta G_c = -ze(\eta_{dep} - U_{app}) \tag{3.6}$$

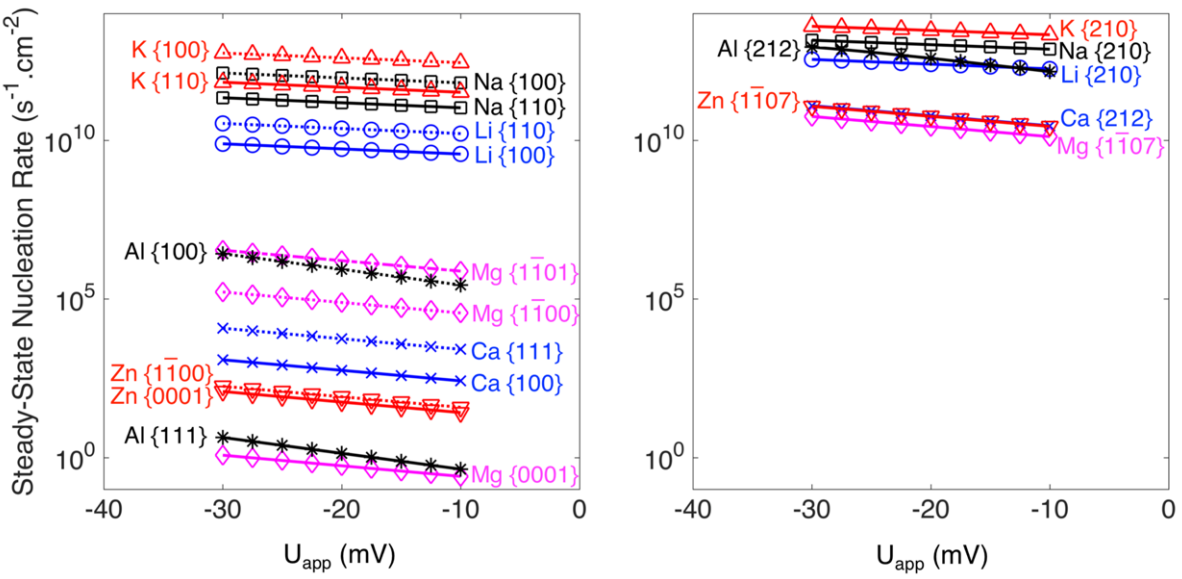


**Figure 3.5** Steady-state nucleation rate as a function of applied potential, $U_{app}$, for plating on (a) terrace and (b) step sites on seven metal negative electrodes. $U_{app}$ is varied from -30 to -10 mV vs. the corresponding equilibrium potential for each metal. Nucleation model was the contribution of Dr. Saeed Kazemiabnavi and Prof. Katsuyo Thornton.[163]

The calculated steady-state nucleation rate and formation energy of the critical nucleus for electrodeposition on terrace and step sites at an applied potential of –10 mV are listed in Table A.2.

Figure 3.5 shows the steady-state nucleation rate as a function of applied potential for electrodeposition on terrace and step sites obtained using our calculated TOs as input to Eq. 3.1. The relatively small TOs predicted for the alkali metals (Li, Na, and K) generally results in higher steady-state nucleation rates compared to the other metals, regardless of whether plating occurs on terraces or at steps. However, as discussed earlier and as demonstrated in Figures 3.2-3.4, the TO for plating at step sites is smaller than that on terrace sites. This results in a steady-state nucleation rate that is several orders of magnitude higher at steps compared to terrace sites, independent of the choice of metal. This is attributed to the exponential relationship between the reaction energies of initial deposition and the nucleation rate as defined by Eq. 3.2. The relative

ordering of the surfaces/metals with respect to their nucleation rate is similar for step and terrace deposition sites. Nevertheless, the rates on the step sites are more tightly clustered, suggesting that deposition in these cases is less sensitive to the metal's composition.

Figure 3.5 also illustrates that the nucleation rate increases with the application of a more negative potential, as expected. The slope of each line is proportional to the number of transferred electrons, z, during the electrochemical reduction of the corresponding metallic ion. By applying a negative potential, $U_{app}$, the formation energy of the critical nucleus decreases by zeU, which exponentially increases the steady-state nucleation rate.

## 3.4 Conclusions

The thermodynamic overpotentials and associated nucleation rates are calculated for seven metals (Li Na, K, Mg, Ca, Al, and Zn) considered as potential anodes for future rechargeable batteries. The magnitude of the calculated overpotentials are in many cases similar to measured values, and range from tens to hundreds of mV. These calculations also provide insight regarding the inefficiencies associated with electrodeposition of Ca and Mg: the calculated overpotentials for these metals are amongst the largest overall, consistent with measurements.

We observe that the metal's crystal structure correlates with the efficiency of plating and stripping: body-centered cubic alkali metals are predicted to be among the most efficient systems, whereas the remaining metals, all of which possess close-packed crystal structures, are predicted to have higher thermodynamic overpotentials. As expected, electrodeposition/dissolution is most efficient at kink sites on steps, while undercoordinated terrace sites yield the largest thermodynamic overpotentials. Trends involving surface energies are discussed. Differences between the calculated overpotentials and experimental measurements

highlight the importance of kinetic factors (which are not accounted for in the present approach), such as ohmic resistance in electrolytes, diffusion through solid electrolyte interphases, surface diffusion, electron transfer, etc.

Steady-state nucleation rates were estimated using a classical nucleation model informed by the present DFT calculations. These simulations allow for a comparison of electrodeposition nucleation rates on different metallic surfaces and surface features (e.g., terraces vs. step edges). The small thermodynamic overpotentials predicted for plating at step edges results in higher nucleation rates at these features, suggesting that a large population of kink sites will promote efficient cycling. Nucleation rates on terraces differ by several orders of magnitude across the metals, with rates on the body-centered cubic metals predicted to be fastest. In contrast, nucleation rates at step edges are within a few orders of magnitude of each other, indicating a weak dependence on metal composition. This approach demonstrates a technique for linking atomistic data with a continuum nucleation model, and highlights the sensitivity of nucleation behavior on the structure and composition of the electrode surface.

# Chapter 4

## Anisotropic Elastic Properties of Battery Anodes

### 4.1 Introduction

The propensity for metallic anodes to form dendrites during charging implies that the use of interfacial protection schemes or solid electrolytes (SE) may be necessary for these systems to be practical. In principle, a stiff and dense SE could prohibit dendrite initiation simply by pressing against the anode. The pressure applied by the SE is expected to inhibit inhomogeneous metal deposition and the protrusions (i.e. dendrite nuclei) that would result.[101] This hypothesis has sparked interest in understanding the mechanical properties of the anode, the SE, and their interfacial region. For example, Monroe and Newman proposed a relationship between a SE's elastic properties and its ability to mitigate dendrites.[102] To suppress the formation of surface protrusions (i.e., dendrite nuclei) on the anode, their model suggested that the ratio of the shear modulus of the SE to that of the anode should be greater than approximately two.

Nevertheless, numerous examples exist of lithium metal-based cells undergoing failure due to dendrite formation.[103-110] These failures have been observed at relatively low current densities (0.2 $mA/cm^2$) and in cells using solid electrolytes possessing shear moduli far in excess of that for Li (~4.25 GPa).

These observations suggest that mechanical phenomena beyond (or in combination with) the elastic regime may be important in understanding the failure of solid state batteries. Consequently, other mechanical properties related to the anode, solid electrolyte, and their interfaces have been topics of recent interest. For example, Barai *et al*. developed a model of the metal/SE interface that included the effects of plastic deformation.[182] They concluded that increasing the yield strength of the solid electrolyte can stabilize metal deposition, even if the

SE's elastic modulus is significantly lower than the Monroe and Newman criterion. Other work has explored the role of pressure,[183] the possibility for increased mechanical strength at small sizes,[184-190] electrochemically activated mechanisms such as "grain coating,"[191] stress accumulation at the electrode/SE interface and at defects in the SE,[107] creep within the anode,[192-194] and softening at grain boundaries.[195]

To aid in the design of robust solid electrolyte/metal anode interfaces, as well as to inform strategies for implementing Si-based anodes, the present study employs first-principles calculations to evaluate the elastic constants and aggregated, polycrystalline elastic properties of 8 next-generation anode materials, including Al, Ca, Li, Na, K, Mg, Zn, and Si. Based on the calculated elastic constants, the anisotropic Young's moduli and shear moduli are derived. Additionally, the effects of temperature on these elastic properties are evaluated at 150 K, 300 K, and 450 K using the quasi-harmonic approximation.[196] Accurate predictions of the elastic properties are shown to require careful convergence of the elastic constants with respect to the density of the k-point grid. Prior first-principles calculations have successfully predicted the elastic constants for metals,[197-198] Si,[199] and alloys.[200-201]

In general, excellent agreement between the present calculations and experimental measurements is obtained for the elastic constants and polycrystalline elastic moduli. The calculated elastic properties are mapped as a function of crystallographic direction. Extrema in these properties are identified under axial and shear loading. Interestingly, in the cubic systems the locations of these extrema are diametrically opposed: under axial loading the stiffest (most compliant) orientation is <111> (<100>), while in shear <100> (<111>) is the stiffest (most compliant).

The alkali metals (Li, Na, and K) are found to be the softest metals overall, with softness increasing with atomic number. The alkali metals are also the most anisotropic, and, unlike the other elements examined here, the degree of anisotropy of the alkali metals increases with increasing temperature. A larger degree of anisotropy implies that the mechanical properties of these metals will vary more significantly with orientation, potentially resulting in different likelihoods for dendrite formation/growth at the anode/SE interface. In contrast, Al and Mg are the most isotropic metals examined; their elastic properties are more sensitive to temperature than for the other elements studied here. Si, the only non-metal, is the stiffest overall.

Based on the criterion of Monroe and Newman, the present calculations suggest that the thiophosphates are only appropriate as a solid electrolyte in conjunction with anodes based on K. In the case of anti-perovskite-based SE's, anodes based on alkali metals (Li, Na and K) would satisfy the MN criterion, while NASICON-type and garnets further expand the number of suitable anode compositions to include Ca and Mg in addition to the alkali metals. Perovskite SEs satisfy MN for all anode compositions studied here except Si. In sum, the directionally-resolved and temperature-dependent elastic properties reported here will be of value in the construction of mechano-electrochemical models of phenomena at metal/solid electrolyte interfaces.

## 4.2 Methodology

Density functional theory calculations[116] were performed using the Vienna *ab-initio* Simulation Package (VASP).[121-123, 202] Blöchl's projector augmented wave method[124] (PAW) was used to describe the interaction of core and valence electrons, and a conjugate-gradient algorithm with corrector steps was used to relax the ion positions. For the metallic systems, orbital occupancies were determined using the Methfessel-Paxton method[203] with a smearing

width of 0.1 eV; a Gaussian-type method with a sigma value of 0.1 eV was used for Si. The electronic self-consistency iterations were terminated when the change in total energy and the change in electronic eigenvalues were both less than $10^{-7}$ eV. Hellmann-Feynman forces were converged to within 0.005 eV/Å.

The plane-wave cutoff energies used for Al, Ca, Li, Na, K, Mg, Zn, and Si were 400 eV, 300 eV, 300 eV, 250 eV, 360 eV, 300 eV, 610 eV, and 420 eV, respectively. Extremely dense k-point sampling mesh densities were employed, with respective values of $40^3$, $19^3$, $49^3$, $44^3$, $27^3$, $40^3$ , $37^3$, and $14^3$. These densities often exceed those used in prior studies; for example, in the Dryad data repository, de Jong et al.[204-205] used grids of size 45000 (~$35^3$) for Al, 20000 (~$27^3$) for Li and Na, and 7000 (~$19^3$) for K, Ca, Mg, Zn, and Si. Our tests confirm that thorough k-point sampling is necessary for achieving converged elastic properties, as illustrated in Figure B.1. Further details regarding the convergence behavior of the elastic properties with respect to the plane-wave cutoff energy and k-point sampling are provided in the Appendix.

A total of 5 exchange-correlation functionals were evaluated for each element by comparing the calculated elastic constants with experimental data measured at absolute zero, or at low temperatures approaching 0 K. The results of these tests are summarized in Table B.2. The exchange-correlation functional of Perdew-Burke-Ernzerhof[120] (PBE) was determined to most closely match experimental data, and was therefore used for the remainder of the study.

The stiffness matrix was calculated via a stress-strain relationship.[206] Three axial and three shear strains of ±1% of the lattice vector were applied to the unit cell, and the resulting stresses were calculated. The elements of the stiffness matrix, $C_{ij}$, were derived from a series of linear least-squares fits to this stress-strain data. The compliance matrix, $S_{ij}$, was calculated as the inverse of the stiffness matrix. It should be noted that the value that VASP reports as $C_{44}$ is

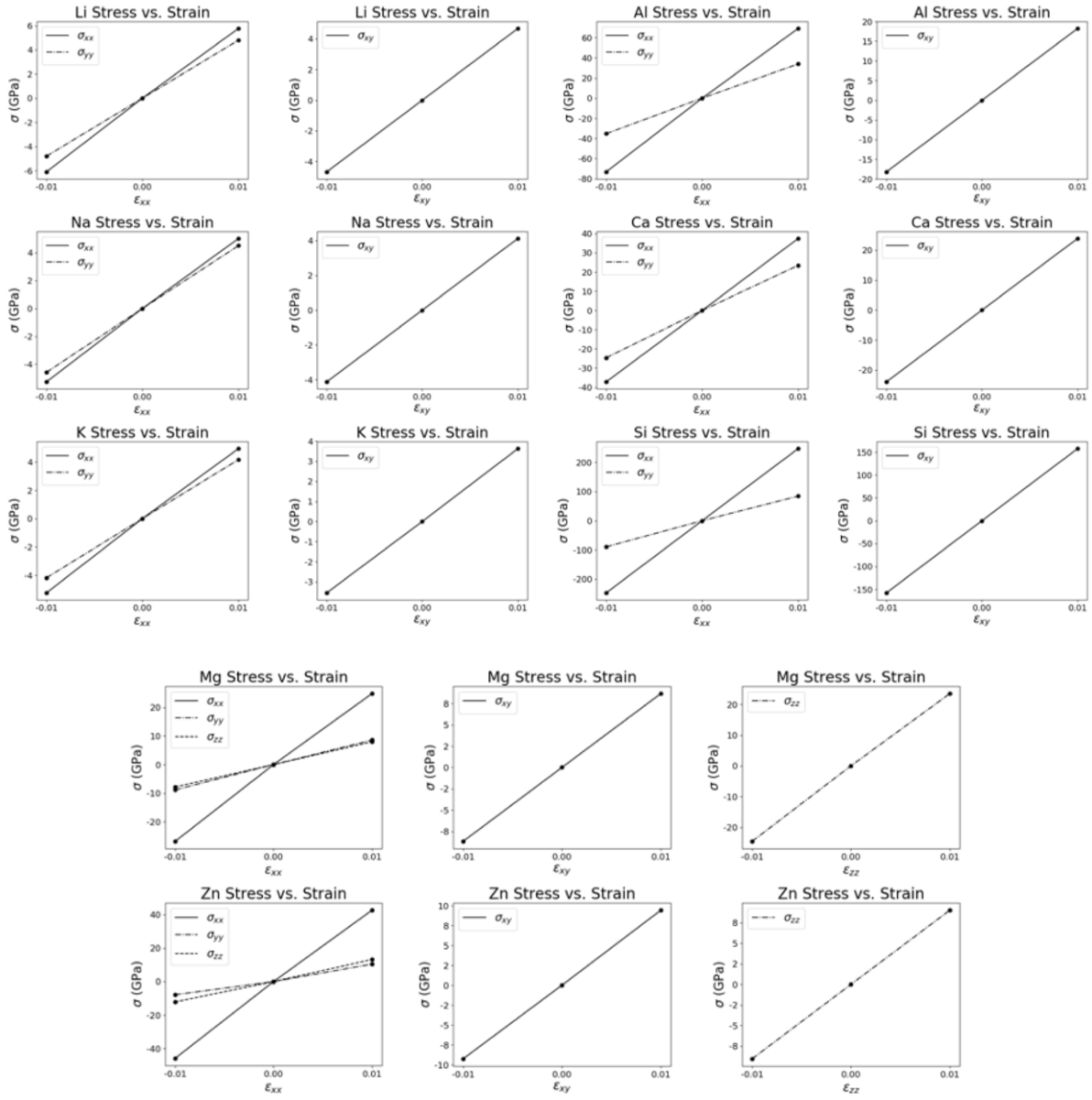


**Figure 4.1** Example stress-strain curves for the explored materials. The small strains yield linear stress profiles, indicating elasticity.

defined by Nye[207] as the $C_{66}$ stiffness coefficient; Nye's convention is used for all elastic properties discussed hereafter. Example stress-strain curves are shown in Figure 4.1, indicating that the strains occur within the elastic regime.

Several elastic properties were calculated from the elements of the compliance and stiffness matrices. The bulk and shear moduli of aggregated, polycrystalline materials as defined by Voigt, Reuss, and Hill[208] were calculated according to

$$B_{Voigt} = \frac{C_{11}+C_{22}+C_{33}+2(C_{12}+C_{23}+C_{31})}{9}$$

$$B_{Reuss} = \frac{1}{S_{11}+S_{22}+S_{33}+2(S_{12}+S_{23}+S_{31})}$$

$$B_{Hill} = \frac{B_{Voigt}+B_{Reuss}}{2} \quad (4.1)$$

$$G_{Voigt} = \frac{C_{11}+C_{22}+C_{33}-(C_{12}+C_{23}+C_{31})+3(C_{44}+C_{55}+C_{66})}{15}$$

$$G_{Reuss} = \frac{15}{4(S_{11}+S_{22}+S_{33})-4(S_{12}+S_{23}+S_{31})+3(S_{44}+S_{55}+S_{66})}$$

$$G_{Hill} = \frac{G_{Voigt}+G_{Reuss}}{2} \quad (4.2)$$

from which the Voigt, Reuss and Hill elastic moduli and Poisson ratios were calculated as

$$E = \frac{9BG}{3B+G}, \nu = \frac{3B-2G}{2(3B+G)} \quad (4.3)$$

Anisotropic elastic properties were also calculated from the stiffness and compliance matrices. For comparison, the amount of elastic anisotropy was determined using the Universal Anisotropy index ($A^U$),[209]

$$A^U = 5\left(\frac{G_{Voigt}}{G_{Reuss}}\right) + \left(\frac{B_{Voigt}}{B_{Reuss}}\right) - 6 \quad (4.4)$$

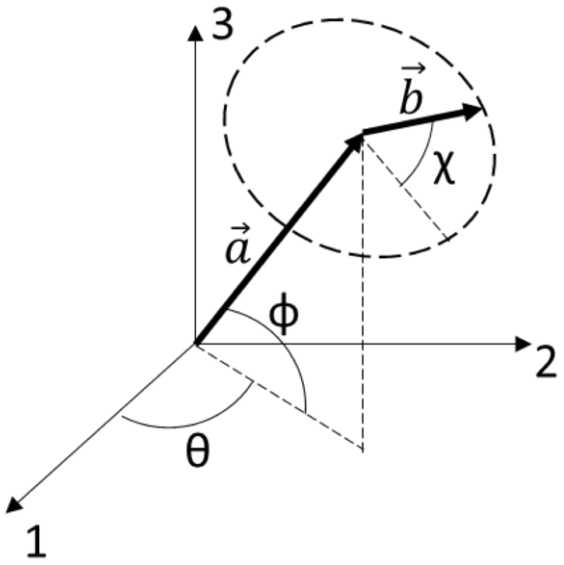


**Figure 4.2** Coordinate system for evaluation of directionally-resolved elastic properties. $\vec{b}$ is anti-parallel to $\vec{3}$ when $\chi=\phi=0°$.

for which a value of 0 indicates perfect isotropy, and a larger value indicates greater anisotropy. The anisotropic Young's[207] and shear[210] moduli are given, respectively, as

$$E(a_1, a_2, a_3)^{-1} = S_{11}{a_1}^4 + S_{22}{a_2}^4 + S_{33}{a_3}^4 + (2S_{12} + S_{66}){a_1}^2{a_2}^2 + (2S_{23} + S_{44}){a_2}^2{a_3}^2 + (2S_{13} + S_{55}){a_1}^2{a_3}^2 \quad (4.5)$$

$$\begin{aligned} G(a_1, a_2, a_3, b_1, b_2, b_3)^{-1} &= 4\left(S_{11}{a_1}^2{b_1}^2 + S_{22}{a_2}^2{b_2}^2 + S_{33}{a_3}^2{b_3}^2\right) + 8(S_{12}a_1b_1a_2b_2 + S_{23}a_2b_2a_3b_3 \\ &+ S_{13}a_1b_1a_3b_3) + S_{44}(a_2b_3 + a_3b_2)^2 + S_{55}(a_1b_3 + a_3b_1)^2 \\ &+ S_{66}(a_1b_2 + a_2b_1)^2 \end{aligned} \quad (4.6)$$

Here, $\vec{a}$ is a vector that points radially from the origin, and represents a vector normal to a surface on a crystal that is centered at the origin. Vector $\vec{b}$ is perpendicular to $\vec{a}$, as indicated in

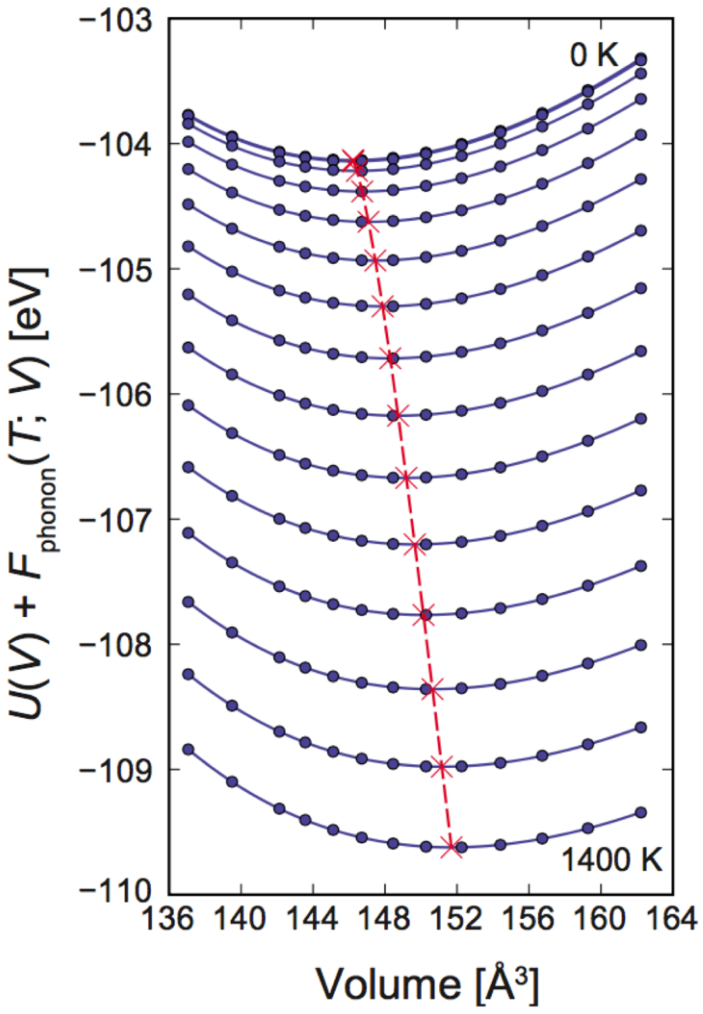


**Figure 4.3** Predicted lattice expansion of $Ti_3SiC_2$ as a function of temperature as implemented via the Phonopy code. Adapted from Togo *et al.*[209]

Figure 4.2, and represents the direction of a shear stress parallel to the surface that is normal to $\vec{a}$.

The Cartesian components of these vectors are defined as:

$$\begin{aligned} a_1 &= \cos\phi\cos\theta \\ a_2 &= \cos\phi\sin\theta \\ a_3 &= \sin\phi \\ b_1 &= \sin\phi\cos\theta\cos\chi - \sin\theta\sin\chi \\ b_2 &= \sin\phi\sin\theta\cos\chi + \cos\theta\sin\chi \\ b_3 &= -\cos\phi\cos\chi \end{aligned} \tag{4.7}$$

The angles $\theta$ and $\varphi$ are the polar and azimuthal angles, respectively, while $\chi$ defines the direction of the shear, given by $\vec{b}$.

The effect of temperature on the calculated elastic properties was evaluated within the quasi-harmonic approximation[211] (Phonopy code).[212] An example plot showing the lattice expansion of $Ti_3SiC_2$ as a function of temperature calculated with the Phonopy code is shown in Figure 4.3. Equilibrium volumes were calculated at three temperatures: 150 K, 300 K, and 450 K. Elastic constants at these temperatures were calculated using the lattice volumes predicted by the quasi-harmonic calculations (Table B.3). Following Ref. 196, static energy contributions to the free energy were assumed to be dominant, thus allowing for the vibrational free energy and thermal electronic free energy contributions to be neglected.[196] Hence, the primary impact of finite temperatures on the elastic properties is assumed to arise from thermal expansion or contraction of the lattice.

## 4.3 Results and Discussion

### 4.3.1 Elastic Constants

Emphasis was placed on achieving converged predictions with respect to sampling of the Brillouin zone (i.e., k-point sampling). The more complex Fermi surface of metals generally

**Table 4.1** Calculated elastic constants, $C_{ij}$ and Isotropic Elastic Properties (in GPa), as a function of temperature. For comparison, experimental values within 30 K of 300 K are also reported ("Expt: 300±30").[a]

| | Temp. (K) | $C_{11}$ | $C_{12}$ | $C_{13}$ | $C_{33}$ | $C_{44}$ | % error | B | E | G | $A^U$ |
|---|---|---|---|---|---|---|---|---|---|---|---|
| Al | 150 | 112.5 | 55.0 | | | 29.8 | 9.6 | 74.2 | 77.9 | 29.4 | 0.00 |
| | 300 | 108.8 | 53.0 | | | 28.4 | 8.0 | 71.6 | 74.8 | 28.2 | 0.00 |
| | Expt: 300±30 | 108 ± 2.1 | 61.5 ± 2.1 | | | 28.3 ± 0.3 | | 76.9 ± 2.1 | 70.4 ± 0.4 | 26.1 ± 0.2 | |
| | 450 | 104.3 | 50.7 | | | 26.7 | 9.4 | 68.6 | 71.0 | 26.7 | 0.00 |
| Ca | 150 | 22.3 | 14.6 | | | 13.9 | | 17.2 | 21.5 | 8.3 | 2.30 |
| | 300 | 21.8 | 14.2 | | | 13.8 | 13.6 | 16.7 | 21.3 | 8.3 | 2.29 |
| | Expt: 300±30 | 25.3 ± 2.5 | 17.1 ± 1.1 | | | 15.2 ± 1.2 | | 19.8 ± 1.6 | 23.5 ± 2.5 | 9.0 ± 1.0 | |
| | 450 | 21.3 | 13.7 | | | 13.6 | | 16.2 | 21.0 | 8.2 | 2.26 |
| Li | 150 | 14.9 | 12.2 | | | 11.2 | 7.6 | 13.1 | 13.5 | 5.1 | 7.59 |
| | 300 | 14.3 | 11.6 | | | 11.0 | 15.0 | 12.5 | 13.2 | 5.0 | 7.60 |
| | Expt: 300±30 | 13.3 ± 0.2 | 11.3 ± 0.2 | | | 8.8 ± 0.1 | | 12.0 ± 0.2 | 10.7 ± 0.1 | 4.0 ± 0.0 | |
| | 450 | 13.6 | 11.0 | | | 10.7 | | 11.9 | 12.8 | 4.9 | 7.66 |
| Na | 150 | 7.9 | 6.9 | | | 5.9 | 7.7 | 7.2 | 6.5 | 2.4 | 12.61 |
| | 300 | 7.1 | 6.3 | | | 5.5 | 18.1 | 6.6 | 6.0 | 2.2 | 13.17 |
| | Expt: 300±30 | 6.3 ± 0.9 | 5.1 ± 0.9 | | | 4.8 ± 0.8 | | 5.5 ± 0.9 | 5.8 ± 0.6 | 2.2 ± 0.3 | |
| K | 150 | 3.8 | 3.0 | | | 2.5 | 8.3 | 3.3 | 3.3 | 1.2 | 5.78 |
| | 300 | 3.4 | 2.8 | | | 2.4 | 10.1 | 3.0 | 3.0 | 1.1 | 6.50 |
| | Expt: 300±30 | 3.8 ± 0.4 | 3.2 ± 0.1 | | | 2.3 ± 0.4 | | 3.4 ± 0.2 | 2.7 ± 0.7 | 1.0 ± 0.3 | |
| Mg | 150 | 60.9 | 22.6 | 17.9 | 59.7 | 19.2 | 10.8 | 33.1 | 46.1 | 18.2 | 0.09 |
| | 300 | 56.1 | 20.7 | 16.8 | 54.4 | 17.7 | 13.6 | 30.6 | 42.2 | 16.6 | 0.08 |
| | Expt: 300±30 | 58.9 ± 1.0 | 25.4 ± 1.0 | 21.0 ± 1.2 | 61.1 ± 1.0 | 16.5 ± 0.2 | | 34.8 ± 1.1 | 44.6 ± 0.1 | 17.3 ± 0.1 | |
| | 450 | 50.4 | 18.6 | 15.6 | 48.2 | 15.9 | | 27.6 | 37.6 | 14.8 | 0.08 |
| Zn | 150 | 140.7 | 35.7 | 46.3 | 40.3 | 29.2 | 25.1 | 51.8 | 70.7 | 27.8 | 4.17 |
| | 300 | 114.3 | 30.8 | 41.0 | 33.7 | 24.3 | 30.1 | 42.9 | 54.9 | 21.3 | 5.29 |
| | Expt: 300±30 | 161 ± 8.6 | 30.2 ± 7.5 | 48.0 ± 7.1 | 60.7 ± 6.4 | 39.5 ± 0.9 | | 64.3 ± 6.2 | 101 ± 3.5 | 40.6 ± 1.3 | |
| | 450 | 76.7 | 33.5 | 37.3 | 26.6 | 14.2 | 44.2 | 27.3 | 23.5 | 8.7 | 27.52 |
| Si | 150 | 150.1 | 53.9 | | | 85.9 | 11.8 | 85.9 | 150.3 | 62.2 | 0.22 |
| | 300 | 149.5 | 53.3 | | | 85.3 | 12.6 | 85.3 | 149.9 | 62.1 | 0.22 |
| | Expt: 300±30 | 166 ± 0.9 | 64.5 ± 0.8 | | | 80.5 ± 1.8 | | 98.6 ± 0.9 | 164 ± 2.1 | 67.1 ± 0.9 | |
| | 450 | 148.4 | 52.2 | | | 84.3 | | 84.3 | 149.2 | 61.9 | 0.22 |

[a] $\%\ error\ = \sqrt{\frac{1}{n}\sum_{i=1}^{n}\left(\frac{C_{i,expt}-C_{i,calc}}{C_{i,expt}}\right)^2}\ x\ 100$. Here, i indexes the Voigt subscripts of the elastic coefficients, and $n$ = 3 for cubic systems and $n$ = 5 for hexagonal systems.

requires denser k-point sampling than for materials with a band gap (semi-conductors and insulators). These sampling requirements are further compounded by the lattice strains needed to evaluate elastic constants; these strains lower the symmetry of the Brillouin zone, thereby increasing the number of symmetry-distinct k-points that must be sampled. Finally, materials

with small elastic constants, such as the alkali metals, present additional challenges to achieving convergence. For example, in the case of lithium, use of an insufficient k-point mesh results in an elastic tensor that is not positive definite, and therefore violates the Born stability conditions.[204-205, 213-214] (See Fig B.1)

Calculated elastic constants for the eight elements examined in this work are summarized in Table 4.1. The cubic elements, (Al, Ca, Li, Na, K, and Si) possess three independent elastic constants, $C_{11}$, $C_{12}$, and $C_{44}$, while the elements with hexagonal close-packed crystal structures, Mg and Zn, possess two additional independent elastic constants, $C_{13}$ and $C_{33}$. The elastic constants are calculated for three temperatures, 150 K, 300 K, and 450 K, using the lattice constants determined for each temperature from the quasi-harmonic approximation. The elastic constants and elastic properties of Na and K were not calculated at 450 K because this temperature exceeds their melting temperatures (371 K and 337 K, respectively). As expected, in all cases the elastic constants decrease as the temperature increases.[215] Table B.3 presents a comparison between the calculated and experimental lattice constants as a function of temperature.

Overall, very good agreement is achieved between the calculated and experimentally measured elastic coefficients. The PBE functional, which was observed to be the most accurate functional out of those examined, yields an average error of 8.6% at low temperatures, Table B.2. (See Table B.4 for a summary of experimental data at 150 K, 300 K, and 450 K). Deviations between the experimental data and the values calculated here are also summarized in Table 4.1. The calculations on Al exhibit the best agreement with experiments, with deviations across all temperatures of less than 10%. The calculated values for Si, Ca, Li, Na, K, and Mg deviate from experiment by 3-18% across all temperatures, with the size of the deviation

increasing with temperature. (One exception is Na, which has a greater difference at 0 K than at 150 K). It should be noted that the alkaline metals (Li, Na, and K) have small elastic coefficients which tend to inflate the deviation percentages reported in Table 4.1. Disagreement between the calculated and experimental coefficients is greatest for Zn, ranging from 22.7% - 44.2%; the variation in the elastic constants with temperature for Zn is also much greater than for the other materials. Nevertheless, the Born stability requirements for Zn are satisfied at all temperatures, and the 0 K values calculated by other authors[205] are consistent with the values reported here (Table B.2). Table 4.1 shows that a relatively large standard deviation exists in the experimental elastic constant data for Zn.

### 4.3.2 Isotropic Elastic Properties

Figure 4.4 summarizes the calculated isotropic elastic properties, as determined using equations 4.1–4.3 and the elastic coefficients in Table 4.1. These data indicate that the alkali metals generally have the smallest values of these moduli (i.e., are the softest), followed in order of increasing stiffness by Ca, Mg, Zn, Al, and Si. The values of the moduli for Li, Na, K, Ca, and Si show little change with temperature, while Mg, Al, and Zn exhibit greater sensitivity to temperature. As with the elastic constants, there is generally excellent agreement between experiments and the calculated isotropic values for E and G (see Tables 4.1, B.5, and B.6). With the exception of Si and Zn, deviations are on the order of a few GPa. For Si, deviations range from 7 - 9%, and 33-79% for Zn.

To place these values in context, it is helpful to compare with the experimental Young's modulus for several solid electrolytes. These moduli vary widely across the different SE classes:

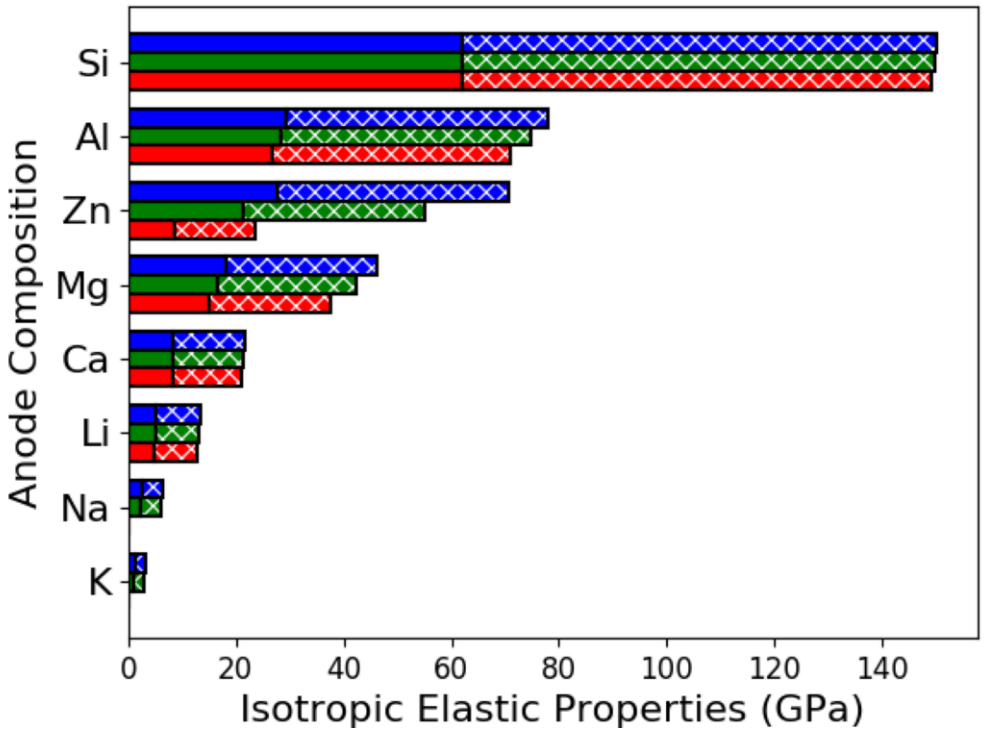


**Figure 4.4** Variation of the isotropic elastic moduli with temperature. Differently colored bars correspond to 150 K (blue), 300 K (green), and 450 K (red). The entire bar length (solid + hatched) represents the Young's modulus, while the solid portion of the bar represents the shear modulus.

10 – 100 MPa for polymers,[216-217] 17 – 36.9 GPa for alkaline thiophosphates,[218-220] 77 GPa for LiPON,[221] 57.4 – 99.7 GPa for alkaline anti-perovskites,[218, 222] 115 – 143.7 GPa for NASICON,[218, 223] 140 – 175.1 GPa for garnets,[218, 223-224] and 143 – 262.5 GPa for perovskites.[218, 223] With the exception of the polymer-based systems, all of these SE classes exhibit values for *E* that are larger than those calculated for alkali metal anodes.

### 4.3.3 Anisotropic Young's Moduli

Figure 4.5 plots the anisotropic behavior (i.e., directional dependence) of the Young's and shear moduli at 300 K. Here, solid bars represent the minimum values of the modulus, and the hatched bars represent the difference between the maximum and minimum values. The length of the hatched bar relative to the length of the entire bar reflects the amount of anisotropy, which is quantified by $A^U$, and listed in Table 4.1. These data show that Al is the most isotropic element

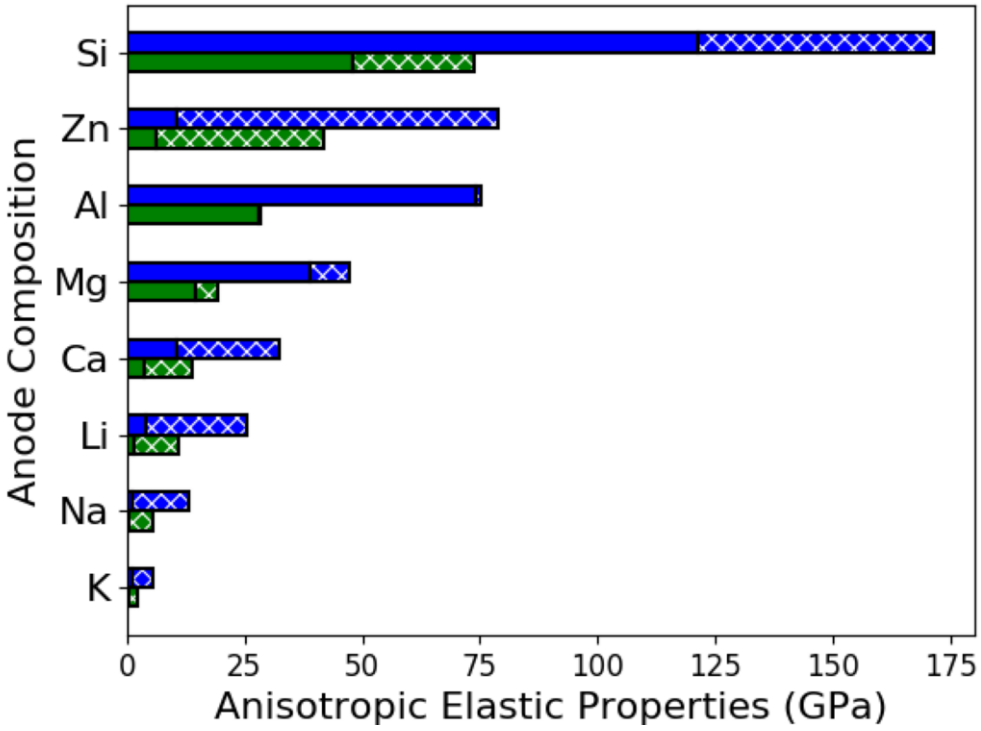


**Figure 4.5** Anisotropy in elastic moduli. Differently colored bars correspond to the anisotropic Young's (blue) and shear (green) modulus at 300 K. The entire bar (solid + hatched) represents the maximum value, and the solid bar represents the minimum value.

considered here, having $A^U = \sim 0$. In contrast, the alkali metals ($A^U$ = 6 to 13) and Zn ($A^U$ =4 to 27) exhibit significant anisotropy in their elastic moduli. The alkaline earths and Si fall between these two extremes.

Figure 4.6 shows the calculated Young's moduli, *E*, at 300 K as a function of crystallographic direction for each of the 8 elements examined. (Figures B.18 and B.19 show the same data at 150 K and 450 K, respectively.) The shape of each plot indicates the degree of anisotropy in *E*: compact shapes such as spheres and cubes represent more isotropic behavior, while star-shaped plots suggest a greater degree of anisotropy. As expected, the degree of anisotropy implied by a given plot's shape closely matches that element's universal anisotropy index, $A^U$, shown in Table 4.1. In agreement with the calculated $A^U$ values, the data plotted in Fig. 4.6 indicate that the alkali metals and Zn exhibit the most anisotropy in *E*. For these

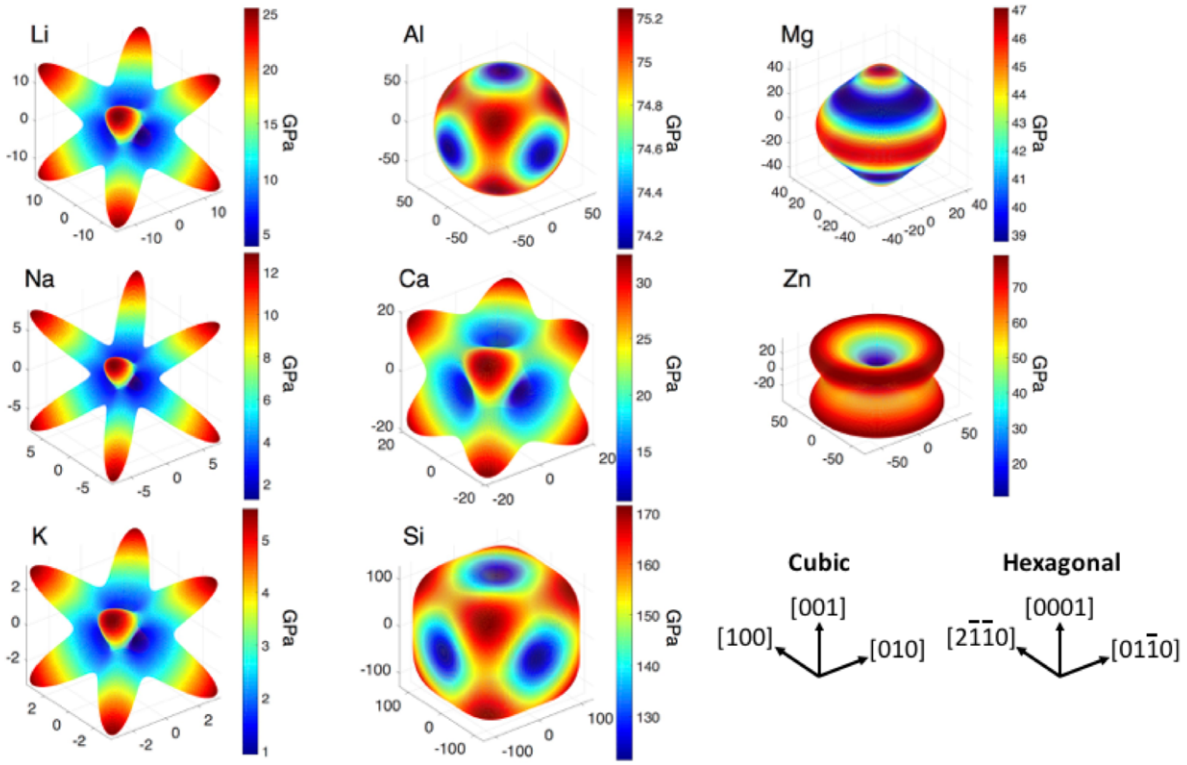


**Figure 4.6** Calculated Young's modulus, $E$, as a function of crystallographic direction for Li, Na, K, Al, Ca, Si, Mg, and Zn at 300 K. The value of the modulus in a given crystallographic direction $\vec{a}$ is specified (redundantly) using the magnitude of the protrusion from the origin and with color coding. The range of the modulus scale varies from element-to-element. The shape of the plot indicates the degree of anisotropy: compact shapes such as cubes and spheres represent isotropic behavior; star-shaped plots suggest a greater degree of anisotropy.

systems the maximum Young's modulus, $E_{max}$, occurs in <111> directions, while the minimum values, $E_{min}$, occur along <100>. The one exception to this trend is Al at 450 K (see Fig. B.19). This deviation can be explained by the fact that Al is almost perfectly isotropic at elevated temperature; variations in $E$ as a function of direction are minimal in Al, spanning only 0.2 GPa.

The behavior of Mg as depicted in Fig. 4.6 differs from the other elements. In particular, Mg is unique in that $E_{max}$ = 47.1 GPa occurs in the <0001> direction at 300 K. Similarly, at 150 K, $E_{max}$ = 52.0 GPa also occurs in the <0001> direction. At these temperatures, local maxima exist as an equatorial band within the basal plane, $\varphi = 0°$, $0 \leq \theta \leq 360°$, ($E$ = 46.2 and 50.2 GPa at 300 and 150 K, respectively). At 450 K the value for $E$ projected to the equatorial plane

overtakes the value along <0001>, becoming the global maximum: $E(0001) = 41.2$ GPa < $E$(equatorial) = 41.3 GPa. For the temperature range examined here, the minimum value for $E$ inMg, $E_{min}$, occurs in the directions defined by $\varphi \cong 45°$, $0 \leq \theta \leq 360°$.

Finally, Fig. 4.6 shows that the directional dependence of $E$ for Zn is also unique, and resembles a 'yo-yo' shape. $E_{max}$ for Zn occurs in two parallel rings defined by $0 \leq \theta \leq 360°$ and $\varphi \cong \pm 67°$, $\pm 64°$, and $\pm 60°$ at 150, 300, and 450 K, respectively. $E_{min}$ appears as a depression on the surface located along <0001>; $E$ also decreases as $\varphi$ approaches 0. These local minima in $E$ become more pronounced at 450 K (Fig. B.19), at which point the plot resembles two cones joined at their apexes.

As noted in Ledbetter's review,[140] Zn exhibits a high degree of elastic anisotropy, in agreement with the present results. This behavior is consistent with Zn's high c/a ratio of ~1.87 (Table B.3) – the ideal ratio being 1.63 – suggesting stronger intra-basal-plane bonding than between basal planes. (The c/a ratio predicted by the present calculations at 300 K, 1.90, is in good agreement with experimental measurements.) The resolved Young's modulus data shown for Zn in Figure 4.6 is consistent with these trends: $E_{min} = 10.6$ GPa occurs along <0001>, consistent with relatively weaker bonding between basal planes, while E within the basal plane, corresponding to $\varphi = 0°$ and $0° \leq \theta \leq 360°$ is much larger, 59.0 GPa.

### 4.3.4 Anisotropic Shear Moduli

Figures 4.7 and 4.8 illustrate the directionally-resolved shear modulus, G, for all 8 elements at 300 K. Figure 4.7 plots the maximum shear modulus, $G^{Max}$, within a plane perpendicular to the crystallographic direction specified by $\vec{a}$. (See Equations 4.6-4.7 and Fig. 4.2). Similarly, Figure 4.8 plots the minimum shear modulus, $G^{Min}$, applied perpendicularly to

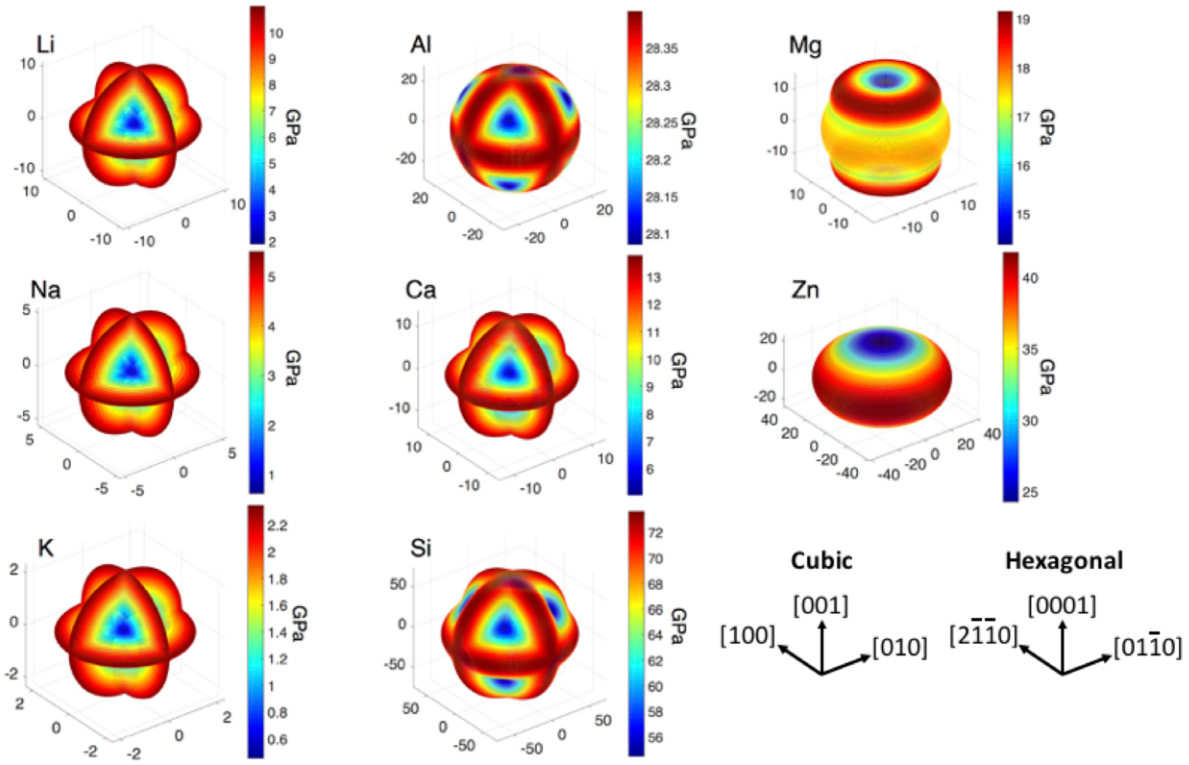


**Figure 4.7** Calculated maximum shear modulus, $G^{Max}$, as a function of crystallographic direction for Li, Na, K, Al, Ca, Si, Mg, and Zn at 300 K. $G^{Max}$ represents the maximum G over all directions $\vec{b}$ perpendicular to $\vec{a}$. The coordinate system for $\vec{a}$ is shown for cubic and hexagonal crystal structures; the relationship between $\vec{b}$ and $\vec{a}$ is shown in Fig. 4.1. The modulus value is specified (redundantly) using the magnitude of the protrusion from the origin and with color coding. Note that the range of the modulus scale varies from element-to-element.

each crystallographic direction indexed by $\vec{a}$. Figures B.20-B.23 show the same data at 150 K and 450 K.

As was observed for the Young's moduli, the shapes of the resolved shear modulus plots indicate the degree of anisotropy. More compact shapes (e.g. spheres) indicate greater isotropy, whereas shapes with significant directional dependence indicate greater anisotropy. For example, for cubic materials, the more anisotropic $G^{Max}$ plots resemble three orthogonal circles with common centers that intersect in <100> directions; the plots of $G^{Min}$ also convey anisotropic behavior and resemble three intersecting rods parallel to <100> directions.

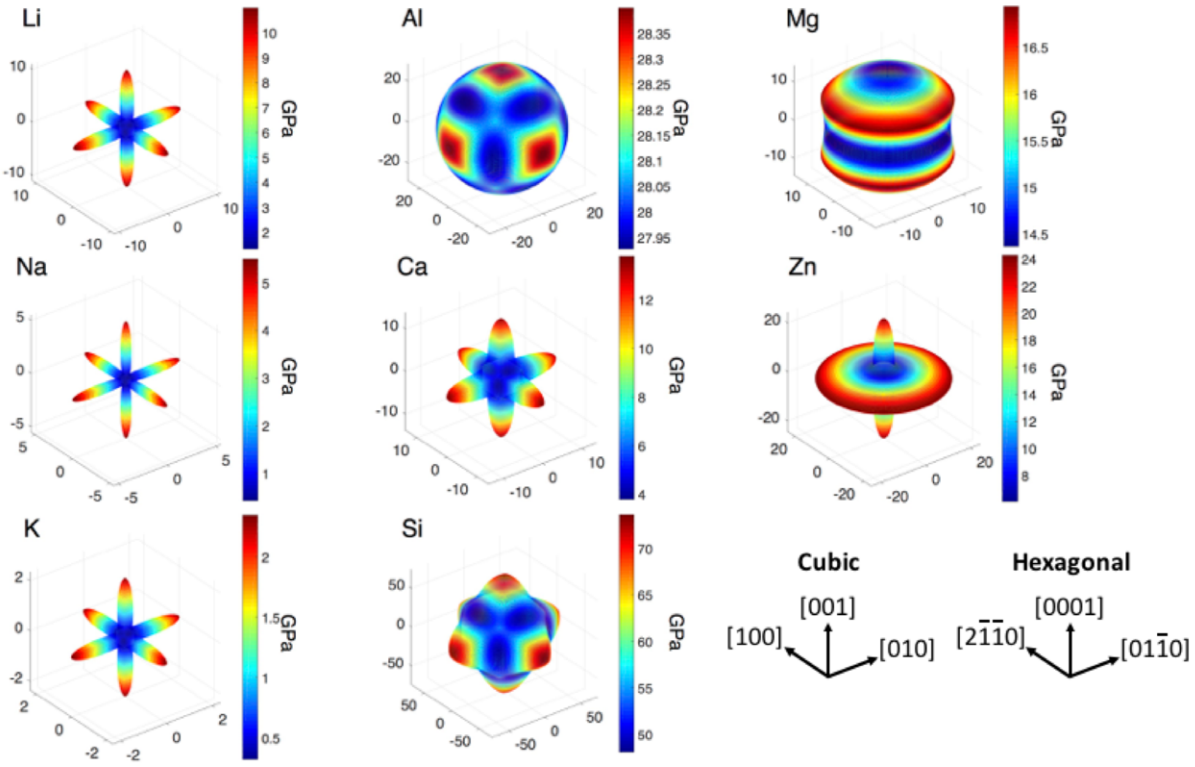


**Figure 4.8** Calculated minimum shear modulus, $G^{Min}$, as a function of crystallographic direction for Li, Na, K, Al, Ca, Si, Mg, and Zn at 300 K. $G^{Min}$ represents the smallest G for all directions $\vec{b}$ perpendicular to $\vec{a}$. The coordinate system for $\vec{a}$ is shown for cubic and hexagonal crystal structures; the relationship between $\vec{b}$ and $\vec{a}$ is shown in Fig. 4.1. The modulus value is specified (redundantly) using the magnitude of the protrusion from the origin and with color coding. Note that the range of the modulus scale varies from element-to-element.

Figure 4.9 plots the behavior of the shear modulus within the selected low-index crystallographic planes at 300 K for $0° \leq \chi \leq 360°$ (i.e., for all orientations of $\vec{b}$ within the plane {hkl} normal to $\vec{a}$ = [hkl], as shown in Fig. 4.2). For the cubic systems the high-symmetry planes include $\vec{a} = \{100\}$, $\{110\}$, and $\{111\}$. Similar plots at 150 K and 450 K are shown in Figures B.24-B.25; Table B.7 summarizes the Young's modulus and maximum/minimum shear modulus for each orientation at 300 K.

In the case of the cubic systems, in {100} G is independent of $\chi$ and equal to the global maximum shear modulus (see Table B.8). This is consistent with earlier analysis by Turley and Sines, where it was predicted that G does not depend on direction within these planes.[225] In

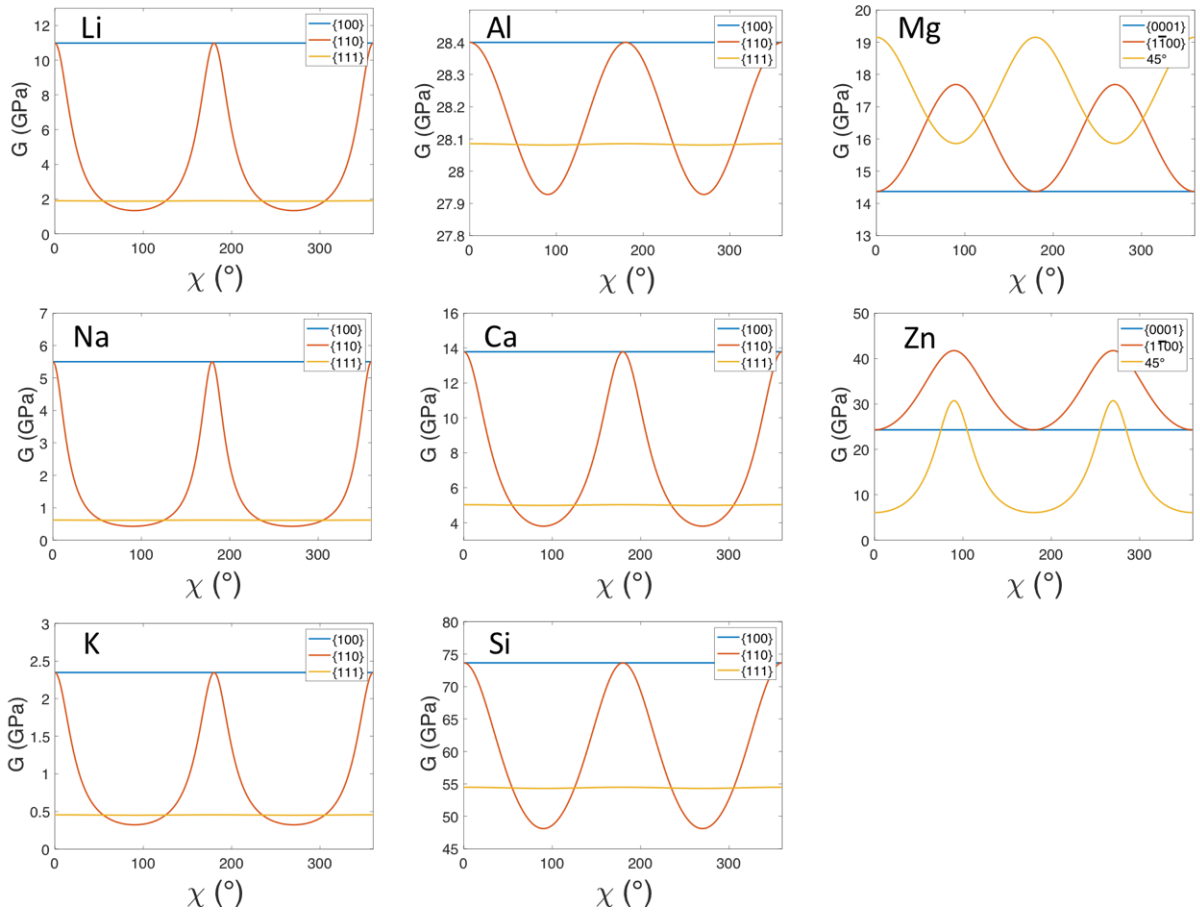


**Figure 4.9** Variation in the shear modulus for Li, Na, K, Al, Ca, Si, Mg, and Zn at 300 K within several low-index crystallographic planes. Low-index planes for the cubic system include {100}, {110}, and {111}. $\chi$ identifies the angle of the shear direction $\vec{b}$ within each {hkl} plane perpendicular to the direction vector $\vec{a}$ = <hkl>. See Fig. 1 for a description of the relationship between $\vec{a}$, $\vec{b}$, and $\chi$.

contrast, the shear moduli within {110} planes vary periodically between the global maximum, located in <001> directions, and the global minimum G, which occur parallel to <$\bar{1}$10>. Within the {111} planes, the values for G are nearly constant, with slight undulations; the maxima occur at 0° and 180° (<$\bar{1}\bar{1}\bar{1}$>), and the minima occur at 90° and 270° (<1$\bar{1}$0>).

In the case of hexagonal systems, Mg and Zn, the value of G within the basal plane, {0001}, is independent of $\chi$, with (constant) values of G = 14.4 GPa for Mg, and G = 24.3 GPa for Zn. Within the prismatic planes, {1$\bar{1}$00}, the shear moduli for Mg oscillate between G = 17.7 GPa at 90° and 270°, and the global minimum, $G_{min}$ = 14.4 GPa at 0° and 180°; for Zn, the

oscillations occur between the global maximum, $G_{max}$ = 41.7 GPa at 90° and 270° and G = 24.3 GPa at 0° and 180° ($\vec{b}$ is perpendicular to <0001> when $\chi = 0°$ or 180° for both Mg and Zn). Note that the prismatic planes occur within a continuum corresponding to $\varphi = 0°$ and $0° \leq \theta \leq 360°$, and that $G^{Max}$ and $G^{Min}$, as well as G versus $\chi$, are independent of $\theta$ within this continuum. Also plotted in Figure 4.9 are G for a continuum of planes corresponding to $\varphi = \pm 45°$ and $0° \leq \theta \leq 360°$. Here, the shear moduli oscillate for Mg between $G_{max}$ = 19.2 GPa at 0° and 180° and G = 15.9 GPa at 90° and 270°, and G = 30.7 GPa at 90° and 270° and $G_{min}$ = 6.1 GPa at 0° and 180° for Zn.

## 4.4 Discussion

Xu et al. used the quasi-harmonic approximation within density functional theory to predict the anisotropic elastic properties of Li as a function of temperature.[189] Although the present calculations are in good agreement with Xu's values for the $C_{11}$ and $C_{12}$ elastic constants, differences exist for $C_{44}$ at low temperatures. More specifically, the present calculations predict a value of 11.6 GPa at 0 K (11.2 GPa at 150 K), while Xu et al report values of 8–9 GPa. The experimentally measured value for $C_{44}$, 10.8 GPa at 78 K, is closer to the present results. We attribute this discrepancy to incomplete convergence of $C_{44}$ with respect to sampling of the Brillouin zone in the Xu et al. study.[189]

The Materials Project (MP) also contains a tabulation of elastic constants for the elements considered here, as derived from DFT calculations. Compared to the MP database, the present work reports the elastic properties over a range of temperatures, whereas the data in the MP is reported only for T = 0 K. The present study also aims to achieve well-converged predictions with respect to planewave cutoff energy and k-point sampling. Consequently, the present predictions are in good agreement with the available low-temperature experimental data: Table

B.2 demonstrates that the elastic properties predicted here are within 8.6% of experiments, whereas the data in the MP for these elements differs by 11.6% on average. Another consequence of incomplete convergence can be seen in the MP values for the potassium stiffness tensor: in violation of the Born stability criterion,[205] the MP reports $C_{12} > C_{11}$.

As was mentioned earlier, the criterion of Monroe and Newman proposes that in order to suppress dendrite initiation, the shear modulus of a solid electrolyte should be larger than that of a metallic anode placed in contact with it by a factor of approximately two. If these dendrites are crystalline, then the anisotropic elastic response of the metal should be considered, rather than the average or polycrystalline elastic properties. The data reported here demonstrate that for some metals the maximum value of the anisotropic shear modulus can be more than twice as large as the polycrystalline shear modulus. Metals that fall into this category include the alkaline metals (Li, Na, and K) and Zn. In these cases, the maximum resolved shear moduli at 300 K are 11.0 GPa, 5.5 GPa, 2.4 GPa, and 41.7 GPa, respectively, while the respective polycrystalline values are 5.0 GPa, 2.2 GPa, 1.1 GPa, and 21.3 GPa.

It is helpful to review the shear moduli of common SE classes for the purpose of evaluating their viability. These values range from: 7.9 – 14.1 GPa for alkaline thiophosphates,[218-220] 31 GPa for LiPON,[221] 23.6 – 41.5 GPa for alkaline anti-perovskites,[218, 222] 47.7 – 57.6 GPa for NASICON,[218, 223] 54.8 – 68.9 GPa for garnets,[218, 223-224] and 91.2 – 104 GPa for perovskites.[218, 223] In the context of the Monroe-Newman criterion and the orientation-dependent shear moduli presented here, the viability of a given SE class for a given anode composition can be projected by comparing the lower bound of the SE shear modulus (mentioned above) with twice the maximum resolved shear modulus of the anode at 300 K. Within this approximation, the thiophosphates, which are the most compliant of the SE

considered, are projected to be appropriate only for use with anodes based on K, the most compliant metal examined. The slightly stiffer anti-perovskites are in principle suitable for use with any of the alkaline metal anodes (Li, Na, and K). NASICON-type and garnet electrolytes expand this window beyond the alkali metals to include MV anodes such as Ca and Mg. Finally, the perovskites, which are the stiffest SE overall, are projected to be compatible with all of the anode materials examined here, with the exception of Si.

## 4.5 Conclusions

First-principles calculations were employed to calculate the elastic constants and aggregate, polycrystalline elastic properties of several anode materials of relevance for battery applications: Al, Ca, Li, Na, K, Mg, Zn, and Si. It is demonstrated that careful sampling of reciprocal space is required to converge the elastic constants. Direction-dependent elastic properties were derived from the stiffness tensors, and the effect of temperature on these properties was evaluated using the quasi-harmonic approximation. In general, excellent agreement between the present calculations and experimental measurements of the elastic constants and polycrystalline elastic moduli is obtained.

The elastic properties were mapped as a function of crystallographic direction. For cubic materials under axial loading, the stiffest (most compliant) orientation is <111> (<100>), while in shear <100> (<111>) is the stiffest (most compliant). The alkali metals are predicted to be the softest, growing softer with increasing atomic number. These systems are also the most anisotropic, with the degree of anisotropy increasing with increasing temperature. In contrast, multivalent Al and Mg are the most isotropic; nevertheless, their elastic properties are the most sensitive to temperature among the elements studied here. As expected, Si, the only non-metal, is the stiffest overall.

These data demonstrate that the maximum anisotropic shear modulus of some metals can be more than twice as large as their averaged or polycrystalline shear modulus. Hence, in the context of Monroe and Newman's theory of dendrite initiation, anisotropic elastic behavior may be an important factor in rationalizing the relative tendencies of different anode compositions to form dendrites during electrodeposition. The viability of several SE classes for use in conjunction with a given anode was projected by comparing the SE shear modulus with twice the maximum resolved shear modulus of the associated anode at 300 K.

In addition to providing insight into dendrite initiation for several combinations of anodes and solid electrolytes, the elastic properties data presented here will be of value as input to more detailed models of mechano-electrochemical behavior at anode/solid electrolyte interfaces.

# Chapter 5

## Atomistic Study of $Li_7La_3Zr_2O_{12}$ Grain Boundaries

### 5.1 Introduction

In addition to exhibiting high bulk ionic conductivity, a suitable solid electrolyte (SE) should possess low grain boundary (GB) resistance. One may reasonably expect that a low-cost SE will be polycrystalline. Thus, the migration of Li-ions through the SE during battery operation will require that the Li flux cross (multiple) GBs. In some SE's, GB resistance has been reported to be significant. For example, the most thermodynamically stable GB's in the anti-perovskite $Li_3OCl$ are predicted to reduce Li-ion conductivity by an order of magnitude compared to the bulk.[226] A solid's ability to serve as a fast ionic conductor is known to depend on its structure,[12] and given that the high mobility in bulk LLZO is largely attributable to a combination of the arrangement and partial occupation of polyhedral interstitial sites, it is possible that disruption of this structure at GBs can impede Li-ion mobility in the presence of GBs. However, in contrast to lithium lanthanum titanate, which possesses 2D ion diffusion pathways and thus is significantly impacted by the presence of GB's,[227-230] the 3D diffusion pathways present in LLZO may result in less disruption.

Numerous studies have examined the impact of GB's on the performance of LLZO. Consistently, greater relative density as a result of various processing techniques, including pressing and sintering,[231-232] rapid induction hot pressing,[23, 112-113] hot isostatic pressing,[233-234] hot pressing under flowing oxygen,[235] co-sintering with a $LiCoO_2$ cathode,[236] micro-wave reactive sintering,[237] and multi-step sintering methods,[238] resulted in improved Li mobility. Interestingly, there are conflicting reports on the effect of grain size on performance. When processed via rapid induction hot pressing, larger grain sizes were shown to improve performance,[113] while

reduced performance was observed when the sample was pressed then sintered.[231] The former trend was supported with molecular dynamics simulations, where decreased diffusivity and elevated activation energies at the GB's compared to the bulk were predicted.[239] This was attributed to disruption of Li ion trajectories at the GB, resulting in numerous immobile Li ions.

To date, computational studies have been limited to a few selected GB's,[239-240] but it is unclear if these GBs are representative of the behavior of the GBs that may be present in LLZO. Conversely, experimental measurements of GB resistance do not distinguish between different GB geometries, and thus present an average picture of aggregated GB phenomena. A study of GB phenomena that examines a wider range of GB's, while resolving the structure-dependent properties of each boundary separately, would be helpful in revealing the role of GB's in LLZO and in other solid ion conductors.

The aim of the present study is to provide insights into the mobility of Li ions at GB's by combining classical molecular dynamics and classical Monte Carlo simulation techniques across a broad set of GB's. The structures of thirty-five symmetric tilt and twist GB's, as well as eight amorphous GB's, were predicted via a multi-step process utilizing classical molecular dynamics and Monte Carlo simulations. Of these, sixteen representative tilt, twist, and amorphous GB's were selected for Li diffusivity calculations.

The data presented show a slight increase in Li concentration at crystalline GB's in some cases, while amorphous GB's show significant depletion in some cases. Shortened pair distances between Zr atoms are present in the GB regions, but absent in the bulk. Transport calculations show consistently faster Li diffusion in the bulk than in the GB's, consistent with experiments, and Li diffusion generally decreases with grain boundary energy (GBE). Interestingly, activation energy shows a similar trend, suggesting the importance of other contributing factors;

subsequently, a linear relationship between $\ln(D_0)$ and activation energy, known as a compensation effect, was observed. Observations of direction-dependent diffusion show faster mobility normal to the GB plane than within the GB plane. The results of this study suggest that lower-energy GB's are preferable in processed LLZO samples, and production methods should seek to minimize the number of higher-energy GB's by processing at elevated temperatures, while taking care not to significantly disrupt the crystallinity.

## 5.2 Methods

Calculations were performed using a model cubic polymorph of LLZO described in an earlier study,[224] where Li was quasi-randomly distributed on 24d tetrahedral and 96h octahedral sites, resulting in occupancies of 0.542 and 0.448, respectively, consistent with experimentally measured Li distributions in cubic LLZO.[91]

Grain boundary energies (GBE's) were calculated for 35 symmetric tilt and twist GB's listed in Table C.1. Symmetric tilt axis GB's were calculated for coincidence-site lattice (CSL) designations up to Σ29 for the $[0\bar{1}0]$ rotation axis, Σ33 for the $[1\bar{1}0]$ rotation axis, and Σ31 for the $[1\bar{1}1]$ rotation axis. The twist axis GB's Σ25(100)/[100], Σ13(100)/[100], Σ17(100)/[100], and Σ5(100)/[100] were considered due to their prominence in ionic crystals.[241-242]

Static molecular dynamics and Monte Carlo simulations were conducted using LAMMPS, utilizing the force field of Adams *et al.*, which possesses a Morse-type formulation with parameters derived from *softBV* bond valence parameters.[243-244] Studies utilizing this force field have yielded structural and dynamic properties in good agreement with experiments.[244-246] A timestep of 2 fs was used for all calculations.

The appropriate low-energy configurations for the GB's were determined via a multi-step process, implemented using the LAMMPS parallel molecular dynamics code.[247] All simulations

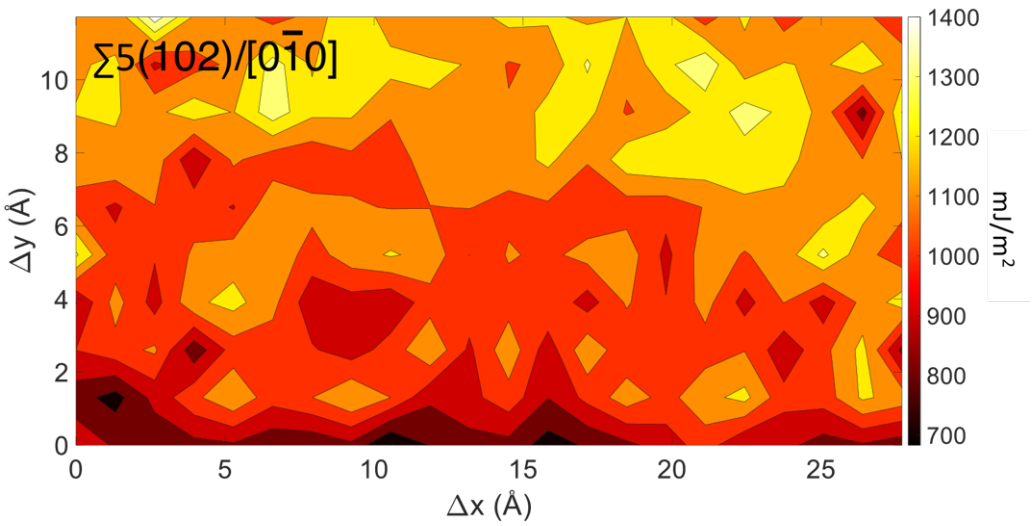


**Figure 5.1** Plot of GBE $\gamma$-surface as a function of displacement in directions parallel to the GB plane for $\Sigma5(102)/[0\bar{1}0]$ GB. Darker colors signify configurations possessing lower GBE, lighter colors signify configurations possessing higher GBE.

were performed using bi-crystal computational cells in conjunction with periodic boundary conditions,[248] resulting in a boundary plane at the center of the cell in the direction normal to the GB, as well as at the edges. The x- and y-directions were defined to be parallel to the GB plane, while the z-direction was defined to be normal to the GB plane. The width of the grains were ~30 Å in order to prevent interactions between GB's. The unrelaxed cell was constructed with a 1 Å gap to allow the structure to relax to a width that minimized its energy, as well as to avoid small interatomic distances. The grains were joined in order to approximate the appropriate CSL structure.

The first step of the process consisted of a grid search, where the unrelaxed, bi-crystal GB structure was introduced into LAMMPS.[249-252] One of the grains was shifted in ~1.3 Å increments with respect to the other in directions parallel to the plane of the GB for grid sizes ranging from 221 – 1261. The cell was minimized first with only the atoms allowed to relax, and then with both atoms and lattice parameters. This was allowed to proceed until the entire GB plane was scanned, and the location with the lowest GBE identified. GBE was calculated as:

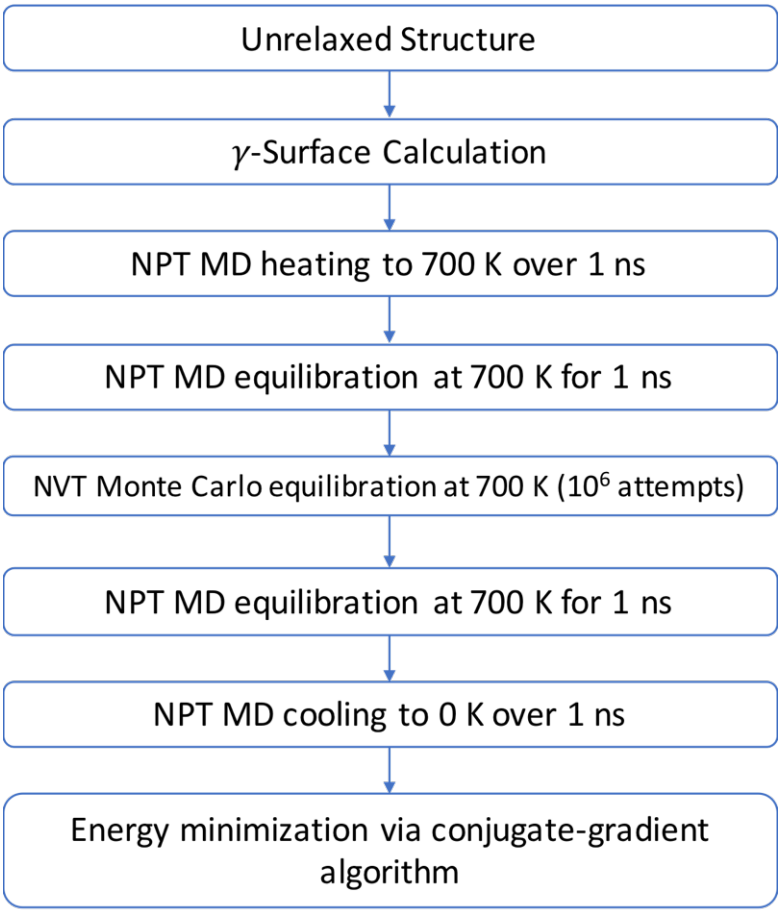


**Figure 5.2** Flow chart of structure optimization procedure.

$$\gamma_{GB} = (E_{GB}\text{-}nE_{bulk})/2A \tag{5.1}$$

where $E_{GB}$ is the total energy of the GB-containing cell, n is the number of LLZO formula units in the GB cell, $E_{bulk}$ is the total energy per formula unit of bulk LLZO, and A is the area of the GB plane. The factor of 2 accounts for the presence of 2 GB's within each simulation cell. A 3x3x3 expansion of the conventional unit cell of LLZO was used for bulk calculations.

Of the four elements comprising a formula unit of LLZO, the Zr sublattice possesses the highest symmetry, a body-centered cubic lattice; terminations of Zr at grain surfaces were assumed. The conventional unit cell of LLZO has 16 Zr atoms, and symmetry-distinct variations in surface compositions can be created per terminal plane. GBE's were evaluated for all GB's with these variations in terminations (~100 GB's). Figure 5.1 shows an example plot of the $\gamma$-

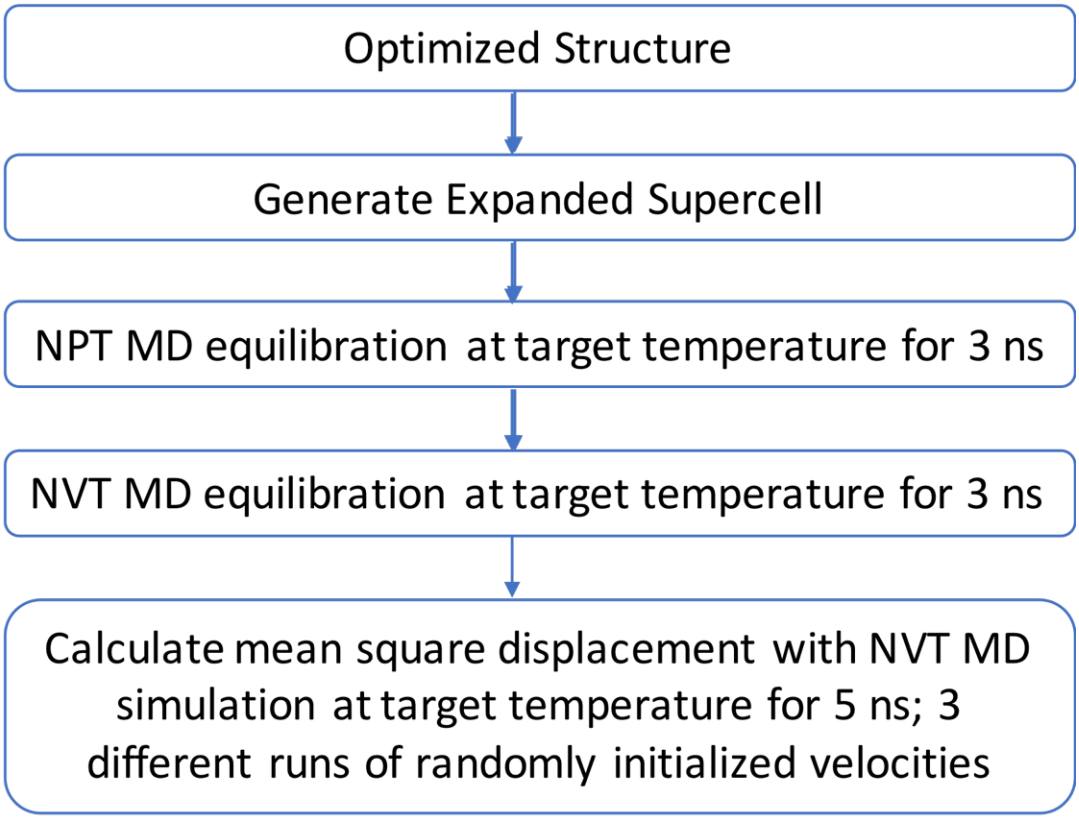


**Figure 5.3** Flow chart of Li transport calculations.

surface resulting from these calculations for a representative GB. Figures C.1-C.4 show $\gamma$-surface plots for all GB's studied with the lowest-energy Zr-terminated surfaces.

The configuration corresponding to the lowest GBE from the static grid-search calculations was heated in an NPT molecular dynamics simulation to 700 K over a 1 ns interval at 1 atm pressure, and then held at 700 K for 1 ns at 1 atm. The resulting high-temperature structure was subjected to a Monte Carlo simulation under NVT conditions at 700 K, with attempts restricted to atoms in regions within 10%vol of both GB's, for a total sampling of 20%vol. A compromise between phase-space sampling and attempt frequency resulted in a 0.25 Å hopping distance, yielding an acceptance ratio of ~0.25. A subsequent NPT simulation at 700 K for 1 ns at 1 atm followed by a ramp-down in temperature at the same conditions over 1 ns followed the Monte Carlo simulation. Finally, energy minimization was performed via the

conjugate gradient algorithm. The resulting sizes of the optimized simulation cells are listed in Table C.1, and GBE's for static and optimized cells are organized by rotation axis are listed in Tables C.2 – C.5. See Figure 5.2 for a flow diagram of the structure optimization procedure. See Figure 5.4 for optimized structures for 5 representative GB's.

Eight high-energy GB's from the multi-step configuration optimization procedure were further treated with intense heating to generate an amorphous phase at the GB's, using an established amorphization procedure.[253] The GB region was heated at 2000 K for 2 ns, and then cooled at a rate of 1 K/ps to 0 K, at which point the structure was minimized using the conjugate gradient algorithm.

Finally, Li ion diffusion was calculated using 16 representative GB's (4 $[0\bar{1}0]$ tilt crystalline, 6 $[1\bar{1}0]$ tilt crystalline, 2 $[1\bar{1}1]$ tilt crystalline, 2 [100] twist crystalline, and 2 amorphous). Diffusivity was calculated as

$$D=\frac{1}{2dt}\langle[\mathbf{r}(t+t_0)-\mathbf{r}(t_0)]^2\rangle \tag{5.2}$$

where d is dimensionality, $t_0$ is the initial time, and the angled brackets indicate an average over all Li ions.

The cells were expanded from their unit sizes (see Table C.1 for the numbers of surface unit cell replicas for each simulation cell). The simulation cells were equilibrated via an NPT simulation at 1 atm and the appropriate target temperature (700K, 800K, 900K, 1000K, or 1100K) for 3 ns, followed by an NVT simulation for 3 ns. Following this equilibration step, the cells were subjected to an NVT simulation for a further 6 ns; the 1$^{st}$ ns was neglected as an initialization step, and atomic coordinates were recorded for the remaining 5 ns for further

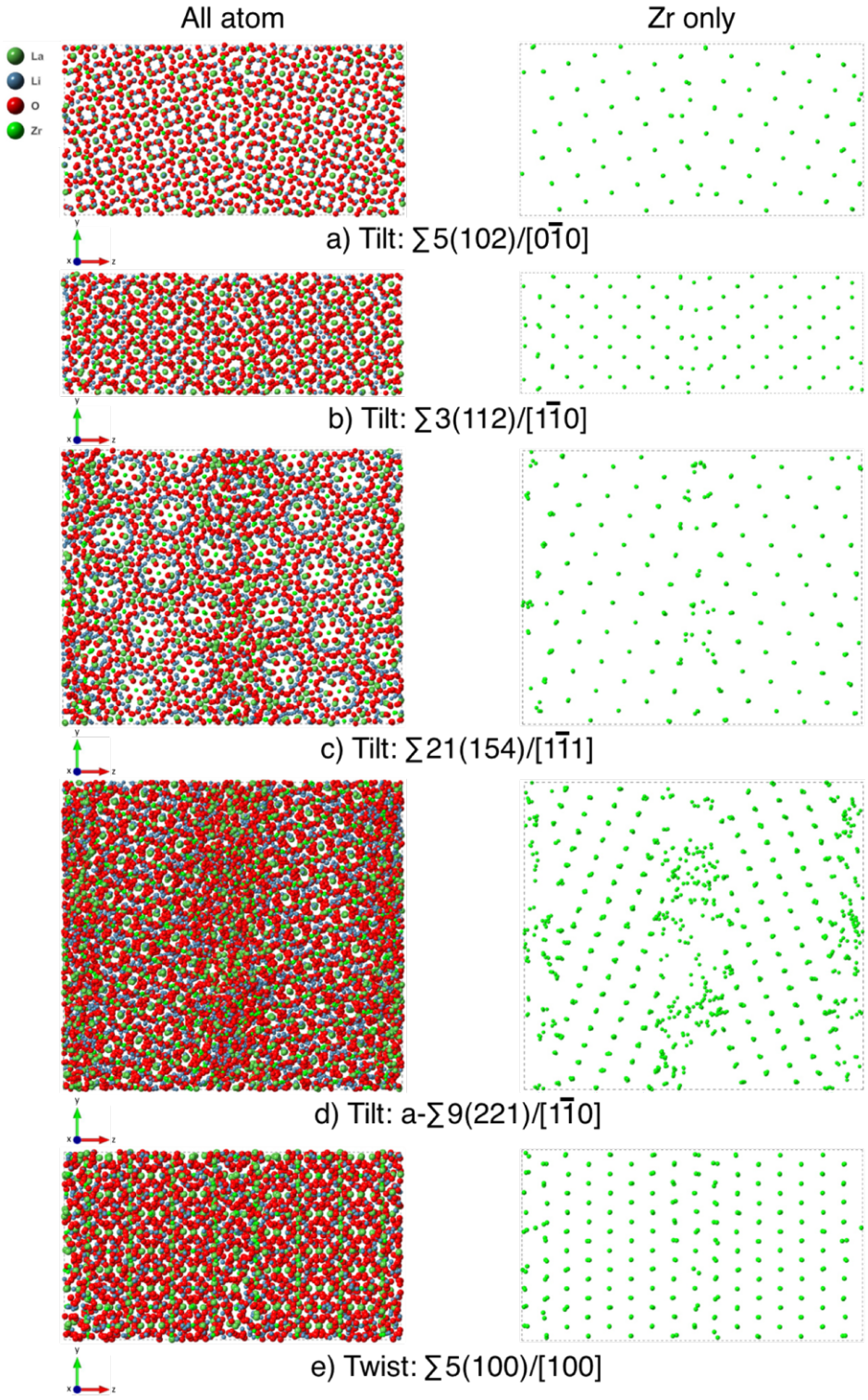


**Figure 5.4.** Relaxed structures of a) Σ5(102)/[0$\bar{1}$0], b) Σ3(112)/[1$\bar{1}$0], c) Σ21(154)/[1$\bar{1}$1], d) amorphous Σ9(221)/[1$\bar{1}$0], and e) Σ5(100)/[100] representing crystalline tilt axis GB's (a-c), an amorphous tilt axis GB (d), and a twist axis GB (e). The left-hand structures show all four constituent elements of LLZO (Li, La, Zr, and O), while the right-hand structures show only the Zr-sublattice, which possesses the BCC crystal structure in bulk LLZO.

randomly initialized velocities for all of the atoms in the cell. See Figure 5.3 for a flow diagram of the Li transport calculations.

Mean square displacements (MSD) were tracked for Li ions in the simulation cells for the purpose of calculating their average total diffusivities. The simulation cells were divided into 10 subregions of equal volume; 2 subregions contained the two GB's, while the remaining subregions were in the grain interiors (GI's). The diffusivities were calculated over 1 ns intervals, and then the five values were averaged in order to minimize attribution errors resulting from atoms changing regions during the simulation.

## 5.3 Results and Discussion

### 5.3.1 Grain Boundary Structures

The GBE's for the various GB's were evaluated using a multi-step process. Figures 5.1, C.1-C.4 show $\gamma$-surface plots of the GBE's. Dark colors correspond to cell configurations possessing low GBE's, while lighter colors correspond to cell configurations with high GBE's. Minimum energy configurations are clustered around the x-axis, indicating their tendency to occur with small, rigid shifts in the y-direction from the initial, unrelaxed GB cell. This is consistent with the construction of the unrelaxed cells to approximate the CSL structure.

Following the identification of the structure yielding the lowest GBE from the $\gamma$-surface calculations, the GB cells were further processed. Figures 5.4a – 5.4c, 5.4e show representative GB structures following from this procedure, which yielded crystalline GB's. Figure 5.4d shows a representative amorphous GB.

There are similarities between the GBE vs. misorientation angle plots presented in Figure 5.5, and those from single element metals possessing the body-centered cubic crystal structure,[252, 254-255] with low-energy cusps at 53.1º on Figure 5.5a corresponding to the

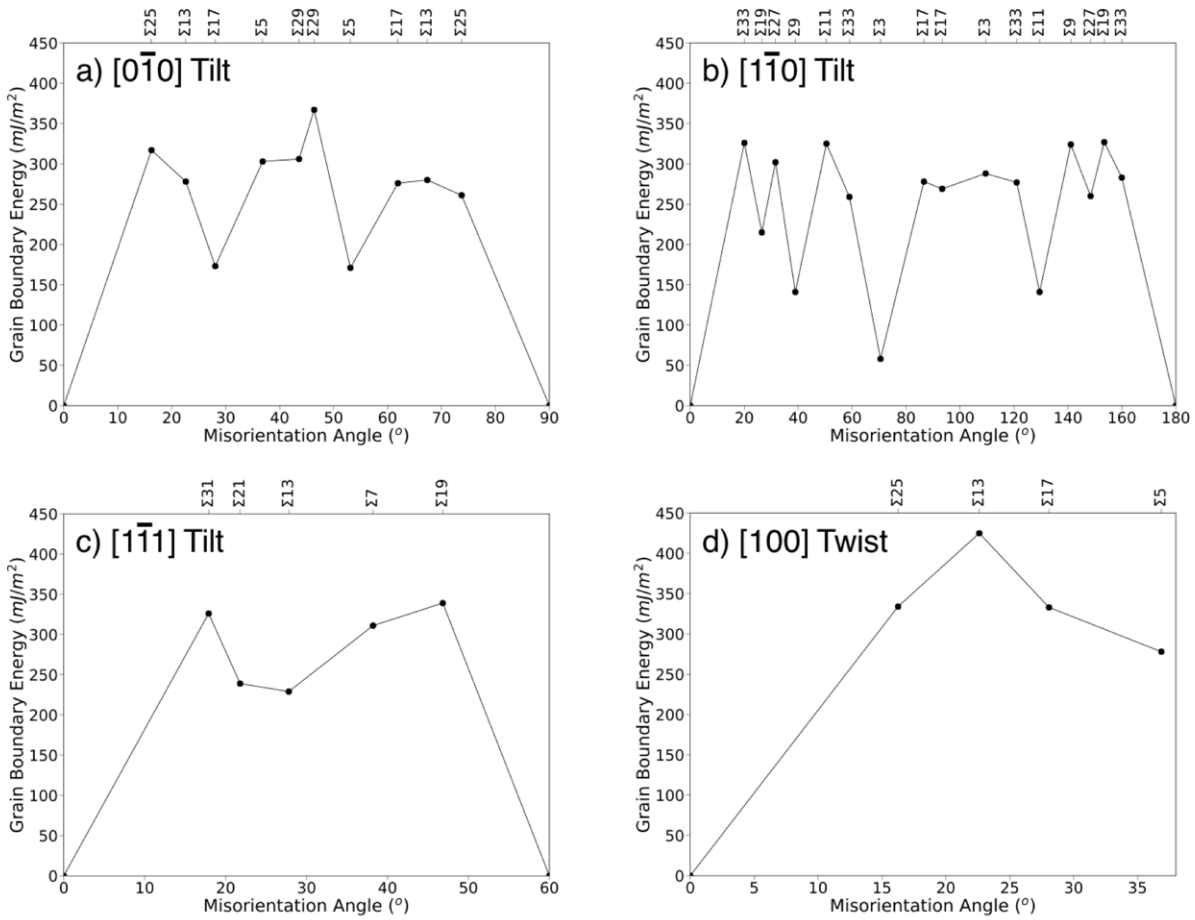


**Figure 5.5** Variation of GBE's with misorientation angle about the a) [0$\bar{1}$0] tilt, b) [1$\bar{1}$0] tilt, c) [1$\bar{1}$1] tilt, and d) [100] twist rotation axis. The values along the top axis indicate the coincidence site lattice (CSL) Σ-value for the GB corresponding to the plotted GBE.

Σ5(102)/[0$\bar{1}$0] GB, and low-energy cusps at 26.5º, 38.9º, 70.5º, and 129.5º on Figure 5.5b corresponding to the Σ19(116)/[1$\bar{1}$0], Σ9(114)/[1$\bar{1}$0], Σ3(112)/[1$\bar{1}$0], and Σ11(332)/[1$\bar{1}$0] GB's, respectively. These cusps appear on plots for both LLZO and bcc metals. The shape of Figure 5.5d, representing the [100] twist rotation axis GB's, is consistent with similar plots for [100] twist GB's in ionic solids.[256-259]

However, differences also exist. There is a prominent cusp at 28.1º on Figure 5.5a, corresponding to the Σ17(104)/[0$\bar{1}$0] GB, whereas the bcc metals show a cusp for the Σ5(103)/[0$\bar{1}$0] GB (36.9º); also, the metals show slight cusps at the Σ3(111)/[1$\bar{1}$0] GB (109.5º), while no such cusp appears on Figure 5.5b. Figure 5.5c shows significant lowering at 21.8º and

27.8º, corresponding to grain boundaries $\Sigma 21(154)/[1\bar{1}1]$ and $\Sigma 13(143)/[1\bar{1}1]$, while the metals show that GBE is largely independent of misorientation angle for tilt GB's rotated about the $[1\bar{1}1]$ rotation axis.

At low misorientation angles (<10 degrees), the relationship with GBE is described by the dislocation model of Read and Shockley.[257-258, 260] However, at misorientations of >10 degrees, GBE is largely independent of misorientation angle, except at special, low-energy GB's. Work by Rohrer *et al.* has shown that solid-state grain growth is analogous to the growth of grains in a liquid or a vapor; GB's in a polycrystalline solid are predominantly delineated by crystal habits corresponding to dominant surfaces on single crystals.[261-267] Experimental evidence has shown that surfaces with the lowest energy exist with the highest probability in samples of a variety of materials, including oxides[261-262, 264-266] and metals.[262-263] As expected, the high-energy GB's presented here are similar in value (250 – 350 $mJ/m^2$), except at low-energy cusps.

### 5.3.2 Amorphous Grain Boundaries

Commonly observed glassy films at the GB's of covalent ceramics prompted Keblinski et. al. to study the origins of this phenomenon.[253] Through classical MD simulations on twist GB's between crystalline Si grains, it was observed that disordered structures were thermodynamically preferred at high-energy GB's, whereas ordered structures were observed at low-energy GB's.

However, more recent work found that these conclusions do not necessarily hold.[268] A significant amount of ordering and a lowering in energy was observed, in agreement with the results of calculations presented here. Here, the majority of disordered structures yielded higher GBE than the optimized, well-ordered structures obtained during the structure optimization

procedure. This suggests that the crystalline structures predicted by the optimization procedure yielded a reliable GB structure.

The exception were two GB's processed with the amorphization procedure at 2000 K, $\Sigma 9(221)/[1\bar{1}0]$ and $\Sigma 7(132)/[1\bar{1}1]$. These yielded GBE's (263 mJ/m$^2$ and 260 mJ/m$^2$, respectively) which were less than the crystalline structure GBE's (324 mJ/m$^2$ and 311 mJ/m$^2$, respectively). These were selected for further Li diffusion calculations.

### 5.3.3 Structure Analysis

In order to characterize the local structure within the GB simulation cells, pair distribution functions (g(r)) were calculated within LAMMPS. The cutoff distance for the computation was 10 Å. The regions sampled were 10% of the total volume, centered at 10 equidistant locations along the z-axis (i.e. region 1: $0.95 < z < 0.05$, region 2: $0.05 < z < 0.15$, region 3: $0.15 < z < 0.25$, region 4: $0.25 < z < 0.35$, region 5: $0.35 < z < 0.45$, region 6: $0.45 < z < 0.55$, region 7: $0.55 < z < 0.65$, region 8: $0.65 < z < 0.75$, region 9: $0.75 < z < 0.85$, region 10: $0.85 < z < 0.95$). For each of the 16 GB's used for Li diffusion calculations, g(r) was computed for the 10 possible pairings among Li, La, Zr, and O. To clearly visualize features, g(r) was divided by the maximum value, $g_{max}$. Blue colors indicate g(r)=0, yellow colors indicate g(r)= $g_{max}$. Figures C.5 – C.20 show the resulting plots at 700 K.

Region 6 from the 16 plots corresponds to the GB region at the center of each GB simulation cell. These have been arrayed in Figures C.21 – C.25 for all 10 pairs at 700 K, 800 K, 900 K, 1000 K, and 1100 K, along with g(r) from bulk LLZO at both 0 K and at the appropriate temperature.

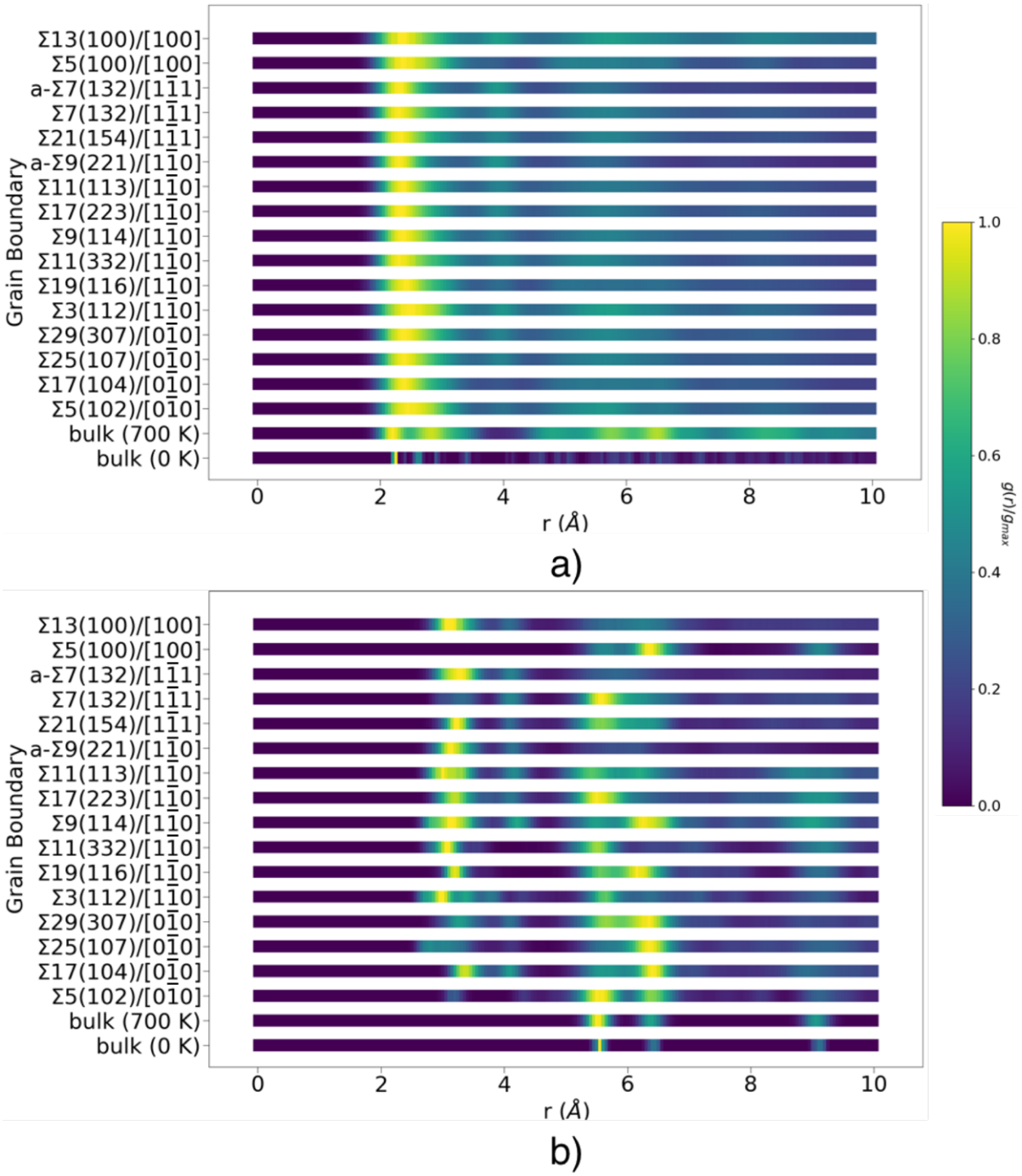


**Figure 5.6.** Radial distribution functions, g(r), for 16 GB's at 700 K, as well as for bulk crystalline LLZO at 0 K and 700 K, for a) Li-Li pairs and b) Zr-Zr pairs. The values of g(r) are divided by the maximum value, $g_{max}$. Yellow indicates g(r) = $g_{max}$, blue indicates g(r) = 0. Prefix "a-" indicates an amorphous grain boundary. The pairs are sampled at $0.45 < z < 0.55$, corresponding to the GB at the center of the simulation cell.

Plots for Li-Li and Zr-Zr pairs counted within $0.45 < z < 0.55$, corresponding to the GB at the center of the simulation cell at 700 K, have been arrayed in Figures 5.6a and 5.6b, along with g(r) from bulk LLZO at 0 K and 700 K. Figures C.26 – C.28 show the same plots in the more familiar "peaked" format.

In the bulk cubic phase of LLZO, Li ions reside in polyhedral interstitial sites at partial occupancy, with 56.8% of the tetrahedral 24d sites occupied, and 44.2% of the octahedral 96h sites occupied.[91] They diffuse according to a coordinated pattern; if an octahedral site is occupied, one of the face-sharing tetrahedral sites must be unoccupied and the other occupied, or if both of the tetrahedral sites are occupied, then the octahedral site must be unoccupied.[91] In agreement with Ref. 230, this pattern is represented in the g(r) profile for bulk LLZO at 0 K and 700 K in Figure 5.4a, with two prominent peaks at r = 2.28 Å and r = 2.93 Å. The peak at r = 2.28 Å coincides with Li-Li pairs occupying adjacent tetrahedral and octahedral sites, while the peak at r = 2.93 Å is a grouping of overlapping peaks, corresponding to distances between octahedral sites.[244] Figure C.28 shows bulk RDF's for Li-Li and Zr-Zr pairs at 0 K and 700 K, presented in the "peaked" format.

Within the GB regions (regions 1 and 6) of the crystalline GB simulation cells, one prominent peak occurs at r = 2.47 Å on average, while a smaller peak occurs at r = 4.03 Å on average (see Fig 5.6a, C.26). The peak associated with distances between octahedral sites is indistinguishable from and appears to overlap with the peak associated with adjacent tetrahedral and octahedral sites. However, within the GI's (regions 2 – 5, 7 – 10), the two peaks are identifiable at r = 2.37 Å and r = 2.86 Å, in agreement with the bulk profiles. The small increase in the pair distances for the first peak is likely attributable to the inclusion of values from regions adjacent to the GB in the average. The exception to the appearance of two peaks occurs for the

Σ13(100)/[100]) crystalline twist GB. Here, a single peak occurs at r = 2.62 Å, signifying overlap. As in the other crystalline GB regions, peaks are observed at r = 2.45 Å and at r = 4.04 Å.

The appearance of the smaller peak at r = 4.03 Å within the GB region signifies a substantial deviation in structure from that of GI/bulk regions. Similar peaks have been associated with reduced ion migration due to the contraction of the free volume available to diffusing ions.[269-270] It is possible that similar phenomena in LLZO GB's may result in decreased ionic mobility.

For the amorphous GB's, a-Σ9(221)/[1$\bar{1}$0] and a- Σ7(132)/[1$\bar{1}$1], the first, most prominent peak in the GI occurs at r = 2.46 Å and r = 2.50 Å, respectively, comparable to those in the GB regions of the crystalline simulation cells. As in the crystalline GB regions, the appearance of a single peak suggests the overlapping of the peak associated with octahedral site distances and tetrahedral-octahedral site distances. Within the GB region, a downward shift in pair distances occurs for the first peak (r = 2.40 Å and r = 2.41 Å, respectively); this indicates that the distance between hopping sites within the GB region for amorphous GB's decreases compared to GI. As in the crystalline GB's, a small peak occurs at r = ~4 Å.

The three Zr – Zr peaks in bulk LLZO remain relatively unchanged from 0 K to 700 K, occurring at r = 5.63 Å, r = 6.48 Å, and r = 9.18 Å at 0 K, and r = 5.58 Å, r = 6.48 Å, and r = 9.13 Å at 700 K (Figures 5.6b, C.28). For the crystalline tilt GB's (GB's with rotation axes [0$\bar{1}$0], [1$\bar{1}$0], or [1$\bar{1}$1] that are parallel to the GB planes), the pair distances associated with these peaks remain relatively unchanged within the GI's (regions 2 – 5, 7 – 10), occurring at r = 5.66 Å, r = 6.49 Å, and r = 9.20 Å on average. However, within the GB's (regions 1 and 6), peaks at substantially shorter pair distances (2.93 Å ≤ r ≤ 4.5 Å) appear, and the sharp peaks at r = 5.66 Å

in the GI's shorten and widen, with maximum peak values occurring in the range 5.53 Å ≤ r ≤ 5.98 Å. The peak at r = 6.49 Å in the GI's undergoes a similar shortening and widening, with maximum peak values occurring in the range 6.03 Å ≤ r ≤ 6.53 Å. The peak at r = 9.20 Å significantly shortens or disappears altogether.

Interestingly, in the Σ5(100)/[100]) crystalline twist GB cell, the peak at shorter Zr – Zr pair distances, which is apparent in the g(r) profiles for the crystalline tilt GB's, is not observed. Furthermore, the three peaks observed in the bulk and GI's are distinguishable at r = 5.68 Å, r = 6.40 Å, and r = 9.18 Å, although the first peak is significantly shortened. However, the Σ13(100)/[100] crystalline twist GB shares similar characteristics with the tilt crystalline GB's, with peaks occurring at shorter pair distances, the first two prominent peaks in the bulk/GI g(r) overlapping, and the third peak gone altogether. For the amorphous GB's, g(r) shows a similar profile to Σ13(100)/[100], with the appearance of shorter peaks, the overlapping of bulk/GI first and second peaks, and the disappearance of the third peak. However, a small peak emerges at r = ~8 Å.

Recall the earlier observation of the emergence of a smaller peak at r = 4.03 Å in the Li – Li g(r) within the GB regions, and the appearance of similar peaks in the literature being associated with decreased ion mobility due to free volume contraction.[269-270] Shorter peaks in the Zr – Zr g(r) GB plots, as well as in the La – La g(r) (Figures C.7 – C.25), may account for a contraction of free volume within the LLZO GB's presented here. Furthermore, a reduction in lattice volume and bottleneck size has been shown to correlate with an increase in activation energy and a decrease in ionic conductivity.[12]

To further characterize the GB simulation cells, plots of composition as a function of position along the direction normal to the GB plane (z-axis) were calculated. Figure 5.7 shows

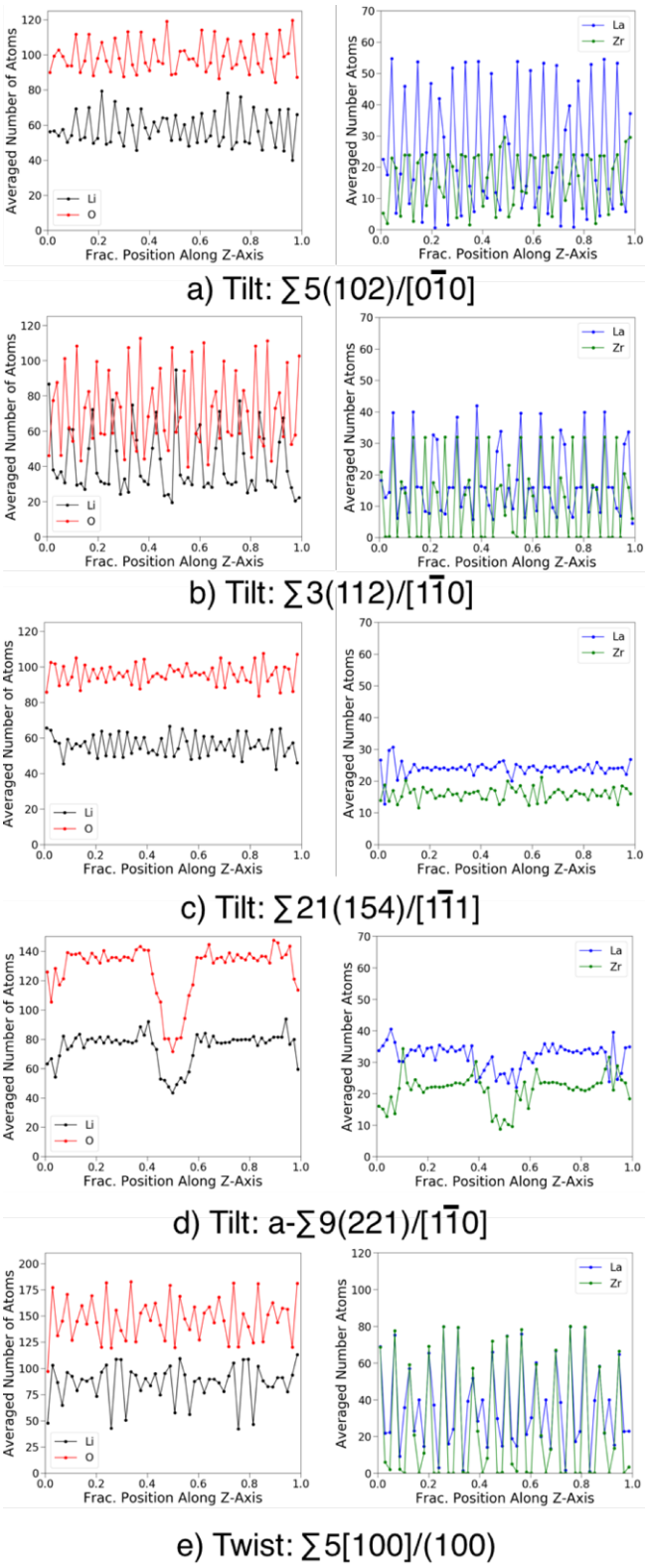


**Figure 5.7.** Time-averaged composition of Li (black), O (red), La (blue), and Zr (green) as a function of position normal to the GB plane (z-axis) at 700 K for supercells containing a) $\Sigma5(102)/[0\bar{1}0]$, b) $\Sigma3(112)/[1\bar{1}0]$, c) $\Sigma21(154)/[1\bar{1}1]$, d) amorphous $\Sigma9(221)/[1\bar{1}0]$, and e) $\Sigma5(100)/[100]$ GB's.

plots of representative GB's at 700 K; Figures C.29 – C.44 show plots for all simulation GB cells at 700 K, 800 K, 900 K, 1000 K, and 1100 K. Each data point represents the number of atoms contained within a ~1 Å slice, time-averaged over the duration of the Li diffusion simulation. Black data indicates the number of Li, red the number of O, blue the number of La, and green the number of Zr.

To compare concentrations of the Li, La, Zr, and O between the GI and GB regions, the ratio of the number of atoms in a GB region (region 6) to the number of atoms in a GI region (region 4) were calculated and tabulated in Table C.6. In general, the difference is small, <0.1. The notable differences are in Li and Zr for the $\Sigma3(112)/[1\bar{1}0]$ GB, with a decrease of 0.20 and 0.33, respectively, as well as an increase in O of 0.13 and 0.19 within $\Sigma3(112)/[1\bar{1}0]$ and $\Sigma9(114)/[1\bar{1}0]$ GB's, respectively. Additionally, as apparent from Figure 5.7d, all elements of the amorphous $\Sigma9(221)/[1\bar{1}0]$) show drastic decreases at the GB vs. in the GI: 0.37 for Li, 0.24 for La, 0.46 for Zr, and 0.37 for O. The decrease in Li concentration seems to contradict the often-observed phenomenon of charge carriers accumulating at defects.[12]

Differences in local structure have been observed between bulk/GI's and GB's. It is possible that these variations could have significant effect on the properties of Li transport within GB's as compared to transport within bulk/GI's. In order to observe these possible changes, Li diffusivities within GB's were evaluated via molecular dynamics simulations and compared to simulations within bulk/GI's.

### 5.3.4 Lithium Diffusion

Optimized GB configurations were used as input structures for Li transport simulations. Figure C.45 shows plots of mean square displacement (MSD) of Li ions within representative GB simulation cells calculated over 5 ns at 700 K, 800 K, 900 K, 1000 K, and 1100 K; plots

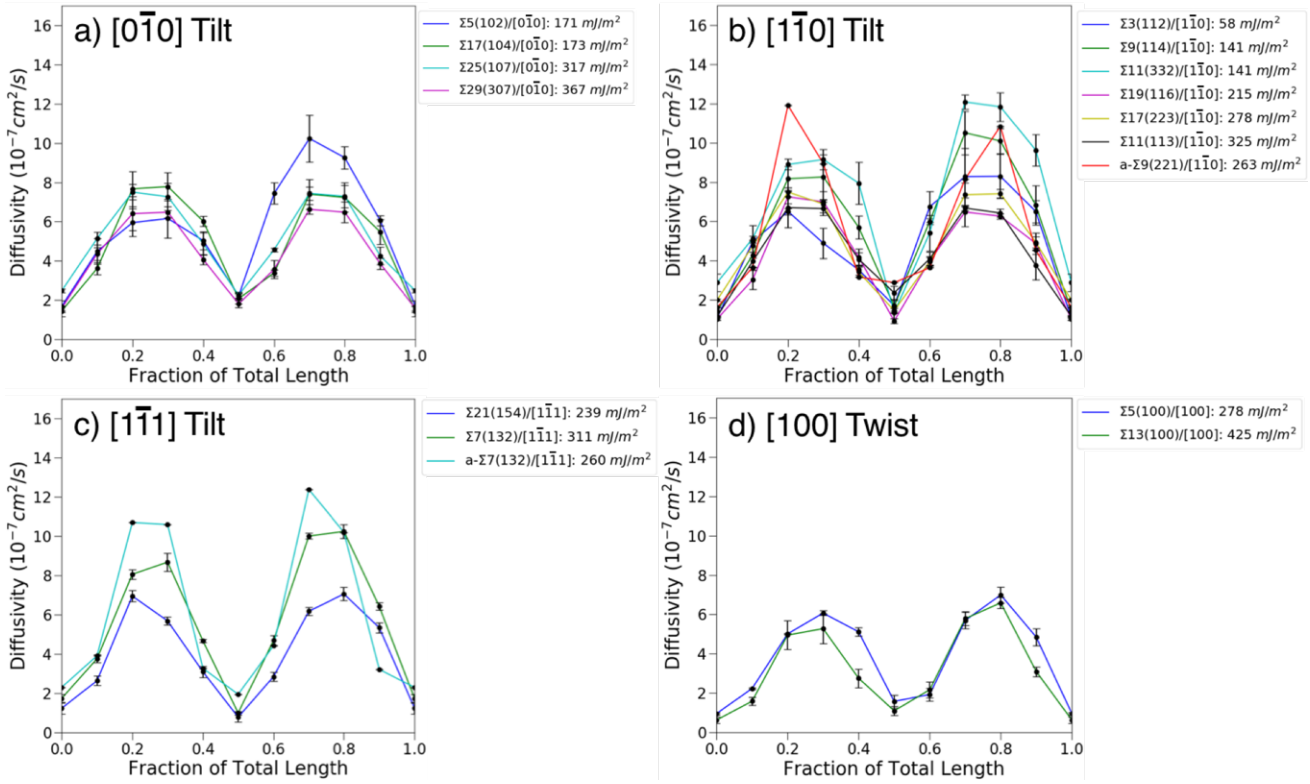


**Figure 5.8.** Variation of average Li diffusivity along the z-direction (normal to GB plane) for a) [0$\bar{1}$0] tilt, b) [1$\bar{1}$0] tilt, c) [1$\bar{1}$1] tilt, and d) [100] twist rotation axis at 700 K. The GBE is included in the plot legends for reference. The average bulk Li diffusivity at 700 K is 7.73 x $10^{-7}$ $cm^2/s$.

calculated within GB and GI regions are included. The same calculations were conducted for an expanded bulk LLZO simulation cell, as well as a total of 16 GB's representing high GBE, low GBE, and amorphous configurations. The MSD calculations were used to calculate Li ion diffusivities via eqn. (2).

In this work, total diffusivity refers to the motion of Li ions among three degrees of freedom. The total diffusivity for each GB system was calculated at 10 regions centered at equidistant locations along the z-axis; these were the same regions introduced during the earlier structure analysis section. It is expected that during the course of the simulation, some atoms will cross regions, thus incorrectly attributing their diffusivity values toward their region of origin. To minimize this error, diffusivities were calculated over five 1 ns intervals, with each

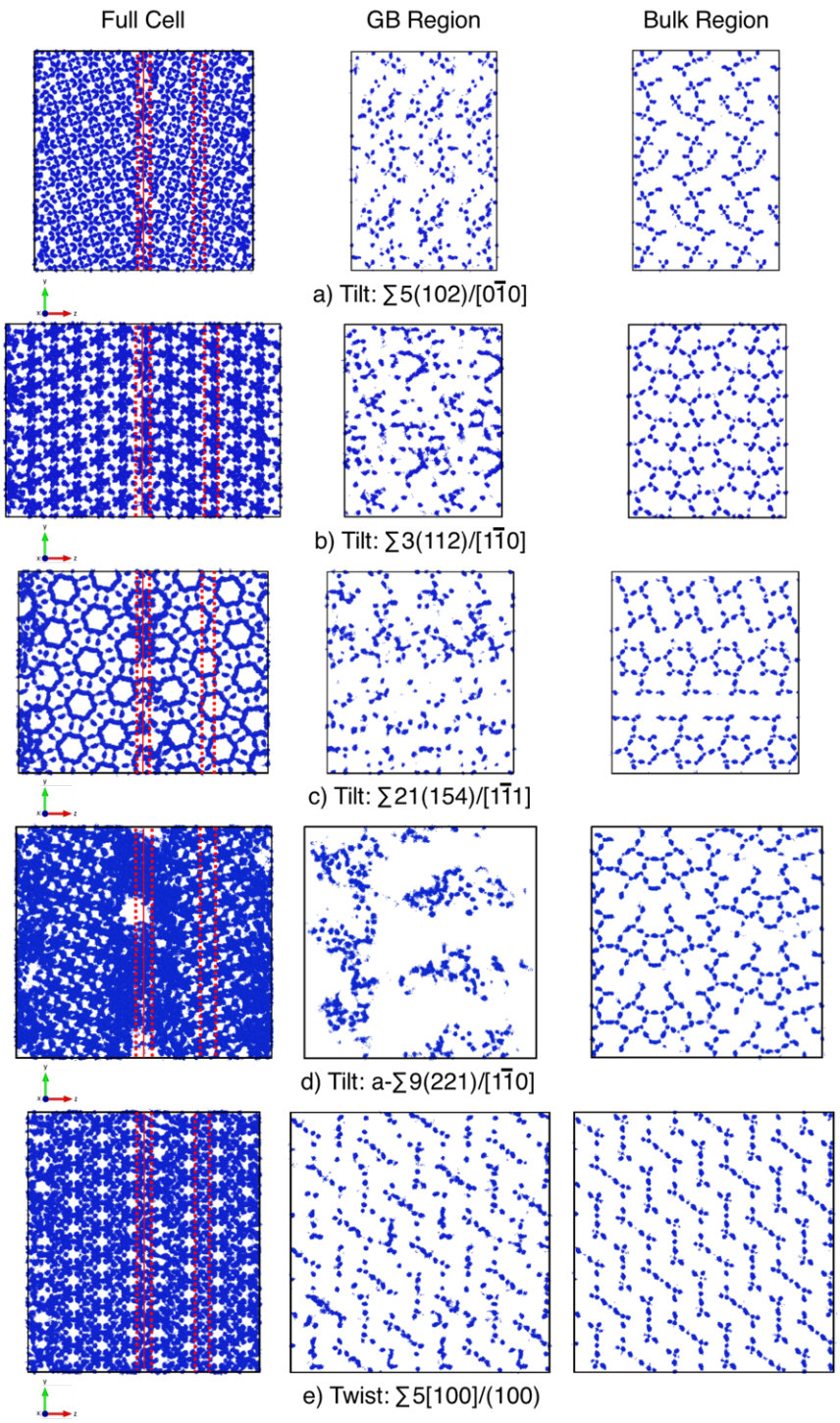


**Figure 5.9.** Li-ion trajectories for the GB simulation cells plotted over 5 ns at 700 K for a) Σ5(102)/[0$\bar{1}$0], b) Σ3(112)/[1$\bar{1}$0], c) Σ21(154)/[1$\bar{1}$1], d) amorphous Σ9(221)/[1$\bar{1}$0], and e) Σ5(100)/[100] GB's. The left-hand plots are viewed along the x-axis (along the GB tilt axis for (a-d), and perpendicular to the GB twist axis for (e)). The center plots are viewed normal to the GB plane (z-direction) for a region centered on the GB at the center of the cell ($0.45 < z < 0.55$). The right-hand plots are viewed normal to the GB plane for a representative bulk region ($0.75 < z < 0.85$). The red dashed boxes indicate the appropriate viewing regions.

interval consisting of a re-evaluation of atom origins. The resulting five diffusivities were then averaged.

The total diffusivity for each GB system at 700 K is plotted as a function of position along the z-axis in Figure 5.8, and the calculated bulk diffusivity value is indicated in the caption, which was calculated to be 7.73 x $10^{-7}$ $cm^2/s$. Total diffusivities for 800 K, 900 K, 1000 K, and 1100 K can be viewed in Figures S46 – S61; the total bulk diffusivities calculated at these temperatures are 2.25 x $10^{-6}$ $cm^2/s$, 4.84 x $10^{-6}$ $cm^2/s$, 9.77 x $10^{-6}$ $cm^2/s$, and 1.71 x $10^{-5}$ $cm^2/s$, respectively.

The plots in all cases share a distinctive "notch" shape, with the total diffusivities in the GB regions (regions 1 and 6) showing decreased diffusivity compared to the regions within the GI. Furthermore, the depths of the notches appear to decrease with increasing temperature, indicating that the variation in total diffusivity between GB's and bulk regions lessen with increasing temperature. Comparable trends were observed in earlier work.[239]

The diffusivity plots for the two amorphous GB's (a-Σ9(221)/[1$\bar{1}$0] and a-Σ7(132)/[1$\bar{1}$1]) show "notches" that are wider and rounder than those of the crystalline GB's, suggesting that the GB phase extends further and transitions more gradually into the GI. The diffusivities at higher temperatures tend to be significantly reduced in comparison to those of crystalline GB's, while the diffusivities at 700 K tend to be higher.

Patterns of ionic motion can be informative as to the causes of diffusivity variations within different phases. To visualize these patterns, Li positions were recorded at 0.5 ps intervals and plotted; plots for five representative GB's can be viewed in Figure 5.9. The left-hand panels for each GB show plots of Li trajectories within the entire simulation cell viewed along the x-axis, which lies parallel to the plane of the GB and rotation axis for tilt GB's, but

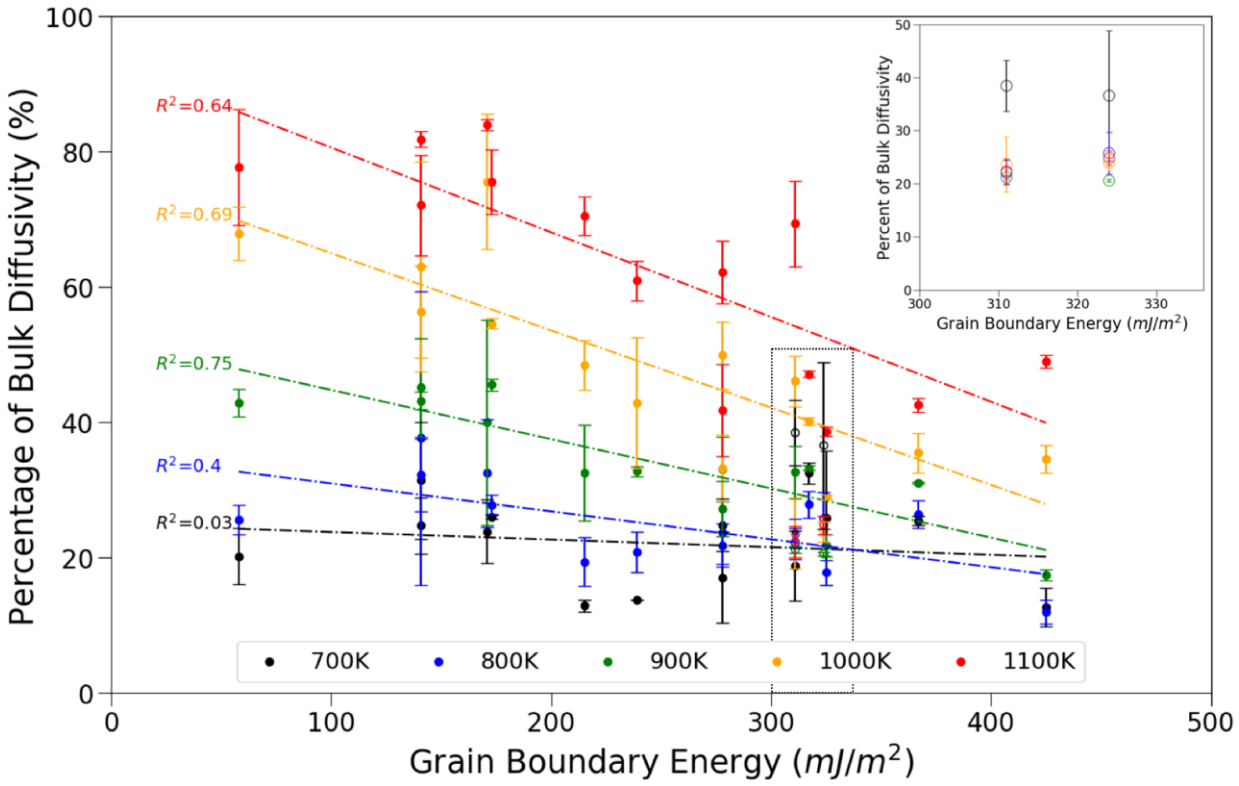


**Figure 5.10** Relationship between average total GB Li diffusivities ($D_{tot}$) and GBE. The $D_{tot}$ are plotted as a percentage of the total diffusivity in bulk crystalline LLZO at the appropriate temperature. Data points are plotted in red for simulations at 1100 K, orange at 1000 K, green at 900 K, blue at 800 K, and black at 700 K. Dash-dotted lines were fit to crystalline GB data via least-squares fitting, and the corresponding $R^2$ value is indicated to the left of each data set. Open circles indicate Li diffusivities for amorphous GB's (see inset).

parallel to the plane of the GB and perpendicular to the rotation axis for the twist GB. The center panels show plots of Li trajectories within a slice centered at the GB region in the center of the simulation cell (region 6), while the right-hand panels show plots of Li trajectories within a slice centered in the GI (region 8). The red boxes on the left-hand plots indicate the regions corresponding to the slices.

Trajectories associated with fast diffusivity are expected to show evidence of well-connected pathways, which is observed within the bulk region slices. The trajectories are periodic in all three directions with no significant disruptions. However, within the majority of the GB region slices, there is significant disruption to the trajectories, as well as isolated pathways, thus increasing the hopping distances between sites and resulting in decreased

diffusivity. This is especially apparent within the amorphous GB region, where there are sizeable pockets of isolated pathways. Interestingly, the twist GB shows little disruption to the periodic pattern observed in the bulk.

A summary of total diffusivity data is presented in Figure 5.10. Total diffusivity, represented as a percentage of bulk diffusivity at the indicated temperature, is plotted as a function of GBE at 700 K, 800 K, 900 K, 1000 K, and 1100 K. Each marker represents the average of six diffusivities: diffusivities at the two GB's, which in turn are the averages of three simulations with randomized initial atom velocities. These data are plotted with respect to GBE, and the error bars represent the standard deviation of the six calculations. The dash-dotted lines represent a linear fit to the crystalline GB data for each temperature; $R^2$ values are displayed to the left of each line.

Total diffusivities trend downward with increasing GBE, and values at higher temperatures approach those of the bulk. The inset shows the total diffusivities for the amorphous GB's; the domain and range are indicated by the box in the main plot. While the amorphous GB diffusivities tend to be higher than the crystalline GB diffusivities at 700 K, at higher temperatures, the amorphous GB diffusivities are significantly lower. Furthermore, as a percentage of bulk diffusivity, they seem to be largely independent of temperature, ranging between 20% – 30%.

Figure 5.11 shows Arrhenius plots for 16 GB's. Each panel contains plots organized by rotation axis, with Figures 5.11a – 5.11c showing plots for the tilt axis GB's, and Figure 5.11d showing plots for the twist axis GB's. Data for bulk LLZO is included in the four plots for comparison. Activation energies, shown in the plot legends, were calculated as slopes of a fitted line.

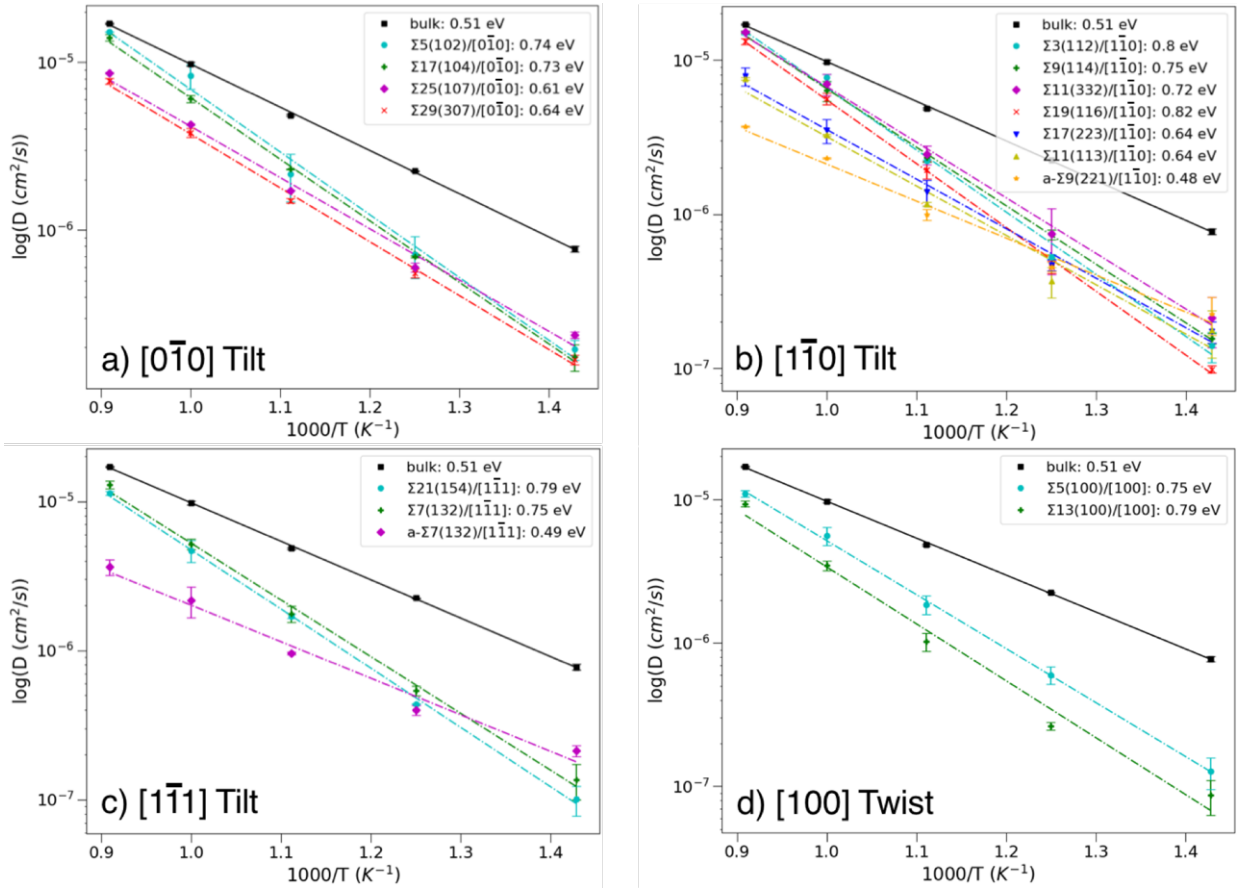


**Figure 5.11** Arrhenius plots showing the variation of average total Li diffusivity ($D_{tot}$) at the GB's with temperature for a) [0$\bar{1}$0] tilt, b) [1$\bar{1}$0] tilt, c) [1$\bar{1}$1] tilt, and d) [100] twist rotation axis. Data for bulk crystalline LLZO is plotted as the solid black line. The activation energy was calculated from a line fitted to log($D_{tot}$) at each value of 1000/T, and is included in the plot legends. Amorphous GB's are indicated with prefix "-a."

Activation energies for the crystalline GB's range from 0.61 eV – 0.82 eV, which are consistently higher than the activation energy for bulk diffusivity (0.51 eV). Amorphous GB activation energies for a-Σ9(221)/[1$\bar{1}$0] and a-Σ7(132)/[1$\bar{1}$1] are comparable to the bulk values (0.48 eV and 0.49 eV, respectively). However, the total diffusivities are consistently lower in the GB's vs. the bulk across the range of temperatures examined.

Figure 5.12 plots activation energies for GB diffusion as a function of GBE. Generally, activation energy decreases with increasing GBE. (Twist GBs present one exception.) As previously mentioned, total diffusivities exhibit a similar trend with GBE (Fig. 5.10). However, if activation energy is the primary determining factor of ionic diffusivity, total diffusivity would

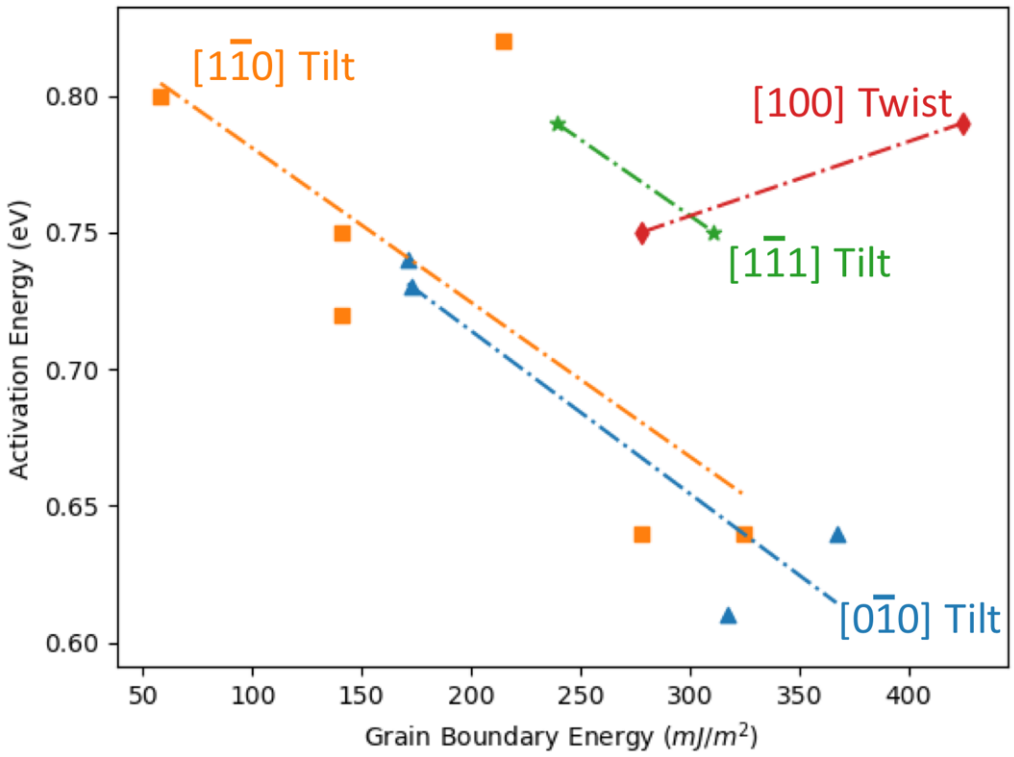


**Figure 5.12** Activation energy vs. grain boundary energy for simulated GB cells. Data is grouped by rotation axis.

be expected to decrease with larger activation energy. This is not the case, and points to the significance of the pre-exponential factor, $D_0$, warranting further examination.

Figure 5.13 plots $\ln(D_0)$ as a function of activation energy for the GBs considered here. There is a strong linear correlation among the GB data ($R^2 = 0.98$). This trend has been reported within related classes of activated processes,[271] and is often referred to as the isokinetic rule,[272] the Meyer-Neldel rule (MNR),[273] or the enthalpy-entropy compensation effect.[274] Several examples exist from condensed matter physics[275] and chemistry[274] (see Refs. 275 and 274 for comprehensive lists of these examples). In the case of diffusion, examples of the compensation effect include self-diffusion on Pd surfaces,[276] diffusion of $Ag^+$ in glass and $Li^+$ in LISICON,[277]

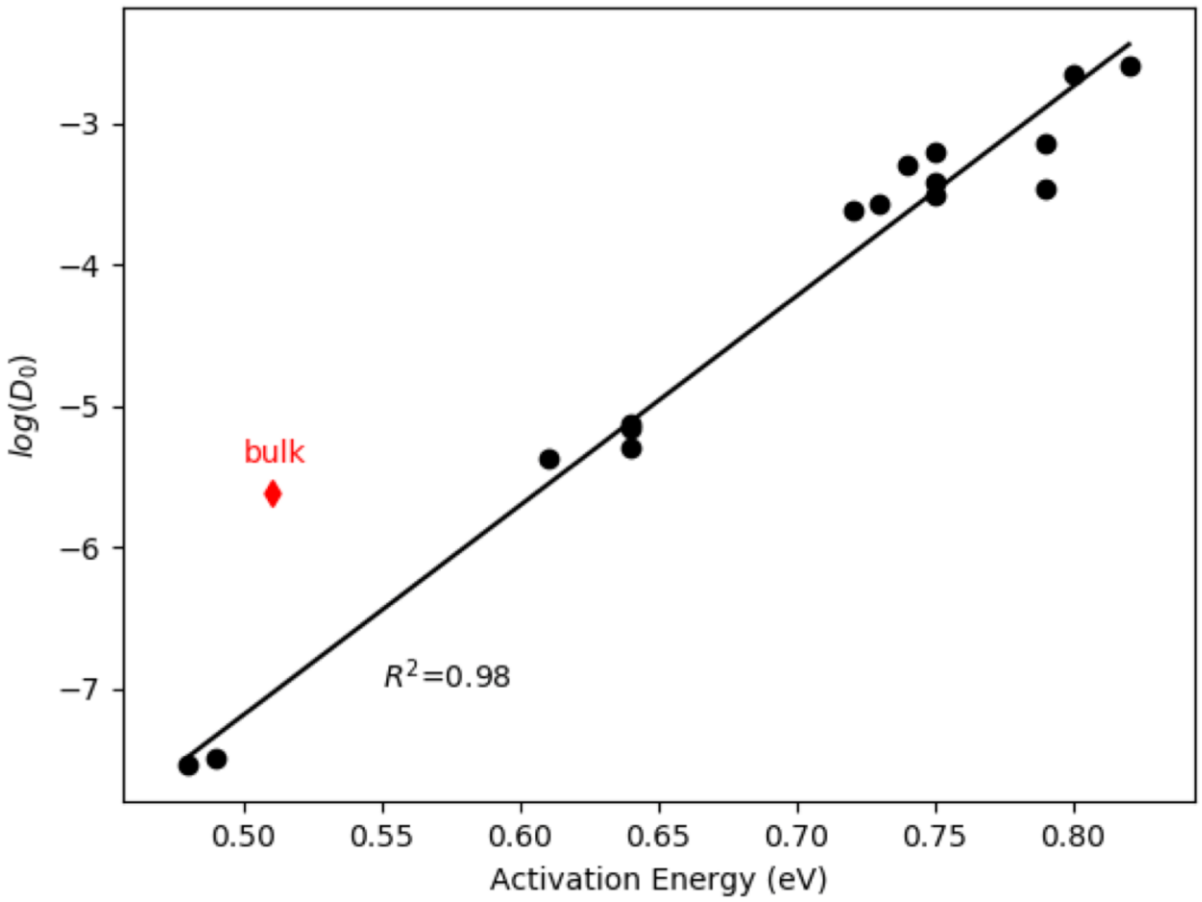


**Figure 5.13** Relationship between $\log(D_0)$ and activation energy. The solid line is fit to the GB data, with $R^2$ indicating the goodness of fit. The red diamond indicates data for bulk LLZO.

Si in silicates,[278] $H^+$ and $O_2$ in perovskite oxides,[279-280] Cu in $In_2S_3$,[281] $H_2$ in Pd,[282] $Li^+$ in polymer electolyte,[283] as well as GB diffusion.[284-285]

The relationship between activation energy ($\Delta E_a$) and diffusivity is described by the Arrhenius equation:

$$D = D_0 \exp\left(-\frac{\Delta E_a}{k_B T}\right) \tag{5.3}$$

where $k_B$ is Boltzmann's constant, T is the absolute temperature, and $D_0$ is a pre-exponential factor. Diffusivity, solely conditioned upon the concept of the random walk, is expressed in three dimensions as[286]:

$$D_r = \frac{1}{6}\Gamma a^2 \tag{5.4}$$

where a is the lattice parameter. Here, the hop rate (Γ) is expressed in terms of the frequency of vibration (ν) of the equilibrium configuration and the Gibbs free energy of activation (ΔG):

$$\Gamma=\nu \exp\left(-\frac{\Delta G}{k_B T}\right) \tag{5.5}$$

From the definition of Gibbs free energy, $\Delta G=\Delta H-T\Delta S$, and formulating ΔH as an activation energy ($\Delta E_a$), the diffusivity is expressed as:

$$D=\gamma f[d]a^2\nu \exp\left(-\frac{\Delta E_a}{k_B T}\right) \tag{5.6}$$

The expressions γ, f, and [d] refer to a geometrical factor, a correlation factor, and concentration of defects, respectively. Note that contributions from entropy are subsumed within the geometrical factor. Comparison of equations (3) and (6) yields an expression for $D_0$,

$$D_0(\nu)=\gamma f[d]a^2\nu \tag{5.7}$$

The compensation effect suggests that a diffusion reaction which must overcome a large $\Delta E_a$ initiates from a potential well of high curvature, corresponding to a high frequency of vibration. Conversely, a reaction with a smaller $\Delta E_a$ initiates from a potential well of low curvature, which corresponds to a low frequency of vibration. The resulting increase in $D_0$ with increasing $\Delta E_a$ is exactly what is observed in Figure 5.13. Finally, note that bulk diffusivity does not follow the trend observed for GB diffusion. This is expected given that these diffusion scenarios are characterized by different local environments - highly ordered crystalline structure in the bulk vs. disordered structure in the GB.

### 5.3.5 Diffusion Anisotropy

Diffusion in bulk LLZO is isotropic,[287] but local anisotropy in diffusivity has been previously predicted to occur at the GB's.[239] To assess this property across the broader set of

**Table 5.1** Bulk Diffusivities and Average Grain Boundary Diffusivities at 700 K, 800 K, 900 K, 1000 K, and 1100 K. Diffusivites reported in units of $10^{-7}$ $cm^2/s$.

| Temp. (K) | $D_{bulk}$ | Average $D_x$ | Average $D_y$ | Average $D_z$ |
|---|---|---|---|---|
| 700 | 7.7 | 1.7 | 1.6 | 1.8 |
| 800 | 22.5 | 5.3 | 5.1 | 6.4 |
| 900 | 48.4 | 14.8 | 14.4 | 20.4 |
| 1000 | 97.7 | 42.6 | 40.9 | 58.2 |
| 1100 | 170.6 | 98.1 | 95.1 | 126.0 |

GB's presented here, diffusivity was calculated along each Cartesian direction within 10 regions (same regions discussed previously). These direction-specific diffusivities are presented as a function of position in Figures C.46 – C.61. Diffusion within the GB plane corresponds to the *xy*-plane, while trans-boundary diffusion occurs in the z-direction. Flattening (or inverting) of z-direction diffusivity in the GI at elevated temperatures is attributed to finite size effects.

These data are summarized in Figure C.62, where the diffusivities in each of the three directions are plotted for the 16 GB's as a percent of bulk diffusivity at 700 K. A black line linking the maximum and minimum diffusivity values at each GB, with a length equal to their differences, is drawn for each GB and is a measure of anisotropy. These differences between maximum and minimum diffusivity are plotted in Figure C.63 as a function of GBE, yielding a Pearson's correlation coefficient of r = -0.39.

Table 5.1 lists the average diffusivities in each direction at 700 K, 800 K, 900 K, 1000K, and 1100 K. At 700 K, average diffusivities are relatively constant in all directions. However, from 800 K - 1100 K, there is a far more noticeable increase in z-direction diffusivity over diffusivities within the GB plane. Average z-direction diffusivity increases by 23.1%, 39.7%, 39.4%, and 30.4% over diffusivity in the x- and y-directions (measured as the average of columns 3 and 4) at 800 K, 900 K, 1000K, and 1100 K. Decreased conductivity in the *xy*-plane than observed in the z-direction may be a consequence of diffusion pathway isolation within the

GB plane observed in Figure 5.9, while pathways in the z-direction appear to show better connectivity.

## 5.4 Conclusions

A method for predicting grain boundary structures was presented; these structures were used as input for the study of Li ion mobility within LLZO. Molecular dynamics simulation showed a consistent decrease in diffusivity at grain boundaries as compared to grain interiors and bulk LLZO.

Structural factors contributing to the decreased diffusivity at grain boundaries were discussed. Pair distribution functions suggested a reduction in free volume by shortened pair distances between Zr - Zr and La - La in the grain boundary compared to the grain interior/bulk. The consistent appearance of a peak in Li - Li profiles in the grain boundary, which were not visible in grain interior/bulk profiles, indicated unsuccessful Li migration. Plots of Li ion trajectories indicated disruption to and isolation of migration pathways. Furthermore, a significant decrease in Li concentration was observed in some grain boundaries.

The energetics of diffusion were also discussed. The observation of the compensation effect was attributed to correlations between activation energy and vibration frequency. This indicates that activation energy alone is not a sufficient descriptor to predict diffusivity.

Grain boundaries with low grain boundary energy were shown to improve Li ion diffusivity within LLZO. However, the deleterious effects of grain boundaries are expected to decrease with increasing temperature. Processing should occur at elevated temperatures to minimize the number of grain boundaries with high grain boundary energy, while taking care not to disrupt the crystalline structure.

# Chapter 6

## Conclusions and Next Steps

### 6.1 Conclusions

The Li-ion battery is a technological marvel that has transformed our society. However, as more demands are placed upon rechargeable batteries, novel chemistries with improved capabilities are highly desirable. Replacement of the carbon-based anode with one which is metallic offers the possibility of significant improvement in energy density. Unfortunately, barriers remain toward the widespread use of metallic anodes. One such hurdle is the formation of dendrites during cycling, which poses a serious safety hazard, and has a deleterious effect on performance. A promising solution to the problem of dendrites is the incorporation of a solid electrolyte, and the ceramic oxide $Li_7La_3Zr_2O_{12}$ (LLZO) is a promising candidate material. The goal of this work is to use atomistic modeling to characterize, and to better understand, the challenges associated with implementing metallic anodes and solid electrolytes in rechargeable batteries.

An important consideration when evaluating the performance of an anode is its cycling efficiency, which in the case of metallic anodes, is governed by electrochemical plating/stripping. This process includes several contributing factors, one of which is the thermodynamics of adsorption and desorption. The thermodynamic overpotential formalism is a means by which Density Functional Theory can be utilized to evaluate the energetics of these reactions. In the present study, thermodynamic overpotentials were assessed at terrace, step, and kink sites on prominent surfaces of 7 metals (Li, Na, K, Al, Ca, Mg, and Zn) of interest for battery applications. In general, overpotentials were observed to be smallest for plating/stripping at step/kink sites, and largest at terrace sites. The local bonding environment of surface atoms was found to correlate

with overpotential magnitude. Alkali metals, which possess the body-centered cubic crystal structure, were predicted to be most efficient for plating/stripping, while Al, Zn, and alkaline earth metals were predicted to be less efficient. A multi-scale, steady-state nucleation model was employed to estimate nucleation rates during electrodeposition. Alkali metals were predicted to show orders of magnitude improvement in nucleation rates compared to other metals. The sensitivity of nucleation behavior on the morphology and composition of the electrode surface was highlighted.

Early attempts to include mechanical properties within an electrochemical model of a metallic electrode/solid electrolyte interface considered elastic properties in describing the formation and propagation of dendrites. Other factors are likely important, however, such as microstructure, plastic deformation, and external pressure, to full understand the problem. At the small scales at which dendritic nuclei form, it is also likely that anisotropies in elastic properties play an important role.

Experimental values of elastic properties can vary by study, likely due to differing measurement techniques, sample handling conditions, and the presence of impurities. Here, highly converged Density Functional Theory calculations were employed to assess the elastic properties of eight candidate anode materials (Li, Na, K, Al, Ca, Mg, Zn and Si); their variation as a function of temperature was predicted within the quasi-harmonic approximation. Elastic properties were resolved as functions of orientation in order to assess their anisotropies. These data accurately represent the idealized elastic responses of contaminant-free samples of these materials, and thus serve as important benchmark data.

The alkali metals were predicted to be softest, growing softer with increasing atomic number. Al and Mg were predicted to exhibit highly isotropic elastic properties, while the alkali

metals were highly anisotropic. Extrema in elastic properties occurred in opposite directions for cubic materials, with stiffest (most compliant) values occurring in the <111> (<100>) directions under axial loading, while the stiffest (most compliant) values occurred in the <100> (<111>) directions under shear loading. The maximum anisotropic shear modulus of some metals was observed to be twice that of their polycrystalline values.

The solid electrolyte LLZO is a super-ionic conductor that is attractive for use in rechargeable batteries possessing a Li metal anode. Unfortunately, devices incorporating LLZO with Li metal tend to fail due to dendrite penetration at moderate to high current densities. These penetrants appear to traverse the electrolyte along defects, such as grain boundaries (GB's). The present study seeks to better understand the impact of GB's on LLZO by predicting the structure of a wide range of tilt and twist axis GB's, including amorphous GB's, with classical molecular dynamics and Monte Carlo simulations. Energetics, composition, and Li transport properties were characterized. Except for amorphous $\Sigma 9(221)/[1\bar{1}0]$, little change in the concentration of Li, La, Zr, or O at GB's in comparison to the bulk was observed. A consistent and quantitative reduction in Li diffusivity was observed at the GB; similarly, qualitative analyses of Li-ion trajectories also suggested a disruption of diffusion pathways near GBs. Li diffusivity was more sensitive to temperature within crystalline GB's, but less so in amorphous analogues. Diffusivity and activation energy both decreased with increasing grain boundary energy, and a logarithmic relationship between the pre-exponential factor and activation energy was observed. This is consistent with the compensation effect, suggesting that the variation of the pre-exponential factor within the group of GB's studied significantly impacts ionic diffusivity. Diffusion was, on average, slower parallel to the GB plane, and faster normal to the GB plane.

## 6.2 Next Steps

The expectation of more efficient plating/stripping at step and kink sites suggests that increasing the population of these sites will improve performance. Strategies with this goal in mind should be explored. For example, this can be achieved by patterning a substrate upon which the metal anode material can be deposited.[288] Or, from the perspective of the solid electrolyte, self-assembly of facets can be promoted on ceramic surfaces.[289] These examples suggest that opportunities exist for optimizing interface geometries for enhanced cycling efficiency.

Current mechano-electrochemical models take as input parameters the elastic properties derived from polycrystalline systems. These 'averaged' properties may be inaccurate when considering the formation of nuclei which are typically crystalline and have nano-scale dimensions. Furthermore, available experimental data for elastic properties of a given material often emcompass a range of values that reflect different measurement techniques, sample processing histories, and the presence of defects and impurities. The data presented here are 'free' from these complications and thus represent idealized values of elastic properties that can serve as a benchmark. The present data show that maximum anisotropic elastic property values can significantly exceed those of polycrystalline values, calling into question the near-universal use of averaged, polycrystalline properties. Revisiting these models with elastic property anisotropies in mind may lead to more accurate models of performance.

The performance of LLZO is improved if the grain boundary character is crystalline as opposed to amorphous: The former (crystalline) GB's generally exhibit greater diffusivity compared the latter. At the same time, improved diffusivity at grain boundaries with lower grain boundary energy means that they are preferable to those that are higher in energy. Rational design of practical LLZO solid electrolytes should optimize processing temperatures; higher temperatures

to minimize the presence of high-energy grain boundaries, while taking care not to overheat, thus disordering the grain boundary structure.

Furthermore, the presented work on LLZO is restricted to pure LLZO. The impact of impurities and additives (e.g. dopants such as Al and Ta) should be explored. It would be helpful to explore the impact of GB impurity segregation on performance.

Energy in the U.S. is predominantly generated by the burning of fossil fuels.[290] Advances in rechargeable batteries have the potential to radically alter our society by replacing this energy source. Safe, energy-dense rechargeable batteries will stimulate the widespread use of electric vehicles. Grid-based energy storage will allow for further implementation of intermittent, renewable wind and solar energy generation. Rechargeable batteries which utilize metal anodes, aided by the implementation of a solid electrolyte, would go a long way toward achieving these goals.

# Appendix A
Supporting Tables and Figures for Chapter 3

**Table A.1** Experimental Overpotentials of Metals at Various Conditions from Cyclic Voltammograms

| Metal | Nucleation Potential (mV) | Scan Rate (mV/s) | Concentration (M) or Ratio (Ionic Liquids) | Electrolyte | Temperature (°C) | Substrate |
|---|---|---|---|---|---|---|
| Li | -299[60] | 25 | 0.01 | $LiPF_6$ \| EC:DEC | 25 | Ni |
| | -161[60] | 25 | 0.1 | $LiPF_6$ \| EC:DEC | 25 | Ni |
| | -145[60] | 25 | 1 | $LiPF_6$ \| EC:DEC | 25 | Ni |
| | -120[291] | 50 | 1 | $LiPF_6$ \| DMC | 25 | Li |
| | -100*[292] | 50 | 2 | LiTFSI \| DME | 25 | Pt |
| | -100*[292] | 50 | 3 | LiTFSI \| DME | 25 | Pt |
| | -100*[292] | 50 | 5 | LiTFSI \| DME | 25 | Pt |
| Na | -190[291] | 50 | 1 | $NaPF_6$ \| EC:DMC | 25 | SS |
| | -120[291] | 50 | 1 | $NaPF_6$ \| EC:PC:DMC | 25 | SS |
| K | -30*[293] | 0.05 | 0.5 | $KPF_6$ \| EC:DEC | 25 | Ni |
| | -50*[294] | 10 | 0.5 | $KPF_6$ \| DME | 25 | Au |
| | -30*[294] | 50 | 0.5 | $KPF_6$ \| DME | 25 | Ag |
| | -50*[294] | 50 | 0.5 | $KPF_6$ \| DME | 25 | Pt |
| Ca | -650[86] | 0.5 | 0.3 | $Ca(BF_4)_2$ \| EC:PC | 100 | Cu |
| | -520[86] | 0.5 | 0.45 | $Ca(BF_4)_2$ \| EC:PC | 100 | Cu |
| | -650[86] | 0.5 | 0.65 | $Ca(BF_4)_2$ \| EC:PC | 100 | Cu |
| | -800[86] | 0.5 | 0.8 | $Ca(BF_4)_2$ \| EC:PC | 100 | Cu |
| Al | -540*[52] | 10 | 1/0.6/2.9 | $AlCl_3$ \| EnPS \| Toluene | 70 | Mo |
| | -110*[52] | 10 | 1/1/2.9 | $AlCl_3$ \| EnPS \| Toluene | 25 | Mo |
| | -1040*[52] | 10 | 1/1.2/2.9 | $AlCl_3$ \| EnPS \| Toluene | 80 | Mo |
| | -960*[52] | 10 | 1/4 | $AlCl_3$ \| EiPS | 80 | Mo |
| | -1010*[52] | 10 | 1/4 | $AlCl_3$ \| EiPS | 80 | Mo |
| | -1100*[52] | 10 | 1/4 | $AlCl_3$ \| EnPS | 80 | Mo |
| | -180*[52] | 10 | 1/4 | $AlCl_3$ \| DnPS | 80 | Mo |
| | -540*[52] | 10 | 1/4 | $AlCl_3$ \| EsBS | 25 | Mo |
| | -540*[52] | 10 | 4/3 | $AlCl_3$ \| EnPS | 25 | Mo |
| | -270*[52] | 10 | 2/1 | $AlCl_3$ \| EMICl | 25 | Mo |
| | -110*[50] | 20 | 2/1 | $AlCl_3$ \| (EMIm)Cl | 60 | W |
| | -90[51] | 20 | 2/1 | $AlCl_3$ \| TMPAC | 22.5 | W |
| Mg | -240*[295] | 1 | 0.5 | $Mg(TFSI)_2$/G3 | 100 | Pt |
| | -160*[296] | 5 | 0.09 | $MgCl_2$ + $AlCl_3$\|THF (MACC) | 25 | Pt |
| | -280*[58] | 5 | 0.25 | $[AlCl_2EtBu]_2Mg$ \| THF | 25 | Pt |
| | -400*[58] | 5 | 0.25 | $[BPh_2Bu_2]_2Mg$ \| THF | 25 | Pt |
| | -370*[63] | 5 | 0.25 | $[AlCl_2EtBu]_2Mg$ \| THF | 25 | Au |
| | -290*[297] | 5 | 0.25 | $[AlCl_2EtBu]_2Mg$ \| THF | 25 | Au |
| | -290*[297] | 5 | 0.25 | $[AlCl_2Bu]_2Mg$ \| THF | 25 | Au |
| | -250*[34] | 5 | 0.75 | MMC \| G3:DME | 25 | Pt |
| | -250*[34] | 5 | 0.75 | MMC \| G4:DME | 25 | Pt |
| | -130*[63] | 5 | 1 | BuMgCl \| THF | 25 | Au |
| | -120*[297] | 5 | 1 | BuMgCl \| THF | 25 | Au |
| | -150*[56] | 5 | 2 | EtMgCl \| THF:TBAP | 25 | Au |
| | -120*[56] | 5 | 2 | BuMgCl \| THF:TBAP | 25 | Au |
| | -140*[56] | 5 | 2 | EtMgBr \| THF:TBAP | 25 | Au |
| | -120*[58] | 5 | 2 | BuMgCl \| THF | 25 | Pt |
| | -200[298] | 10 | 0.75 | EtMgCl + $AlCl_3$ \| THF | 25 | Pt |
| | -190[298] | 10 | 0.75 | EtMgCl + $AlCl_3$ \| THF | 25 | Cu |
| | -240*[299] | 20 | 0.01 | $Mg(BH_4)_2$ \| diglyme | 25 | Pt |
| | -380*[299] | 20 | 0.01 | $Mg(BH_4)_2$ \| DME | 25 | Pt |

| | | | | | | |
|---|---|---|---|---|---|---|
| | -420*[299] | 20 | 0.01 | $Mg(BH_4)_2$ \| THF | 25 | Pt |
| | -270*[299] | 20 | 0.1 | $Mg(BH_4)_2$+ various conc. $LiBH_4$ \| diglyme | 25 | Pt |
| | -280*[300] | 20 | 0.25 | $[AlCl_2EtBu]_2Mg$ \| THF | 25 | Pt |
| | -410*[300] | 20 | 0.25 | $[AlCl_2EtBu]_2Mg$ \| Diglyme | 25 | Pt |
| | -190*[300] | 20 | 0.25 | $[AlCl_2EtBu]_2Mg$ \| Tetraglyme | 25 | Pt |
| | -190*[300] | 20 | 0.25 | $[AlCl_2EtBu]_2Mg$ \| glyme | 25 | Pt |
| | -200[301] | 25 | 0.03 | (1:1,2:1) MACC \| THF | 25 | Pt |
| | -2706[60] | 25 | 0.05 | EtMgCl \| THF:Me2AlCl | 25 | Pt |
| | -270[302] | 25 | 0.1 | 1:2 $AlCl_3$+PhMgCl \| THF | 25 | Pt |
| | -195[302] | 25 | 0.1 | 1:4 $AlCl_3$+PhMgCl \| THF | 25 | Pt |
| | -1118[60] | 25 | 0.1 | EtMgCl \| THF:dimethylaluminum chloride | 25 | Pt |
| | -250[302] | 25 | 0.2 | 1:2 $AlCl_3$+PhMgCl \| THF | 25 | Pt |
| | -352[65] | 25 | 0.2 | $Mg_2(\mu\text{-}Cl)_3{\cdot}6(THF)(Ph_4Al)$ \| THF | 21 | Pt |
| | -352[65] | 25 | 0.2 | $Mg_2(\mu\text{-}Cl)_3{\cdot}6(THF)(Ph_3AlCl)$ \| THF | 21 | Pt |
| | -352[65] | 25 | 0.2 | $Mg_2(\mu\text{-}Cl)_3{\cdot}6(THF)(Ph_2AlCl_2)$ \| THF | 21 | Pt |
| | -352[65] | 25 | 0.2 | $Mg_2(\mu\text{-}Cl)_3{\cdot}6(THF)(PhAlCl_3)$ \| THF | 21 | Pt |
| | -350*[65] | 25 | 0.2 | $Mg_2(\mu\text{-}Cl)_3{\cdot}6(THF)(EtAlCl_3)$ \| THF | 21 | Pt |
| | -300*[65] | 25 | 0.2 | $Mg_2(\mu\text{-}Cl)_3{\cdot}6(THF)(HMDSAlCl_3)$ \| THF | 21 | Pt |
| | -300*[65] | 25 | 0.2 | $Mg_2(\mu\text{-}Cl)_3{\cdot}6(THF)(HMDS_2AlCl_2)$ \| THF | 21 | Pt |
| | -490[303] | 25 | 0.25 | 1:2 $MgBu_2$+$AlEtCl_2$ \| THF | 25 | Pt |
| | -440[303] | 25 | 0.25 | 1:2 $MgBu_2$+$AlEt_3$ \| THF | 25 | Pt |
| | -190*[304] | 25 | 0.25 | 1:2 $MgBu_2$+$AlEtCl_2$ \| THF | 25 | Pt |
| | -260[302] | 25 | 0.25 | 1:2 $MgBu_2$+$AlEtCl_2$ \| THF | 25 | Pt |
| | -215[302] | 25 | 0.25 | 1:2 $AlCl_3$+PhMgCl \| THF | 25 | Pt |
| | -294[60] | 25 | 0.25 | EtMgCl\|THF:dimethylaluminum chloride | 25 | Pt |
| | -340*[305] | 25 | 0.25 | APC \| THF | 25 | Pt |
| | -200[306] | 25 | 0.25 | 2:1 MACC \| DME | 25 | Pt |
| | -295[302] | 25 | 0.3 | 3:4 $AlCl_3$+PhMgCl \| THF | 25 | Pt |
| | -220*[304] | 25 | 0.4 | 1:2 $AlCl_3$+PhMgCl \| THF | 25 | Pt |
| | -195[302] | 25 | 0.4 | 1:2 $AlCl_3$+PhMgCl \| THF | 25 | Pt |
| | -320[302] | 25 | 0.4 | 1:1 $AlCl_3$+PhMgCl \| THF | 25 | Pt |
| | -305[302] | 25 | 0.4 | 2:3 $AlCl_3$+PhMgCl \| THF | 25 | Pt |
| | -430[303] | 25 | 0.5 | 1:2 $MgBu_2$+$AlEtCl_2$ \| THF | 25 | Pt |
| | -195[302] | 25 | 0.6 | 1:2 $AlCl_3$+PhMgCl \| THF | 25 | Pt |
| Zn | -29[128] | 10 | 8.6 | KOH/water (saturated w/ zincate) | 25 | Zn |
| | -370[44] | 10 | 0.1 | $Zn(TfO)_2$\|EMIm with $Ni(TfO)_2$ | 25 | Cu |

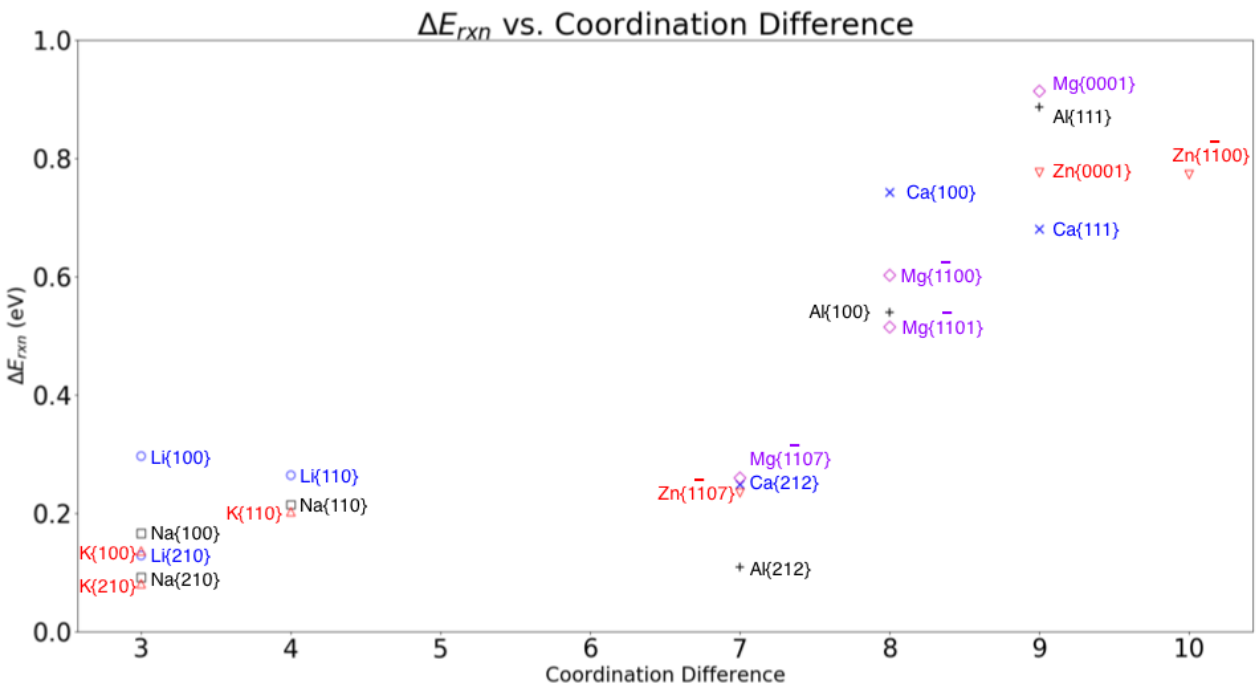


**Figure A.1** Plot of reaction energy vs. coordination difference. Coordination difference is defined as the difference between the number of nearest neighbors of a single deposited atom and an atom in the bulk state.

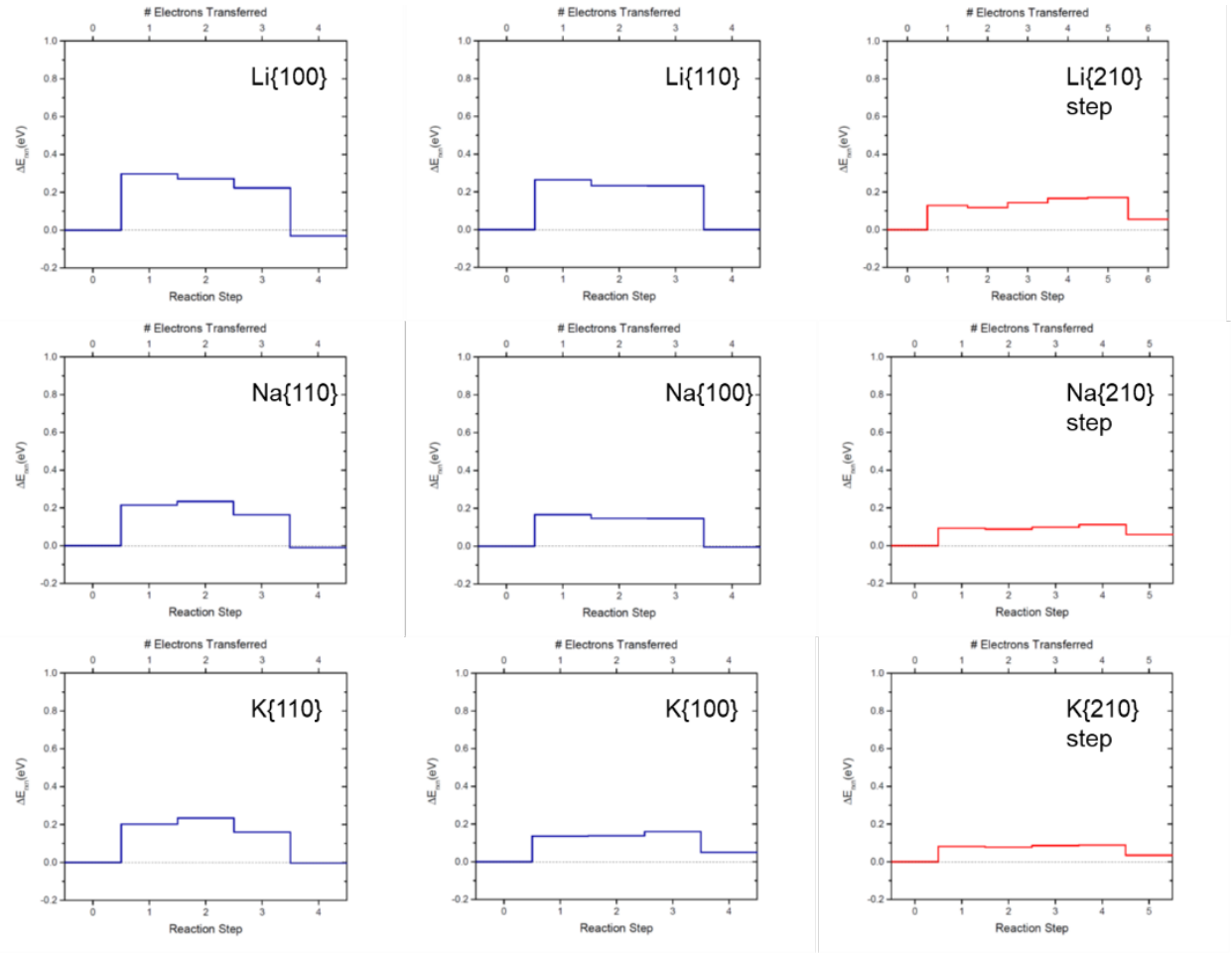


**Figure A.2** Plots of deposition/dissolution reaction energies on the alkali metals. Alkali metals all share the body-centered cubic crystal structure, and are expected to be among the most efficient metals to cycle. Note that the final step does not equal zero in these and subsequent plots because of the disparity between the bonding state of the surface atoms and the bulk atoms used for the calculation.

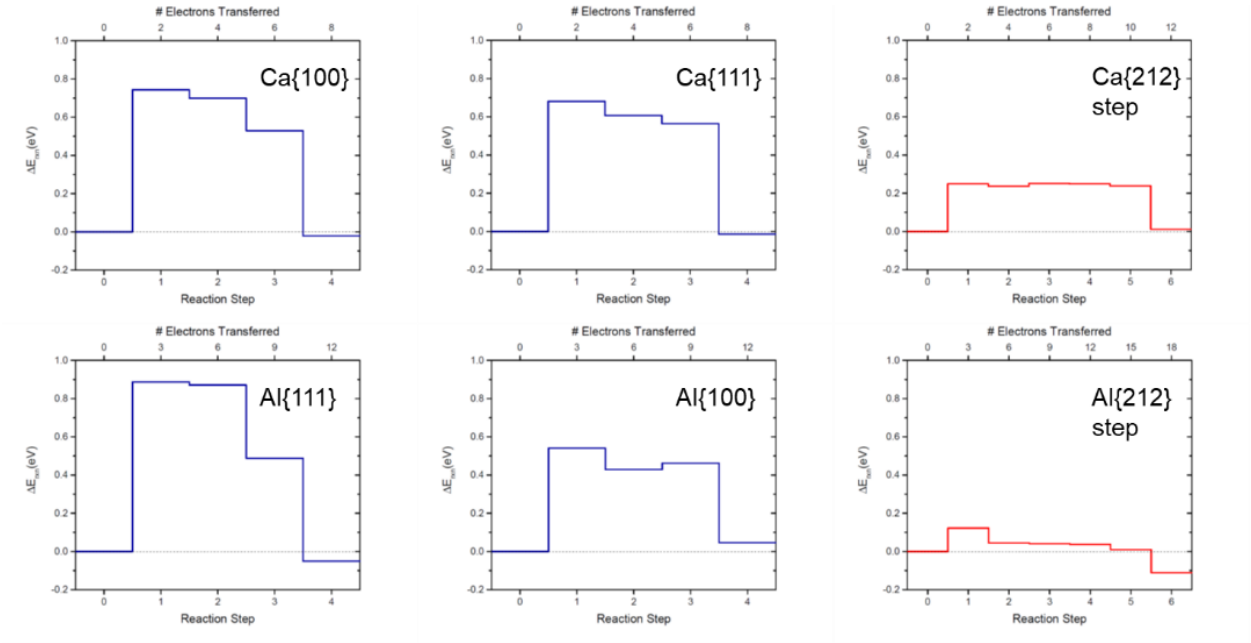


**Figure A.3** Plots of deposition/dissolution reaction energies on calcium and aluminum. These metals share the face-centered cubic crystal structure. Note that the profile of the Al step surface plot has a dramatically different shape than all other plots, returning to a value much less than zero at the last step. This is likely a result of finite size effects in the calculation.

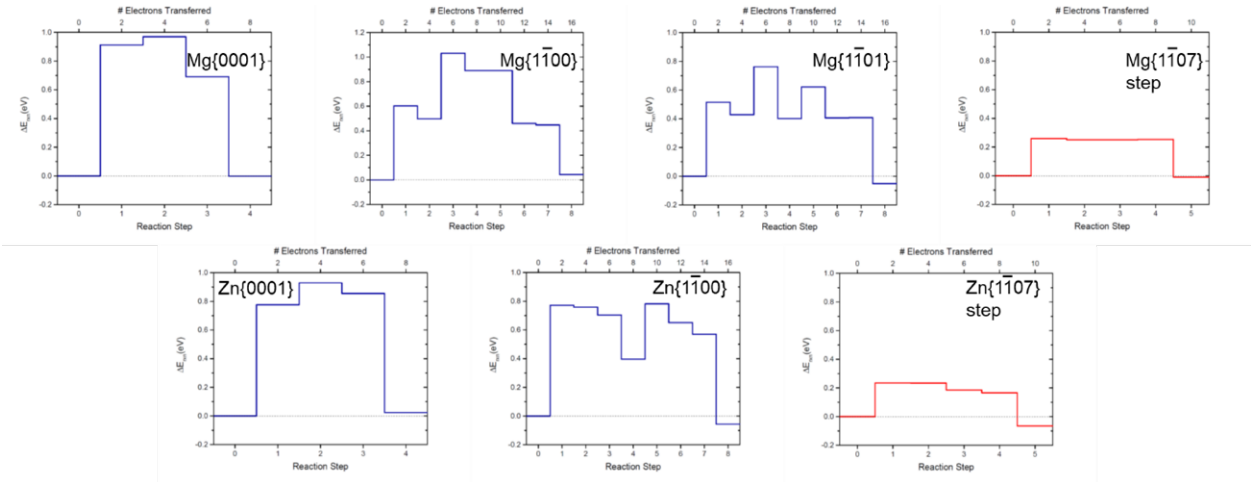


**Figure A.4** Plots of deposition/dissolution reaction energies on magnesium and zinc. These metals share the hexagonal close-packed crystal structure. The surfaces Mg{1$\bar{1}$00}y, Mg{1$\bar{1}$01}, and Zn{1$\bar{1}$00} are corrugated surfaces, and step four represents initiation of a new row.

**Table A.2** Calculated Steady-State Nucleation Rate and Critical Formation Energy for Electrodeposition on Terrace and Step Sites at an Applied Potential of -10 mV.

| | Metal | Critical Formation Energy (eV) | Steady-State Nucleation Rate ($s^{-1}.cm^{-2}$) |
|---|---|---|---|
| Terrace | Li{100} | 0.29 | 3.72E+09 |
| | Li{110} | 0.25 | 1.64E+10 |
| | Na{110} | 0.21 | 1.07E+11 |
| | Na{100} | 0.16 | 6.54E+11 |
| | K{110} | 0.19 | 3.30E+11 |
| | K{100} | 0.13 | 2.82E+12 |
| | Mg{0001} | 0.89 | 2.57E-01 |
| | Mg{$1\bar{1}00$} | 0.58 | 3.63E+04 |
| | Mg{$1\bar{1}01$} | 0.50 | 7.60E+05 |
| | Ca{100} | 0.72 | 2.63E+02 |
| | Ca{111} | 0.66 | 2.61E+03 |
| | Al{111} | 0.86 | 4.33E-01 |
| | Al{100} | 0.51 | 2.77E+05 |
| | Zn{0001} | 0.76 | 2.63E+01 |
| | Zn{$1\bar{1}00$} | 0.75 | 3.86E+01 |
| Step | Li{210} | 0.12 | 1.80E+12 |
| | Na{210} | 0.09 | 7.50E+12 |
| | K{210} | 0.07 | 2.14E+13 |
| | Mg{$1\bar{1}07$} | 0.24 | 1.31E+10 |
| | Ca{212} | 0.23 | 2.88E+10 |
| | Al{212} | 0.09 | 1.48E+12 |
| | Zn{$1\bar{1}07$} | 0.21 | 2.77E+10 |

# Appendix B

Supporting Tables and Figures for Chapter 4

**Table B.1** Pseudopotentials, planewave cutoff energies, and k-point grid sizes used to achieve converged elastic constants. The '% Difference' column gives the largest relative deviation between an elastic constant calculated using the specified k-point grid and the average elastic constant (red dotted lines in Figures B.1-B.8) calculated over the five densest k-grids shown in Figs. B.1-B.8. The size of the densest k-grid was determined by memory constraints.

| Pseudopotential | Cutoff Energy (eV) | K-Point Grid | % Difference |
|---|---|---|---|
| Al | 400 | $40^3$ | 6 |
| Ca_sv | 300 | $19^3$ | 1 |
| Li | 300 | $49^3$ | 3 |
| Na | 250 | $44^3$ | 2 |
| K_pv | 360 | $27^3$ | 2 |
| Mg | 300 | $40^3$ | 5 |
| Zn_GW | 610 | $37^3$ | 8 |
| Si | 420 | $14^3$ | 1 |

## CONVERGENCE WITH RESPECT TO K-POINT SAMPLING DENSITY

Figures B.1 – B.8 illustrate the convergence of the elastic constants with respect to the density of the k-point grid. The red dashed line is the average of the elastic constants evaluated from the five densest k-point grids; the blue dash-dotted lines represent the standard deviation of these same five values.

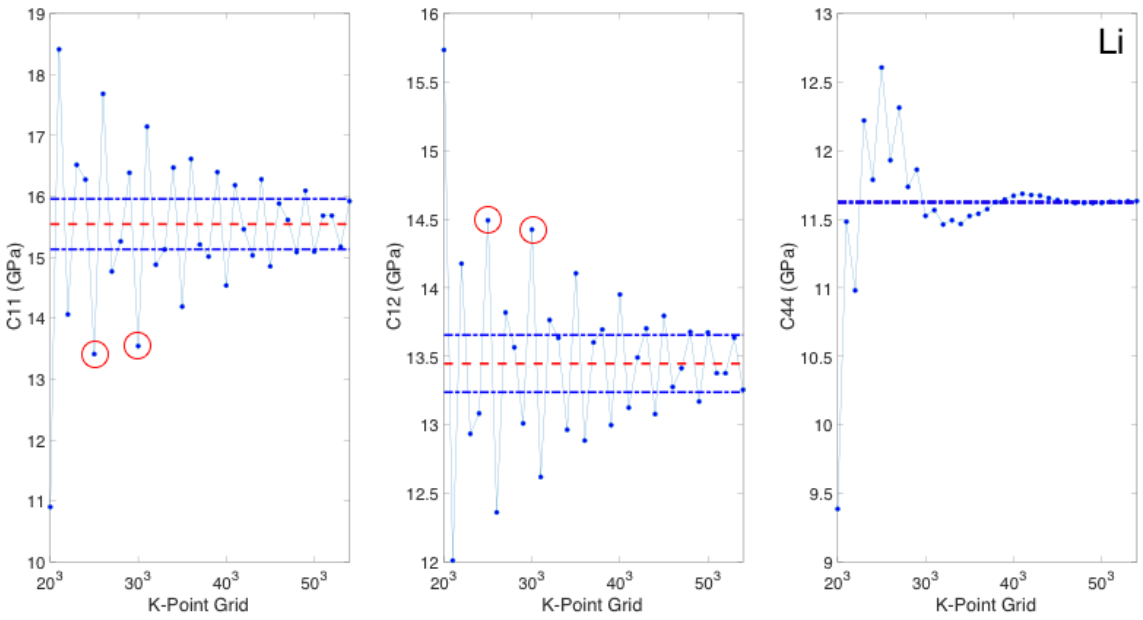


**Figure B.1** Calculated elastic constants for lithium vs. k-point grid density. The red circles highlight cases where, due to poor k-point sampling, $C_{11}$ is predicted to be smaller than $C_{12}$. These values violate the Born stability condition and incorrectly imply an unstable system.

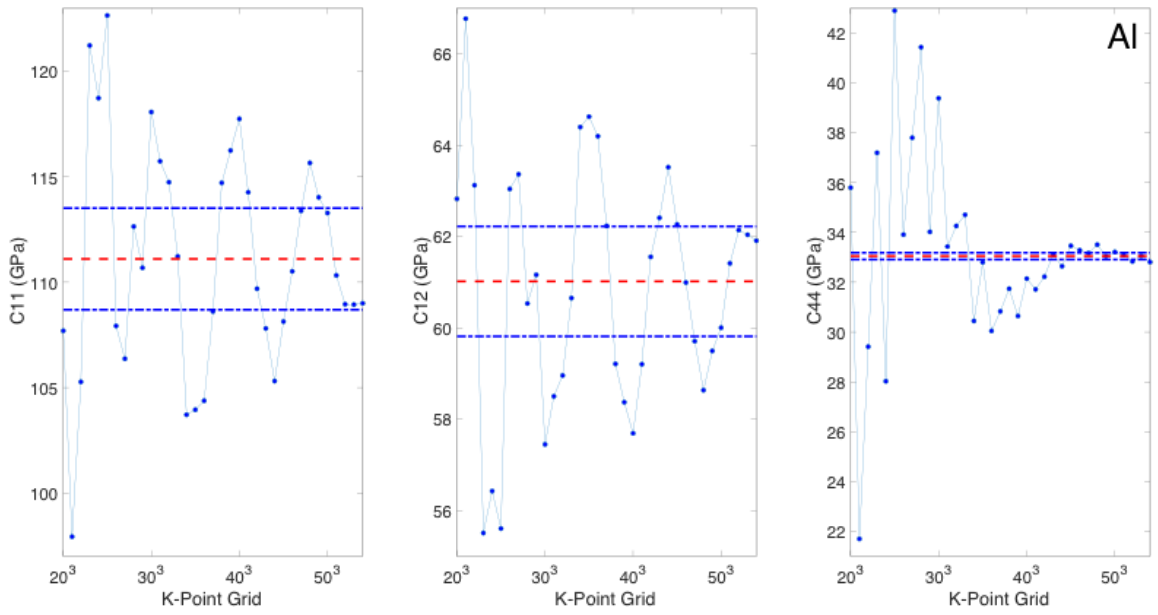


**Figure B.2** Calculated elastic constants for aluminum vs. k-point grid density.

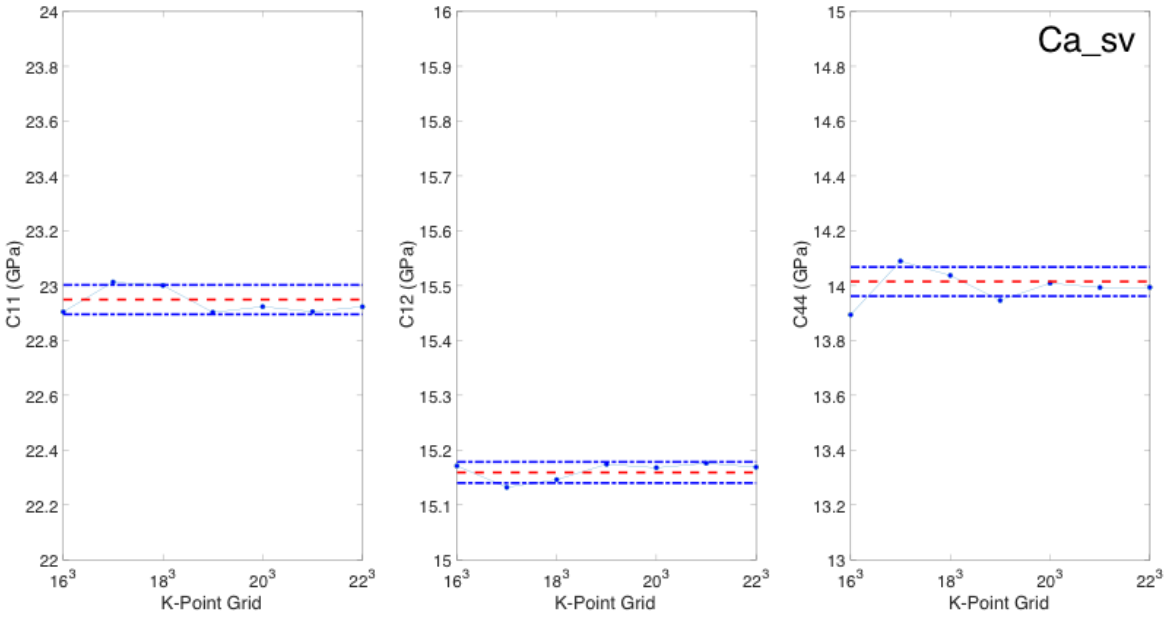


**Figure B.3** Calculated elastic constants for calcium vs. k-point grid density.

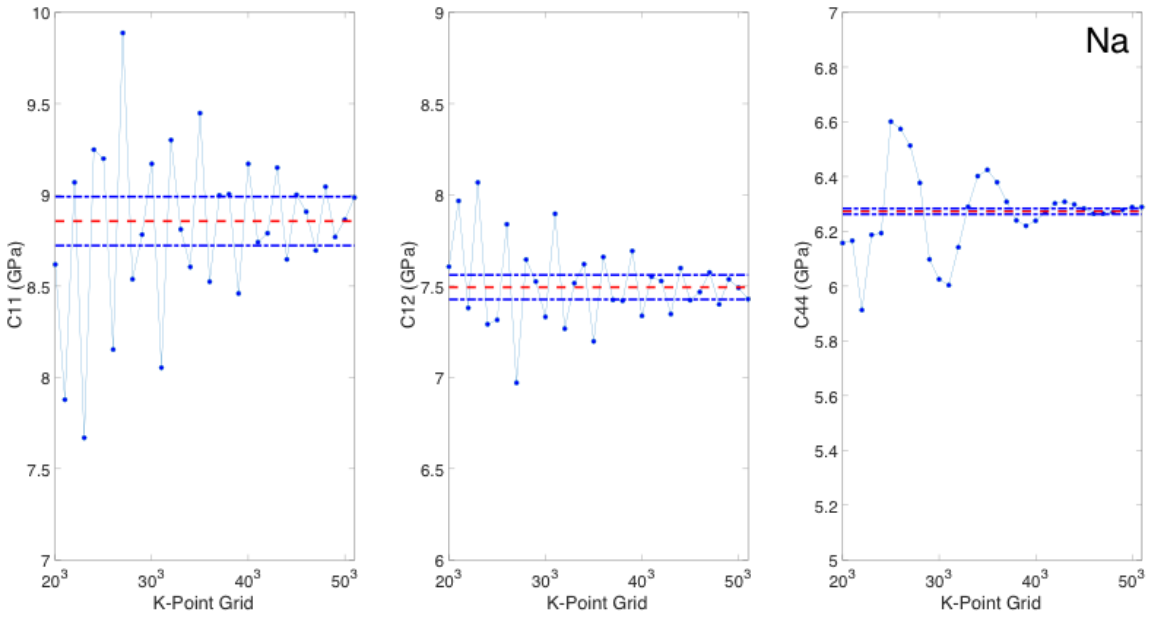


**Figure B.4** Calculated elastic constants for sodium vs. k-point grid density.

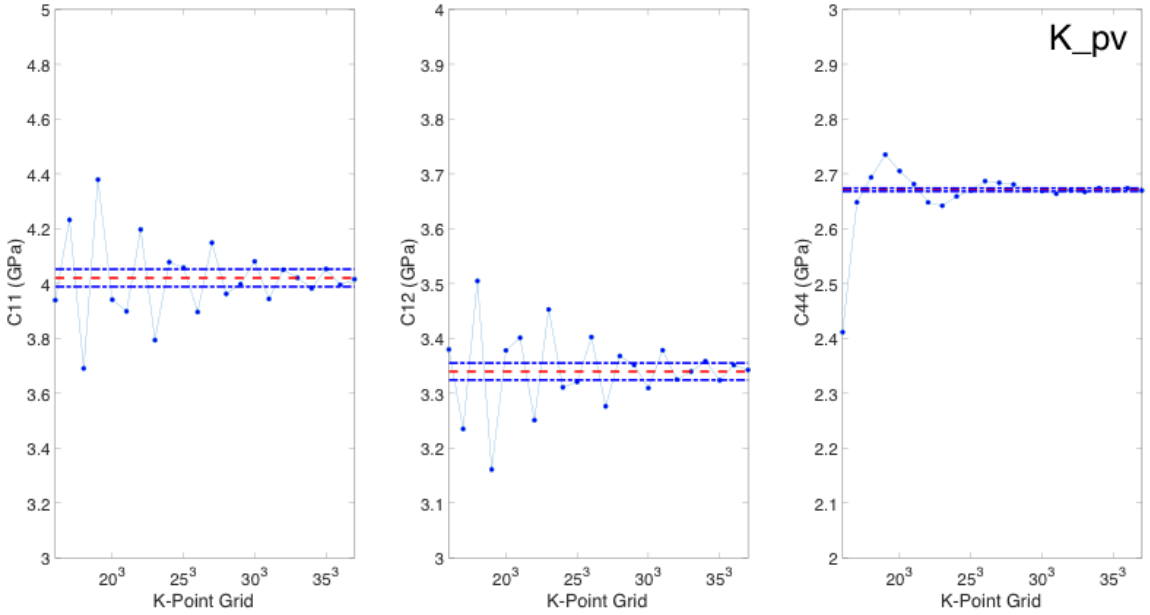


**Figure B.5** Calculated elastic constants for potassium vs. k-point grid density.

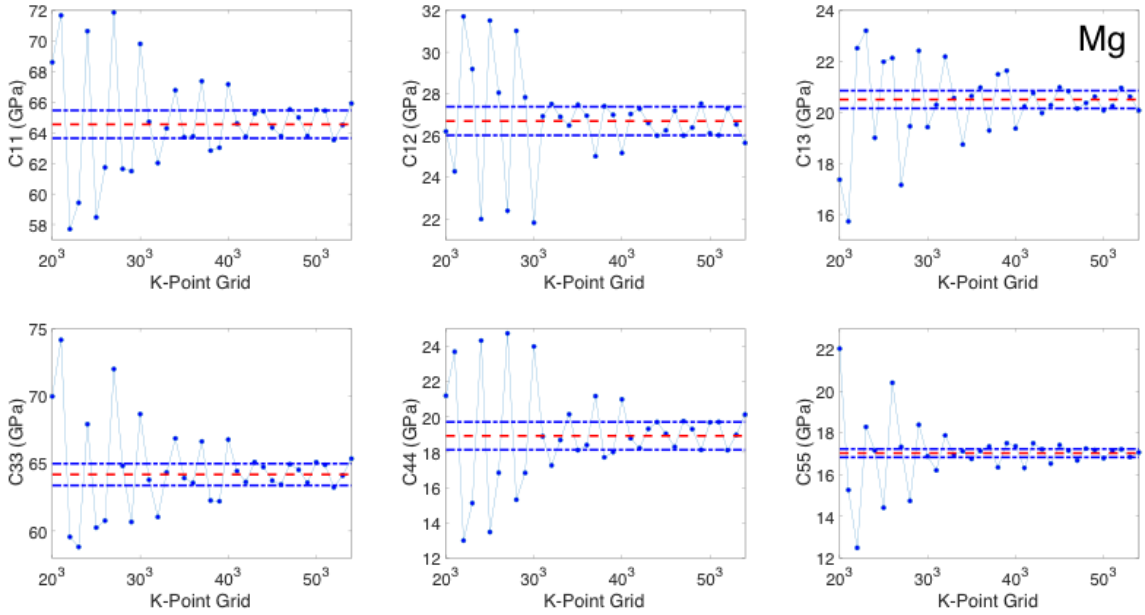


**Figure B.6** Calculated elastic constants for magnesium vs. k-point grid density.

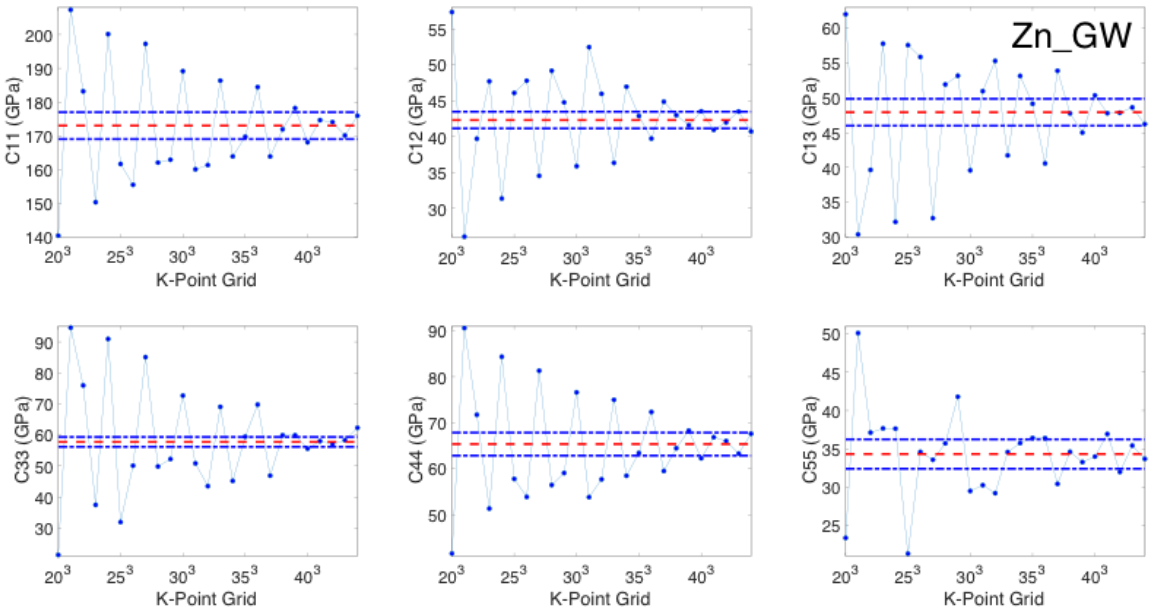


**Figure B.7** Calculated elastic constants for zinc vs. k-point grid density.

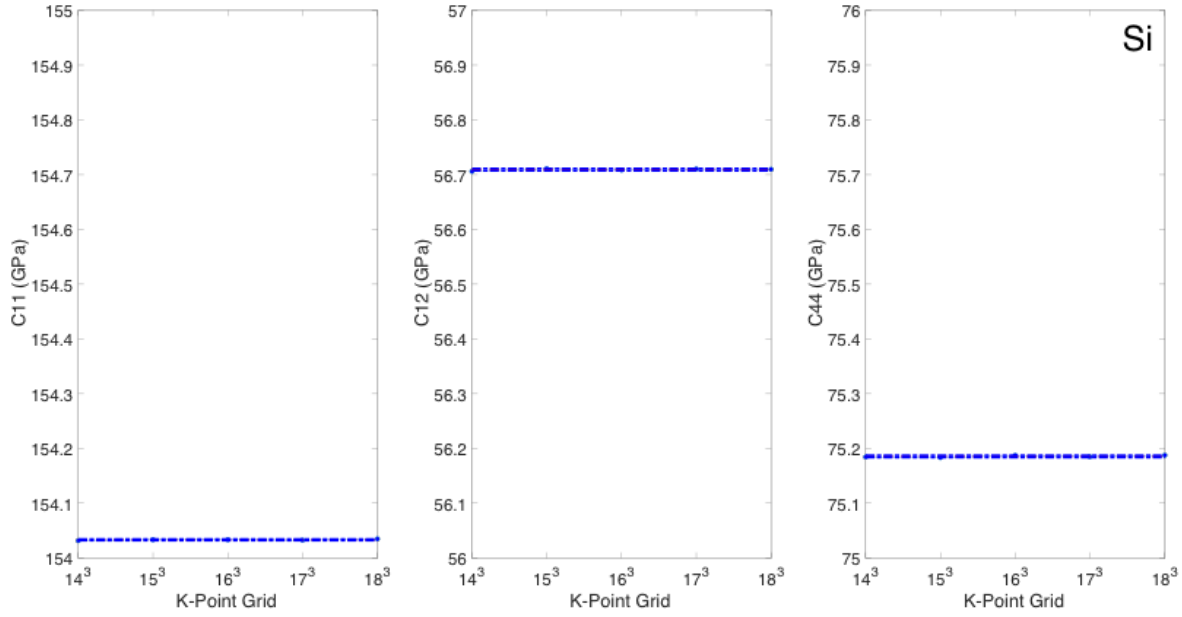


**Figure B.8** Calculated elastic constants for silicon vs. k-point grid density.

## CONVERGENCE WITH RESPECT TO PLANE-WAVE CUTOFF ENERGY

Figures B.9 – B.17 illustrate the convergence of the calculated elastic constants with respect to the planewave cutoff energy. An elastic constant was considered converged if its value was within 1% of the value calculated using the highest cutoff energy examined.

Calculations employing the Zn PAW POTCAR exhibited discontinuities in the elastic constants as a function of cutoff energy. The Zn_GW POTCAR did not exhibit this undesirable behavior, and was therefore adopted for all calculations on Zn.

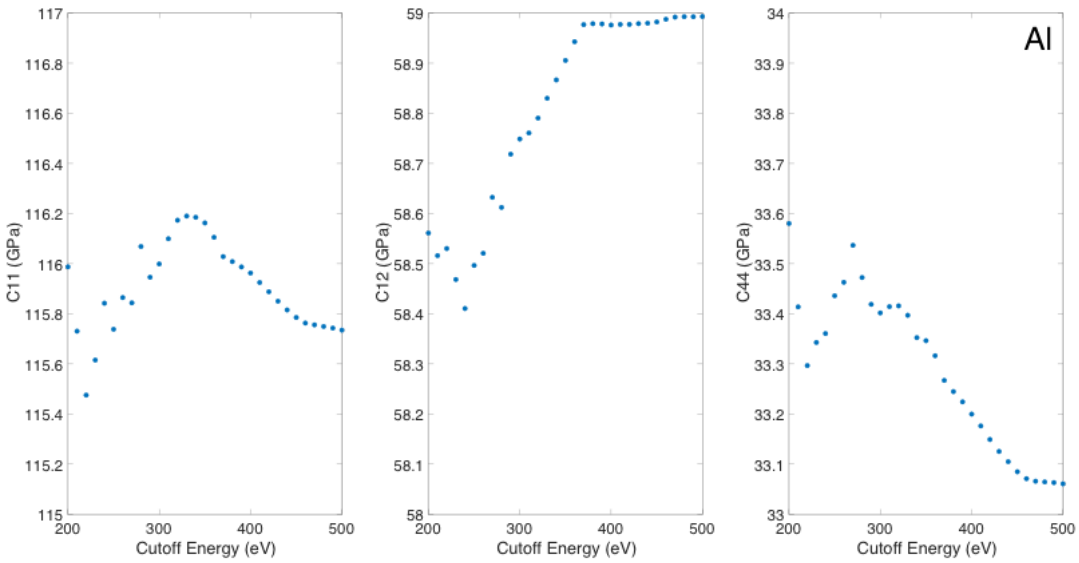


**Figure B.9** Convergence of elastic constants for aluminum with respect to the planewave cutoff energy.

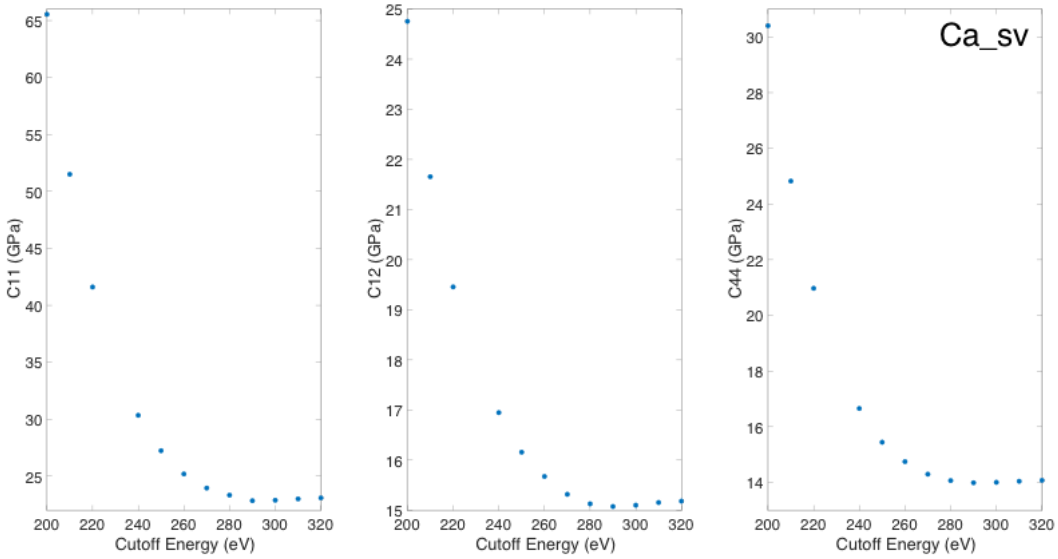


**Figure B.10** Convergence of the elastic constants for calcium with respect to the planewave cutoff energy.

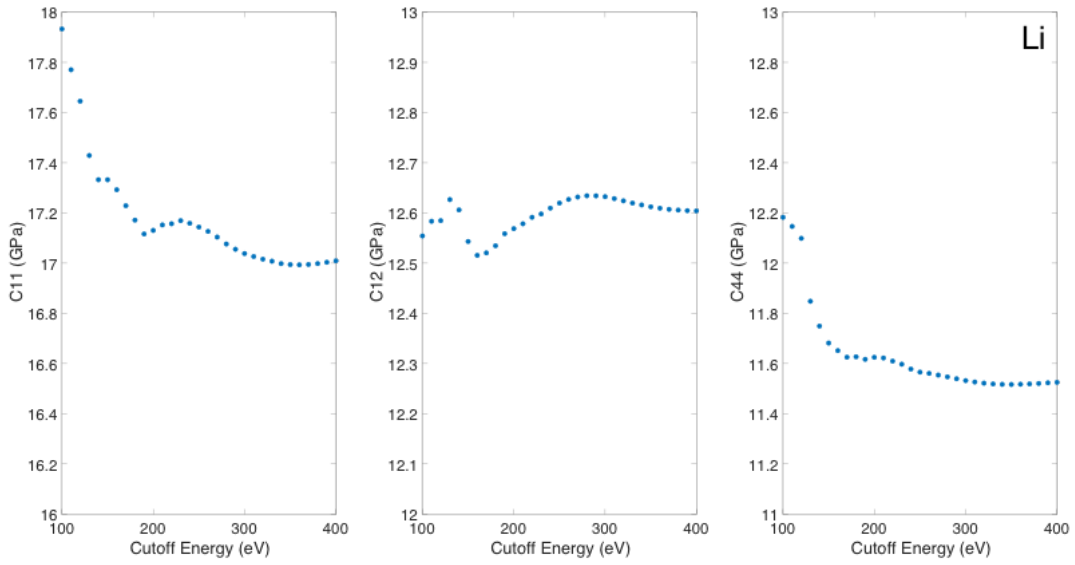


**Figure B.11** Convergence of the elastic constants for lithium with respect to the planewave cutoff energy.

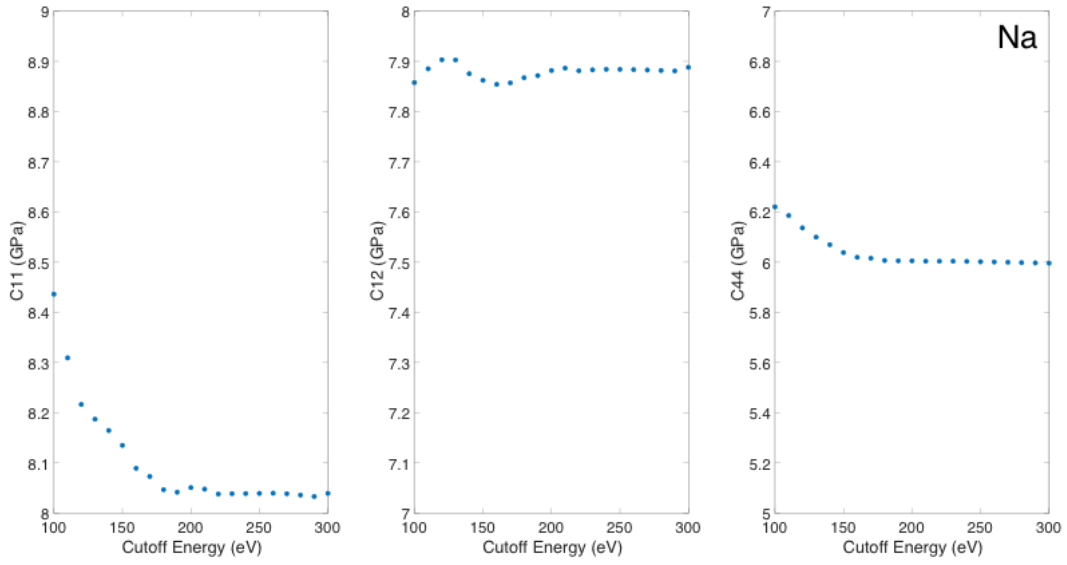


**Figure B.12** Convergence of the elastic constants for sodium with respect to the planewave cutoff energy.

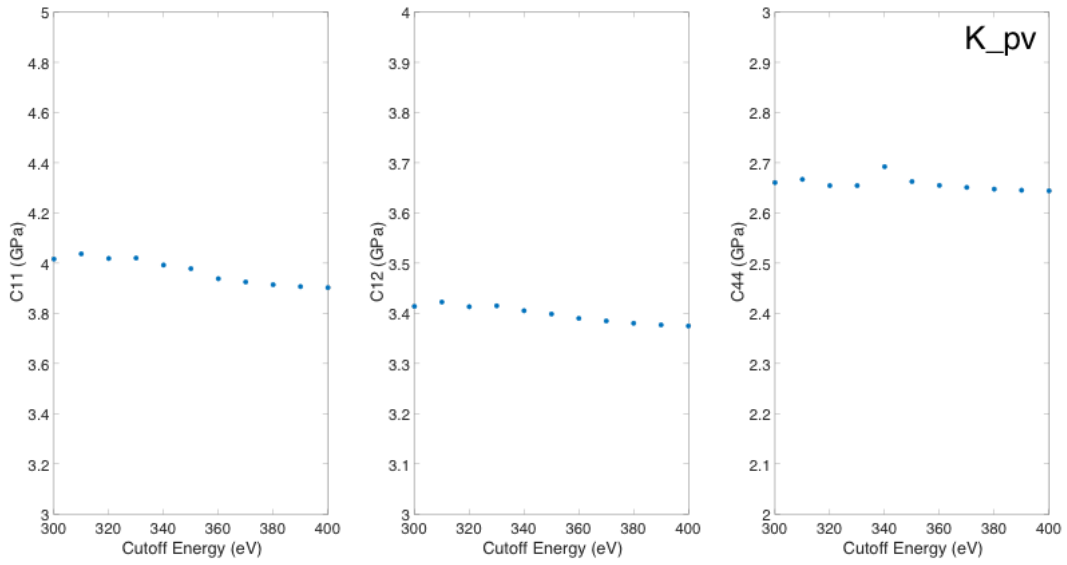


**Figure B.13** Convergence of the elastic constants for potassium with respect to the planewave cutoff energy.

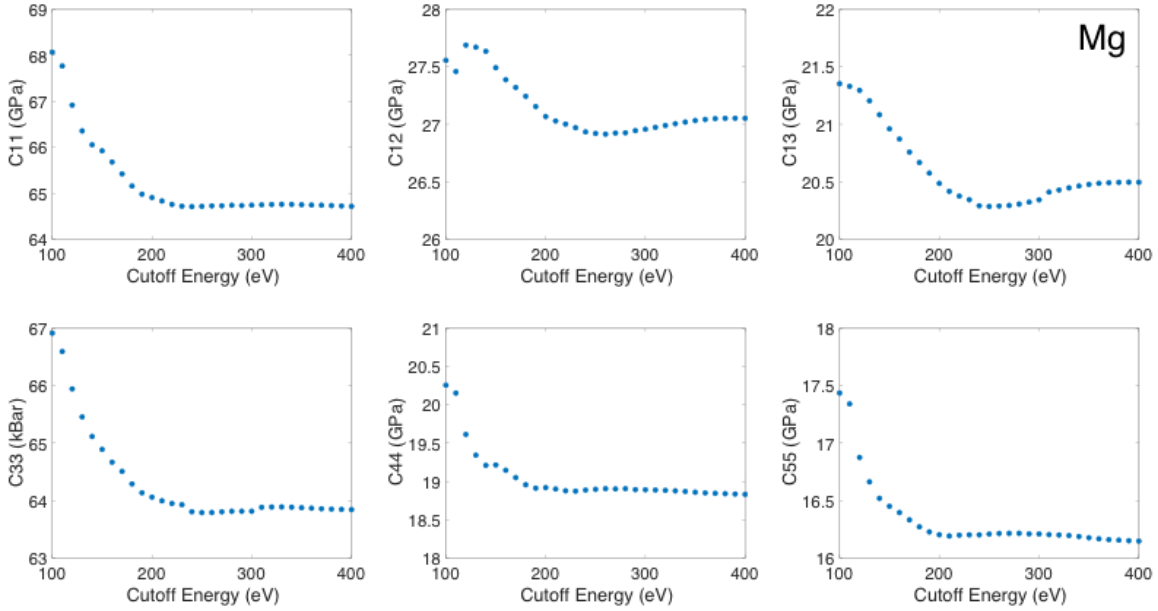


**Figure B.14** Convergence of the elastic constants for magnesium with respect to the planewave cutoff energy.

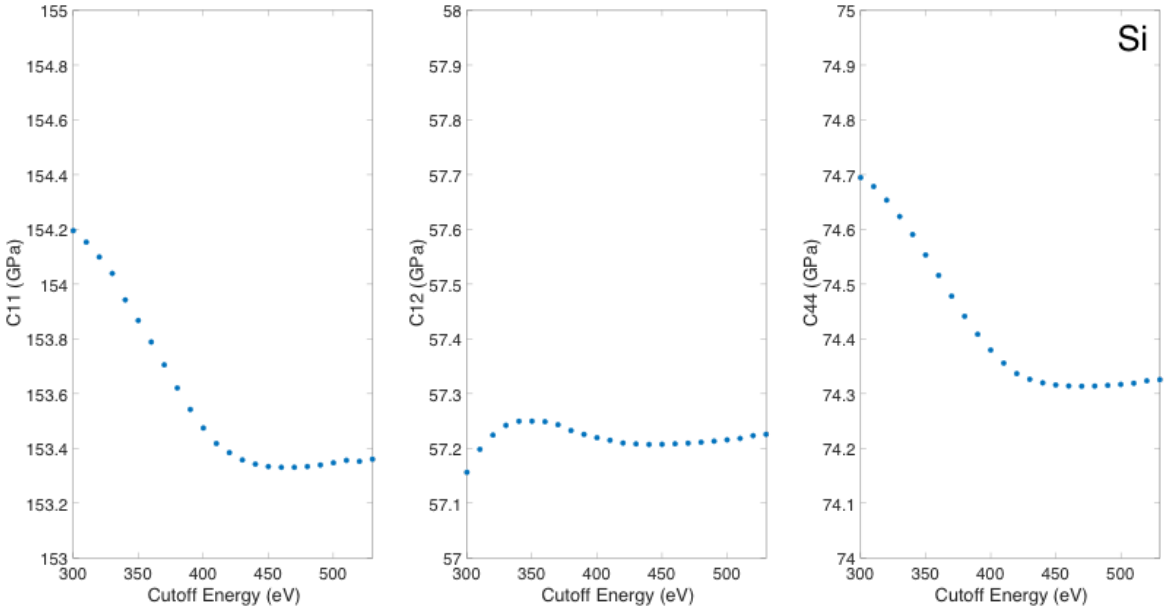


**Figure B.15** Convergence of the elastic constants for silicon with respect to the planewave cutoff energy.

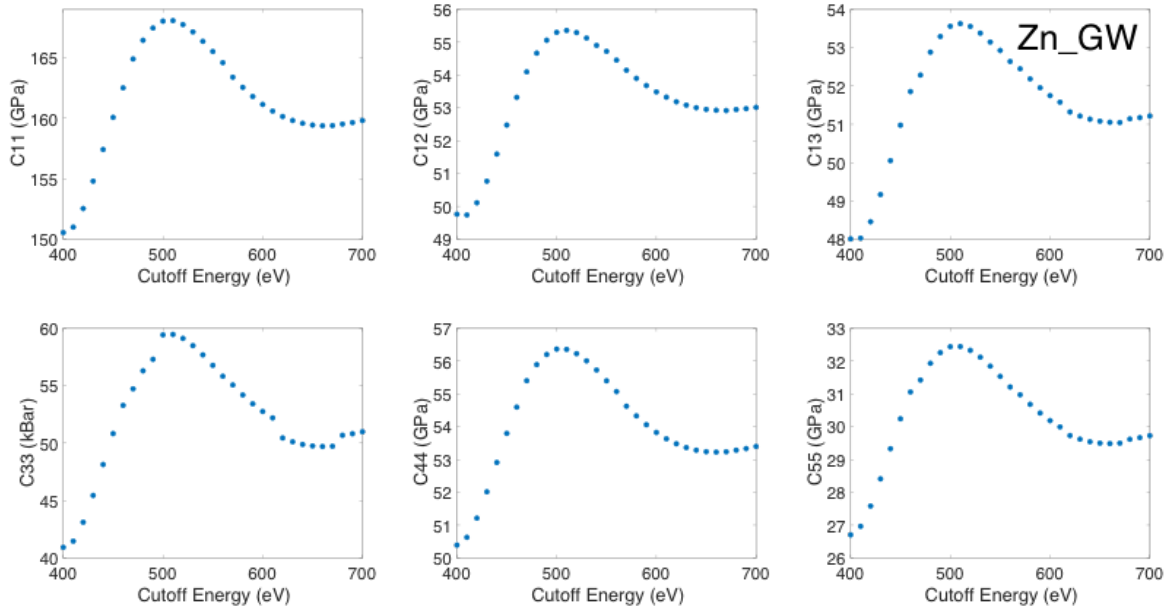


**Figure B.16** Convergence of the elastic constants for zinc (using the 'Zn_GW' PAW potential) with respect to the planewave cutoff energy.

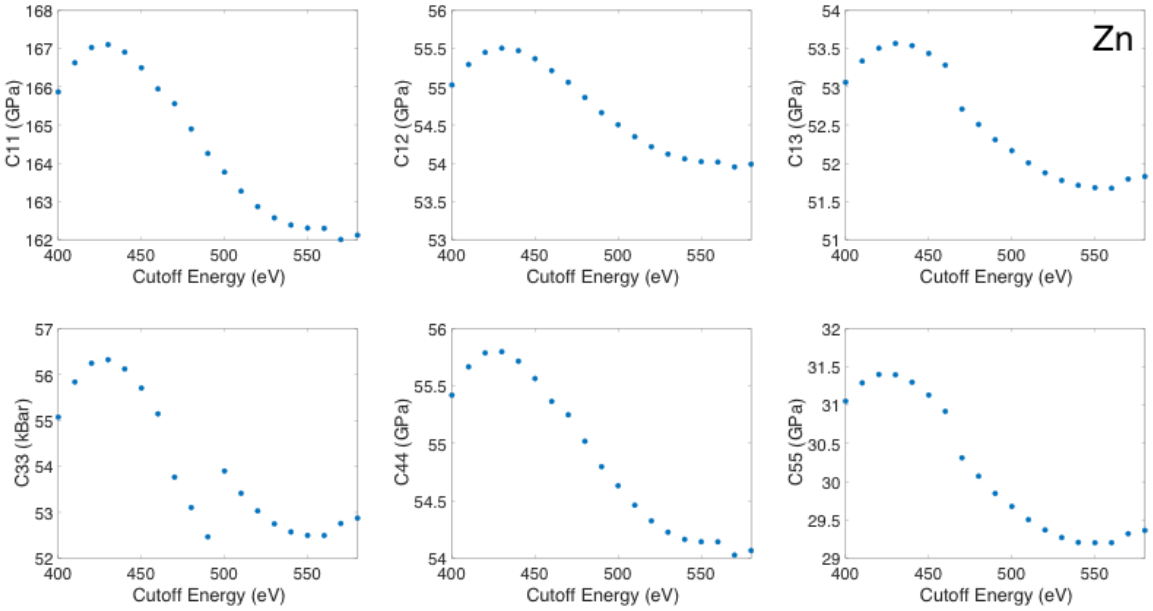


**Figure B.17** Convergence of the elastic constants for zinc (using the 'Zn' PAW potential) with respect to the planewave cutoff energy.

**Table B.2** Comparison of elastic constants (in GPa) calculated using various exchange-correlation functionals with low-temperature experimental data.[143, 307-313] Calculated values are reported at 0 K; experimental data is reported for the lowest temperature identified in the literature. Values reported by de Jong et al. in the Dryad database were calculated with the PBE functional.[204-205]

| | | Experimental Temperature | Expt. | PBE | AM05 | PBEsol | rPBE | PW91 | Materials Project/ Dryad |
|---|---|---|---|---|---|---|---|---|---|
| Al | $C_{11}$ | 0 K | 118.63* | 118.02 | 119.02 | 117.09 | 121.45 | 116.14 | 103.93 |
| | $C_{12}$ | | 66.36* | 58.17 | 59.95 | 57.70 | 60.46 | 56.15 | 72.95 |
| | $C_{44}$ | | 31.26* | 31.95 | 35.68 | 32.26 | 33.66 | 29.75 | 31.86 |
| | % error | | - | 7.25 | 9.88 | 7.79 | 6.91 | 9.39 | 9.23 |
| Ca | $C_{11}$ | 298 K | 22.8 | 22.90 | 22.51 | 22.05 | 23.83 | 24.15 | 20.83 |
| | $C_{12}$ | | 16.0 | 15.17 | 15.17 | 14.71 | 14.21 | 16.07 | 15.09 |
| | $C_{44}$ | | 14.0 | 13.95 | 14.12 | 13.35 | 15.44 | 13.76 | 14.09 |
| | % error | | - | 3.00 | 4.73 | 7.24 | 6.51 | 4.68 | 5.98 |
| Li | $C_{11}$ | 78 K | 14.8 | 15.99 | 15.95 | 15.82 | 16.69 | 15.85 | 15.22 |
| | $C_{12}$ | | 12.5 | 13.18 | 13.18 | 13.03 | 13.79 | 13.05 | 13.41 |
| | $C_{44}$ | | 10.8 | 11.58 | 11.59 | 11.59 | 11.72 | 11.58 | 10.96 |
| | % error | | - | 6.99 | 6.92 | 6.28 | 10.68 | 6.36 | 4.59 |
| Na | $C_{11}$ | 78 K | 8.21 | 8.65 | 8.62 | 8.39 | 9.29 | 8.71 | 8.86 |
| | $C_{12}$ | | 6.83 | 7.60 | 7.45 | 7.34 | 8.10 | 7.62 | 6.84 |
| | $C_{44}$ | | 5.77 | 6.29 | 6.49 | 6.32 | 6.52 | 6.30 | 6.55 |
| | % error | | - | 8.93 | 9.33 | 7.08 | 15.15 | 9.24 | 9.05 |
| K | $C_{11}$ | 4.2 K | 4.16 | 3.90 | 3.86 | 3.64 | 4.35 | 3.81 | 3** |
| | $C_{12}$ | | 3.41 | 3.38 | 3.25 | 3.14 | 3.70 | 3.28 | 4** |
| | $C_{44}$ | | 2.86 | 2.71 | 2.75 | 2.65 | 2.80 | 2.65 | 3** |
| | % error | | - | 4.72 | 5.50 | 9.59 | 5.63 | 6.70 | - |
| Mg | $C_{11}$ | 0 K | 63.48 | 67.18 | 68.54 | 66.86 | 69.88 | 66.62 | 54.26 |
| | $C_{12}$ | | 25.94 | 25.20 | 25.61 | 24.90 | 26.15 | 24.50 | 34.07 |
| | $C_{13}$ | | 21.70 | 19.43 | 18.22 | 18.88 | 19.73 | 19.58 | 26.82 |
| | $C_{33}$ | | 66.45 | 66.80 | 70.32 | 66.85 | 70.14 | 64.94 | 65.86 |
| | $C_{55}$ | | 18.42 | 17.37 | 18.04 | 17.40 | 18.27 | 17.30 | 19.61 |
| | % error | | - | 6.08 | 8.49 | 7.00 | 6.58 | 6.21 | 18.93 |
| Zn | $C_{11}$ | 4.2 K | 179.09 | 164.39 | 153.61 | 154.61 | 170.67 | 163.92 | 162.28 |
| | $C_{12}$ | | 37.50 | 45.72 | 37.88 | 42.12 | 47.03 | 47.24 | 46.91 |
| | $C_{13}$ | | 55.40 | 54.50 | 51.30 | 53.47 | 55.07 | 55.24 | 48.64 |
| | $C_{33}$ | | 68.80 | 48.31 | 37.95 | 40.11 | 51.94 | 50.54 | 61.03 |
| | $C_{55}$ | | 45.95 | 30.45 | 30.16 | 30.02 | 30.58 | 30.84 | 32.32 |
| | % error | | - | 22.70 | 26.27 | 25.66 | 21.85 | 22.50 | 19.36 |
| Si | $C_{11}$ | 77.2 K | 167.72 | 153.56 | 151.63 | 151.31 | 155.00 | 153.84 | 143.60 |
| | $C_{12}$ | | 64.98 | 57.12 | 56.20 | 57.31 | 57.93 | 56.90 | 52.72 |
| | $C_{44}$ | | 80.36 | 74.72 | 73.21 | 72.74 | 75.49 | 75.22 | 74.63 |
| | % error | | - | 9.43 | 10.86 | 10.41 | 8.41 | 9.39 | 14.30 |

| | | | | | | | |
|---|---|---|---|---|---|---|---|
| Avg % error | - | 8.64 | 10.25 | 10.13 | 10.22 | 9.31 | 11.63 |

*: Average over multiple reported values.

**: Value quoted from the Materials Project website; data not present in Dryad database.

% error = $\sqrt{\frac{1}{n}\sum_{i=1}^{n}\left(\frac{C_{i,expt}-C_{i,calc}}{C_{i,expt}}\right)^2}$ where i indexes the Voigt subscripts of the elastic constants, and $n = 3$ or 5 for cubic or hexagonal systems, respectively.

**Table B.3** Calculated and Experimental Lattice Parameters as a Function of Temperature.[314-323] Values in parentheses represent the c lattice parameter for HCP systems.

| | Experimental Lattice Parameter (Å) | Experimental Temperature (K) | Calculated Lattice Parameter (Å) | Simulation Temperature (K) |
|---|---|---|---|---|
| Al | 4.045 | 150 | 4.059 | 150 |
| | 4.056 | 300 | 4.071 | 300 |
| | 4.079 | 525 | 4.087 | 450 |
| Ca | - | - | 5.554 | 150 |
| | 5.588 | 298 | 5.575 | 300 |
| | - | - | 5.597 | 450 |
| Li | 3.491 | 78 | 3.472 | 150 |
| | 3.509 | 298 | 3.493 | 300 |
| | 3.537 | 424 | 3.517 | 450 |
| Na | 4.235 | 78 | 4.236 | 150 |
| | 4.28 | 298 | 4.286 | 300 |
| K | 5.247 | 78 | 5.344 | 150 |
| | 5.31 | 298 | 5.399 | 300 |
| Mg | - | - | 3.212 (5.273) | 150 |
| | 3.203 (5.200) | 298 | 3.239 (5.318) | 300 |
| | 3.215 (5.221) | 453 | 3.274 (5.374) | 450 |
| Zn | 2.659 (4.904) | 160 | 2.679 (5.078) | 150 |
| | 2.664 (4.946) | 300 | 2.709 (5.135) | 300 |
| | 2.669 (4.989) | 450 | 2.746 (5.204) | 450 |
| Si | 5.419 | 77.4 | 5.487 | 150 |
| | 5.432 | 373.5 | 5.491 | 300 |
| | 5.434[20] | 493.1 | 5.498 | 450 |

**Table B.4** Experimental Elastic Constants (in GPa) as a Function of Temperature. Experimental values within 20 K of each listed temperature are included (i.e. measurements conducted at 170 K are included in the data for 150 K).[143, 307-313] The average and standard deviation are provided in cases where multiple values were reported for a given element/temperature.

| | | $C_{11}$ | $C_{12}$ | $C_{13}$ | $C_{33}$ | $C_{44}$ |
|---|---|---|---|---|---|---|
| Al | 150 K | 116.0 ± 4.0 | 65.7 ± 4.1 | | | 30.1 ± 0.3 |
| | 300 K | 107.8 ± 2.1 | 61.5 ± 2.1 | | | 28.3 ± 0.3 |
| | 450 K | 101.8 ± 1.0 | 60.1 ± 1.1 | | | 25.9 ± 0.3 |
| Ca | 300 K | 25.3 ± 2.5 | 17.1 ± 1.1 | | | 15.2 ± 1.2 |
| Li | 150 K | 14.0 ± 0.1 | 11.8 ± 0.1 | | | 10.1 ± 0.1 |
| | 300 K | 13.3 ± 0.2 | 11.3 ± 0.2 | | | 8.8 ± 0.1 |
| Na | 150 K | 7.8 | 6.5 | | | 5.3 |
| | 300 K | 6.3 ± 0.9 | 5.1 ± 0.9 | | | 4.8 ± 0.8 |
| K | 150 K | 4.0 | 3.3 | | | 2.3 |
| | 300 K | 3.8 ± 0.4 | 3.2 ± 0.1 | | | 2.3 ± 0.4 |
| Mg | 150 K | 62.0 ± 0.2 | 25.9 ± 0.0 | 21.6 ± 0.0 | 64.8 ± 0.2 | 17.8 ± 0.1 |
| | 300 K | 58.9 ± 1.0 | 25.4 ± 1.0 | 21.0 ± 1.2 | 61.1 ± 1.0 | 16.5 ± 0.2 |
| Zn | 150 K | 173.4 | 36.6 | 54.8 | 66.2 | 43.0 |
| | 300 K | 161.3 ± 8.6 | 30.2 ± 7.5 | 48.0 ± 7.1 | 60.7 ± 6.4 | 39.5 ± 0.9 |
| | 450 K | 151.4 | 35.5 | 51.1 | 60.8 | 34.2 |
| Si | 150 K | 166.7 | 64.1 | | | 80.1 |
| | 300 K | 166.4 ± 0.9 | 64.5 ± 0.8 | | | 80.5 ± 1.8 |

**Table B.5** Experimental Isotropic Elastic Moduli (in GPa) and Poisson's ratio as a Function of Temperature.[143, 307-313] In cases where only the elastic constants are known (Table B.4), the elastic moduli were evaluated using equations 4.1-4.3. The average and standard deviation are provided in cases where multiple values were reported.

| | | B | E | G | $\nu$ |
|---|---|---|---|---|---|
| Al | 150 K | 82.5 ± 4.0 | 75.4 ± 0.3 | 28.0 ± 0.2 | 0.347 ± 0.008 |
| | 300 K | 76.9 ± 2.1 | 70.4 ± 0.4 | 26.1 ± 0.2 | 0.347 ± 0.004 |
| | 450 K | 74.5 ± 0.9 | 64.1 ± 0.7 | 23.6 ± 0.3 | 0.357 ± 0.003 |
| Ca | 300 K | 19.8 ± 1.6 | 23.5 ± 2.5 | 9.0 ± 1.0 | 0.304 ± 0.006 |
| Li | 150 K | 12.6 ± 0.1 | 11.9 ± 0.1 | 4.4 ± 0.1 | 0.342 ± 0.001 |
| | 300 K | 12.0 ± 0.2 | 10.7 ± 0.1 | 4.0 ± 0.0 | 0.351 ± 0.002 |
| Na | 150 K | 7.0 | 6.5 | 2.4 | 0.346 |
| | 300 K | 5.5 ± 0.9 | 5.8 ± 0.6 | 2.2 ± 0.3 | 0.320 ± 0.031 |
| K | 150 K | 3.6 | 3.0 | 1.1 | 0.362 |
| | 300 K | 3.4 ± 0.2 | 2.7 ± 0.7 | 1.0 ± 0.3 | 0.368 ± 0.029 |
| Mg | 150 K | 36.3 ± 0.1 | 47.8 ± 0.2 | 18.7 ± 0.1 | 0.281 ± 0.000 |
| | 300 K | 34.8 ± 1.1 | 44.6 ± 0.1 | 17.3 ± 0.1 | 0.287 ± 0.007 |
| Zn | 150 K | 71.2 | 107.0 | 42.8 | 0.250 |
| | 300 K | 64.3 ± 6.2 | 100.6 ± 3.5 | 40.6 ± 1.3 | 0.237 ± 0.022 |
| | 450 K | 65.0 | 90.2 | 35.5 | 0.269 |
| Si | 150 K | 98.3 | 163.8 | 67.0 | 0.222 |
| | 300 K | 98.6 ± 0.9 | 164.1 ± 2.1 | 67.1 ± 0.9 | 0.223 ± 0.000 |

**Table B.6** Calculated Isotropic Elastic Properties (in GPa) and Poisson's ratio at 150 K, 300 K, and 450 K.

| | Temperature (K) | B | E | G | ν |
|---|---|---|---|---|---|
| Al | 150 | 74.2 | 77.9 | 29.4 | 0.325 |
| | 300 | 71.6 | 74.8 | 28.2 | 0.326 |
| | 450 | 68.6 | 71.0 | 26.7 | 0.328 |
| Ca | 150 | 17.2 | 21.5 | 8.3 | 0.292 |
| | 300 | 16.7 | 21.3 | 8.3 | 0.288 |
| | 450 | 16.2 | 21.0 | 8.2 | 0.284 |
| Li | 150 | 13.1 | 13.5 | 5.1 | 0.328 |
| | 300 | 12.5 | 13.2 | 5.0 | 0.324 |
| | 450 | 11.9 | 12.8 | 4.9 | 0.321 |
| Na | 150 | 7.2 | 6.5 | 2.4 | 0.351 |
| | 300 | 6.6 | 6.0 | 2.2 | 0.349 |
| K | 150 | 3.3 | 3.3 | 1.2 | 0.335 |
| | 300 | 3.0 | 3.0 | 1.1 | 0.336 |
| Mg | 150 | 33.1 | 46.1 | 18.2 | 0.268 |
| | 300 | 30.6 | 42.2 | 16.6 | 0.270 |
| | 450 | 27.6 | 37.6 | 14.8 | 0.272 |
| Zn | 150 | 51.8 | 70.7 | 27.8 | 0.272 |
| | 300 | 42.9 | 54.9 | 21.3 | 0.287 |
| | 450 | 27.3 | 23.5 | 8.7 | 0.357 |
| Si | 150 | 85.9 | 150.3 | 62.2 | 0.208 |
| | 300 | 85.3 | 149.9 | 62.1 | 0.208 |
| | 450 | 84.3 | 149.2 | 61.9 | 0.205 |

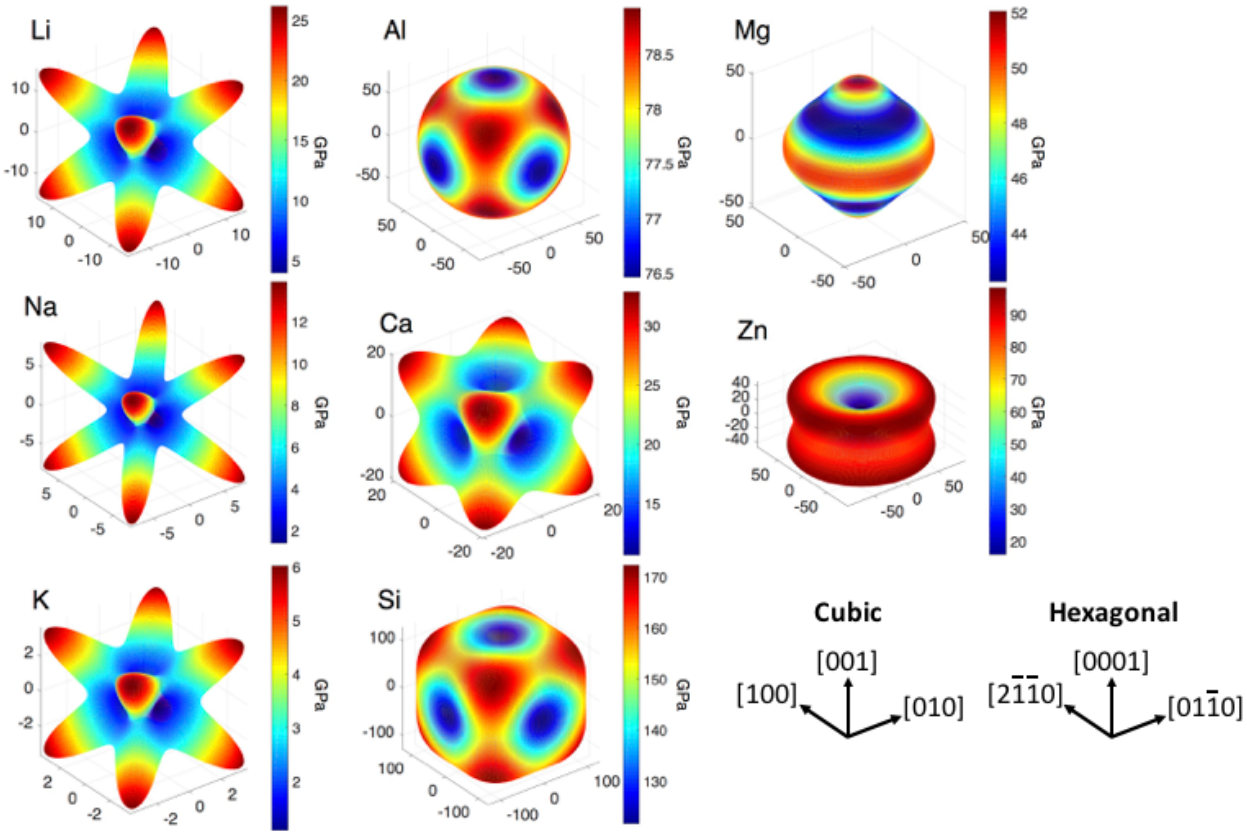


**Figure B.18** Calculated Young's modulus, *E*, as a function of crystallographic direction for Li, Na, K, Al, Ca, Si, Mg, and Zn at 150 K. The value of the modulus in a given crystallographic direction $\vec{a}$ is specified (redundantly) using the magnitude of the protrusion from the origin and with color coding. The range of the modulus scale varies from element-to-element. The shape of the plot indicates the degree of anisotropy: compact shapes such as cubes and spheres represent isotropic behavior; star-shaped plots suggest a greater degree of anisotropy.

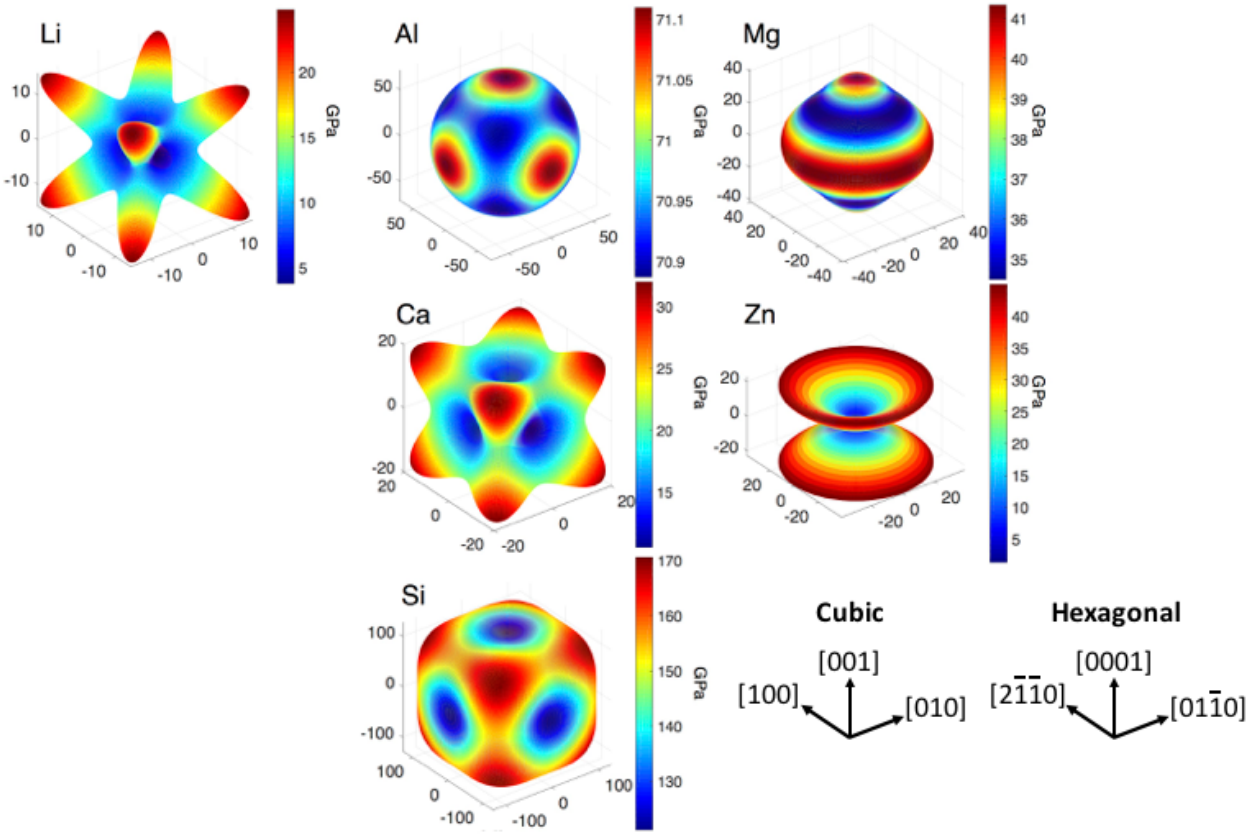


**Figure B.19** Calculated Young's modulus, *E*, as a function of crystallographic direction for Li, Na, K, Al, Ca, Si, Mg, and Zn at 450 K. The value of the modulus in a given crystallographic direction $\hat{a}$ is specified (redundantly) using the magnitude of the protrusion from the origin and with color coding. The range of the modulus scale varies from element-to-element. The shape of the plot indicates the degree of anisotropy: compact shapes such as cubes and spheres represent isotropic behavior; star-shaped plots suggest a greater degree of anisotropy. Data for Na and K are not included because 450 K exceeds their melting points.

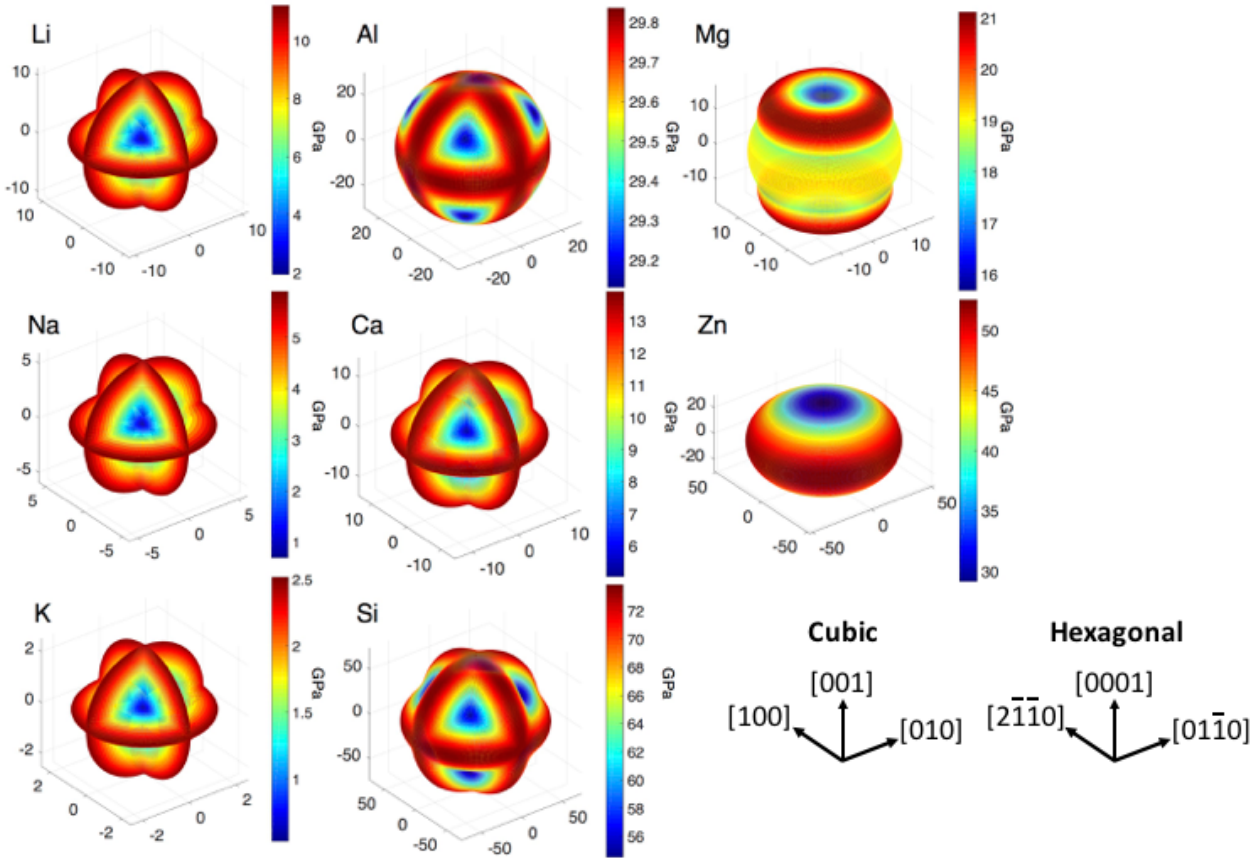


**Figure B.20** Calculated maximum shear modulus, $G^{Max}$, as a function of crystallographic direction for Li, Na, K, Al, Ca, Si, Mg, and Zn at 150 K. $G^{Max}$ represents the maximum G over all directions $\vec{b}$ perpendicular to $\vec{a}$. The coordinate system for $\vec{a}$ is shown for cubic and hexagonal crystal structures; the relationship between $\vec{b}$ and $\vec{a}$ is shown in Fig. 4.1. The modulus value is specified (redundantly) using the magnitude of the protrusion from the origin and with color coding. Note that the range of the modulus scale varies from element-to-element.

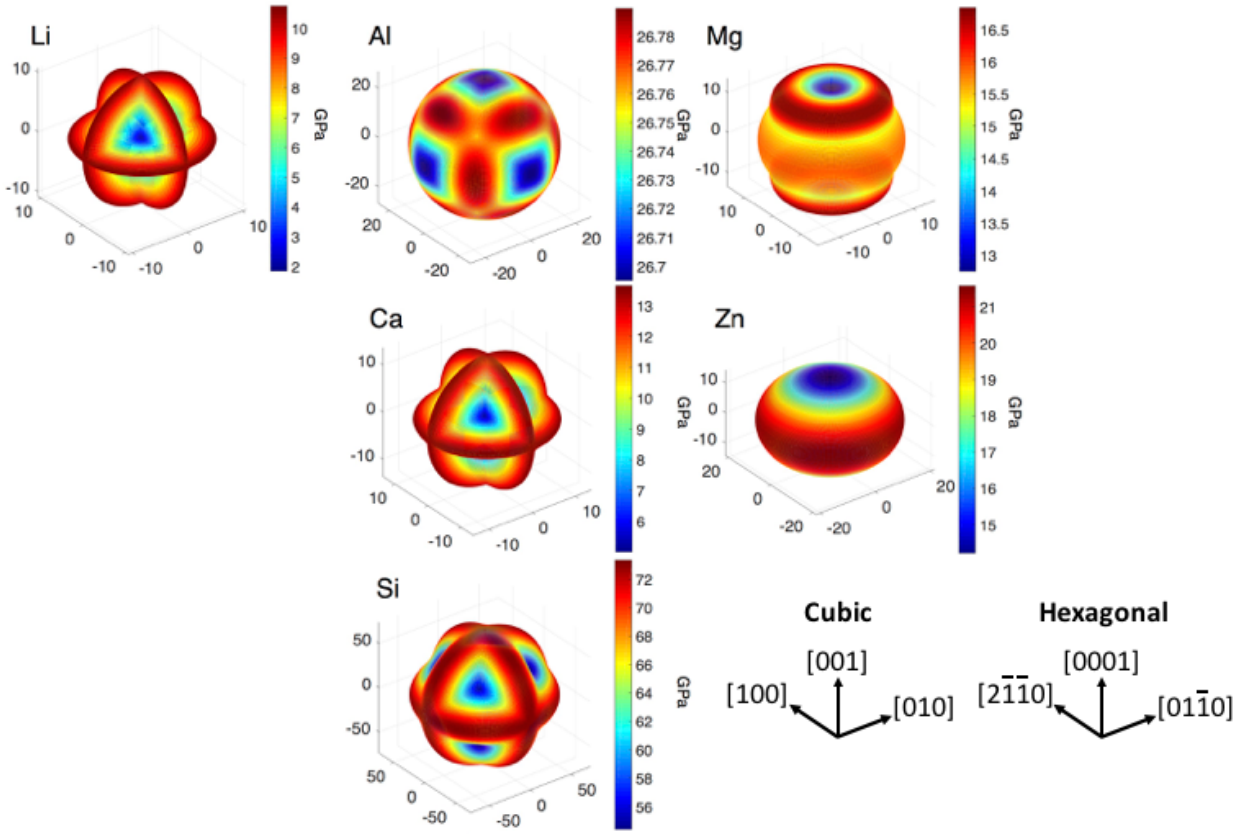


**Figure B.21** Calculated maximum shear modulus, $G^{Max}$, as a function of crystallographic direction for Li, Na, K, Al, Ca, Si, Mg, and Zn at 450 K. $G^{Max}$ represents the maximum G over all directions $\vec{b}$ perpendicular to $\vec{a}$. The coordinate system for $\vec{a}$ is shown for cubic and hexagonal crystal structures; the relationship between $\vec{b}$ and $\vec{a}$ is shown in Fig. 4.1. The modulus value is specified (redundantly) using the magnitude of the protrusion from the origin and with color coding. Note that the range of the modulus scale varies from element-to-element. Data for Na and K are not included because 450 K exceeds their melting points.

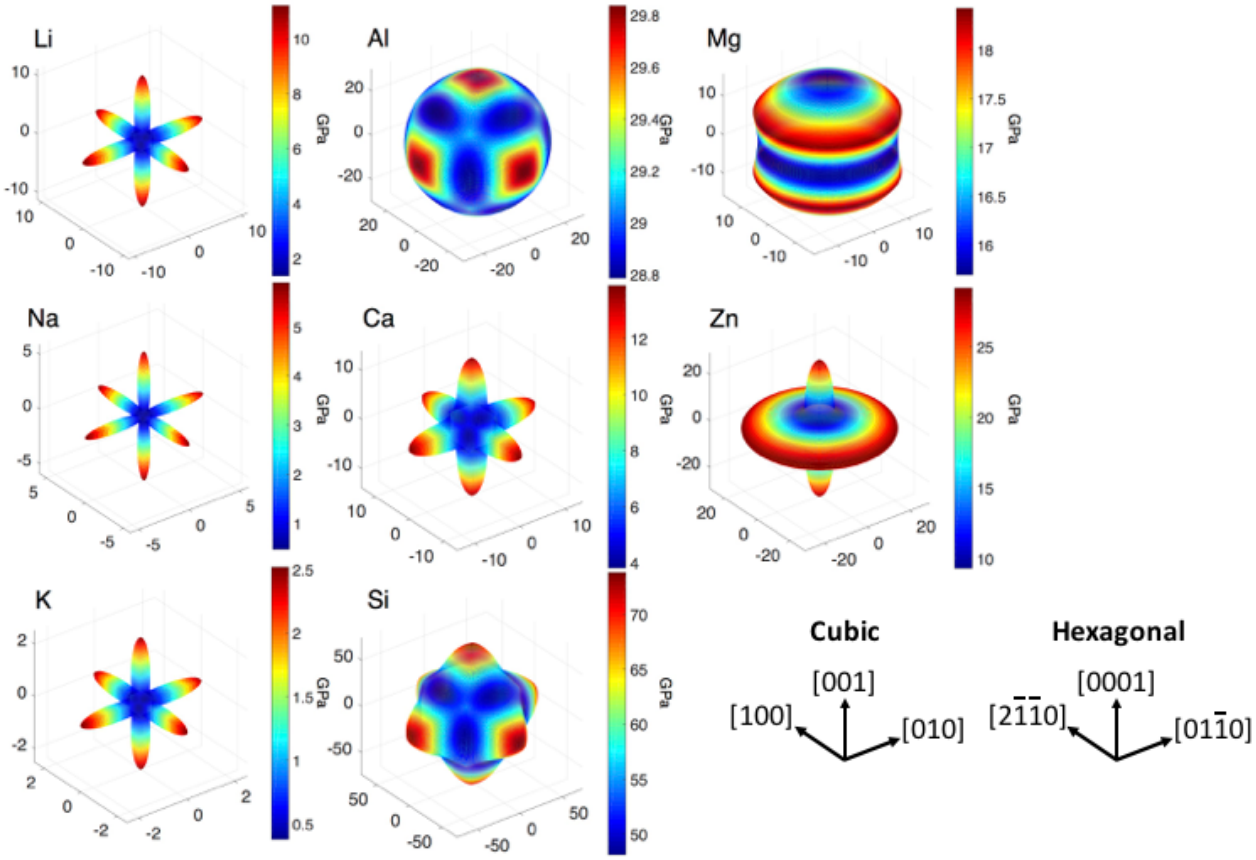


**Figure B.22** Calculated minimum shear modulus, $G^{Min}$, as a function of crystallographic direction for Li, Na, K, Al, Ca, Si, Mg, and Zn at 150 K. $G^{Min}$ represents the smallest G for all directions $\vec{b}$ perpendicular to $\vec{a}$. The coordinate system for $\vec{a}$ is shown for cubic and hexagonal crystal structures; the relationship between $\vec{b}$ and $\vec{a}$ is shown in Fig. 4.1. The modulus value is specified (redundantly) using the magnitude of the protrusion from the origin and with color coding. Note that the range of the modulus scale varies from element-to-element.

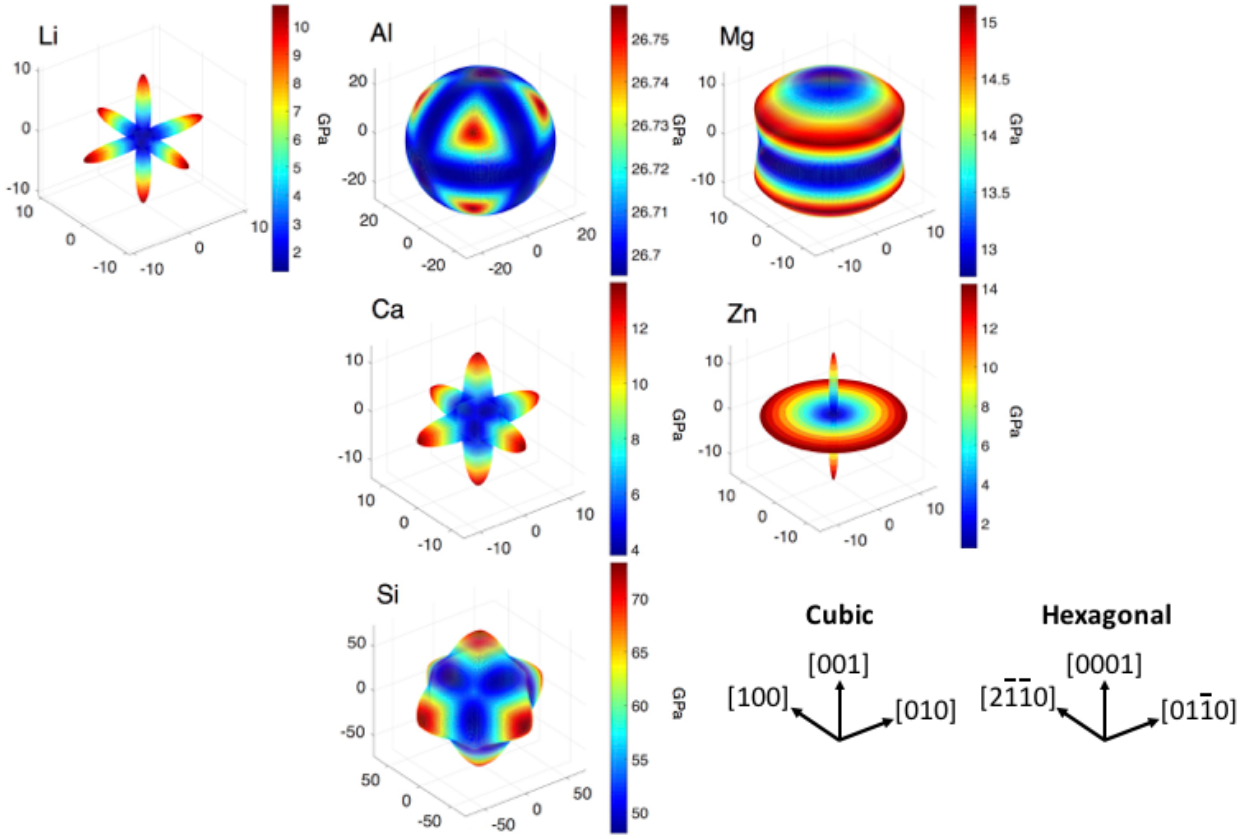


**Figure B.23** Calculated minimum shear modulus, $G^{Min}$, as a function of crystallographic direction for Li, Na, K, Al, Ca, Si, Mg, and Zn at 450 K. $G^{Min}$ represents the smallest G for all directions $\vec{b}$ perpendicular to $\vec{a}$. The coordinate system for $\vec{a}$ is shown for cubic and hexagonal crystal structures; the relationship between $\vec{b}$ and $\vec{a}$ is shown in Fig. 4.1. The modulus value is specified (redundantly) using the magnitude of the protrusion from the origin and with color coding. Note that the range of the modulus scale varies from element-to-element. Data for Na and K are not included because 450 K exceeds their melting points.

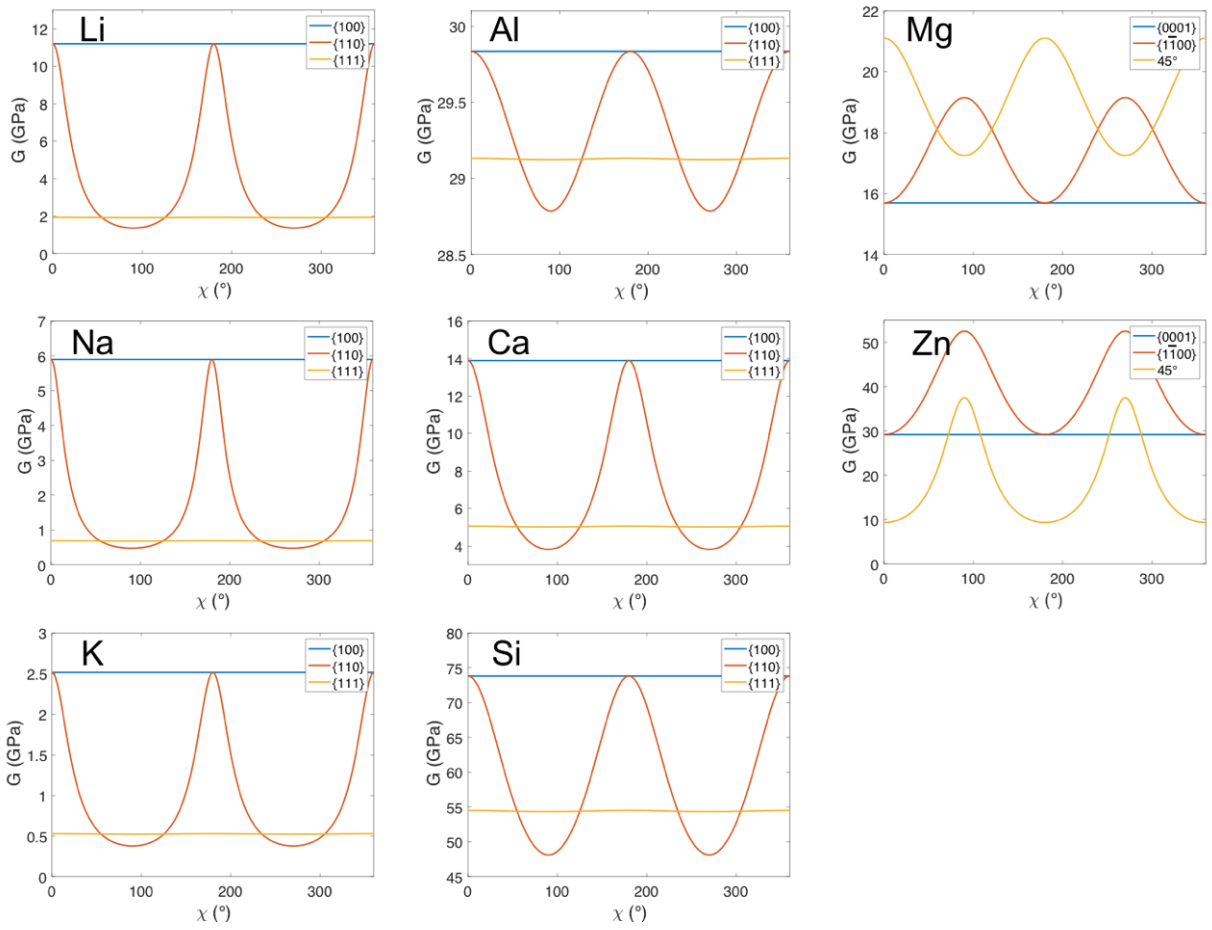


**Figure B.24** Variation in the shear modulus for Li, Na, K, Al, Ca, Si, Mg, and Zn at 150 K within several low-index crystallographic planes. Low-index planes for the cubic system include {100}, {110}, and {111}. $\chi$ identifies the angle of the shear direction $\vec{b}$ within each {hkl} plane perpendicular to $\vec{a}$ = <hkl>. See Fig. 3.1 for a description of the relationship between $\vec{a}$, $\vec{b}$, and $\chi$.

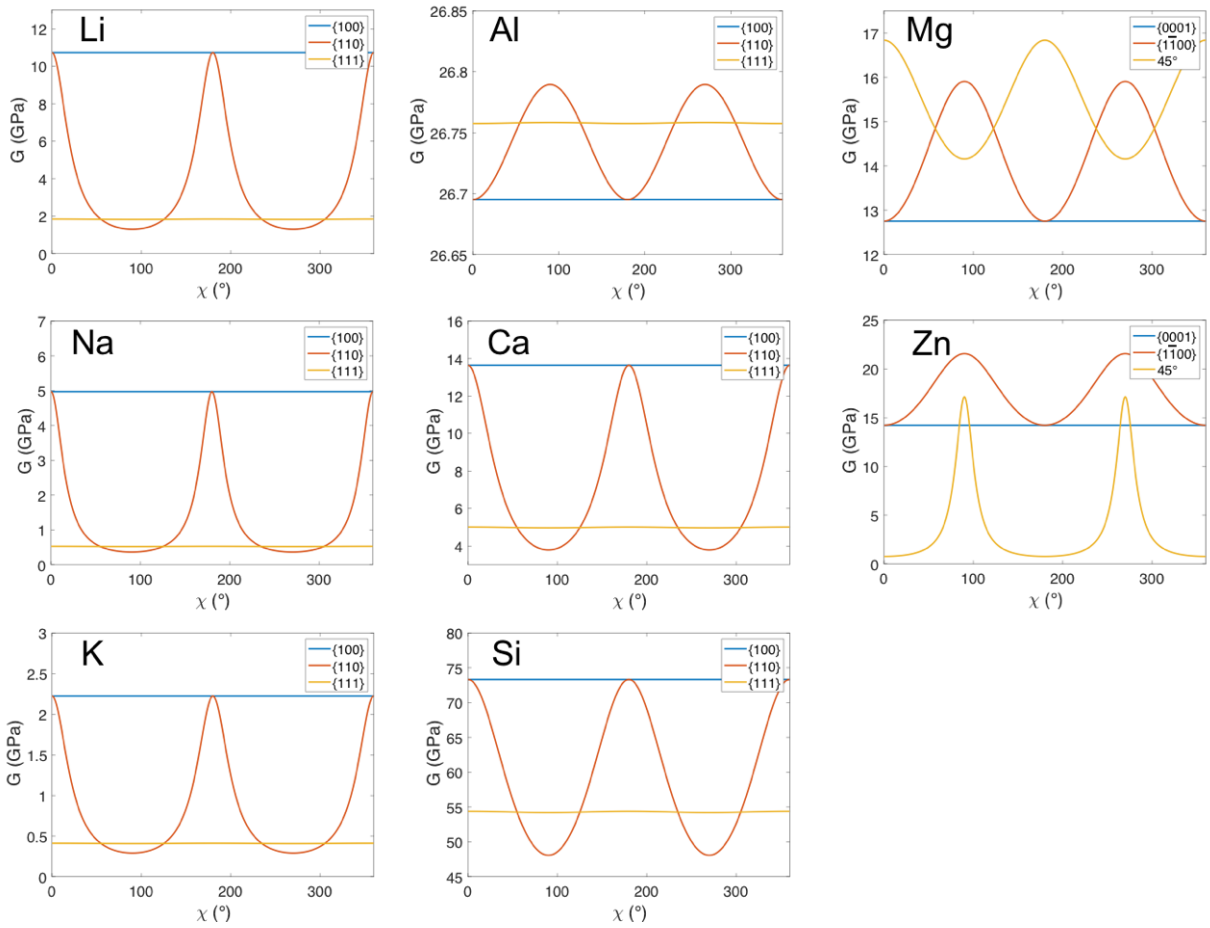


**Figure B.25** Variation in the shear modulus for Li, Na, K, Al, Ca, Si, Mg, and Zn at 450 K within several low-index crystallographic planes. Low-index planes for the cubic system include {100}, {110}, and {111}. $\chi$ identifies the angle of the shear direction $\vec{b}$ within each {hkl} plane perpendicular to $\vec{a}$ = <hkl>. See Fig. 3.1 for a description of the relationship between $\vec{a}$, $\vec{b}$, and $\chi$.

**Table B.7** Calculated Young's and shear moduli (in GPa) as a function of crystallographic direction at 300 K. In the case of shear moduli, maximum ($G_{max}$) and minimum ($G_{min}$) values are given for all possible directions within a plane perpendicular to the specified direction: <hkl> for cubic systems, <hkil> for hexagonal. In hexagonal crystals '45º' indicates a continuum of directions having $\phi=\pm45°$. A description of the coordinate system is provided in Fig. 4.1.

| | <100>/<0001> | | | <110>/<1100> | | | <111>/45° | | |
|---|---|---|---|---|---|---|---|---|---|
| | E | $G_{max}$ | $G_{min}$ | E | $G_{max}$ | $G_{min}$ | E | $G_{max}$ | $G_{min}$ |
| Al | 74.14 | 28.40 | 28.40 | 74.96 | 28.40 | 27.93 | 75.24 | 28.09 | 28.08 |
| Ca | 10.60 | 13.79 | 13.79 | 21.41 | 13.79 | 3.80 | 32.45 | 5.03 | 4.99 |
| Si | 121.47 | 73.65 | 73.65 | 155.54 | 73.65 | 48.10 | 171.58 | 54.48 | 54.30 |
| Li | 3.88 | 10.99 | 10.99 | 10.65 | 10.99 | 1.34 | 25.50 | 1.90 | 1.88 |
| Na | 1.25 | 5.50 | 5.50 | 3.88 | 5.50 | 0.43 | 12.90 | 0.62 | 0.61 |
| K | 0.93 | 2.35 | 2.35 | 2.49 | 2.35 | 0.32 | 5.58 | 0.46 | 0.45 |
| Mg | 47.06 | 14.37 | 14.37 | 46.17 | 17.69 | 14.37 | 38.76 | 19.15 | 15.86 |
| Zn | 10.60 | 24.30 | 24.30 | 58.93 | 41.74 | 24.30 | 40.33 | 30.72 | 6.08 |

**Table B.8** Calculated Resolved Elastic Properties at 150 K, 300 K, and 450 K.[a] In order, these are the maximum Young's modulus, minimum Young's modulus, global maximum shear modulus, and global minimum shear modulus. The reported values are extrema over all crystallographic directions.

| | Temperature (K) | $E_{max}$ | $E_{min}$ | $G_{max}$ | $G_{min}$ |
|---|---|---|---|---|---|
| Al | 150 | 78.92 | 76.46 | 29.84 | 28.79 |
| | 300 | 75.24 | 74.14 | 28.40 | 27.93 |
| | 450 | 71.11 | 70.89 | 26.79 | 26.70 |
| Ca | 150 | 32.81 | 10.66 | 13.89 | 3.82 |
| | 300 | 32.45 | 10.60 | 13.79 | 3.80 |
| | 450 | 31.97 | 10.54 | 13.64 | 3.79 |
| Li | 150 | 26.12 | 3.96 | 11.20 | 1.37 |
| | 300 | 25.50 | 3.88 | 10.99 | 1.34 |
| | 450 | 24.75 | 3.76 | 10.73 | 1.30 |
| Na | 150 | 13.91 | 1.39 | 5.90 | 0.48 |
| | 300 | 12.90 | 1.25 | 5.50 | 0.43 |
| K | 150 | 6.01 | 1.09 | 2.52 | 0.38 |
| | 300 | 5.58 | 0.93 | 2.35 | 0.32 |
| Mg | 150 | 52.04 | 42.26 | 21.11 | 15.70 |
| | 300 | 47.06 | 38.76 | 19.15 | 14.37 |
| | 450 | 41.33 | 34.51 | 16.84 | 12.76 |
| Zn | 150 | 98.10 | 15.99 | 52.52 | 29.16 |
| | 300 | 78.94 | 10.60 | 41.74 | 6.08 |
| | 450 | 44.90 | 1.37 | 21.57 | 0.76 |
| Si | 150 | 172.18 | 121.66 | 73.83 | 48.12 |
| | 300 | 171.58 | 121.47 | 73.65 | 48.10 |
| | 450 | 170.55 | 121.15 | 73.35 | 48.06 |

[a]: Stiffness constants and elastic properties reported in units of GPa.

## Appendix C

Supporting Tables and Figures for Chapter 5

**Table C.1** Rotation axis, grain boundary name, misorientation angle, number of formula units, and dimensions of optimized grain boundary structures. Ionic transport calculations were performed on cells in bold type, with the indicated expansion of GB unit cells.

| Rotation Axis | Grain Boundary | Misorientation Angle (°) | Formula Units | GB Unit Cell Dimensions (Å) $L_x$ | $L_y$ | $L_z$ | # GB Unit Cell Replicas |
|---|---|---|---|---|---|---|---|
| $[0\bar{1}0]$ | **Σ25(107)** | 16.26 | 272 | 90.70 | 12.85 | 62.74 | 1 x 4 x 1 |
| | Σ13(105) | 22.62 | 192 | 65.60 | 12.81 | 61.38 | - |
| | **Σ17(104)** | 28.07 | 160 | 53.04 | 12.83 | 63.01 | 1 x 4 x 1 |
| | Σ5(103) | 36.87 | 128 | 40.78 | 12.84 | 65.83 | - |
| | Σ29(205) | 43.60 | 192 | 69.22 | 12.83 | 58.20 | - |
| | **Σ29(307)** | 46.40 | 272 | 98.46 | 12.85 | 57.73 | 1 x 4 x 1 |
| | **Σ5(102)** | 53.13 | 80 | 28.99 | 12.86 | 57.07 | 2 x 4 x 1 |
| | Σ17(305) | 61.93 | 224 | 75.23 | 12.85 | 62.26 | - |
| | Σ13(203) | 67.38 | 144 | 46.45 | 12.89 | 64.69 | - |
| | Σ25(304) | 73.74 | 192 | 64.65 | 12.81 | 62.62 | - |
| $[1\bar{1}0]$ | Σ33(118) | 20.05 | 304 | 18.17 | 74.05 | 60.74 | - |
| | **Σ19(116)** | 26.53 | 240 | 18.18 | 56.18 | 63.26 | 3 x 1 x 1 |
| | Σ27(115) | 31.59 | 384 | 94.71 | 18.16 | 60.17 | - |
| | **Σ9(114)** | 38.94 | 160 | 18.20 | 38.72 | 60.67 | 2 x 1 x 1 |
| | **Σ11(113)** | 50.48 | 256 | 60.48 | 18.22 | 62.59 | 1 x 3 x 1 |
| | Σ33(225) | 58.99 | 448 | 104.94 | 18.22 | 62.98 | - |
| | **Σ3(112)** | 70.53 | 96 | 18.27 | 22.34 | 62.58 | 2 x 2 x 1 |
| | **Σ17(223)** | 86.63 | 320 | 75.26 | 18.22 | 62.80 | 1 x 4 x 1 |

| | | | | | | | |
|---|---|---|---|---|---|---|---|
| | Σ17(334) | 93.37 | 224 | 18.22 | 53.23 | 62.22 | - |
| | Σ3(111) | 109.47 | 256 | 31.53 | 18.21 | 60.21 | - |
| | Σ33(554) | 121.01 | 304 | 18.26 | 74.02 | 60.40 | - |
| | **Σ11(332)** | 129.52 | 176 | 18.21 | 42.82 | 60.11 | 2 x 1 x 1 |
| | **Σ9(221)** | 141.06 | 224 | 54.69 | 18.24 | 60.47 | 1 x 3 x 1 |
| | Σ27(552) | 148.41 | 272 | 18.25 | 67.07 | 59.81 | - |
| | Σ19(331) | 153.47 | 320 | 79.37 | 18.33 | 59.19 | - |
| | Σ33(441) | 159.95 | 448 | 104.51 | 18.30 | 63.05 | - |
| $[1\bar{1}1]$ | Σ31(165) | 17.90 | 864 | 175.52 | 22.39 | 59.14 | - |
| | **Σ21(154)** | 21.79 | 240 | 22.37 | 48.19 | 59.86 | 2 x 1 x 1 |
| | Σ13(143) | 27.80 | 576 | 113.70 | 22.36 | 61.10 | - |
| | **Σ7(132)** | 38.21 | 432 | 83.56 | 22.33 | 62.36 | 1 x 4 x 1 |
| | Σ19(253) | 46.83 | 672 | 137.35 | 22.38 | 58.84 | - |
| [100] | Σ25(100) | 16.26 | 800 | 64.45 | 64.50 | 51.67 | - |
| | **Σ13(100)** | 22.62 | 416 | 46.49 | 46.31 | 51.64 | 1 x 1 x 1 |
| | Σ17(100) | 28.07 | 1088 | 75.16 | 75.22 | 51.67 | - |
| | **Σ5(100)** | 36.87 | 160 | 28.81 | 28.91 | 51.68 | 2 x 2 x 1 |

**Table C.2** [$0\bar{1}0$] Tilt Grain Boundary Energies

| Misorientation Angle (°) | Coincidence Site Lattice Degree of Fit (Σ) | Zr-terminated Habit Plane | Static Minimum Grain Boundary Energy ($mJ/m^2$) | Optimized Grain Boundary Energy ($mJ/m^2$) |
|---|---|---|---|---|
| 16.26 | 25 | 107A | 934 | 325 |
| | | 107B | 979 | 317 |
| 22.62 | 13 | 105A | 905 | 278 |
| | | 105B | 945 | 346 |
| 28.07 | 17 | 104A | 924 | 274 |
| | | 104B | 817 | 313 |
| | | 104C | 878 | 242 |
| | | 104D | 789 | 173 |
| 36.87 | 5 | 103A | 1007 | 311 |
| | | 103B | 874 | 303 |
| 43.60 | 29 | 205A | 926 | 328 |
| | | 205B | 987 | 306 |
| | | 205C | 980 | 383 |
| | | 205D | 950 | 336 |
| 46.40 | 29 | 307A | 1051 | 382 |
| | | 307B | 1106 | 367 |
| 53.13 | 5 | 102A | 759 | 274 |
| | | 102B | 734 | 279 |
| | | 102C | 683 | 171 |

| | | | | |
|---|---|---|---|---|
| | | 102D | 816 | 222 |
| 61.93 | 17 | 305A | 1044 | 363 |
| | | 305B | 900 | 276 |
| 67.38 | 13 | 203A | 910 | 280 |
| | | 203B | 930 | 302 |
| | | 203C | 994 | 292 |
| | | 203D | 953 | 371 |
| 73.74 | 25 | 304A | 963 | 289 |
| | | 304B | 986 | 261 |
| | | 304C | 1020 | 270 |
| | | 304D | 866 | 264 |

**Table C.3** [$1\bar{1}0$] Tilt Grain Boundary Energies

| Misorientation Angle (°) | Coincidence Site Lattice Degree of Fit (Σ) | Zr-terminated Habit Plane | Static Minimum Grain Boundary Energy ($mJ/m^2$) | Optimized Grain Boundary Energy ($mJ/m^2$) |
|---|---|---|---|---|
| 20.05 | 33 | 118A | 882 | 343 |
| | | 118B | 929 | 326 |
| 26.53 | 19 | 116A | 937 | 265 |
| | | 116B | 797 | 215 |
| 31.59 | 27 | 115A | 1003 | 302 |
| | | 115B | 1051 | 354 |
| | | 115C | 1032 | 312 |
| | | 115D | 1016 | 315 |
| 38.94 | 9 | 114A | 899 | 209 |
| | | 114B | 753 | 141 |
| 50.48 | 11 | 113A | 1010 | 368 |
| | | 113B | 1069 | 342 |
| | | 113C | 1033 | 325 |
| | | 113D | 1051 | 348 |
| 58.99 | 33 | 225A | 1093 | 305 |
| | | 225B | 1052 | 330 |
| | | 225C | 1097 | 328 |
| | | 225D | 1093 | 259 |
| 70.53 | 3 | 112A | 653 | 58 |

| | | | | |
|---|---|---|---|---|
| | | 112B | 927 | 264 |
| 86.63 | 17 | 223A | 1100 | 389 |
| | | 223B | 1042 | 365 |
| | | 223C | 1073 | 399 |
| | | 223D | 1023 | 278 |
| 93.37 | 17 | 334A | 950 | 282 |
| | | 334B | 924 | 269 |
| 109.47 | 3 | 111A | 1035 | 340 |
| | | 111B | 1013 | 410 |
| | | 111C | 922 | 327 |
| | | 111D | 950 | 288 |
| 121.01 | 33 | 554A | 1080 | 277 |
| | | 554B | 993 | 279 |
| 129.52 | 11 | 332A | 592 | 141 |
| | | 332B | 710 | 165 |
| 141.06 | 9 | 221A | 1009 | 352 |
| | | 221B | 1007 | 336 |
| | | 221C | 1007 | 324 |
| | | 221D | 1078 | 349 |
| 148.41 | 27 | 552A | 783 | 260 |
| | | 552B | 920 | 309 |
| 153.47 | 19 | 331A | 1102 | 327 |
| | | 331B | 1131 | 348 |
| | | 331C | 1117 | 369 |

| | | | | |
|---|---|---|---|---|
| | | 331D | 1111 | 392 |
| 159.95 | 33 | 441A | 1109 | 375 |
| | | 441B | 1086 | 287 |
| | | 441C | 1142 | 378 |
| | | 441D | 1088 | 283 |

**Table C.4** [$1\bar{1}1$] Tilt Grain Boundary Energies

| Misorientation Angle (°) | Coincidence Site Lattice Degree of Fit (Σ) | Zr-terminated Habit Plane | Static Minimum Grain Boundary Energy ($mJ/m^2$) | Optimized Grain Boundary Energy ($mJ/m^2$) |
|---|---|---|---|---|
| 17.90 | 31 | 165A | 1150 | 476 |
| | | 165B | 1177 | 326 |
| 21.79 | 21 | 154A | 867 | 324 |
| | | 154B | 1031 | 239 |
| 27.80 | 13 | 143A | 1103 | 312 |
| | | 143B | 948 | 229 |
| 38.21 | 7 | 132A | 1136 | 311 |
| | | 132B | 1126 | 395 |
| 46.83 | 19 | 253A | 1228 | 452 |
| | | 253B | 1126 | 339 |

**Table C.5** [100] Twist Grain Boundary Energies

| Misorientation Angle (°) | Coincidence Site Lattice Degree of Fit (Σ) | Zr-terminated Habit Plane | Static Minimum Grain Boundary Energy ($mJ/m^2$) | Optimized Grain Boundary Energy ($mJ/m^2$) |
|---|---|---|---|---|
| 16.26 | 25 | 100 | 1001 | 334 |
| 22.62 | 13 | 100 | 978 | 425 |
| 28.07 | 17 | 100 | 971 | 333 |
| 36.87 | 5 | 100A | 955 | 325 |
| | | 100B | 915 | 278 |
| | | 100C | 895 | 314 |
| | | 100D | 890 | 375 |

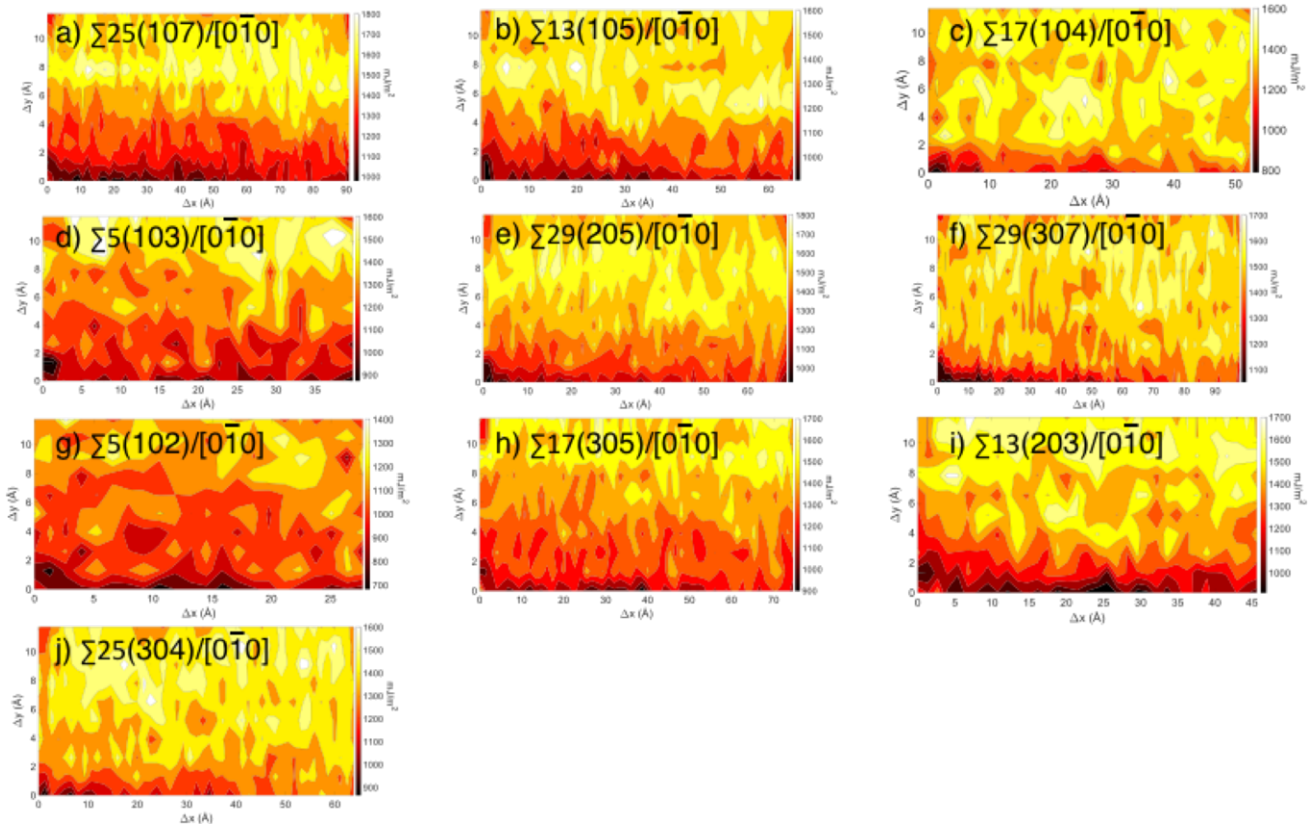


**Figure C.1** $\gamma$-surface plots of grain boundary energies at the a) Σ25(107)/[0$\bar{1}$0], b) Σ13(105)/[0$\bar{1}$0], c) Σ17(104)/[0$\bar{1}$0], d) Σ5(103)/[0$\bar{1}$0], e) Σ29(205)/[0$\bar{1}$0], f) Σ29(307)/[0$\bar{1}$0], g) Σ5(102)/[0$\bar{1}$0], h) Σ17(305)/[0$\bar{1}$0], i) Σ13(203)/[0$\bar{1}$0], and j) Σ25(304)/[0$\bar{1}$0] tilt grain boundaries.

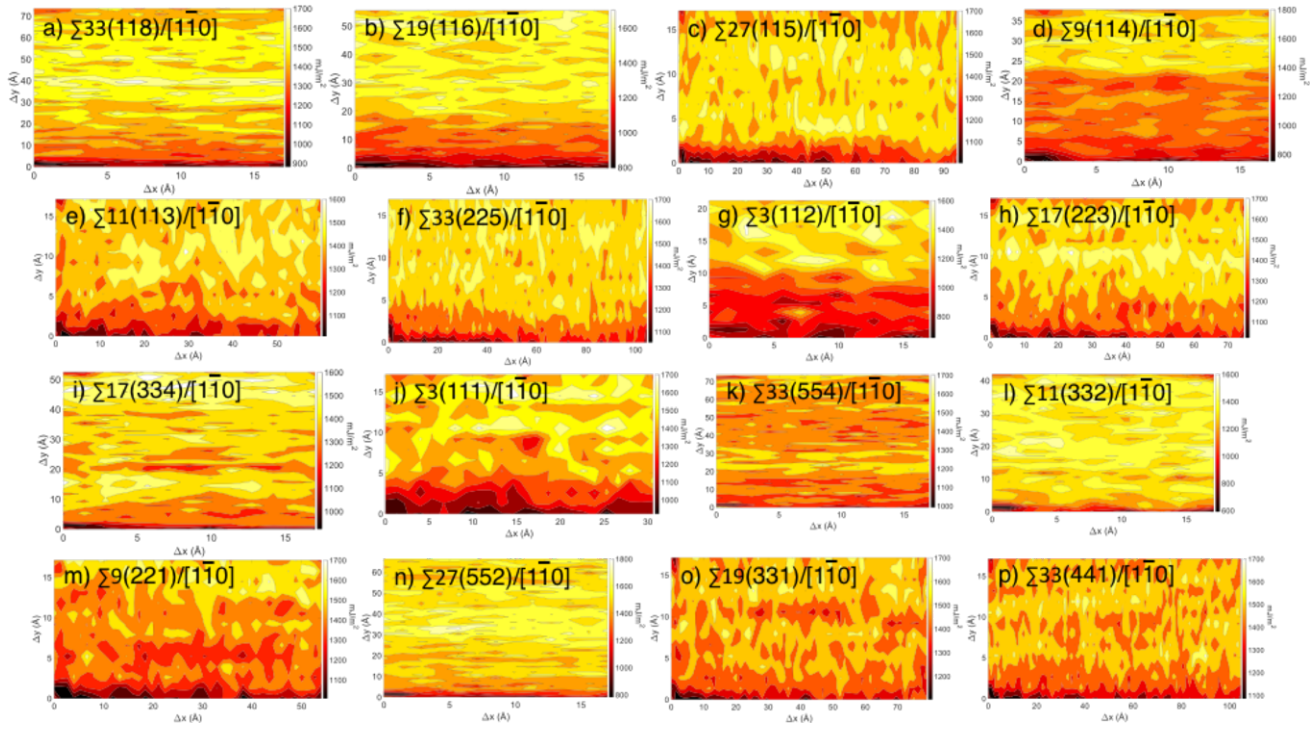


**Figure C.2** $\gamma$-surface plots of grain boundary energies at the a) Σ33(118)/[1$\bar{1}$0], b) Σ19(116)/[1$\bar{1}$0], c) Σ27(115)/[1$\bar{1}$0], d) Σ9(114)/[1$\bar{1}$0], e) Σ11(113)/[1$\bar{1}$0], f) Σ33(225)/[1$\bar{1}$0], g) Σ3(112)/[1$\bar{1}$0], h) Σ17(223)/[1$\bar{1}$0], i) Σ17(334)/[1$\bar{1}$0], j) Σ3(111)/[1$\bar{1}$0], k) Σ33(554)/[1$\bar{1}$0], l) Σ11(332)/[1$\bar{1}$0], m) Σ9(221)/[1$\bar{1}$0], n) Σ27(552)/[1$\bar{1}$0], o) Σ19(331)/[1$\bar{1}$0], and p) Σ33(441)/[1$\bar{1}$0] tilt grain boundaries.

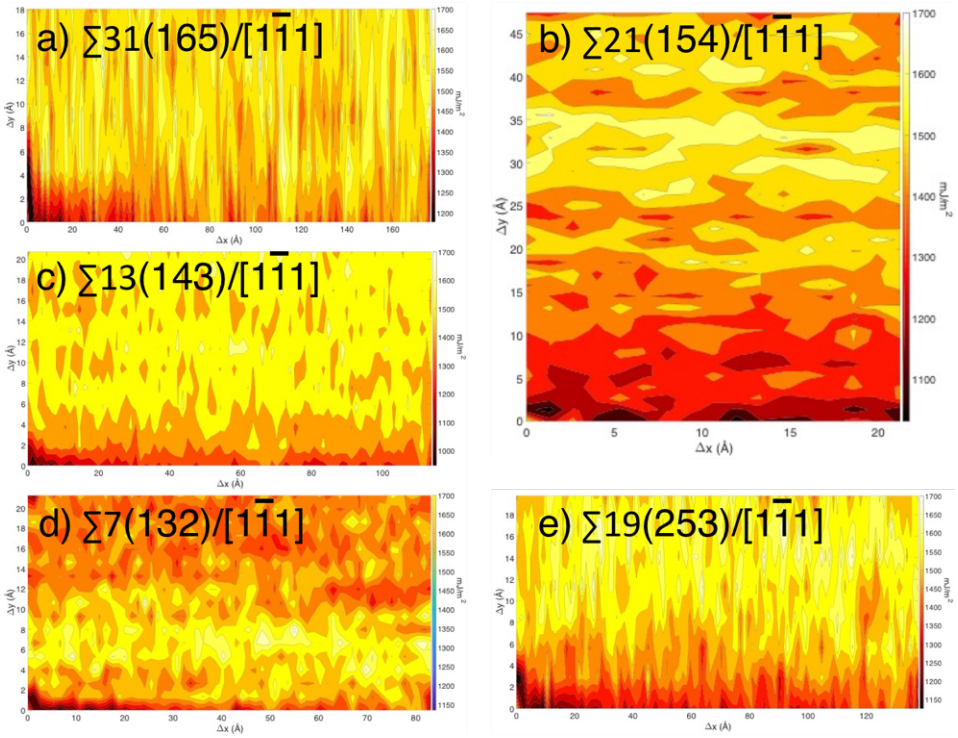


**Figure C.3** $\gamma$-surface plots of grain boundary energies at the a) Σ31(165)/[1$\bar{1}$1], b) Σ21(154)/[1$\bar{1}$1], c) Σ13(143)/[1$\bar{1}$1], d) Σ7(132)/[1$\bar{1}$1], and e) Σ19(253)/[1$\bar{1}$1] tilt grain boundaries.

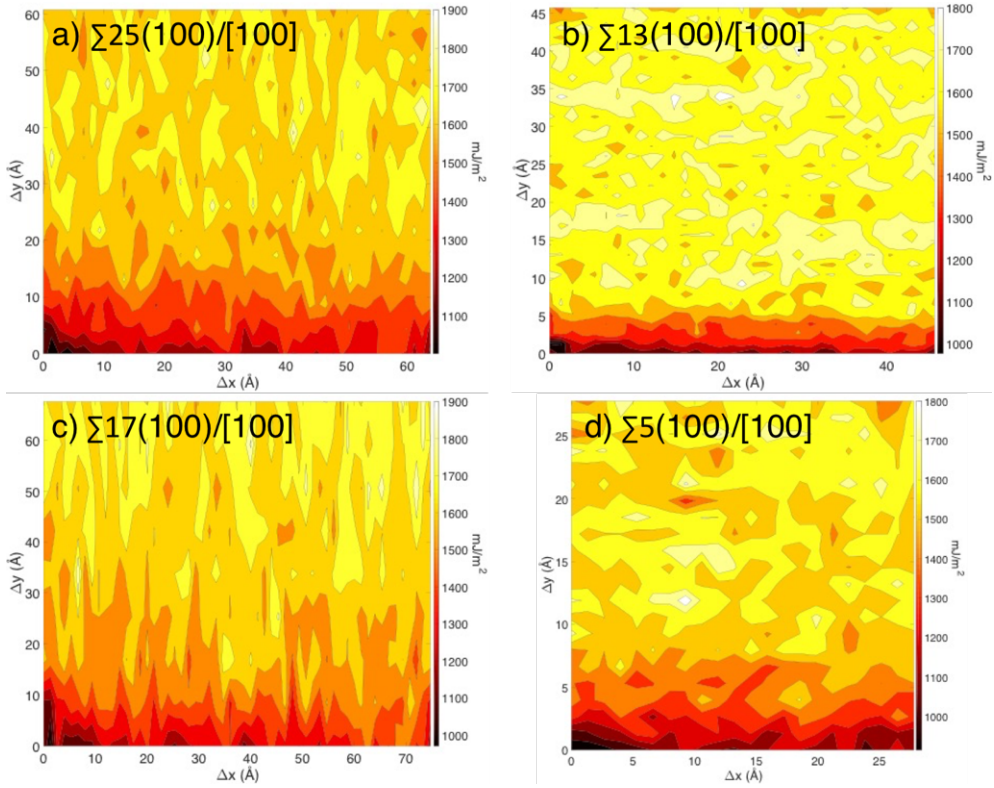


**Figure C.4** $\gamma$-surface plots of grain boundary energies at the a) ∑25(100)/[100], b) ∑13(100)/[100], c) ∑17(100)/[100], and d) ∑5(100)/[100] twist grain boundaries.

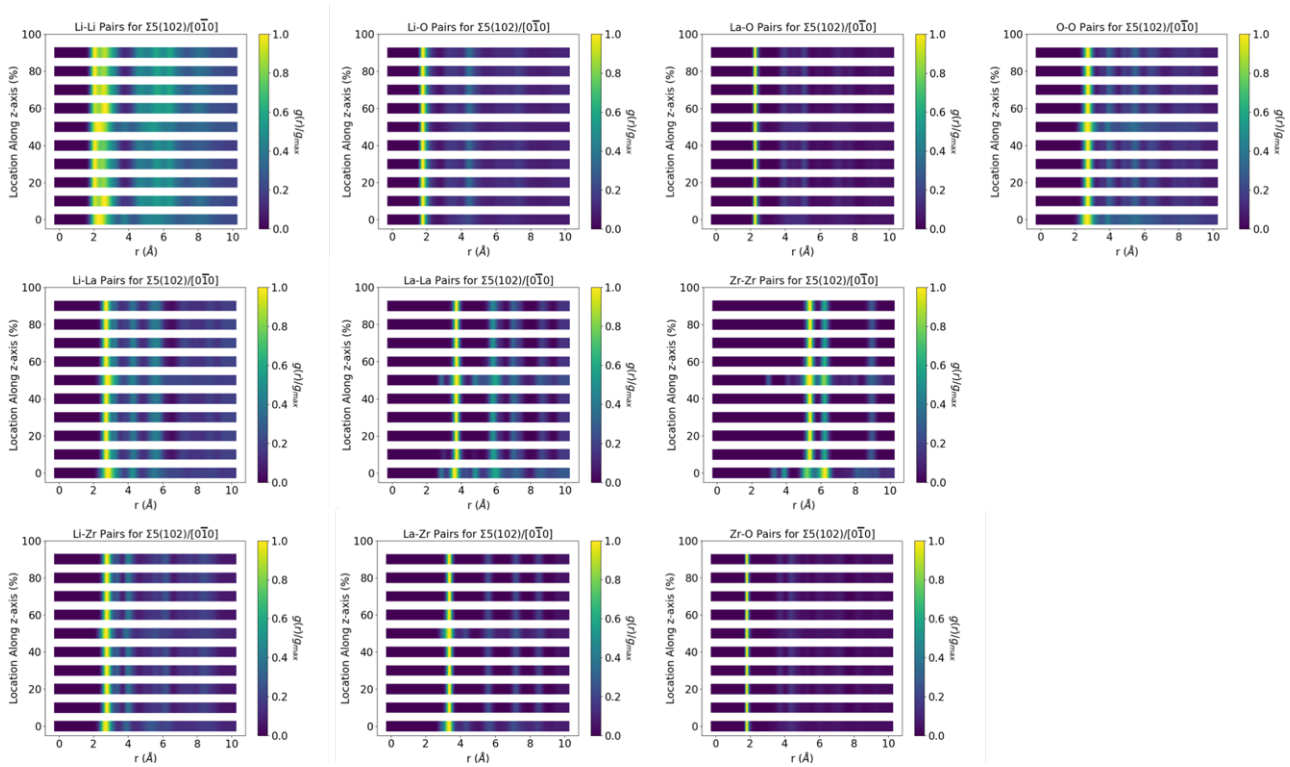


**Figure C.5** RDF plots for indicated atom pairs at various locations along the z-axis at 700K for $\Sigma5(102)/[0\bar{1}0]$ tilt grain boundary. The values of g(r) are divided by the maximum value, $g_{max}$, in order to easily visualize important features, with yellow indicating $g(r)=g_{max}$, and blue indicating g(r)=0. The grain boundaries are located at 0% and 50%.

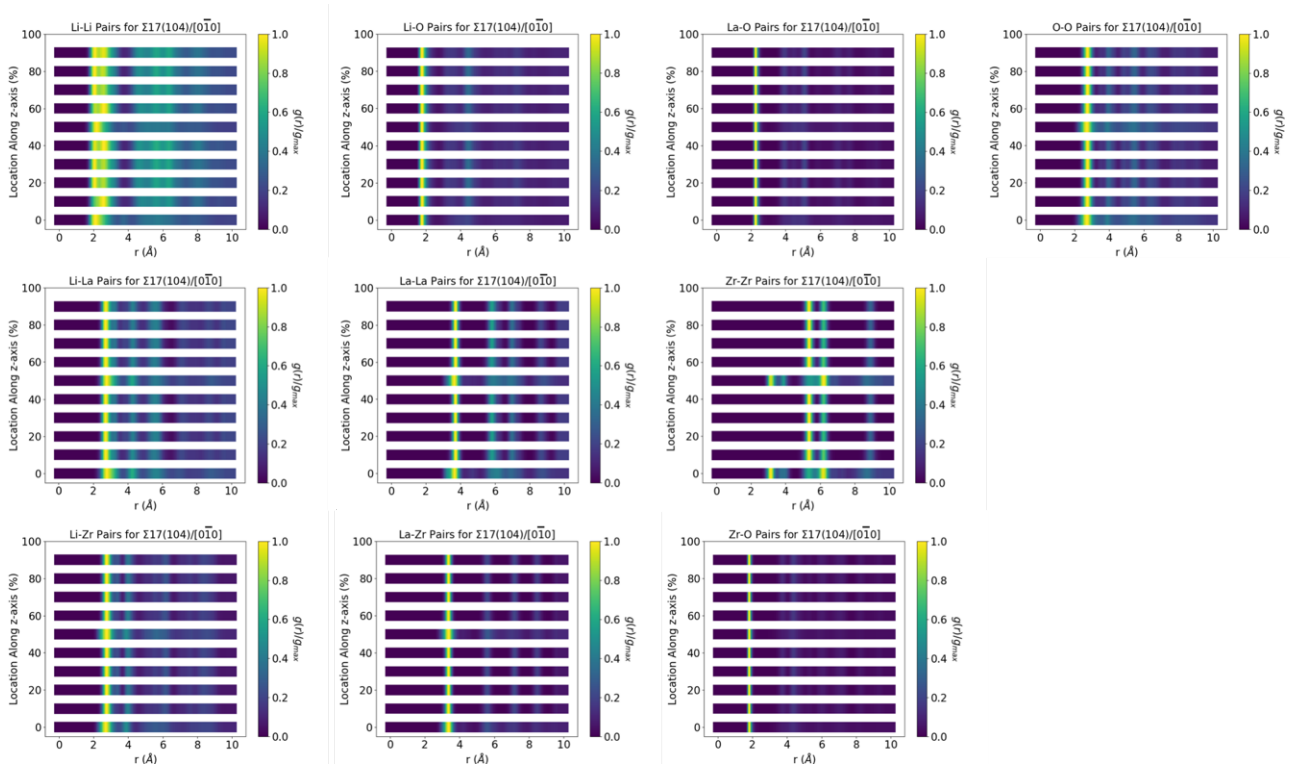


**Figure C.6** RDF plots for indicated atom pairs at various locations along the z-axis at 700K for $\Sigma17(104)/[0\bar{1}0]$ tilt grain boundary. The values of g(r) are divided by the maximum value, $g_{max}$, in order to easily visualize important features, with yellow indicating $g(r)=g_{max}$, and blue indicating g(r)=0. The grain boundaries are located at 0% and 50%.

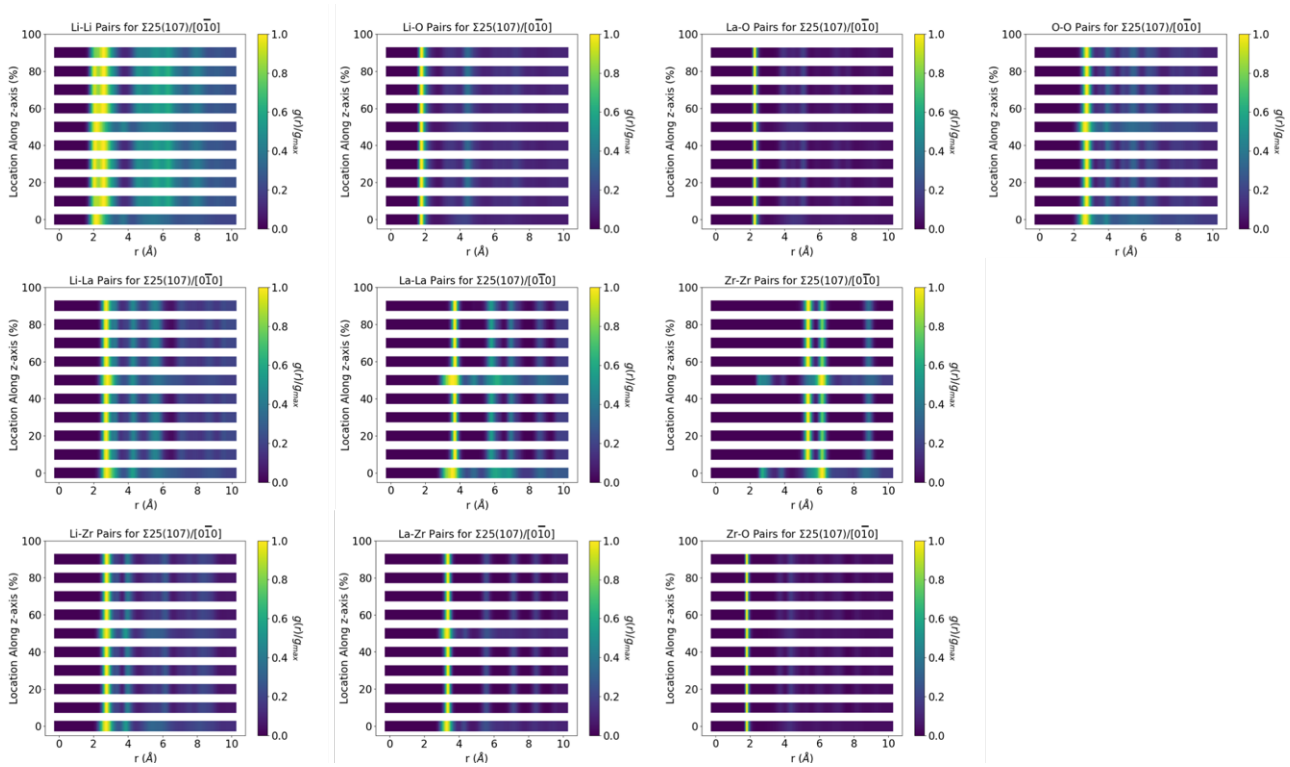


**Figure C.7** RDF plots for indicated atom pairs at various locations along the z-axis at 700K for Σ25(107)/[0$\bar{1}$0] tilt grain boundary. The values of g(r) are divided by the maximum value, $g_{max}$, in order to easily visualize important features, with yellow indicating g(r)=$g_{max}$, and blue indicating g(r)=0. The grain boundaries are located at 0% and 50%.

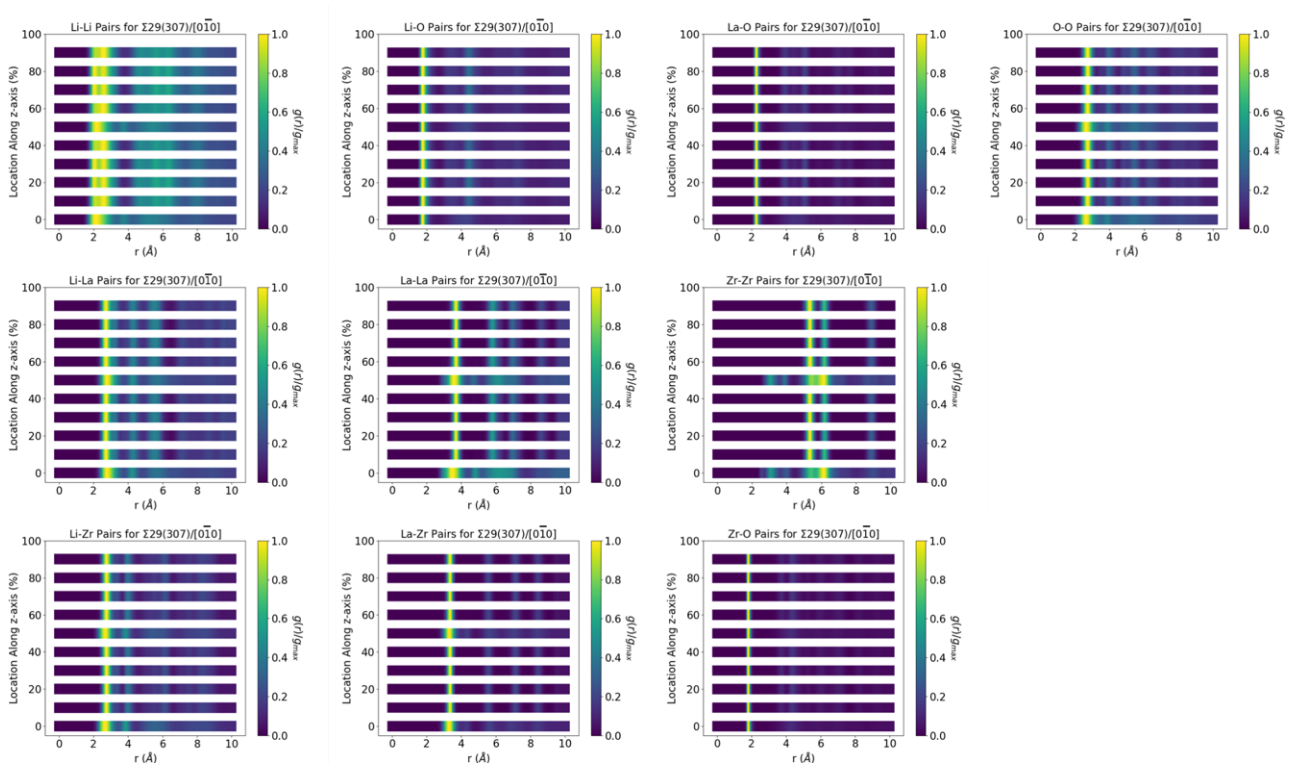


**Figure C.8** RDF plots for indicated atom pairs at various locations along the z-axis at 700K for Σ29(307)/[0$\bar{1}$0] tilt grain boundary. The values of g(r) are divided by the maximum value, $g_{max}$, in order to easily visualize important features, with yellow indicating g(r)=$g_{max}$, and blue indicating g(r)=0. The grain boundaries are located at 0% and 50%.

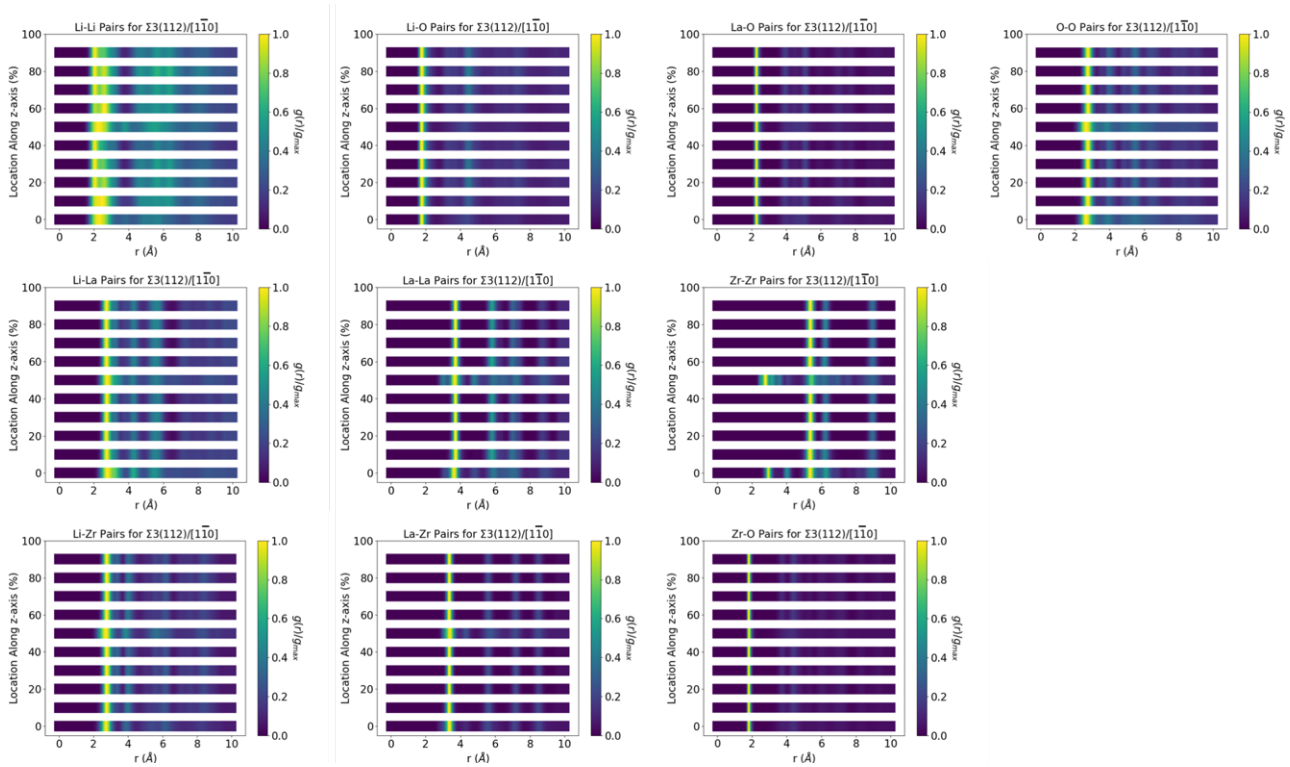


**Figure C.9** RDF plots for indicated atom pairs at various locations along the z-axis at 700K for $\Sigma3(112)/[1\bar{1}0]$ tilt grain boundary. The values of g(r) are divided by the maximum value, $g_{max}$, in order to easily visualize important features, with yellow indicating $g(r)=g_{max}$, and blue indicating g(r)=0. The grain boundaries are located at 0% and 50%.

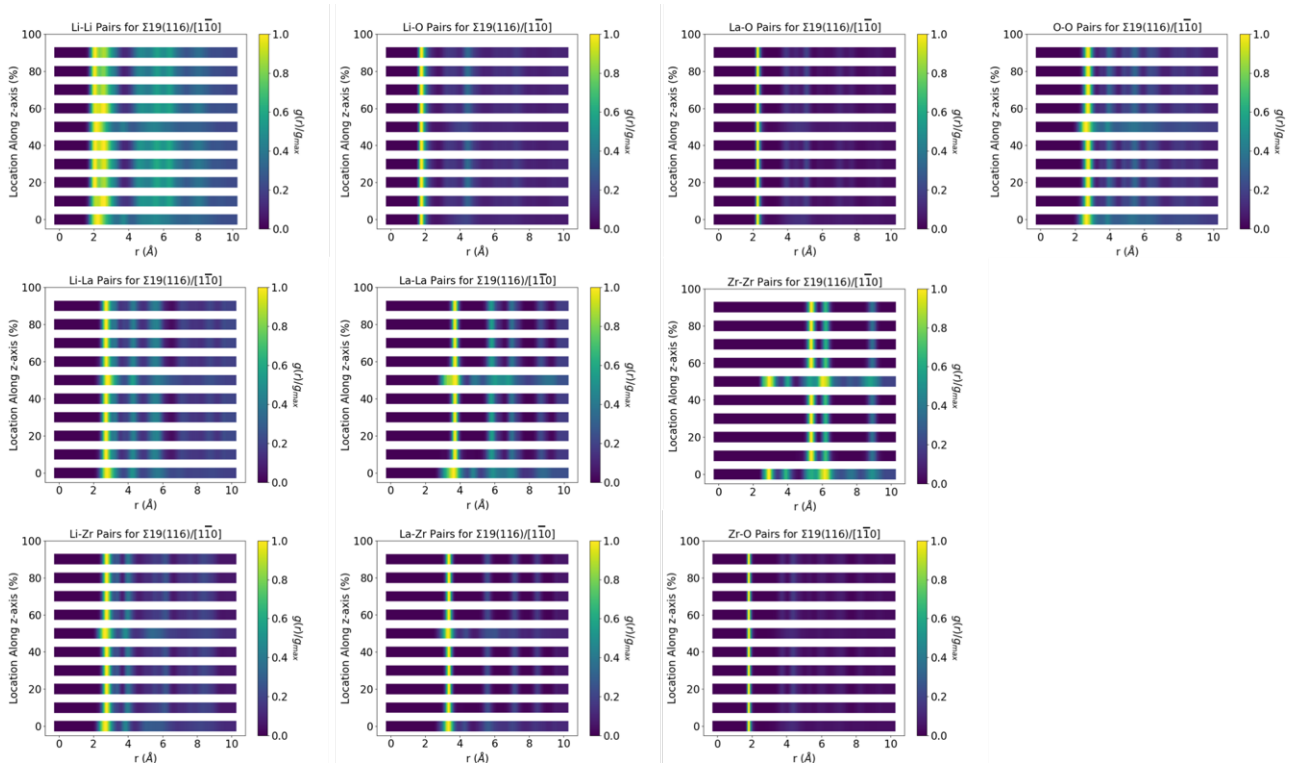


**Figure C.10** RDF plots for indicated atom pairs at various locations along the z-axis at 700K for $\Sigma19(116)/[1\bar{1}0]$ tilt grain boundary. The values of g(r) are divided by the maximum value, $g_{max}$, in order to easily visualize important features, with yellow indicating $g(r)=g_{max}$, and blue indicating $g(r)=0$. The grain boundaries are located at 0% and 50%.

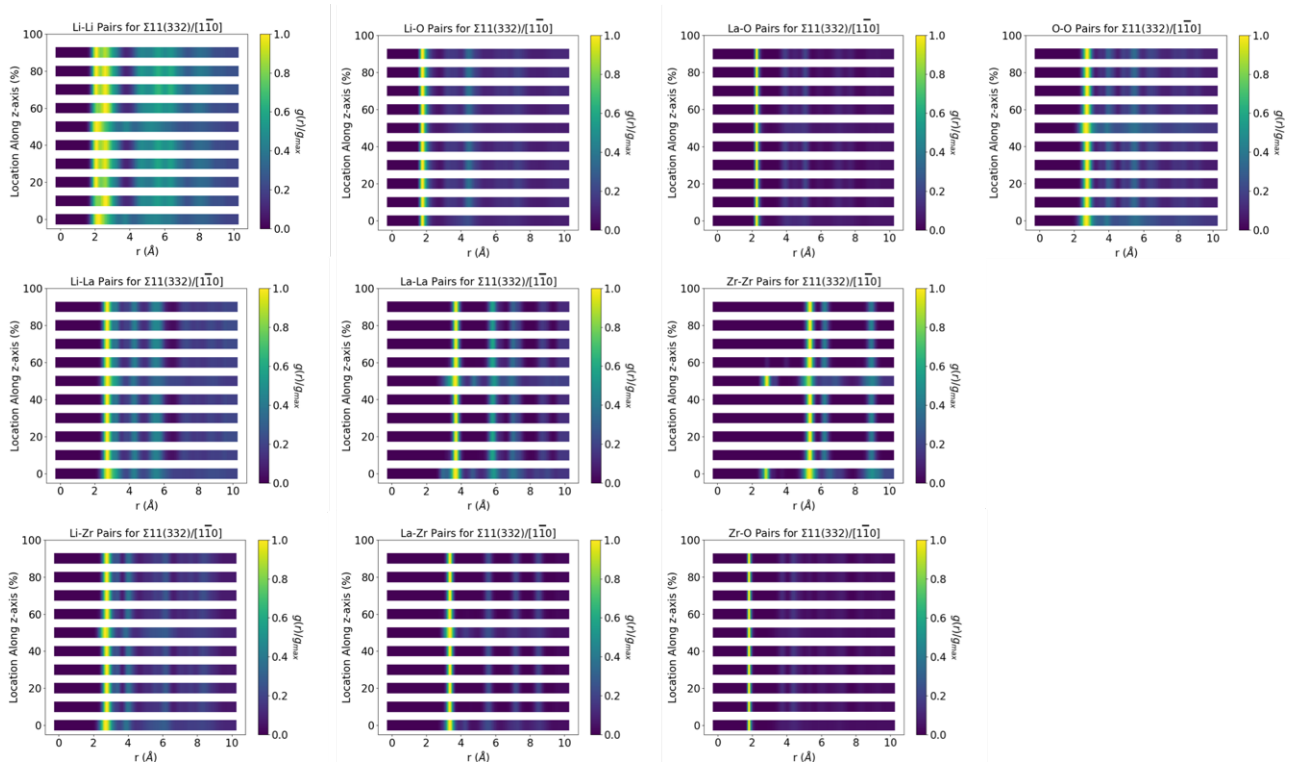


**Figure C.11** RDF plots for indicated atom pairs at various locations along the z-axis at 700K for $\Sigma11(332)/[1\bar{1}0]$ tilt grain boundary. The values of g(r) are divided by the maximum value, $g_{max}$, in order to easily visualize important features, with yellow indicating $g(r)=g_{max}$, and blue indicating $g(r)=0$. The grain boundaries are located at 0% and 50%.

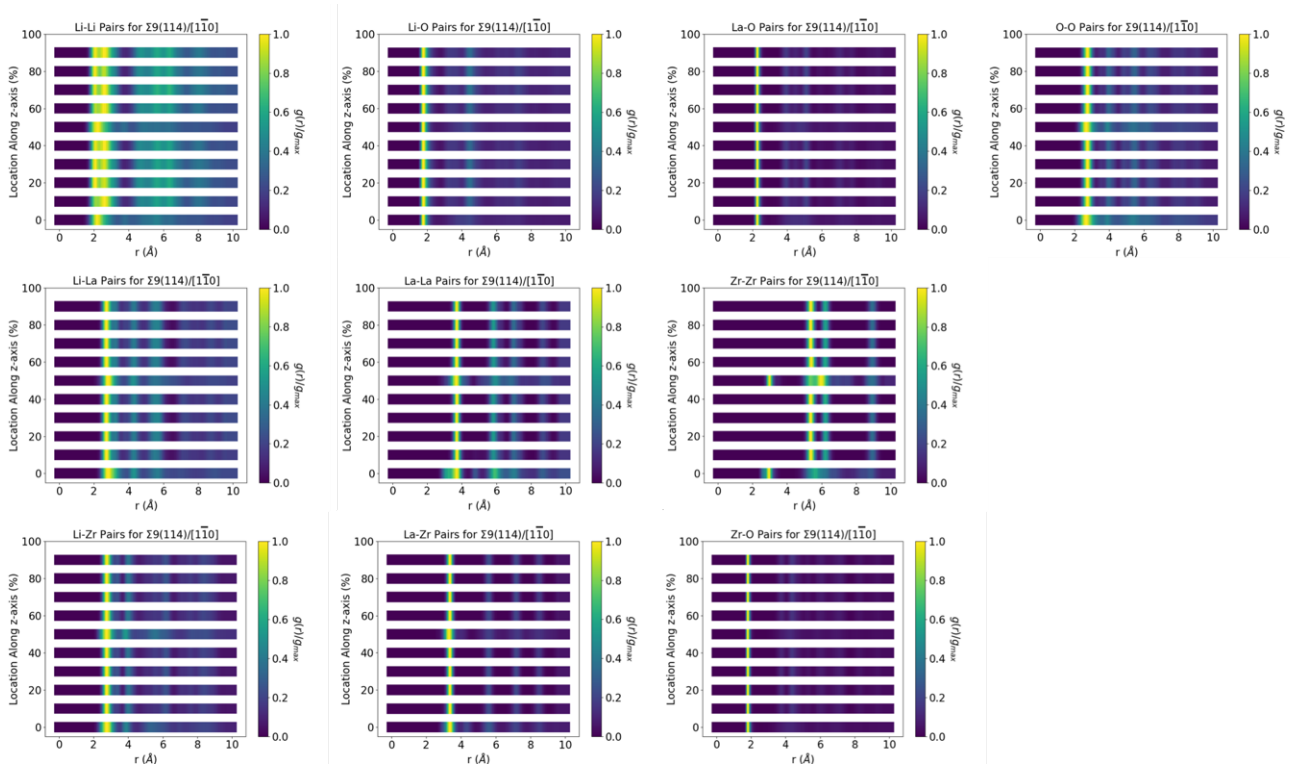


**Figure C.12** RDF plots for indicated atom pairs at various locations along the z-axis at 700K for $\Sigma9(114)/[1\bar{1}0]$ tilt grain boundary. The values of g(r) are divided by the maximum value, $g_{max}$, in order to easily visualize important features, with yellow indicating $g(r)=g_{max}$, and blue indicating g(r)=0. The grain boundaries are located at 0% and 50%.

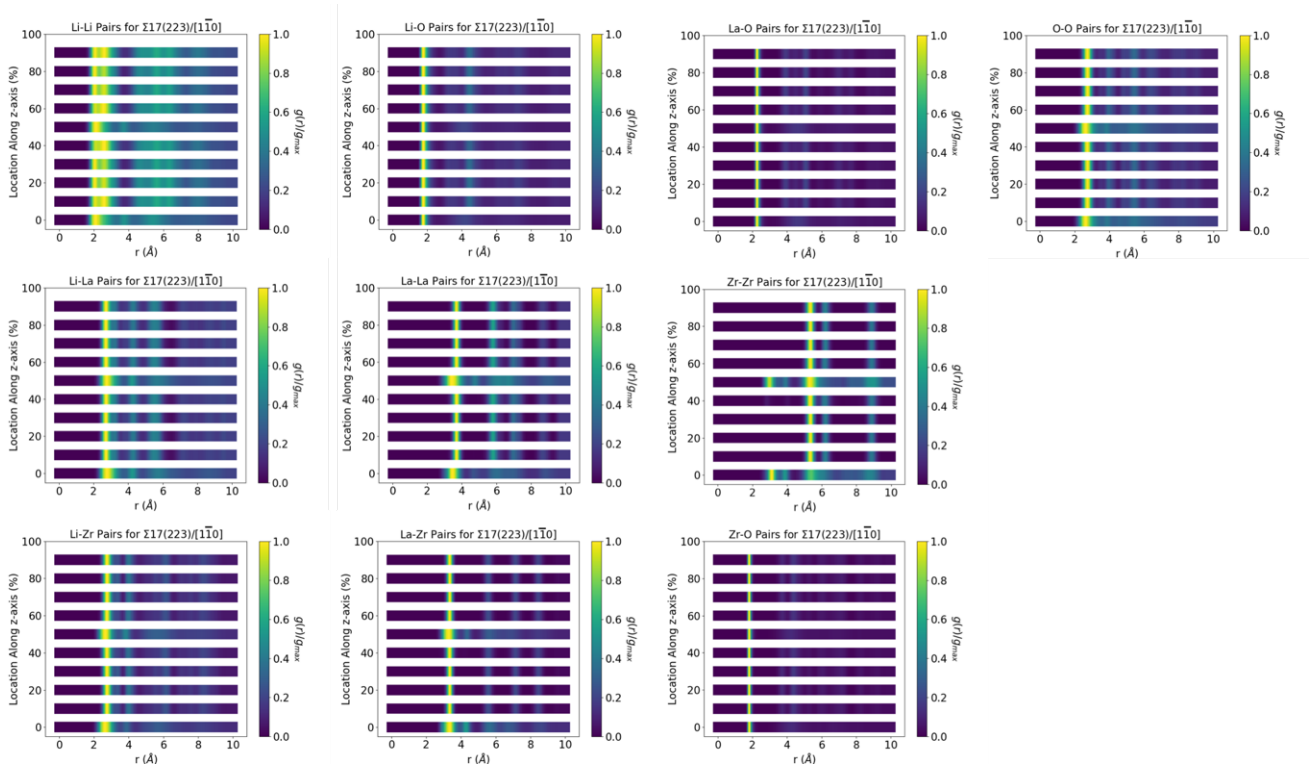


**Figure C.13** RDF plots for indicated atom pairs at various locations along the z-axis at 700K for $\Sigma17(223)/[1\bar{1}0]$ tilt grain boundary. The values of g(r) are divided by the maximum value, $g_{max}$, in order to easily visualize important features, with yellow indicating $g(r)=g_{max}$, and blue indicating $g(r)=0$. The grain boundaries are located at 0% and 50%.

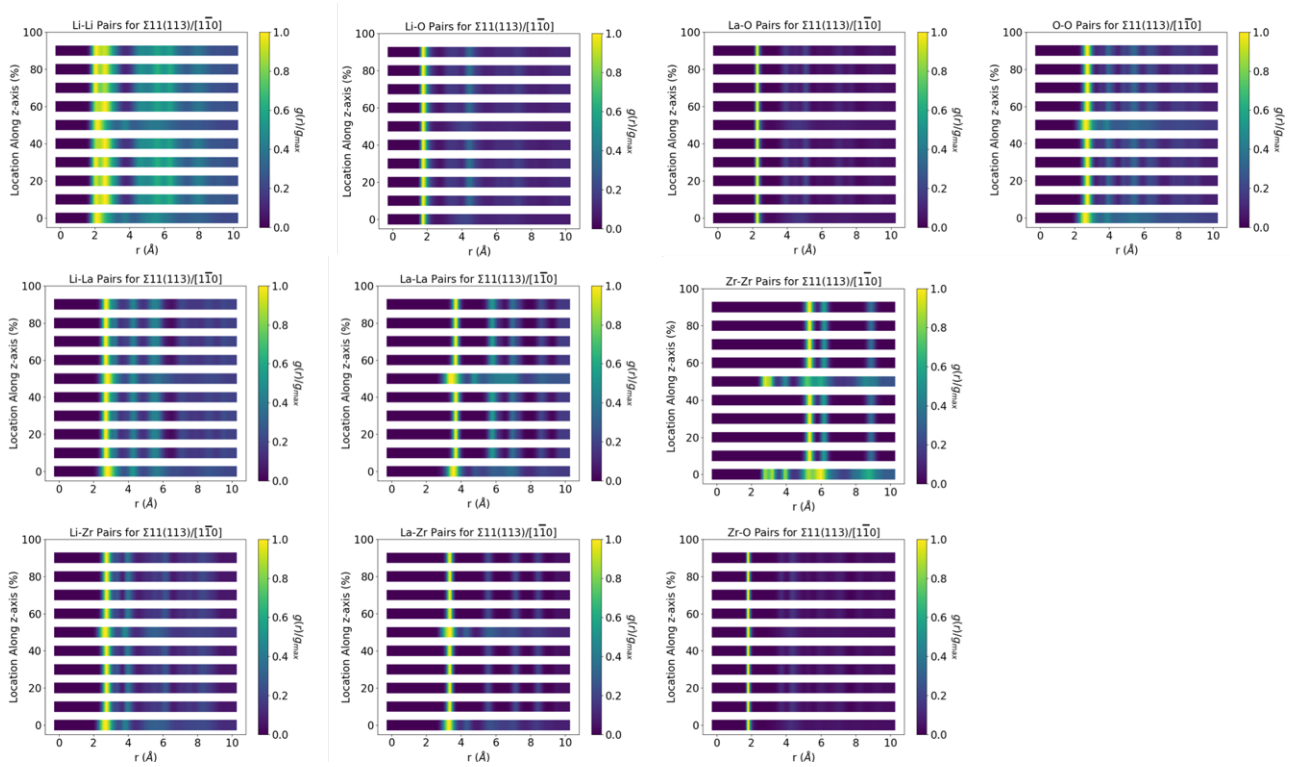


**Figure C.14** RDF plots for indicated atom pairs at various locations along the z-axis at 700K for $\Sigma11(113)/[1\bar{1}0]$ tilt grain boundary. The values of g(r) are divided by the maximum value, $g_{max}$, in order to easily visualize important features, with yellow indicating $g(r)=g_{max}$, and blue indicating $g(r)=0$. The grain boundaries are located at 0% and 50%.

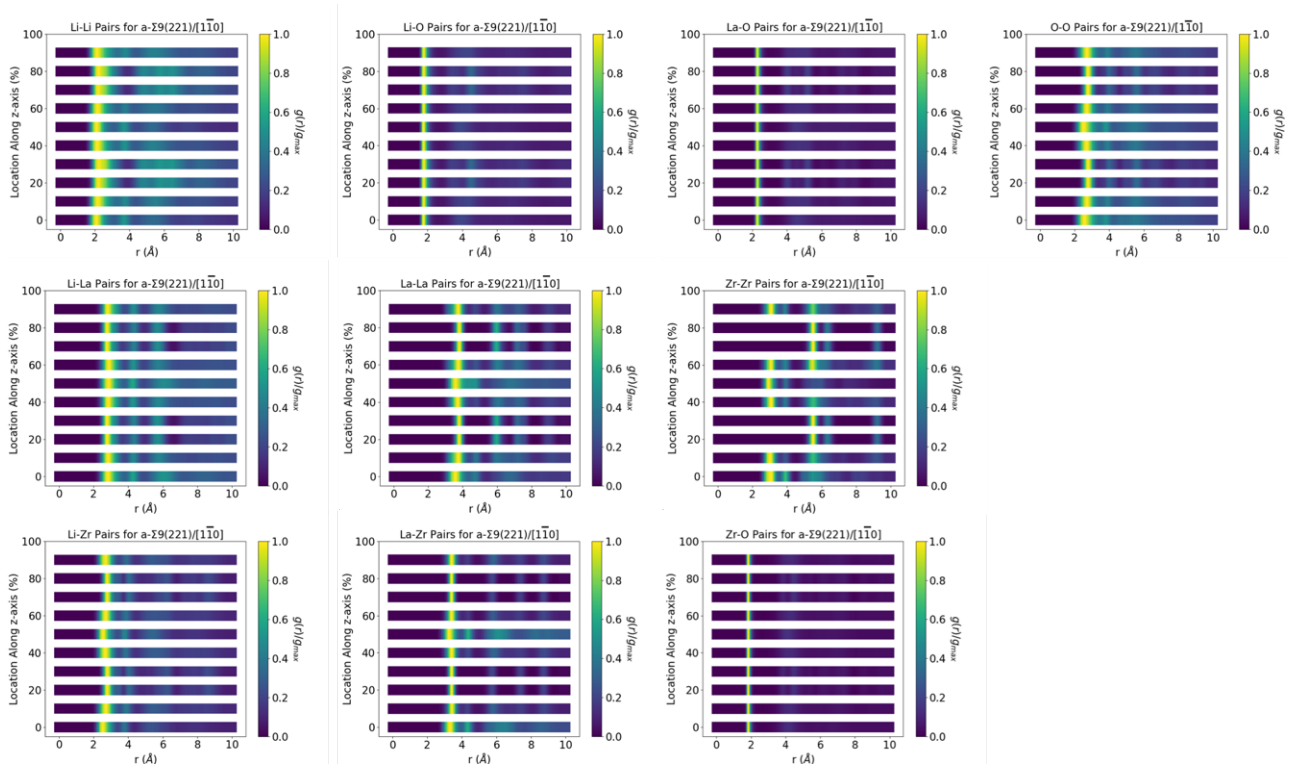


**Figure C.15** RDF plots for indicated atom pairs at various locations along the z-axis at 700K for a-$\Sigma9(221)/[1\bar{1}0]$ tilt grain boundary. The values of g(r) are divided by the maximum value, $g_{max}$, in order to easily visualize important features, with yellow indicating $g(r)=g_{max}$, and blue indicating g(r)=0. The grain boundaries are located at 0% and 50%.

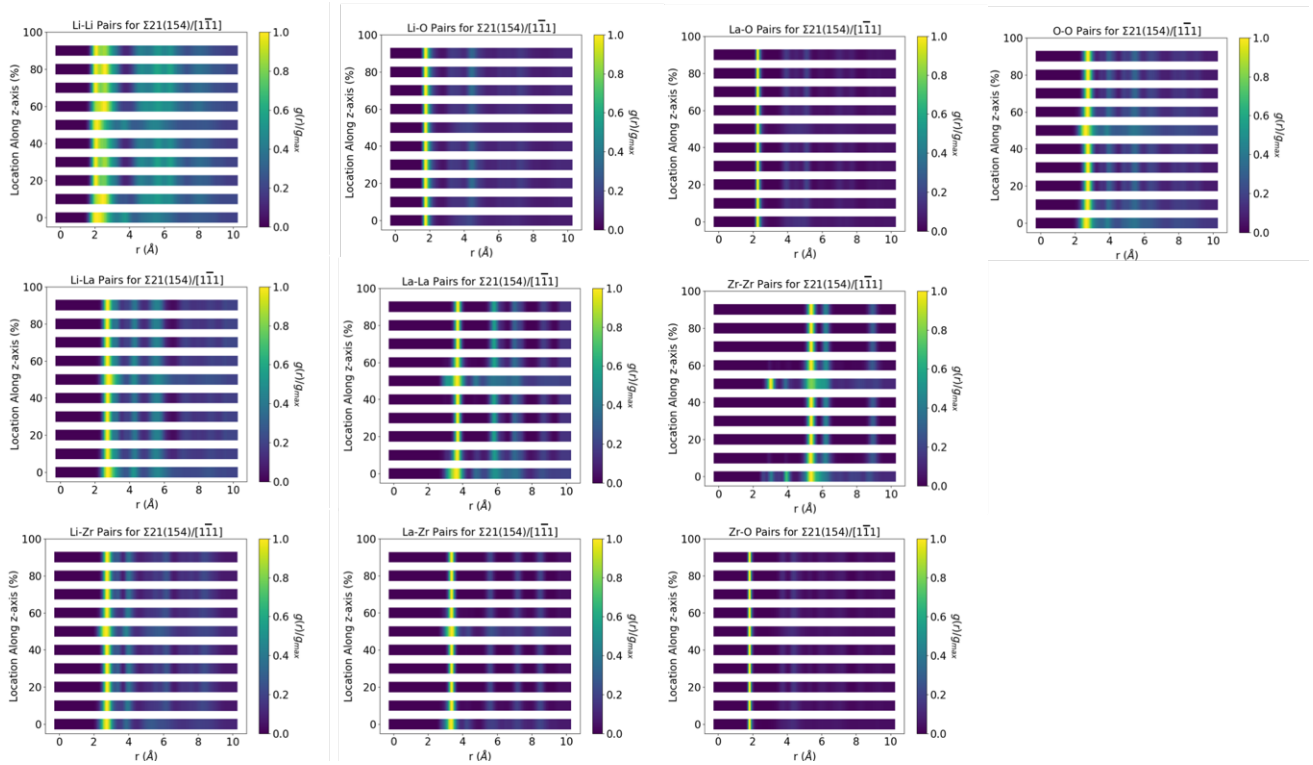


**Figure C.16** RDF plots for indicated atom pairs at various locations along the z-axis at 700K for $\Sigma21(154)/[1\bar{1}1]$ tilt grain boundary. The values of g(r) are divided by the maximum value, $g_{max}$, in order to easily visualize important features, with yellow indicating $g(r)=g_{max}$, and blue indicating $g(r)=0$. The grain boundaries are located at 0% and 50%.

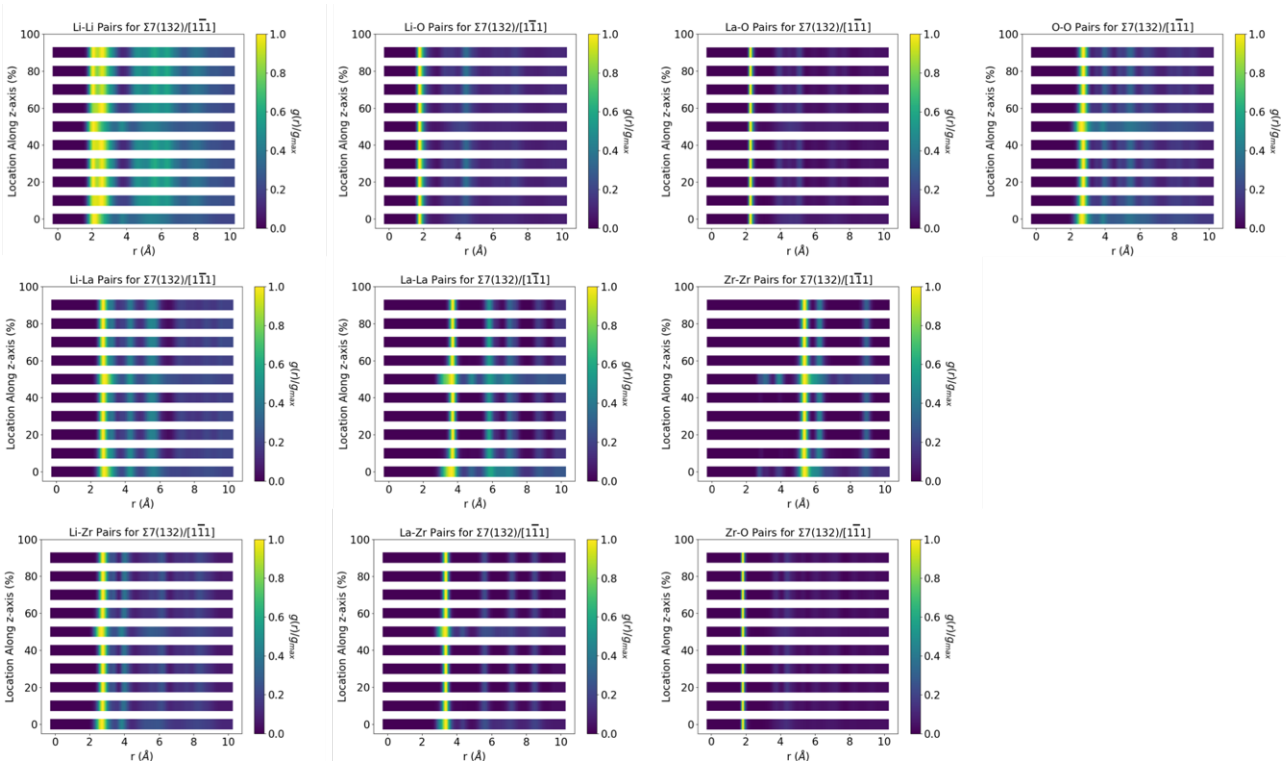


**Figure C.17** RDF plots for indicated atom pairs at various locations along the z-axis at 700K for $\Sigma7(132)/[1\bar{1}1]$ tilt grain boundary. The values of g(r) are divided by the maximum value, $g_{max}$, in order to easily visualize important features, with yellow indicating $g(r)=g_{max}$, and blue indicating g(r)=0. The grain boundaries are located at 0% and 50%.

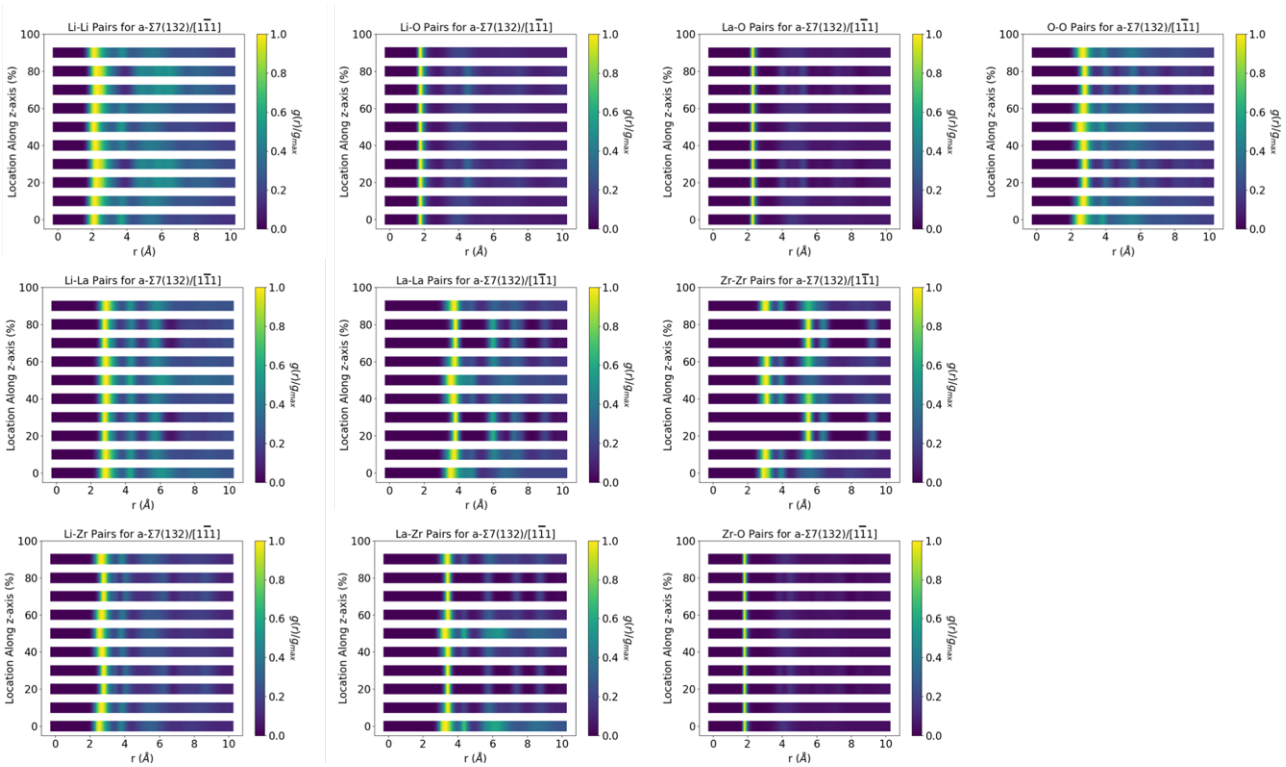


**Figure C.18** RDF plots for indicated atom pairs at various locations along the z-axis at 700K for a-$\Sigma7(132)/[1\bar{1}1]$ tilt grain boundary. The values of g(r) are divided by the maximum value, $g_{max}$, in order to easily visualize important features, with yellow indicating $g(r)=g_{max}$, and blue indicating $g(r)=0$. The grain boundaries are located at 0% and 50%.

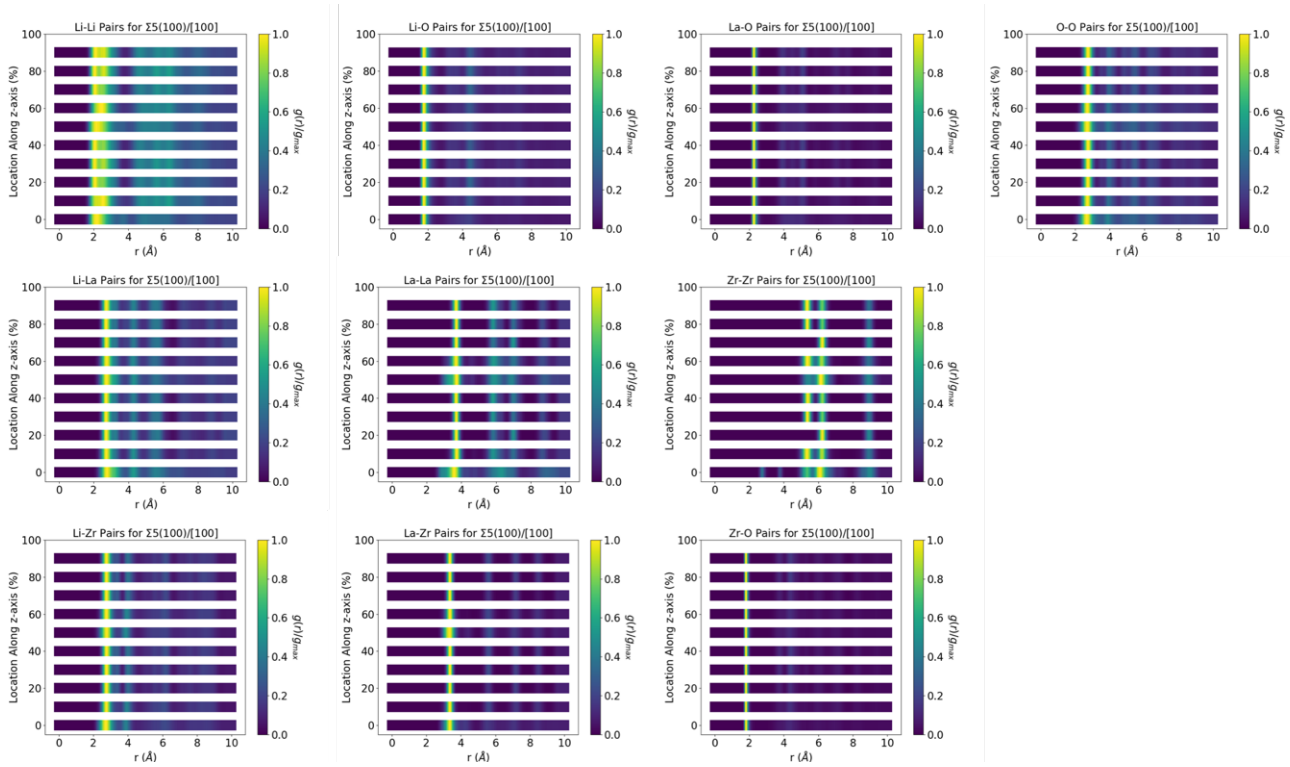


**Figure C.19** RDF plots for indicated atom pairs at various locations along the z-axis at 700K for Σ5(100)/[100] tilt grain boundary. The values of g(r) are divided by the maximum value, $g_{max}$, in order to easily visualize important features, with yellow indicating $g(r)=g_{max}$, and blue indicating g(r)=0. The grain boundaries are located at 0% and 50%.

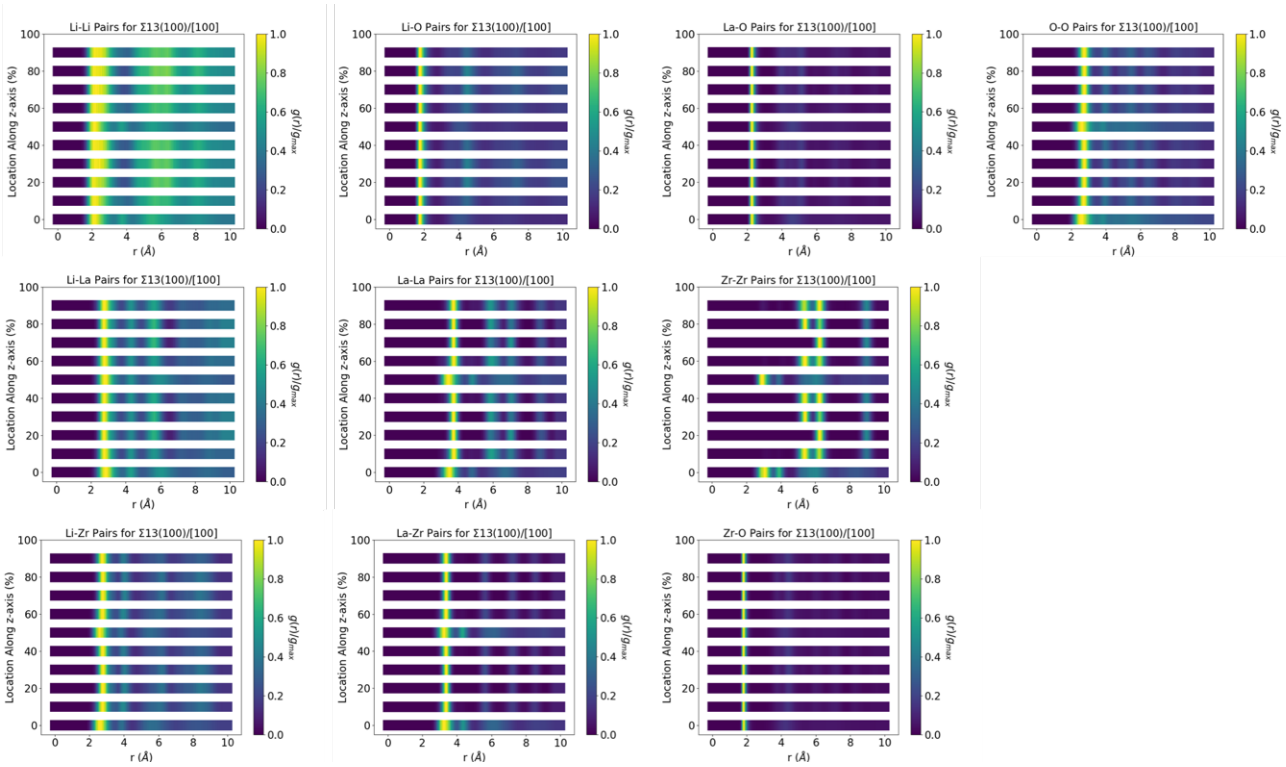


**Figure C.20** RDF plots for indicated atom pairs at various locations along the z-axis at 700K for Σ13(100)/[100] tilt grain boundary. The values of g(r) are divided by the maximum value, $g_{max}$, in order to easily visualize important features, with yellow indicating $g(r)=g_{max}$, and blue indicating g(r)=0. The grain boundaries are located at 0% and 50%.

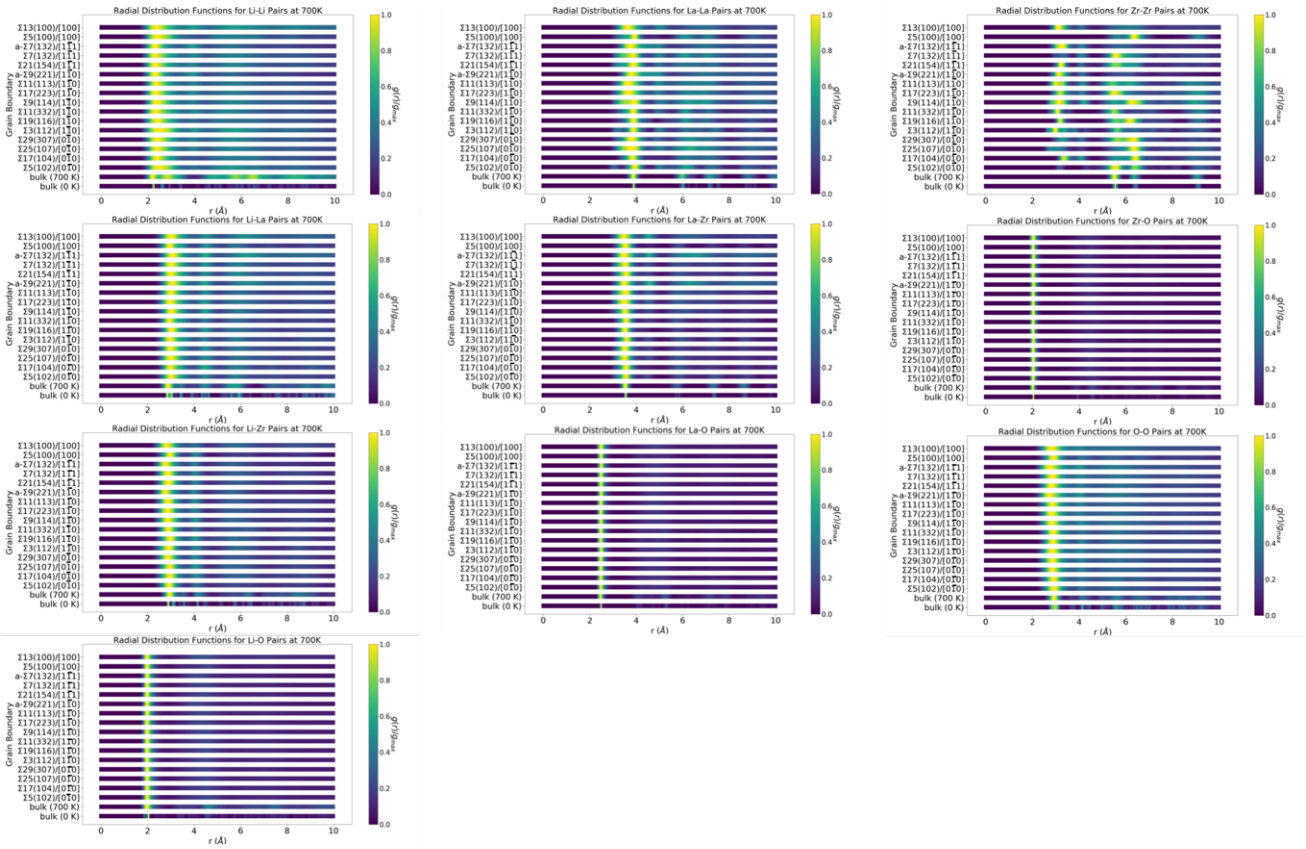


**Figure C.21** RDF plots for indicated atom pairs at the grain boundary of the indicated simulation cell at 700K. The values of g(r) are divided by the maximum value, $g_{max}$, in order to easily visualize important features, with yellow indicating $g(r)=g_{max}$, and blue indicating $g(r)=0$.

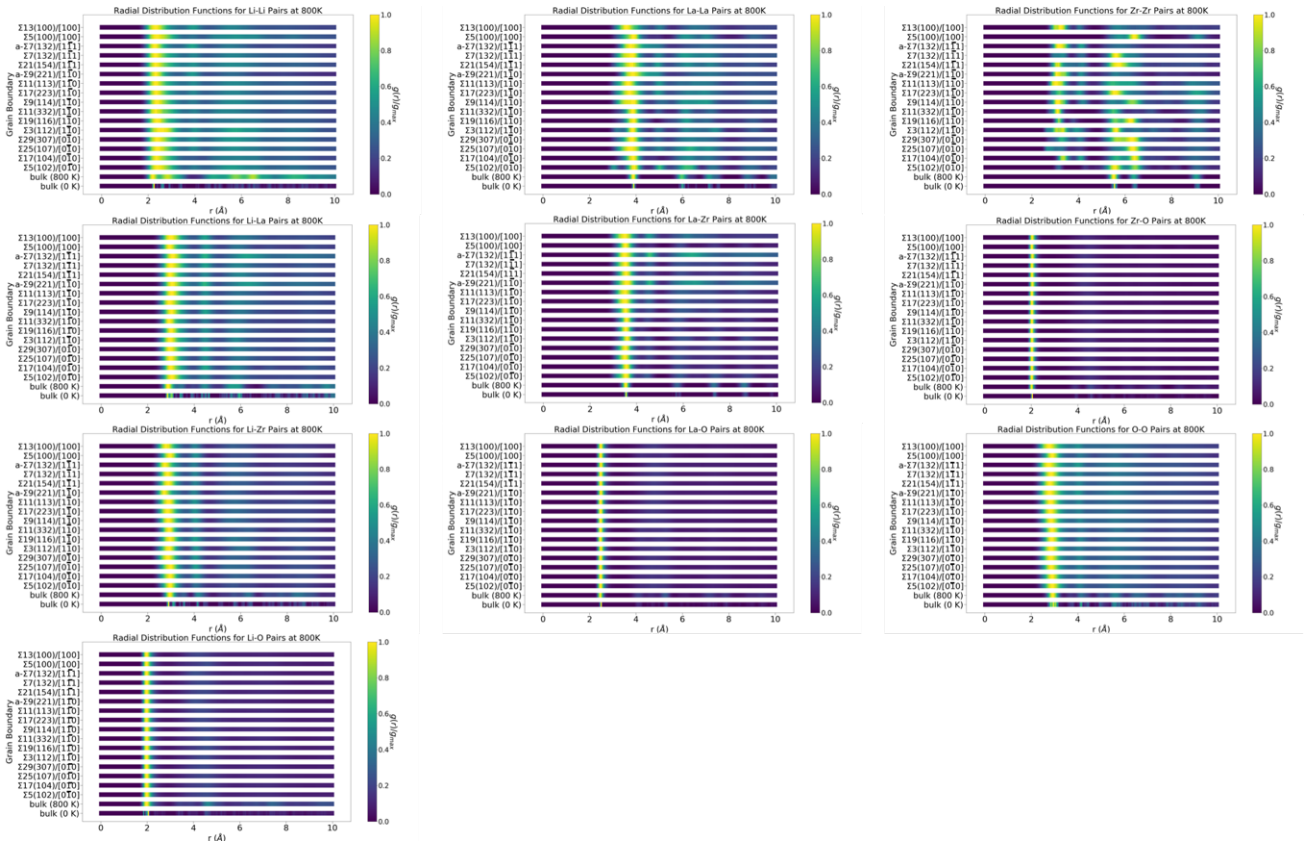


**Figure C.22** RDF plots for indicated atom pairs at the grain boundary of the indicated simulation cell at 800K. The values of g(r) are divided by the maximum value, $g_{max}$, in order to easily visualize important features, with yellow indicating $g(r)=g_{max}$, and blue indicating $g(r)=0$.

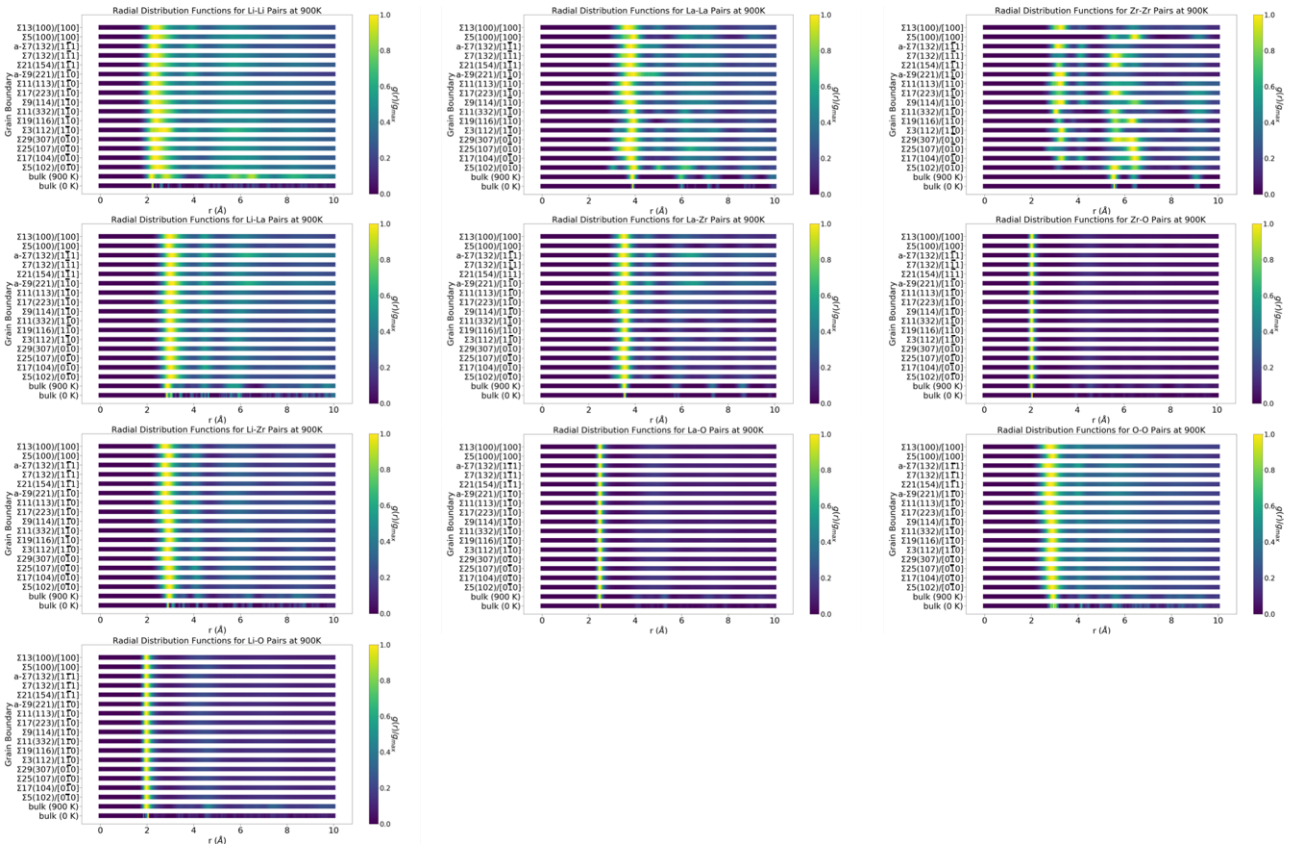


**Figure C.23** RDF plots for indicated atom pairs at the grain boundary of the indicated simulation cell at 900K. The values of g(r) are divided by the maximum value, $g_{max}$, in order to easily visualize important features, with yellow indicating $g(r)=g_{max}$, and blue indicating $g(r)=0$.

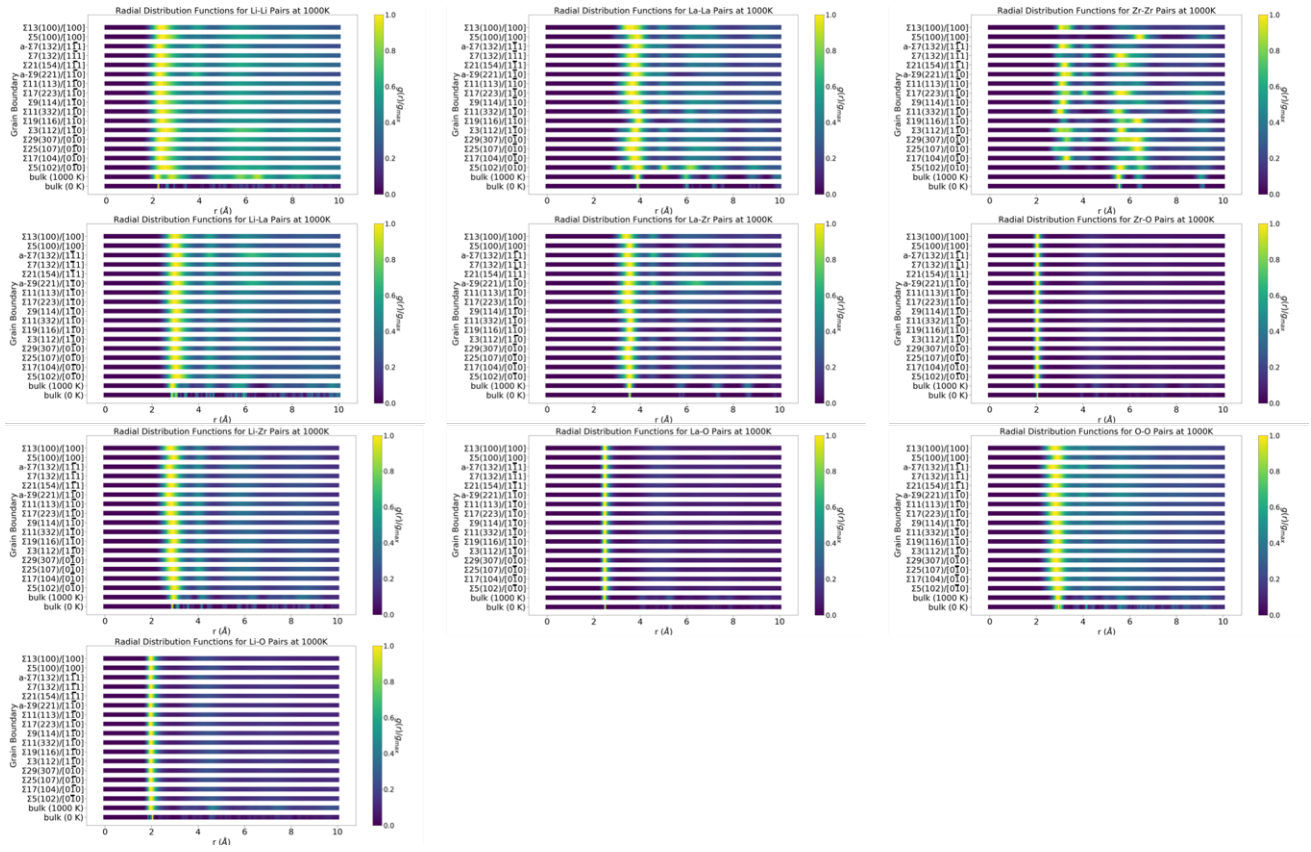


**Figure C.24** RDF plots for indicated atom pairs at the grain boundary of the indicated simulation cell at 1000K. The values of g(r) are divided by the maximum value, $g_{max}$, in order to easily visualize important features, with yellow indicating $g(r)=g_{max}$, and blue indicating $g(r)=0$.

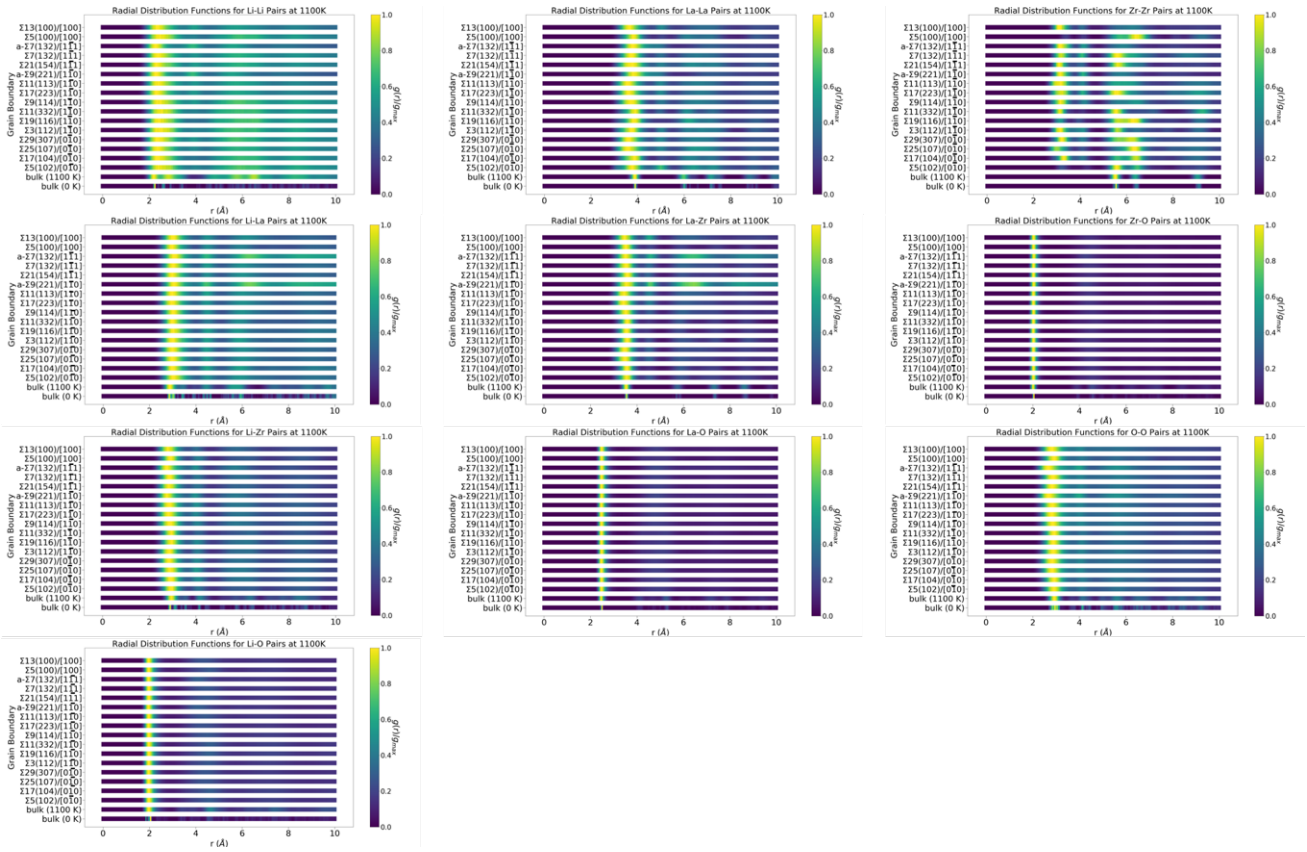


**Figure C.25** RDF plots for indicated atom pairs at the grain boundary of the indicated simulation cell at 1100K. The values of g(r) are divided by the maximum value, $g_{max}$, in order to easily visualize important features, with yellow indicating $g(r)=g_{max}$, and blue indicating $g(r)=0$.

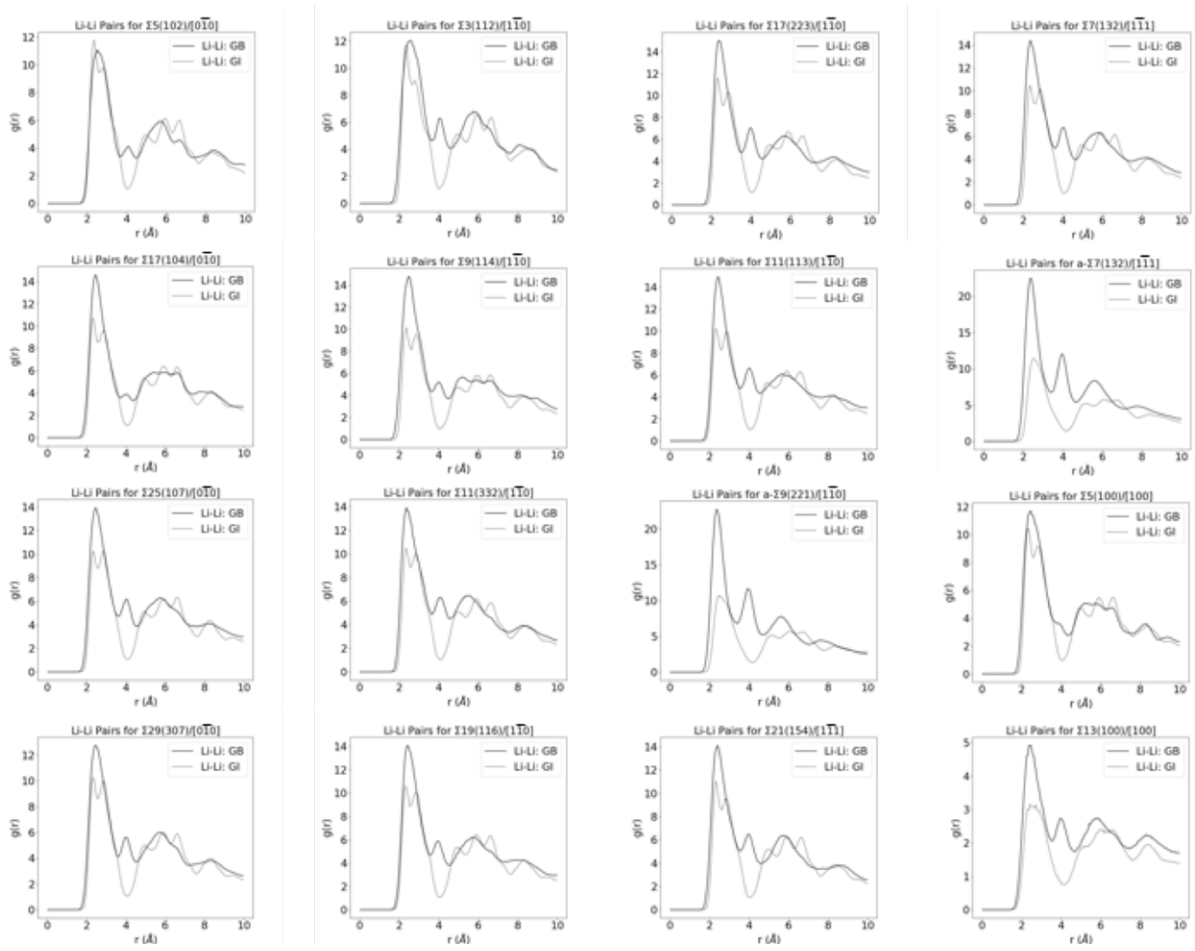


**Figure C.26** RDF plots for Li - Li pairs within GB region. These same data are represented in Figure 4a.

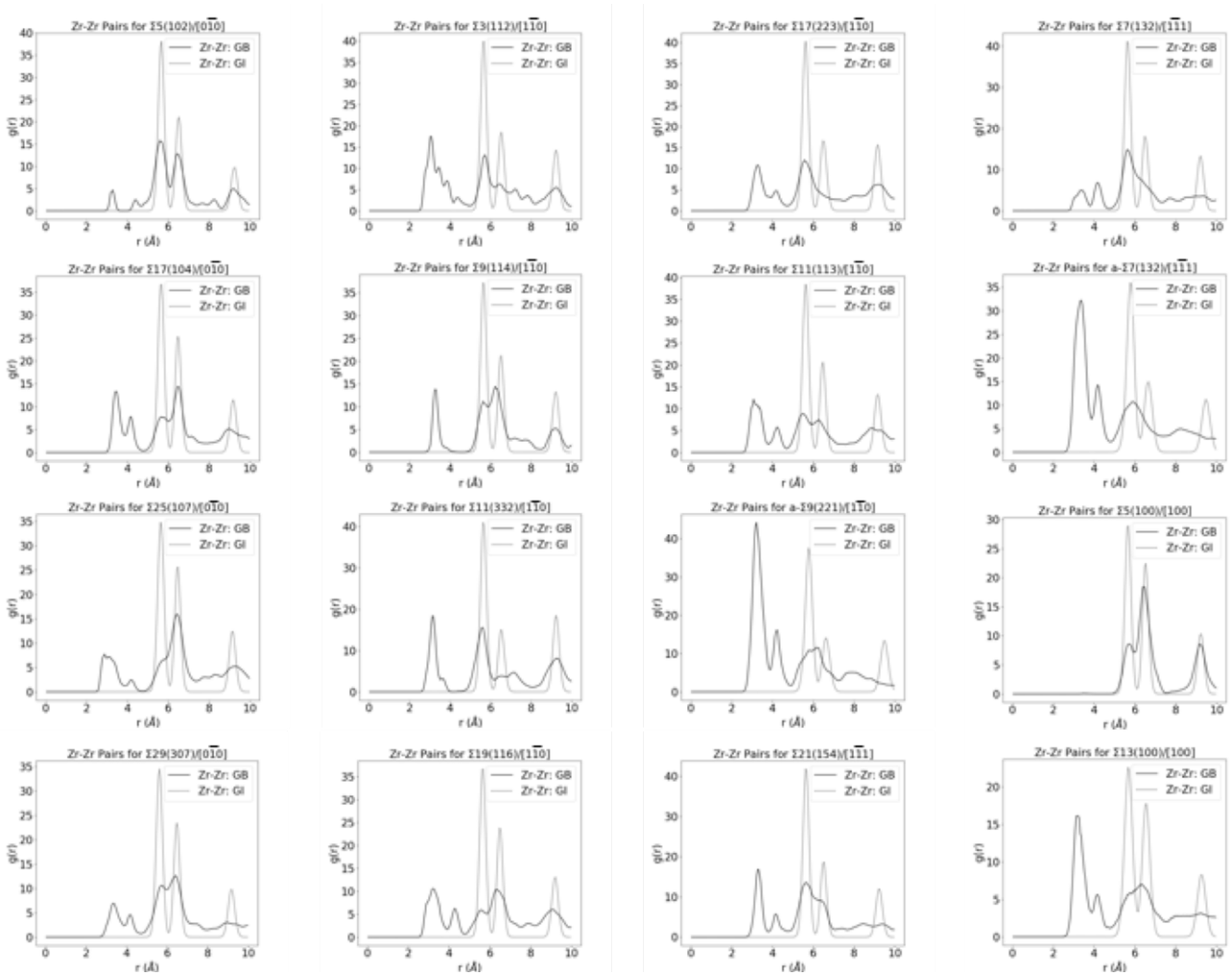


**Figure C.27** RDF plots for Zr - Zr pairs within GB region. These same data are represented in Figure 4b.

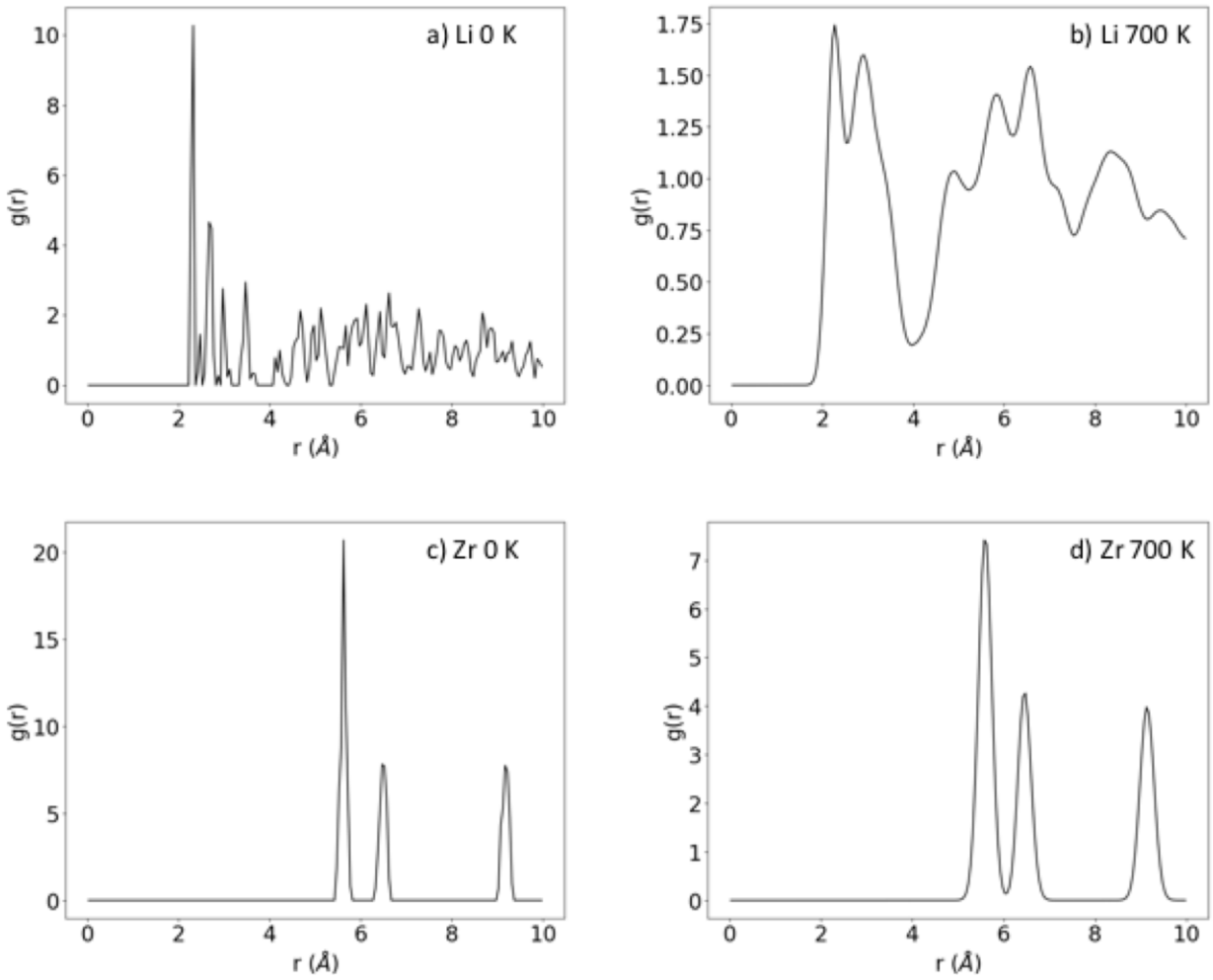


**Figure C.28** RDF plots of pairs within bulk LLZO at 0 K and 700 K. The pairs and temperatures represented are a) Li - Li at 0 K, b) Li - Li at 700 K, c) Zr - Zr at 0 K, and d) Zr - Zr at 700 K. These same data are represented in Figures 4a and 4b.

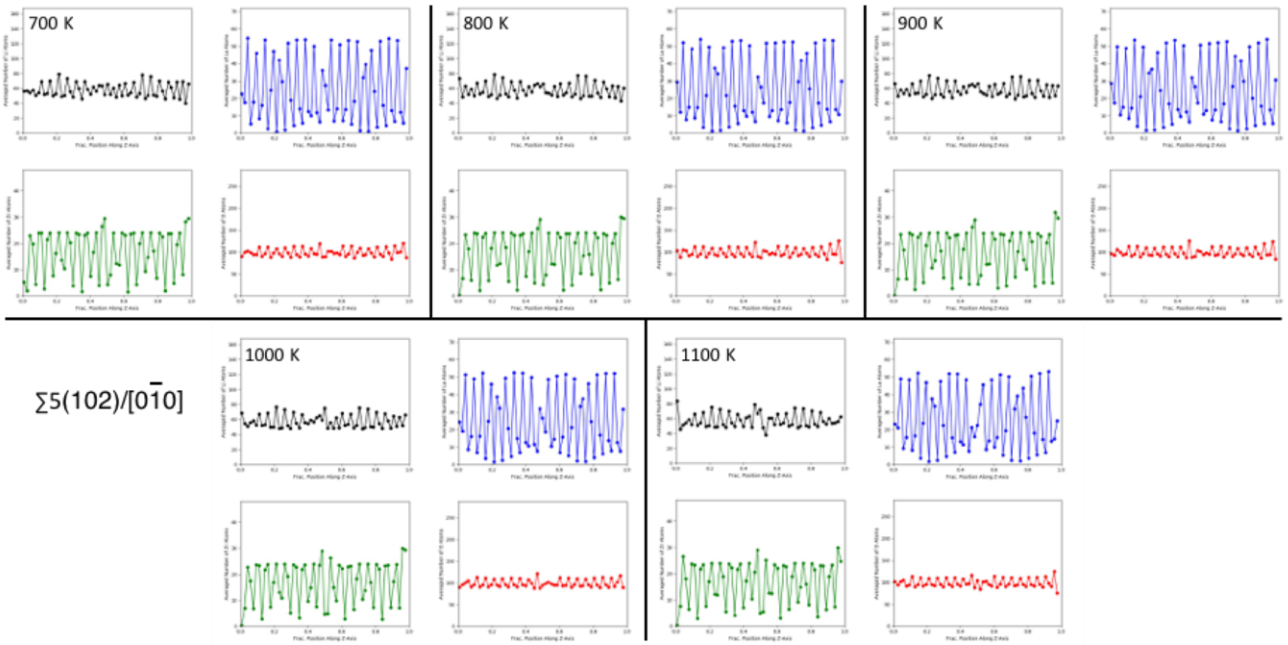


**Figure C.29** Time-averaged plots of Li, La, Zr, and O concentration at 700 K, 800 K, 900 K, 1000 K, and 1100 K for the Σ5(102)/[0$\bar{1}$0] GB. Atom positions were recorded for the duration of the Li diffusivity calculations. Each data point represents the number of atoms contained within ~1 Å intervals along the z-direction. Black data represents Li, blue represents La, green represents Zr, and red represents O.

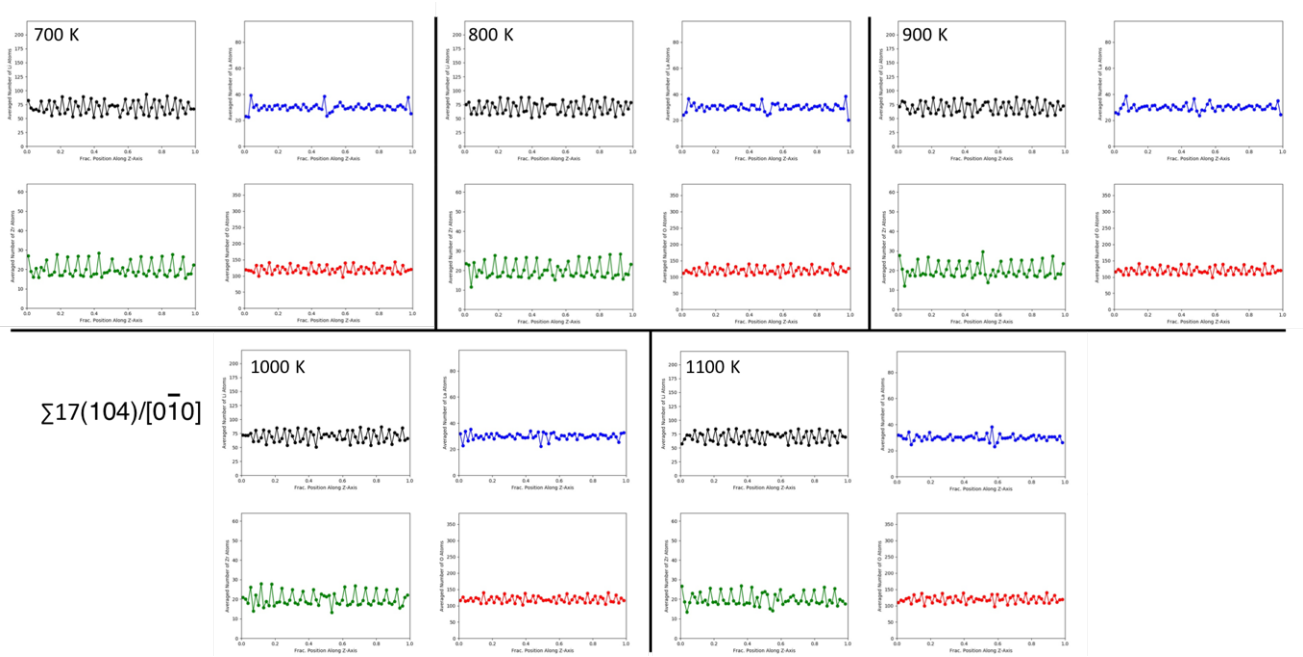


**Figure C.30** Time-averaged plots of Li, La, Zr, and O concentration at 700 K, 800 K, 900 K, 1000 K, and 1100 K for the Σ17(104)/[0$\bar{1}$0] GB. Atom positions were recorded for the duration of the Li diffusivity calculations. Each data point represents the number of atoms contained within ~1 Å intervals along the z-direction. Black data represents Li, blue represents La, green represents Zr, and red represents O.

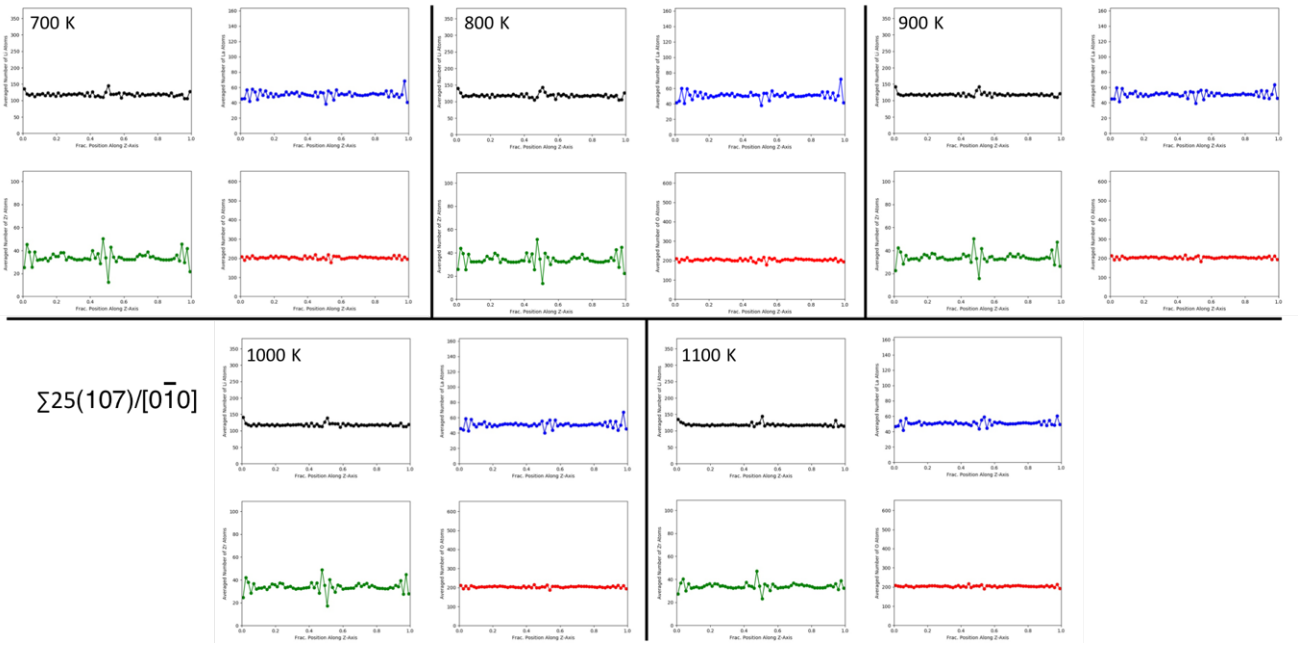


**Figure C.31** Time-averaged plots of Li, La, Zr, and O concentration at 700 K, 800 K, 900 K, 1000 K, and 1100 K for the Σ25(107)/[0$\bar{1}$0] GB. Atom positions were recorded for the duration of the Li diffusivity calculations. Each data point represents the number of atoms contained within ~1 Å intervals along the z-direction. Black data represents Li, blue represents La, green represents Zr, and red represents O.

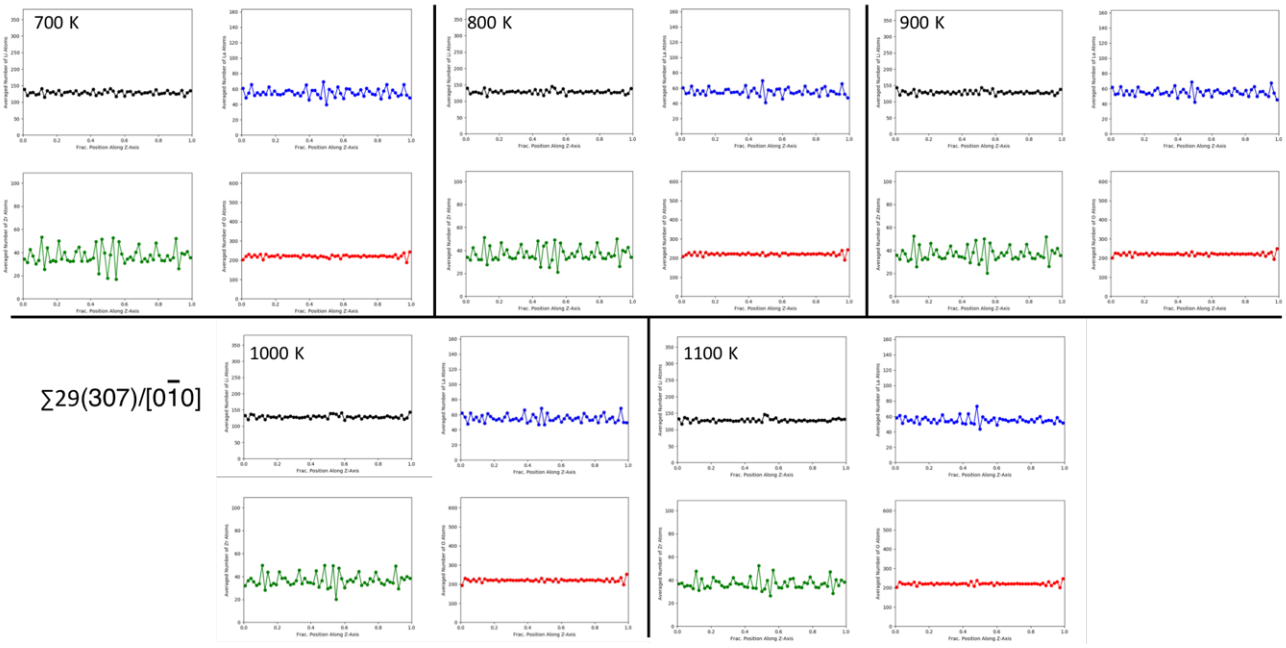


**Figure C.32** Time-averaged plots of Li, La, Zr, and O concentration at 700 K, 800 K, 900 K, 1000 K, and 1100 K for the Σ29(307)/[0$\bar{1}$0] GB. Atom positions were recorded for the duration of the Li diffusivity calculations. Each data point represents the number of atoms contained within ~1 Å intervals along the z-direction. Black data represents Li, blue represents La, green represents Zr, and red represents O.

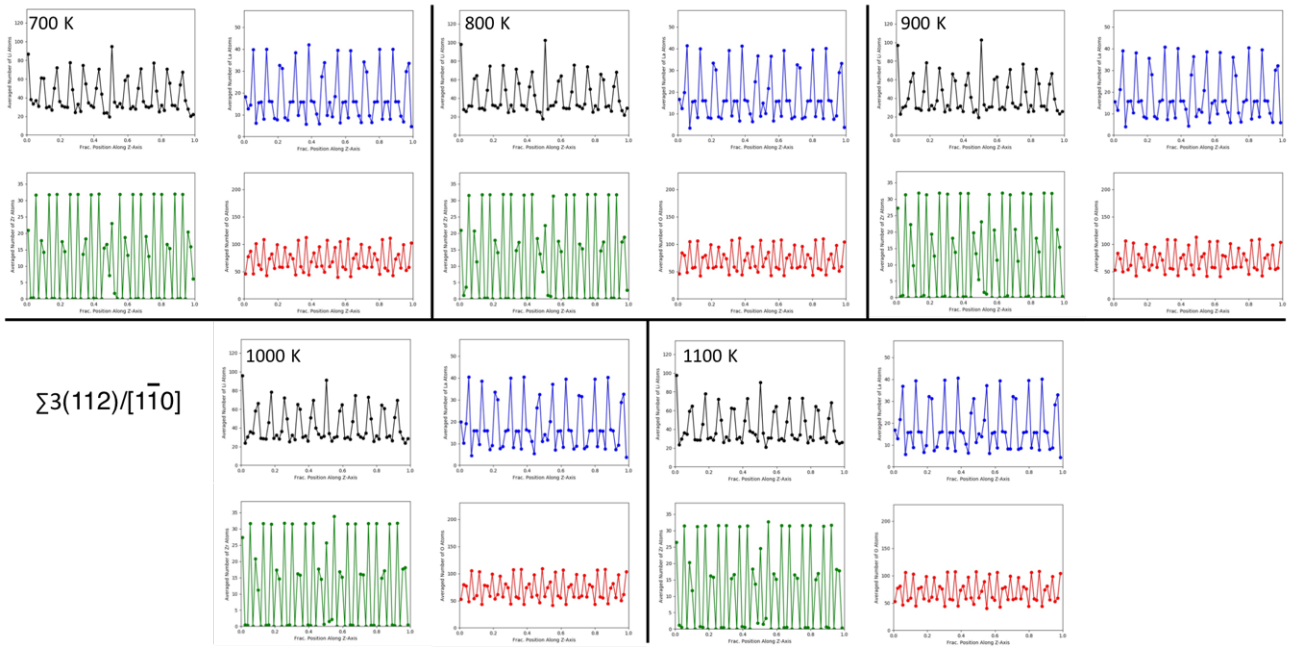


**Figure C.33** Time-averaged plots of Li, La, Zr, and O concentration at 700 K, 800 K, 900 K, 1000 K, and 1100 K for the Σ3(112)/[1$\bar{1}$0] GB. Atom positions were recorded for the duration of the Li diffusivity calculations. Each data point represents the number of atoms contained within ~1 Å intervals along the z-direction. Black data represents Li, blue represents La, green represents Zr, and red represents O.

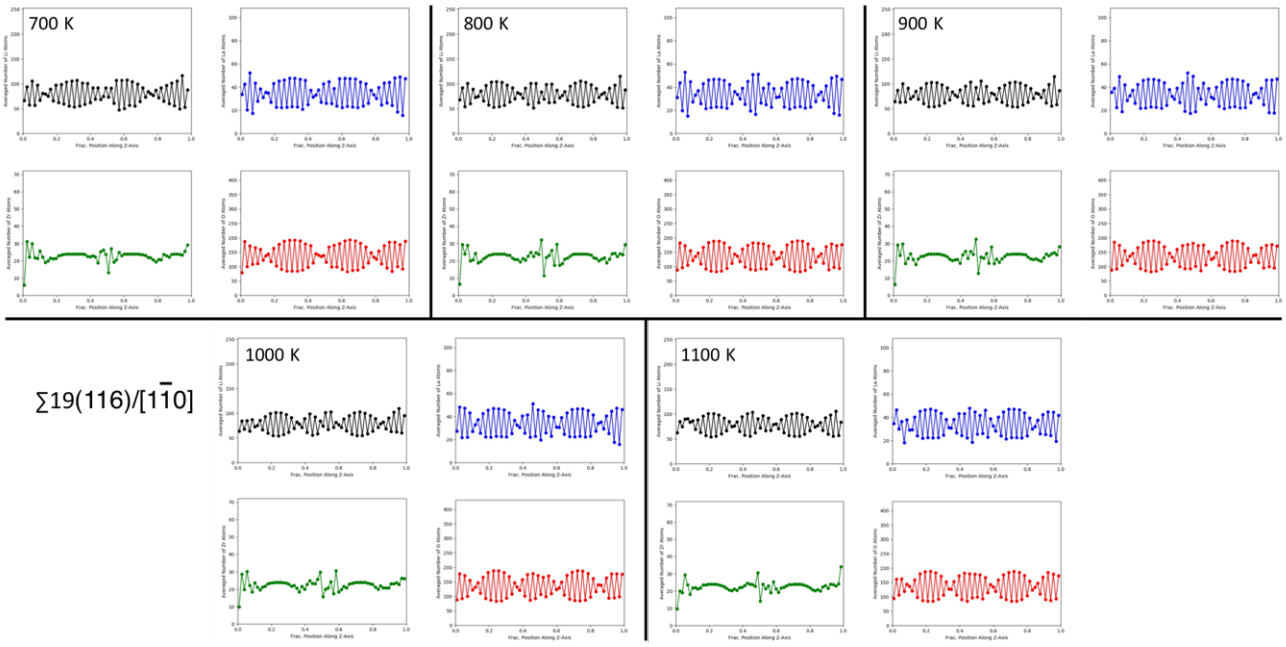


**Figure C.34** Time-averaged plots of Li, La, Zr, and O concentration at 700 K, 800 K, 900 K, 1000 K, and 1100 K for the Σ19(116)/[1$\bar{1}$0] GB. Atom positions were recorded for the duration of the Li diffusivity calculations. Each data point represents the number of atoms contained within ~1 Å intervals along the z-direction. Black data represents Li, blue represents La, green represents Zr, and red represents O.

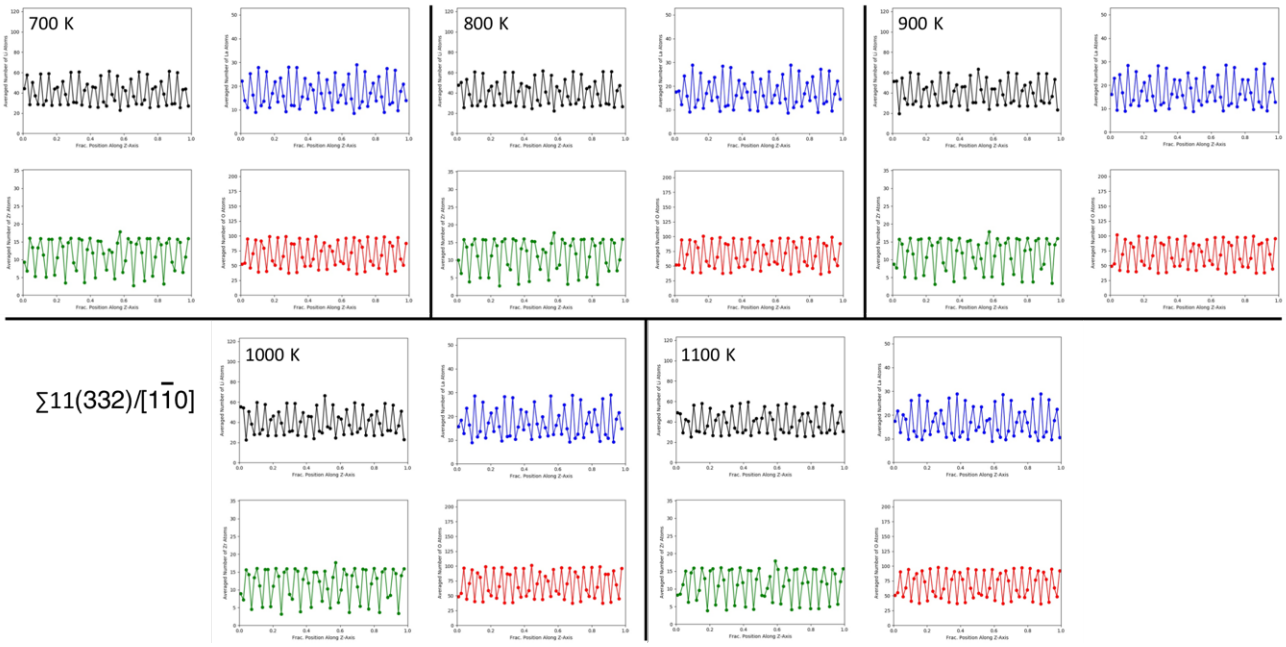


**Figure C.35** Time-averaged plots of Li, La, Zr, and O concentration at 700 K, 800 K, 900 K, 1000 K, and 1100 K for the Σ11(332)/[1$\bar{1}$0] GB. Atom positions were recorded for the duration of the Li diffusivity calculations. Each data point represents the number of atoms contained within ~1 Å intervals along the z-direction. Black data represents Li, blue represents La, green represents Zr, and red represents O.

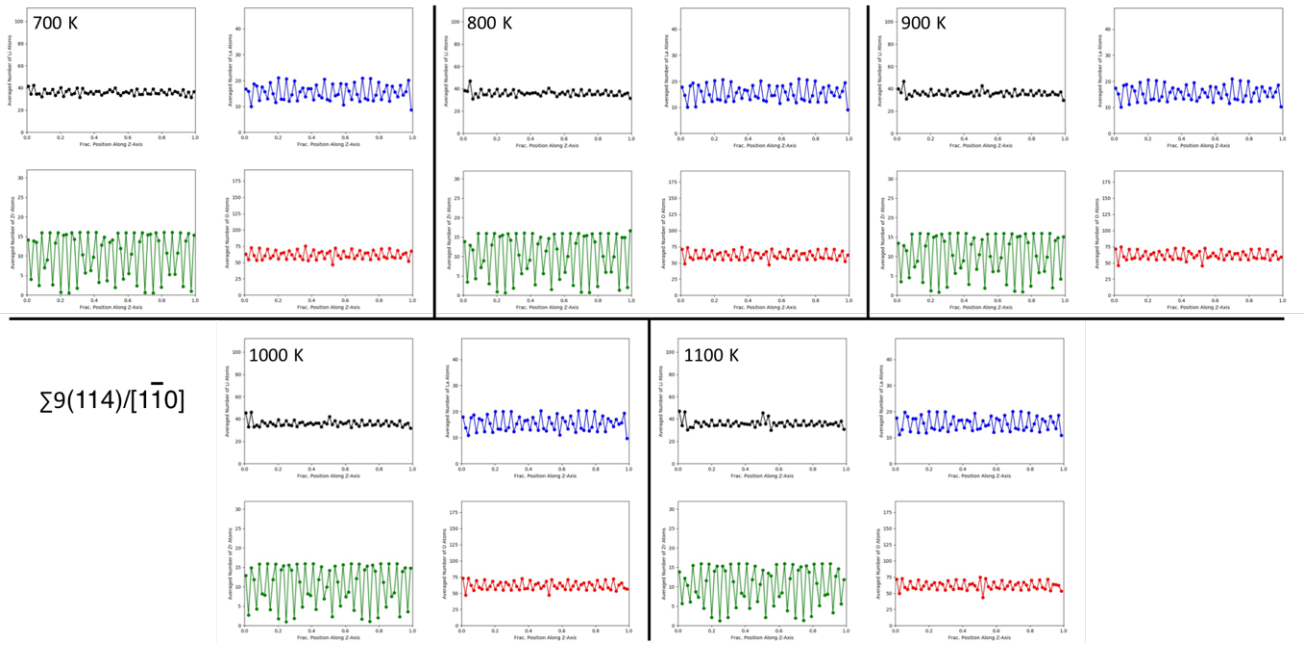


**Figure C.36** Time-averaged plots of Li, La, Zr, and O concentration at 700 K, 800 K, 900 K, 1000 K, and 1100 K for the Σ9(114)/[1$\bar{1}$0] GB. Atom positions were recorded for the duration of the Li diffusivity calculations. Each data point represents the number of atoms contained within ~1 Å intervals along the z-direction. Black data represents Li, blue represents La, green represents Zr, and red represents O.

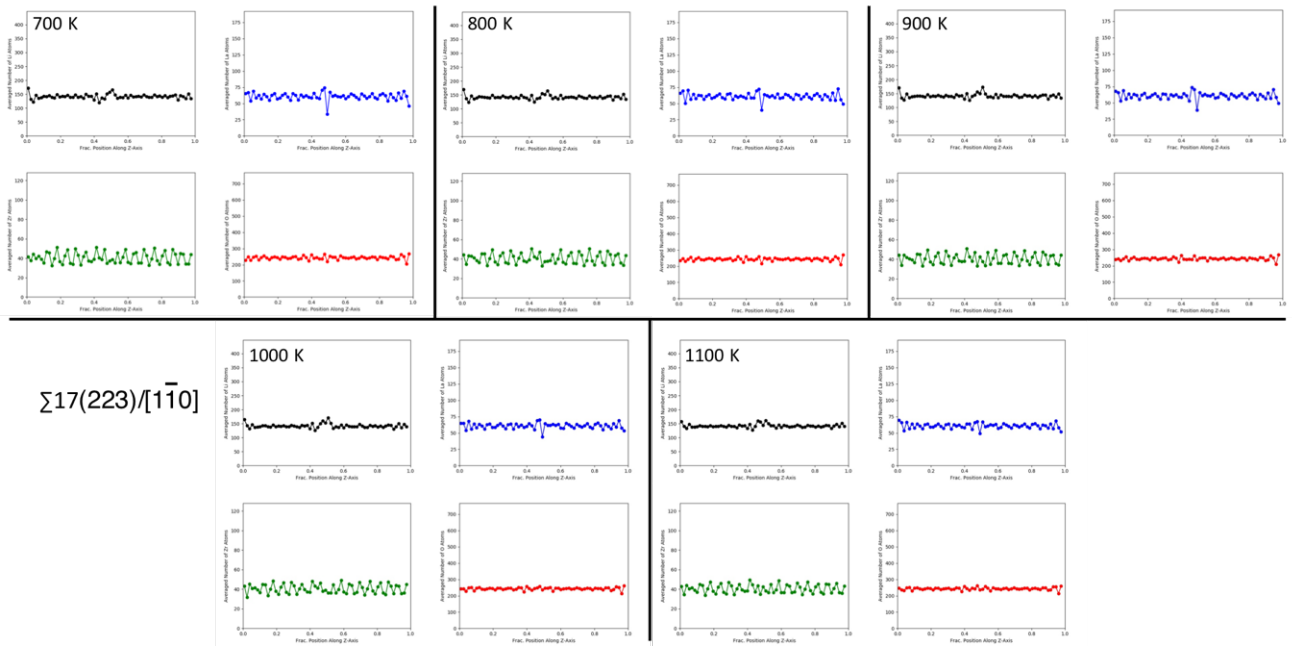


**Figure C.37** Time-averaged plots of Li, La, Zr, and O concentration at 700 K, 800 K, 900 K, 1000 K, and 1100 K for the Σ17(223)/[1$\bar{1}$0] GB. Atom positions were recorded for the duration of the Li diffusivity calculations. Each data point represents the number of atoms contained within ~1 Å intervals along the z-direction. Black data represents Li, blue represents La, green represents Zr, and red represents O.

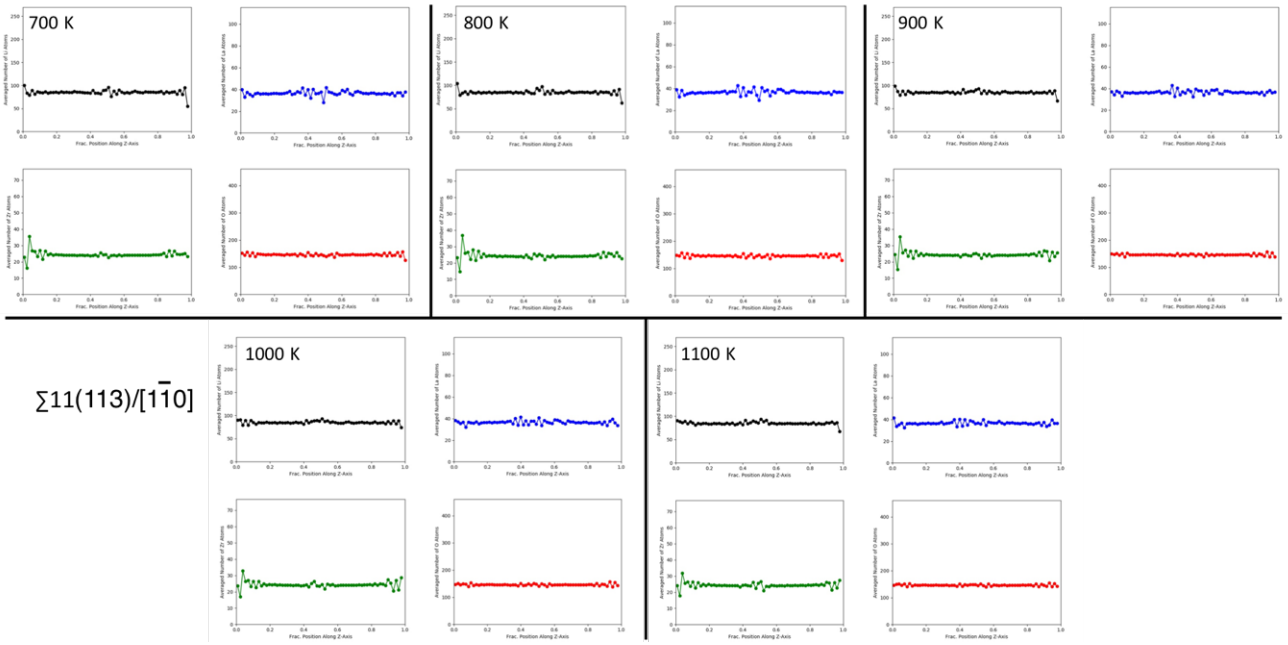


**Figure C.38** Time-averaged plots of Li, La, Zr, and O concentration at 700 K, 800 K, 900 K, 1000 K, and 1100 K for the Σ11(113)/[1$\bar{1}$0] GB. Atom positions were recorded for the duration of the Li diffusivity calculations. Each data point represents the number of atoms contained within ~1 Å intervals along the z-direction. Black data represents Li, blue represents La, green represents Zr, and red represents O.

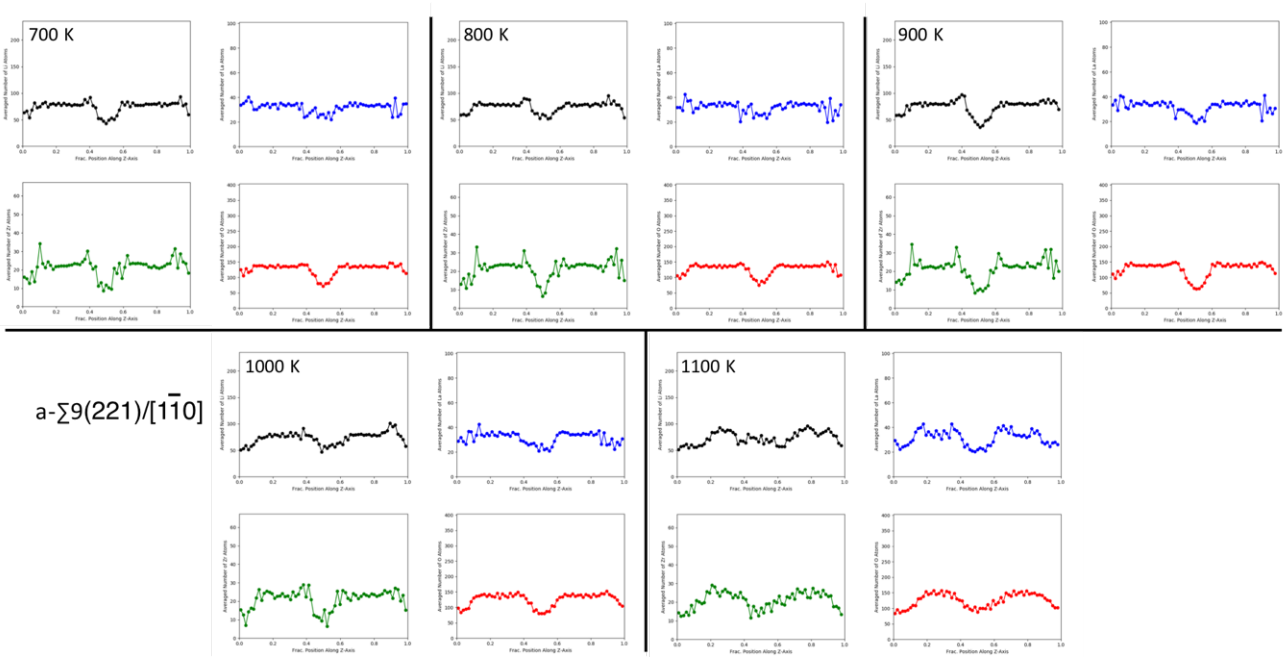


**Figure C.39** Time-averaged plots of Li, La, Zr, and O concentration at 700 K, 800 K, 900 K, 1000 K, and 1100 K for the a-Σ9(221)/[1$\bar{1}$0] GB. Atom positions were recorded for the duration of the Li diffusivity calculations. Each data point represents the number of atoms contained within ~1 Å intervals along the z-direction. Black data represents Li, blue represents La, green represents Zr, and red represents O.

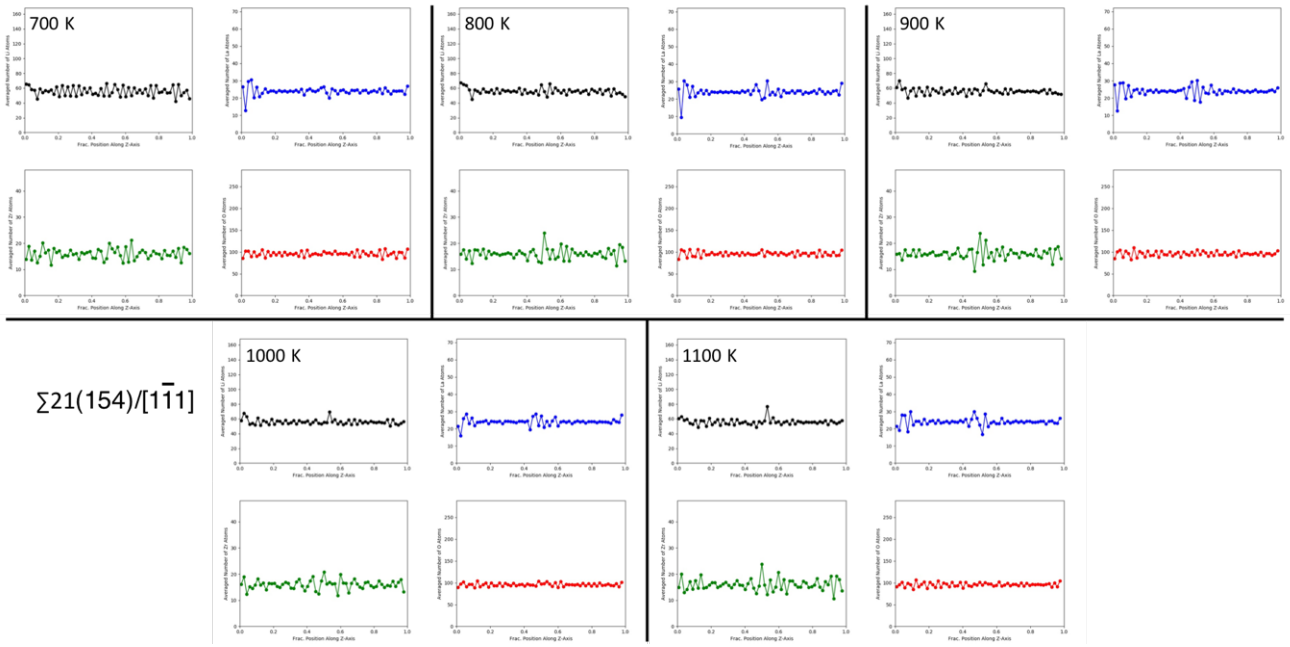


**Figure C.40** Time-averaged plots of Li, La, Zr, and O concentration at 700 K, 800 K, 900 K, 1000 K, and 1100 K for the Σ21(154)/[1$\bar{1}$1] GB. Atom positions were recorded for the duration of the Li diffusivity calculations. Each data point represents the number of atoms contained within ~1 Å intervals along the z-direction. Black data represents Li, blue represents La, green represents Zr, and red represents O.

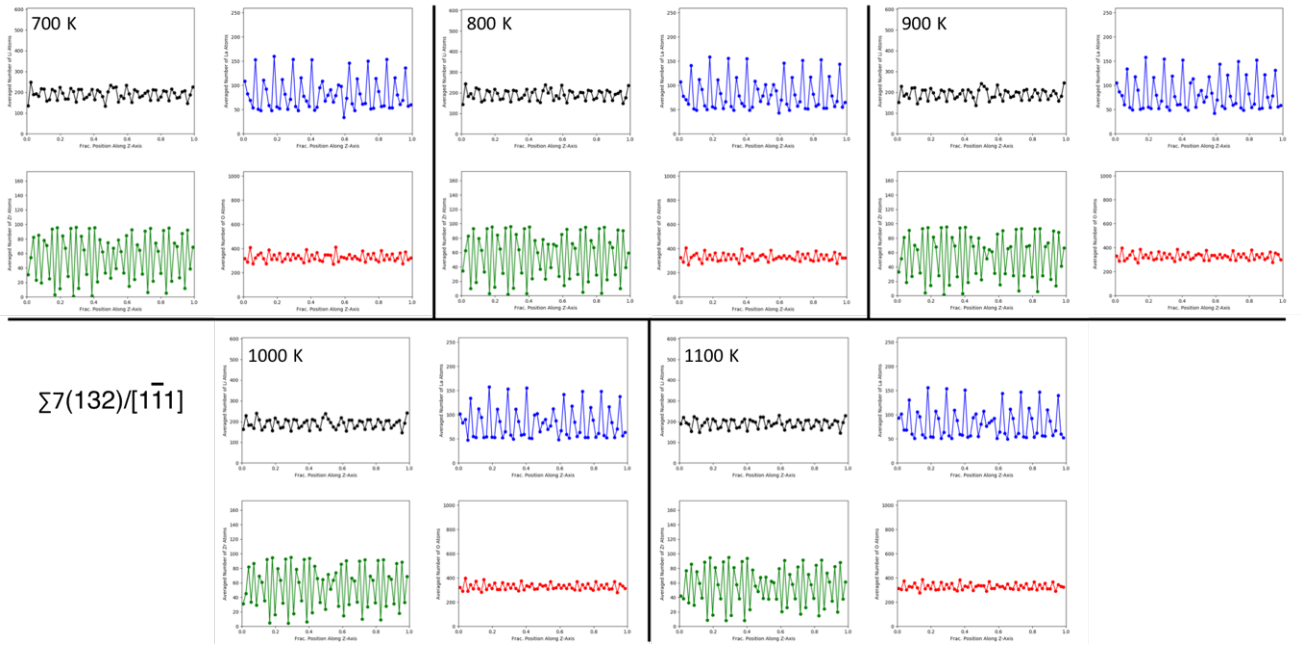


**Figure C.41** Time-averaged plots of Li, La, Zr, and O concentration at 700 K, 800 K, 900 K, 1000 K, and 1100 K for the Σ7(132)/[1$\bar{1}$1] GB. Atom positions were recorded for the duration of the Li diffusivity calculations. Each data point represents the number of atoms contained within ~1 Å intervals along the z-direction. Black data represents Li, blue represents La, green represents Zr, and red represents O.

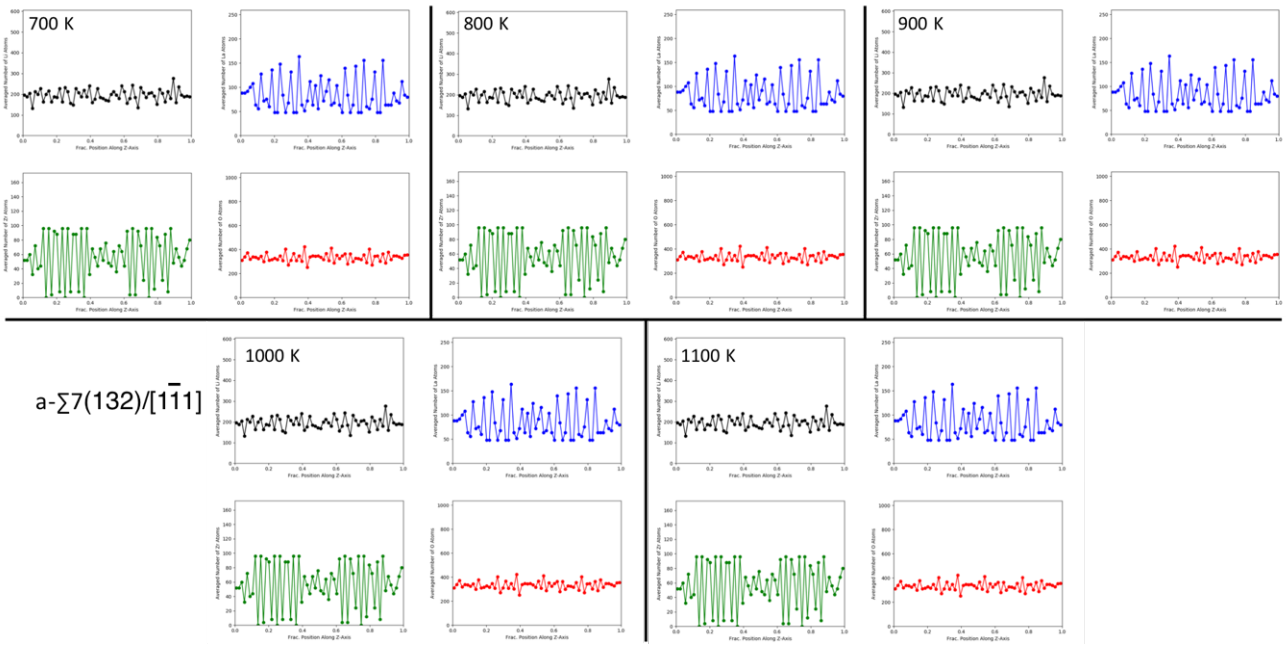


**Figure C.42** Time-averaged plots of Li, La, Zr, and O concentration at 700 K, 800 K, 900 K, 1000 K, and 1100 K for the a-Σ7(132)/[1$\bar{1}$1] GB. Atom positions were recorded for the duration of the Li diffusivity calculations. Each data point represents the number of atoms contained within ~1 Å intervals along the z-direction. Black data represents Li, blue represents La, green represents Zr, and red represents O.

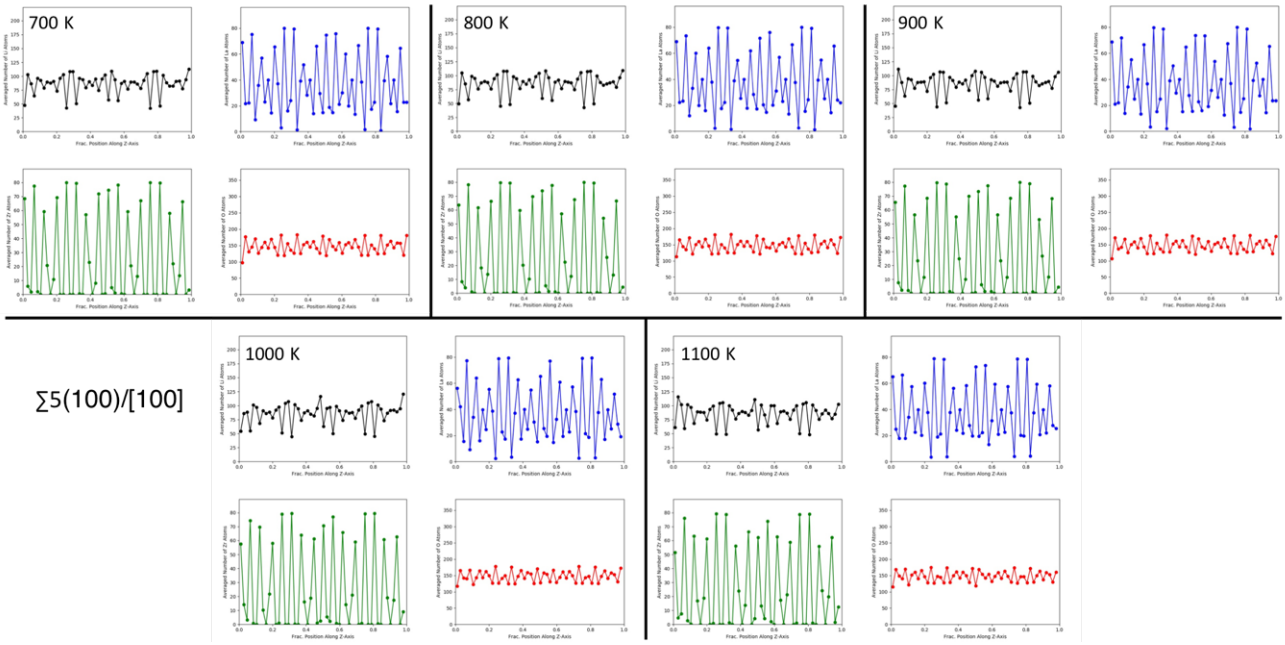


**Figure C.43** Time-averaged plots of Li, La, Zr, and O concentration at 700 K, 800 K, 900 K, 1000 K, and 1100 K for the Σ5(100)/[100] GB. Atom positions were recorded for the duration of the Li diffusivity calculations. Each data point represents the number of atoms contained within ~1 Å intervals along the z-direction. Black data represents Li, blue represents La, green represents Zr, and red represents O.

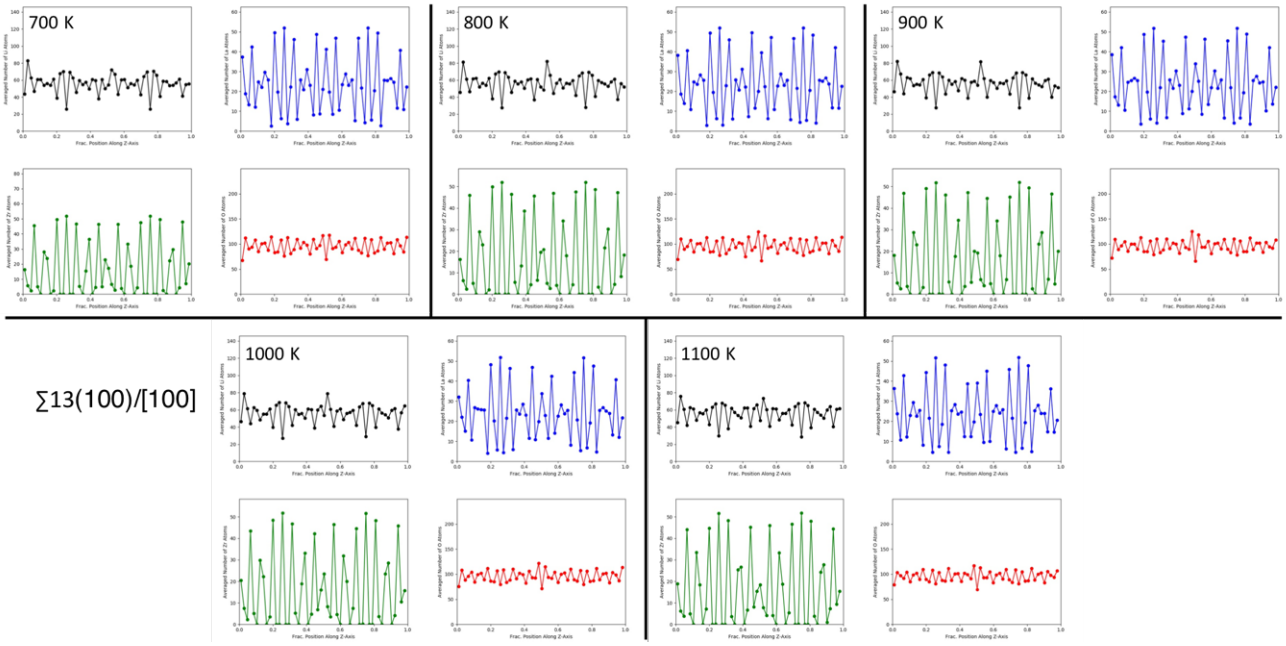


**Figure C.44** Time-averaged plots of Li, La, Zr, and O concentration at 700 K, 800 K, 900 K, 1000 K, and 1100 K for the Σ13(100)/[100] GB. Atom positions were recorded for the duration of the Li diffusivity calculations. Each data point represents the number of atoms contained within ~1 Å intervals along the z-direction. Black data represents Li, blue represents La, green represents Zr, and red represents O.

**Table C.6** Ratio of number of atoms in GB region to number of atoms in GI region. Data obtained from time-averaged composition plots (Figures S31 - S46).

| Grain Boundary | Li Ratio | La Ratio | Zr Ratio | O Ratio |
|---|---|---|---|---|
| $\Sigma5(102)/[0\bar{1}0]$ | 1.01 | 0.90 | 1.01 | 1.02 |
| $\Sigma17(104)/[0\bar{1}0]$ | 0.98 | 0.97 | 1.03 | 0.98 |
| $\Sigma25(107)/[0\bar{1}0]$ | 1.01 | 0.98 | 1.05 | 0.99 |
| $\Sigma29(307)/[0\bar{1}0]$ | 1.01 | 0.97 | 0.93 | 0.99 |
| $\Sigma3(112)/[1\bar{1}0]$ | 0.80 | 1.01 | 0.67 | 1.13 |
| $\Sigma19(116)/[1\bar{1}0]$ | 0.95 | 0.93 | 0.92 | 0.93 |
| $\Sigma11(332)/[1\bar{1}0]$ | 0.99 | 0.98 | 0.96 | 0.99 |
| $\Sigma9(114)/[1\bar{1}0]$ | 1.00 | 0.94 | 1.19 | 1.03 |
| $\Sigma17(223)/[1\bar{1}0]$ | 1.04 | 1.01 | 0.99 | 1.00 |
| $\Sigma11(113)/[1\bar{1}0]$ | 1.01 | 0.99 | 1.00 | 0.99 |
| a-$\Sigma9(221)/[1\bar{1}0]$ | 0.63 | 0.76 | 0.54 | 0.63 |
| $\Sigma21(154)/[1\bar{1}1]$ | 1.01 | 1.00 | 1.05 | 1.01 |
| $\Sigma7(132)/[1\bar{1}1]$ | 1.00 | 1.01 | 1.00 | 1.00 |
| a-$\Sigma7(132)/[1\bar{1}1]$ | 0.96 | 1.00 | 1.01 | 1.02 |
| $\Sigma5(100)/[100]$ | 1.06 | 0.91 | 0.96 | 1.04 |
| $\Sigma13(100)/[100]$ | 1.08 | 0.95 | 0.97 | 1.04 |

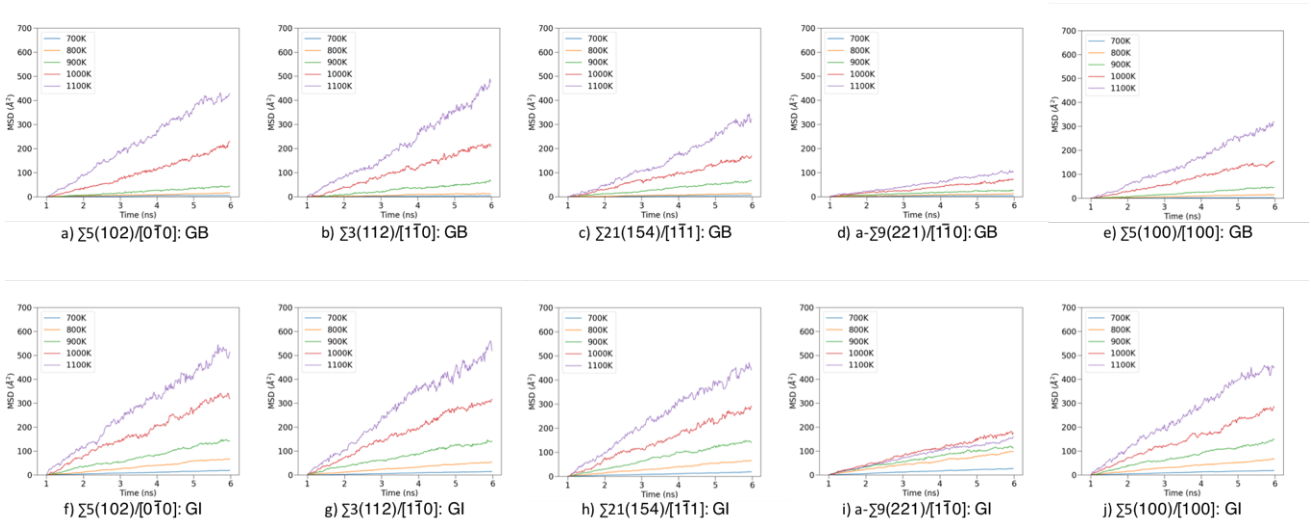


**Figure C.45** Mean square displacement (MSD) plots of Li-ions within GB and GI regions of 5 representative GB cells at 700 K. Panels (a-e) represent MSD's within a) Σ5(102)/[0$\bar{1}$0], b) Σ3(112)/[1$\bar{1}$0], c) Σ21(154)/[1$\bar{1}$1], d) a-Σ9(221)/[1$\bar{1}$0], and e) Σ5(100)/[100] at GB regions. Panels (f-j) represent MSD's within a) Σ5(102)/[0$\bar{1}$0], b) Σ3(112)/[1$\bar{1}$0], c) Σ21(154)/[1$\bar{1}$1], d) a-Σ9(221)/[1$\bar{1}$0], and e) Σ5(100)/[100] at GI regions.

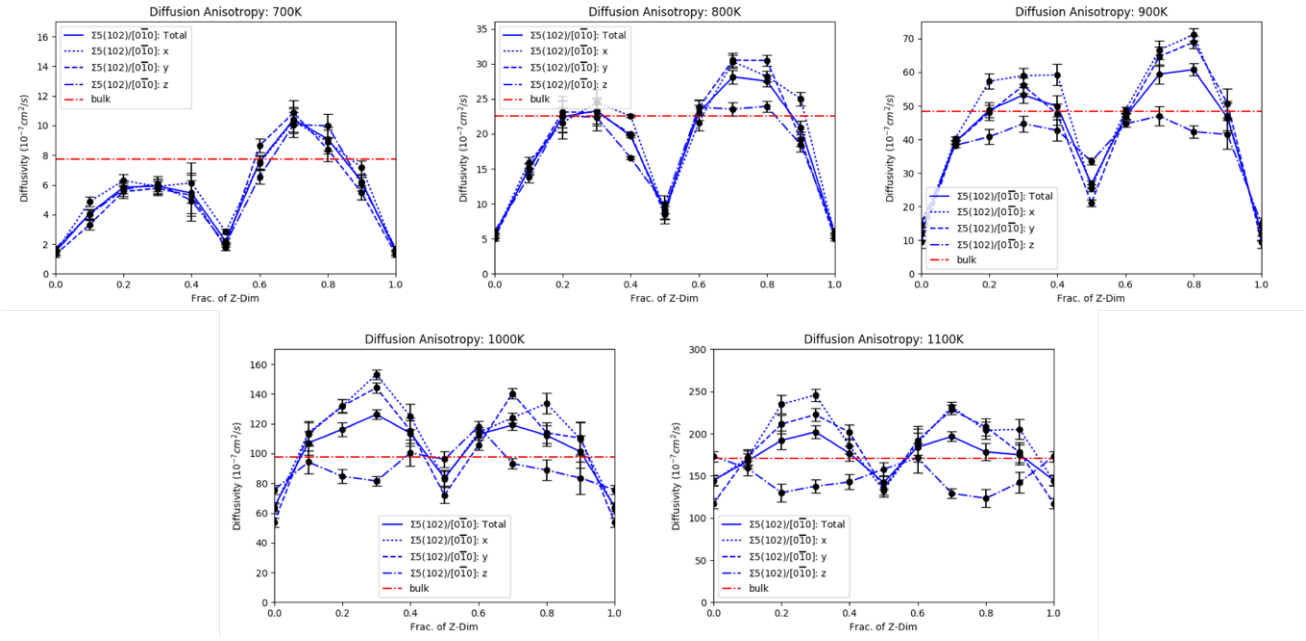


**Figure C.46** Total diffusivities and direction-specific diffusivities calculated at 700 K, 800 K, 900 K, 1000 K, and 1100 K for the $\Sigma5(102)/[0\bar{1}0]$ GB. The horizontal, red, dash-dotted line indicates the value of the bulk diffusivity at the indicated temperature.

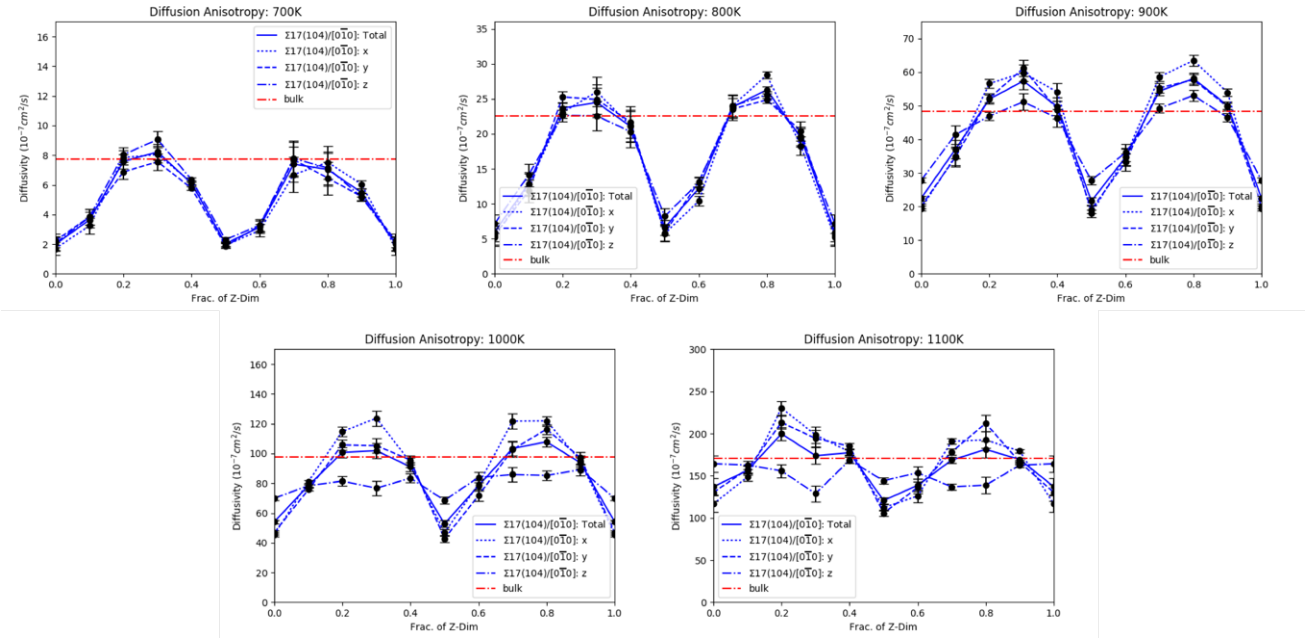


**Figure C.47** Total diffusivities and direction-specific diffusivities calculated at 700 K, 800 K, 900 K, 1000 K, and 1100 K for the Σ17(104)/[0$\bar{1}$0] GB. The horizontal, red, dash-dotted line indicates the value of the bulk diffusivity at the indicated temperature.

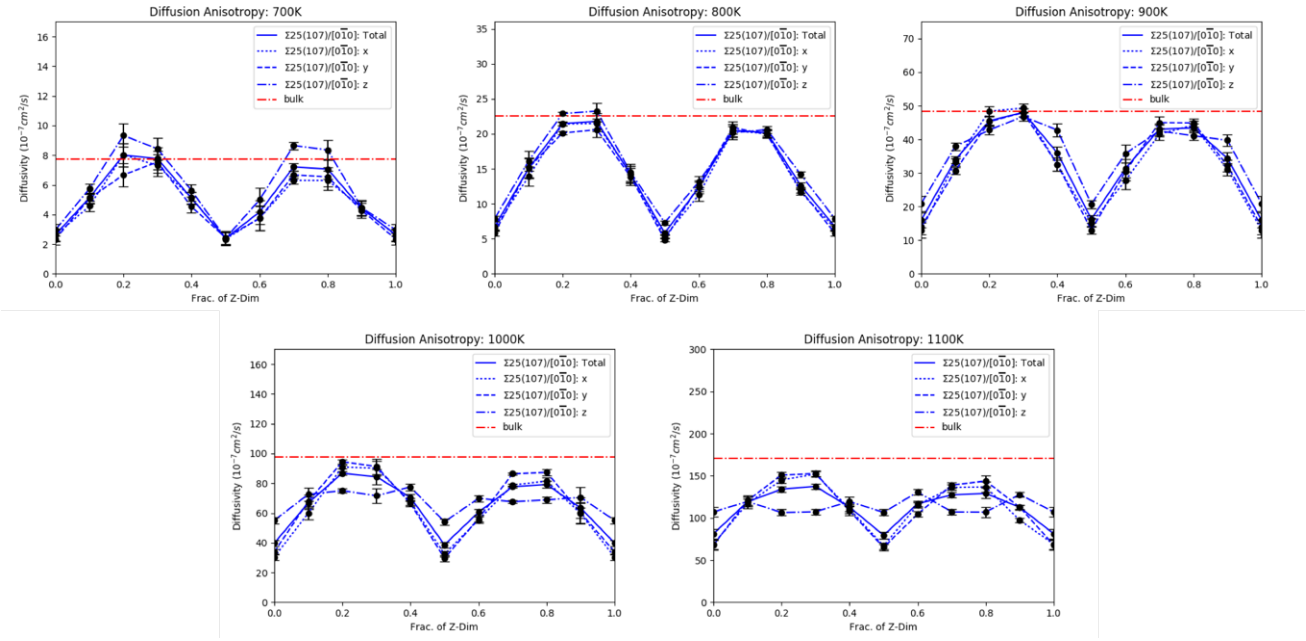


**Figure C48** Total diffusivities and direction-specific diffusivities calculated at 700 K, 800 K, 900 K, 1000 K, and 1100 K for the $\Sigma25(107)/[0\bar{1}0]$ GB. The horizontal, red, dash-dotted line indicates the value of the bulk diffusivity at the indicated temperature.

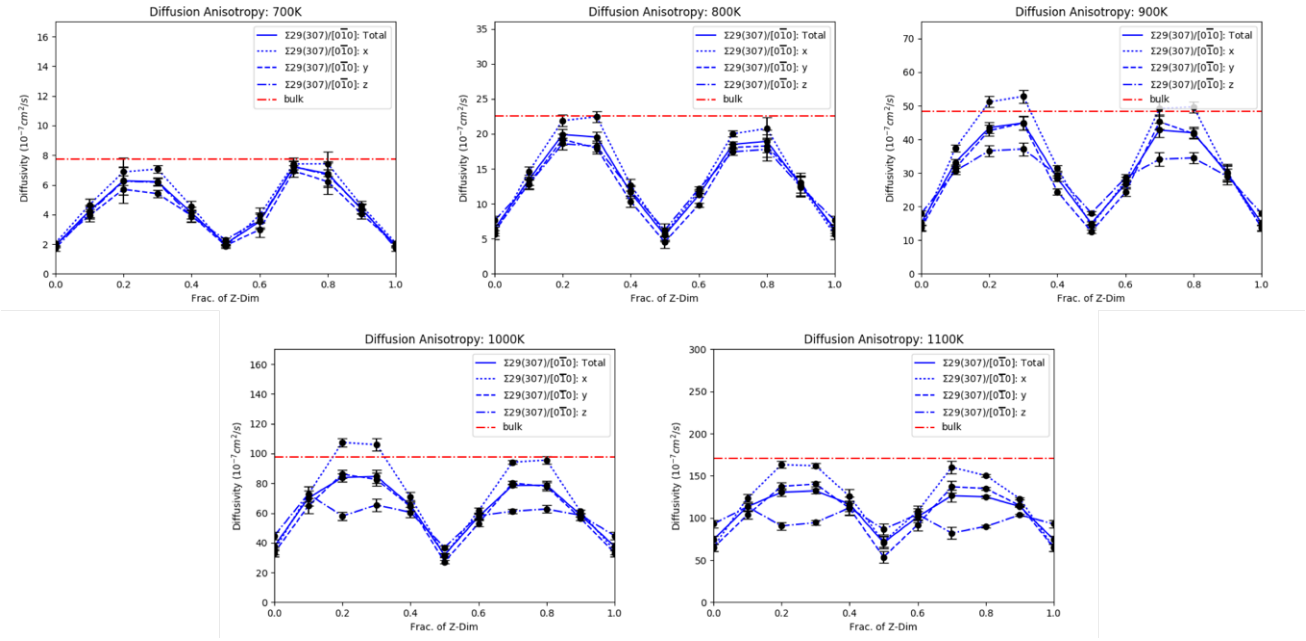


**Figure C.49** Total diffusivities and direction-specific diffusivities calculated at 700 K, 800 K, 900 K, 1000 K, and 1100 K for the $\Sigma 29(307)/[0\bar{1}0]$ GB. The horizontal, red, dash-dotted line indicates the value of the bulk diffusivity at the indicated temperature.

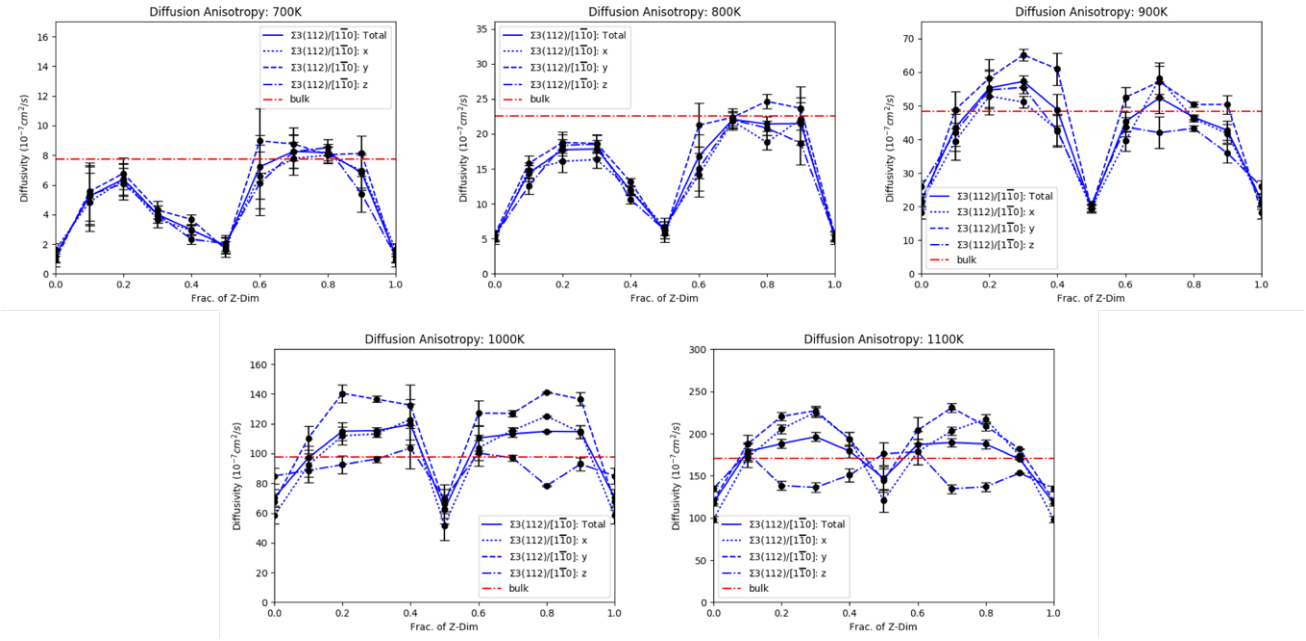


**Figure C.50** Total diffusivities and direction-specific diffusivities calculated at 700 K, 800 K, 900 K, 1000 K, and 1100 K for the $\Sigma3(112)/[1\bar{1}0]$ GB. The horizontal, red, dash-dotted line indicates the value of the bulk diffusivity at the indicated temperature.

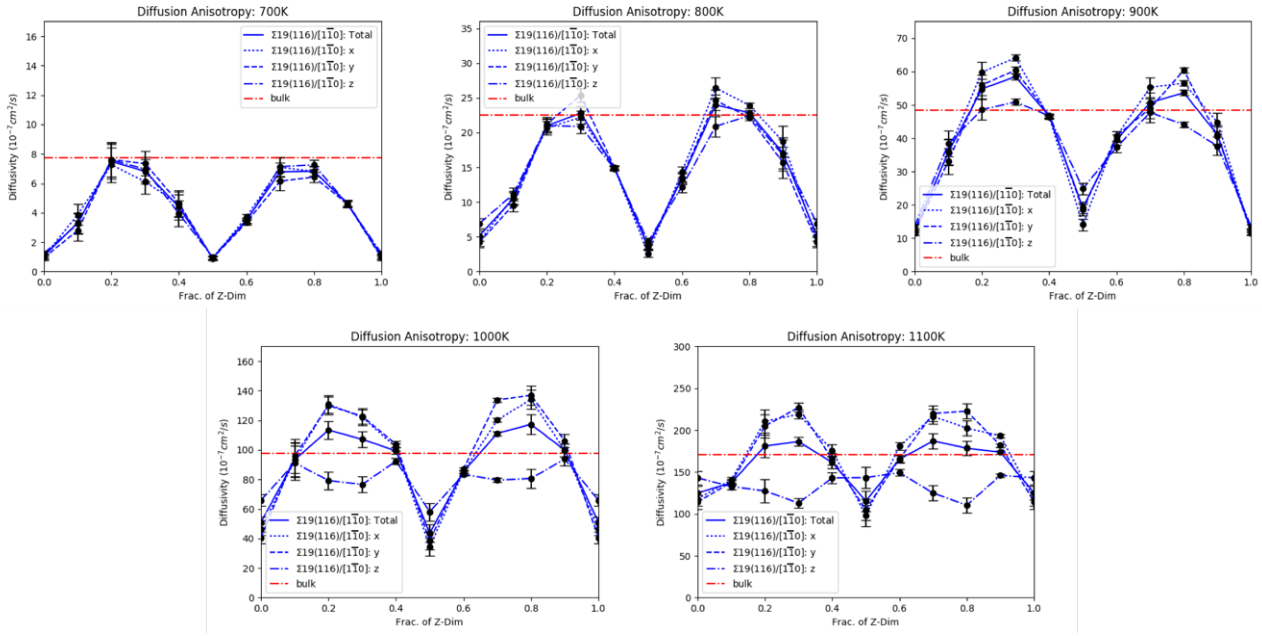


**Figure C.51** Total diffusivities and direction-specific diffusivities calculated at 700 K, 800 K, 900 K, 1000 K, and 1100 K for the $\Sigma19(116)/[1\bar{1}0]$ GB. The horizontal, red, dash-dotted line indicates the value of the bulk diffusivity at the indicated temperature.

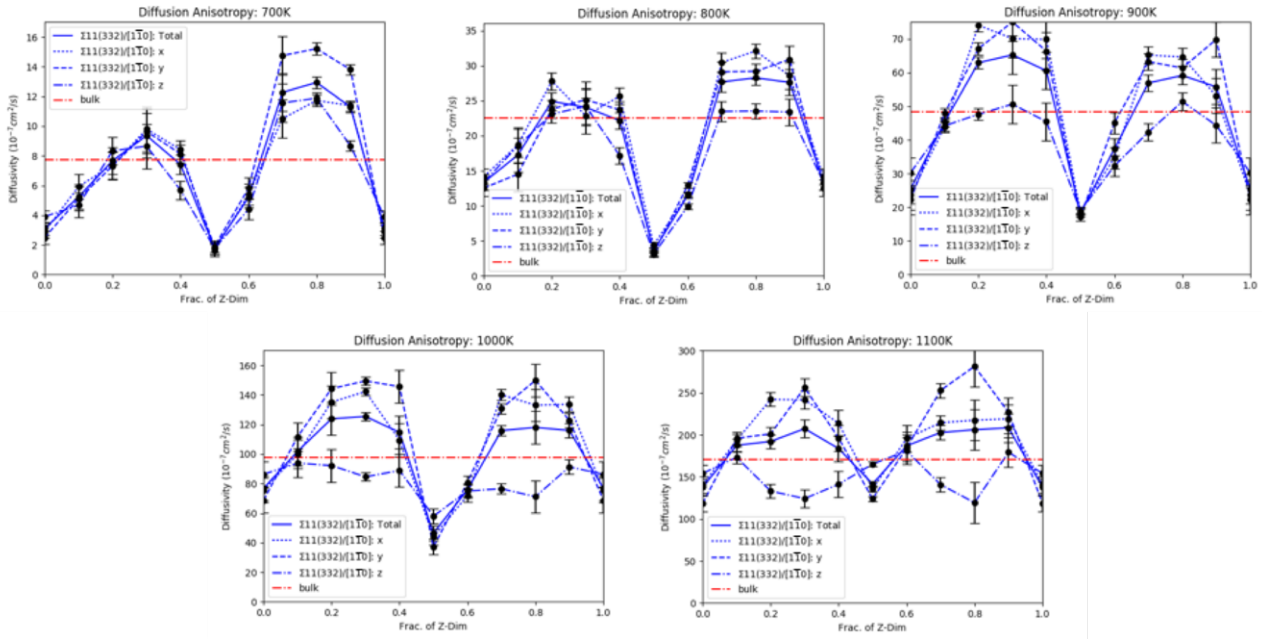


**Figure C.52** Total diffusivities and direction-specific diffusivities calculated at 700 K, 800 K, 900 K, 1000 K, and 1100 K for the $\Sigma 11(332)/[1\bar{1}0]$ GB. The horizontal, red, dash-dotted line indicates the value of the bulk diffusivity at the indicated temperature.

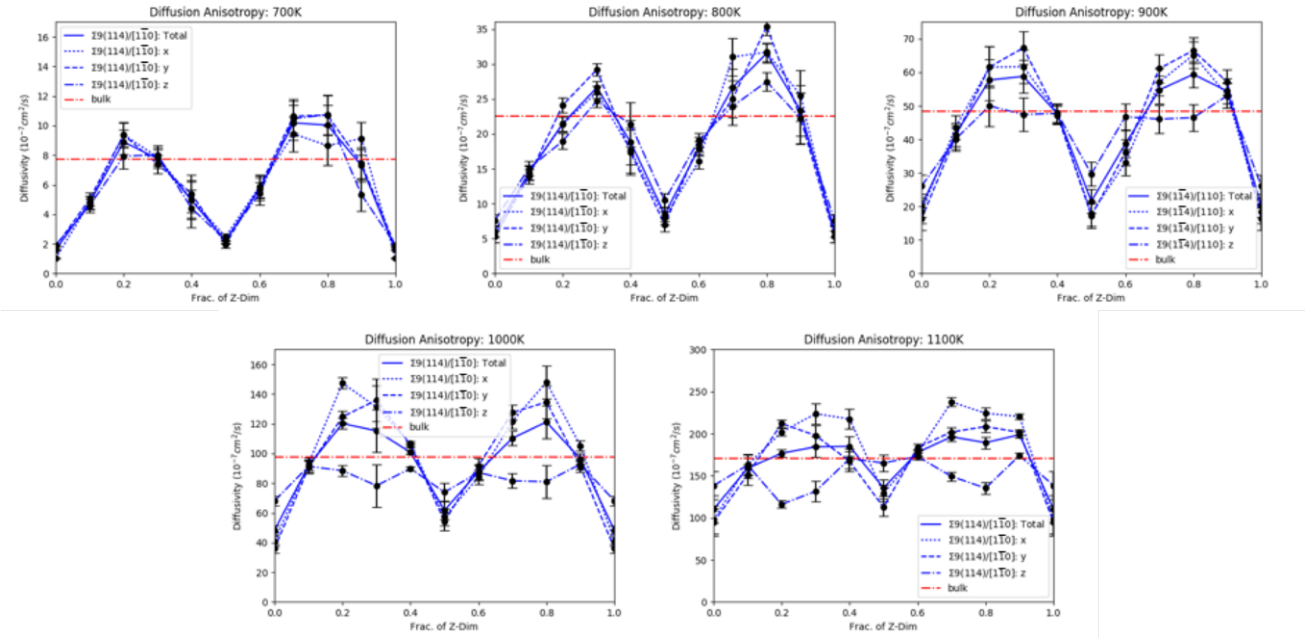


**Figure C.53** Total diffusivities and direction-specific diffusivities calculated at 700 K, 800 K, 900 K, 1000 K, and 1100 K for the $\Sigma 9(114)/[1\bar{1}0]$ GB. The horizontal, red, dash-dotted line indicates the value of the bulk diffusivity at the indicated temperature.

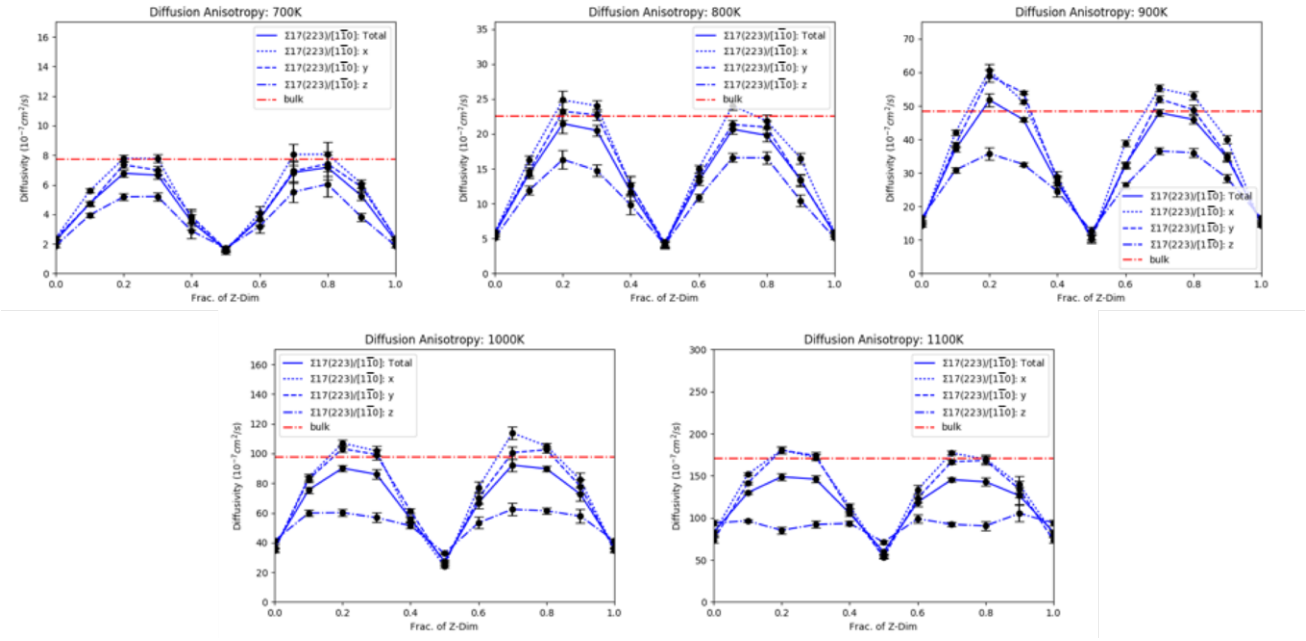


**Figure C.54** Total diffusivities and direction-specific diffusivities calculated at 700 K, 800 K, 900 K, 1000 K, and 1100 K for the Σ17(223)/[1$\bar{1}$0] GB. The horizontal, red, dash-dotted line indicates the value of the bulk diffusivity at the indicated temperature.

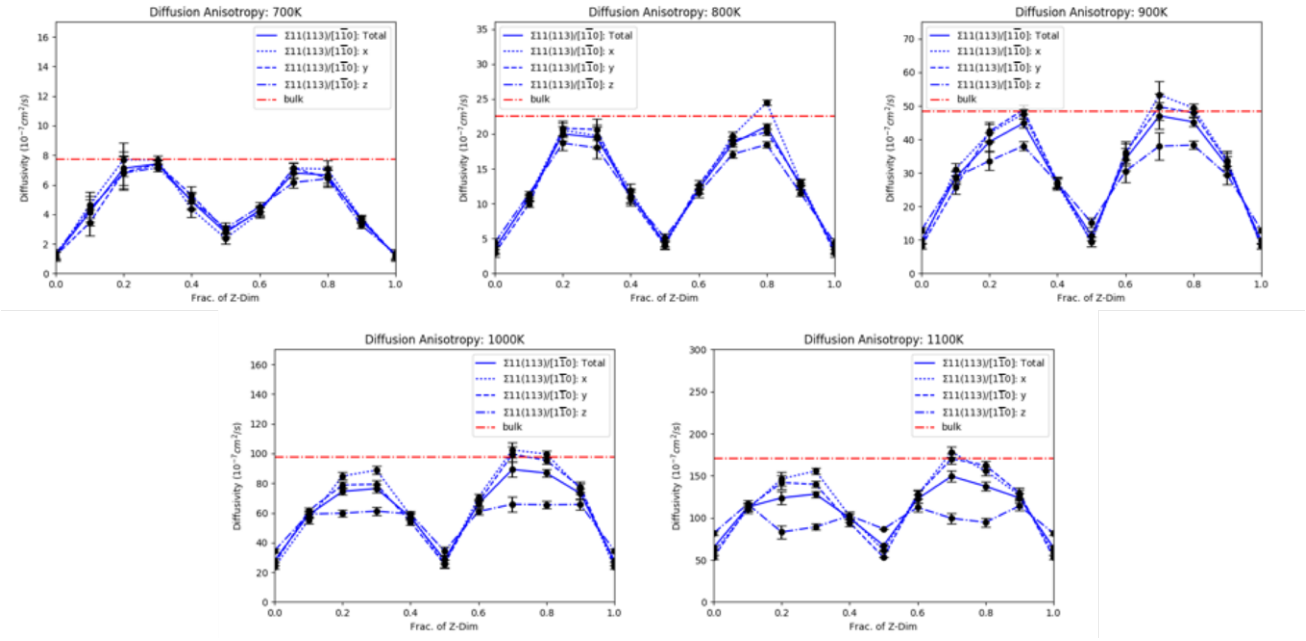


**Figure C.55** Total diffusivities and direction-specific diffusivities calculated at 700 K, 800 K, 900 K, 1000 K, and 1100 K for the $\Sigma 11(113)/[1\bar{1}0]$ GB. The horizontal, red, dash-dotted line indicates the value of the bulk diffusivity at the indicated temperature.

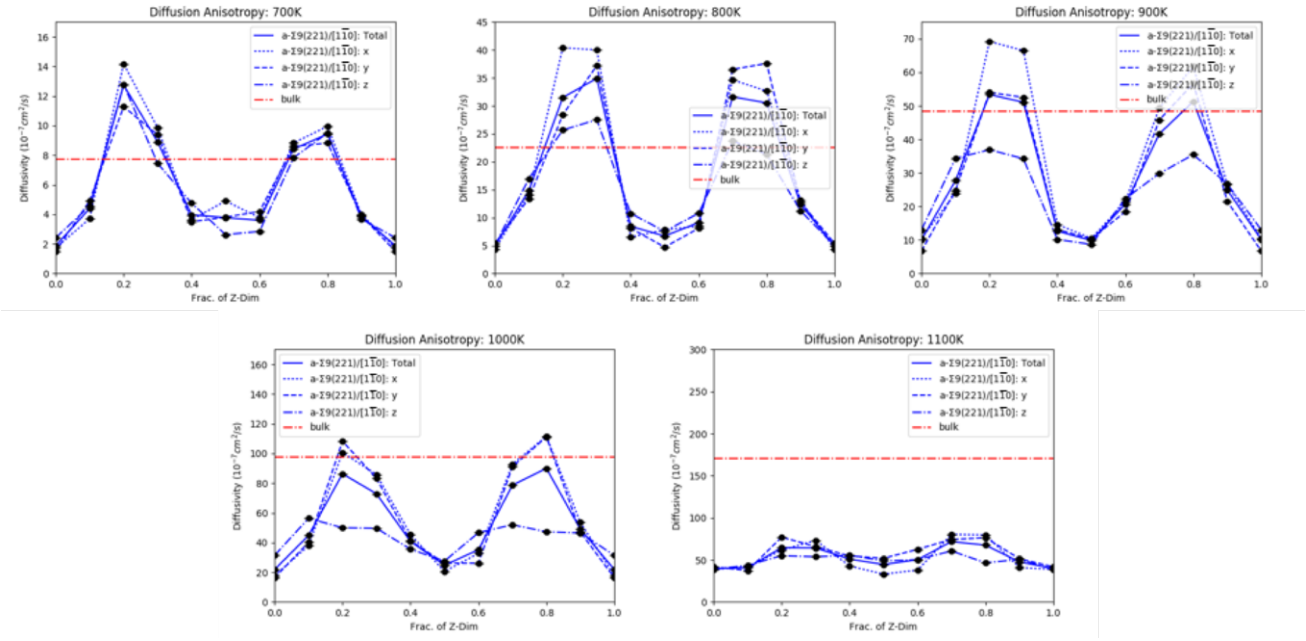


**Figure C.56** Total diffusivities and direction-specific diffusivities calculated at 700 K, 800 K, 900 K, 1000 K, and 1100 K for the a-Σ9(221)/[1$\bar{1}$0] GB. The horizontal, red, dash-dotted line indicates the value of the bulk diffusivity at the indicated temperature.

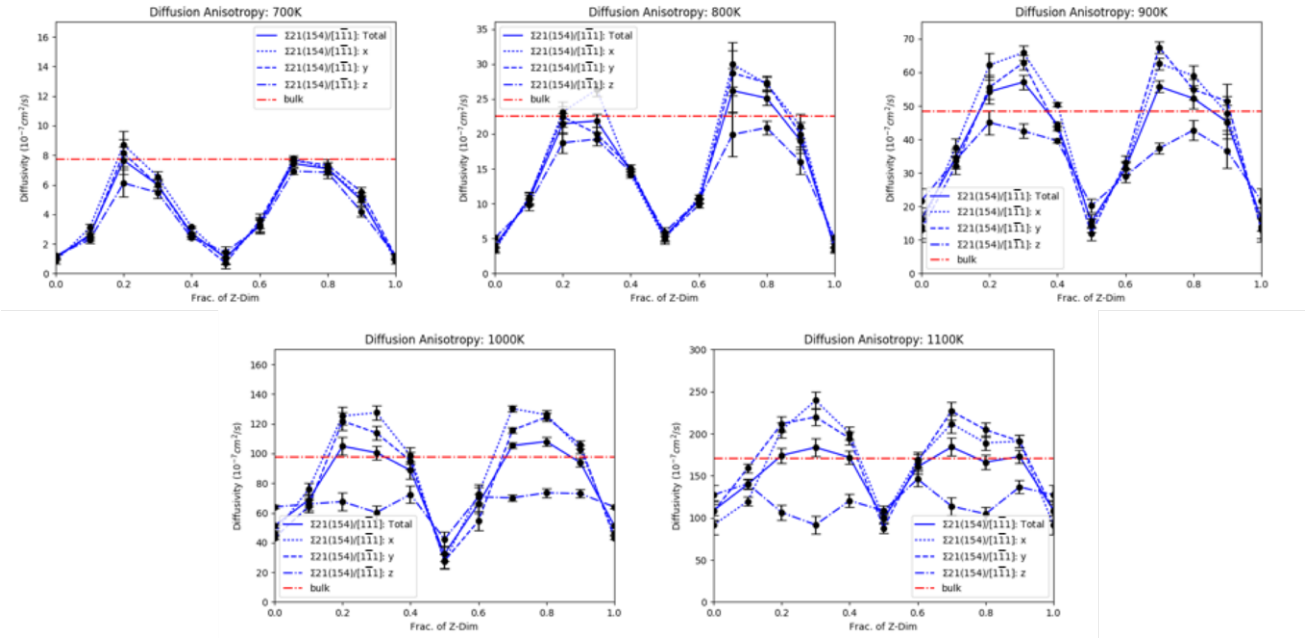


**Figure C.57** Total diffusivities and direction-specific diffusivities calculated at 700 K, 800 K, 900 K, 1000 K, and 1100 K for the $\Sigma 21(154)/[1\bar{1}1]$ GB. The horizontal, red, dash-dotted line indicates the value of the bulk diffusivity at the indicated temperature.

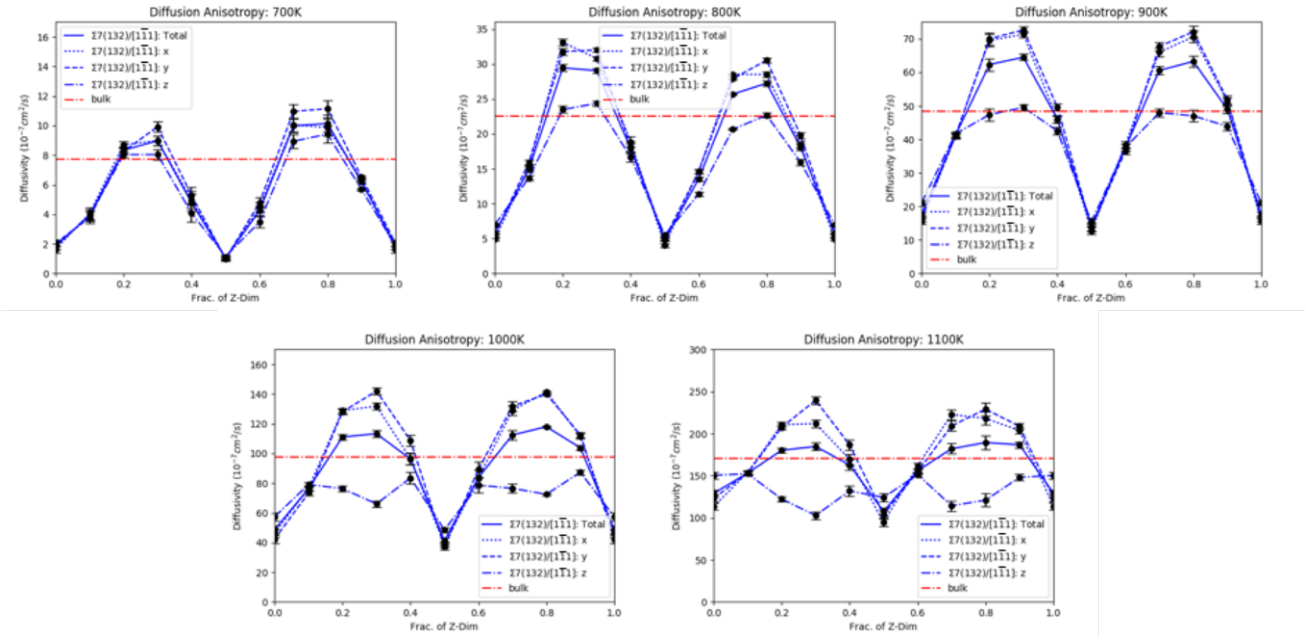


**Figure C.58** Total diffusivities and direction-specific diffusivities calculated at 700 K, 800 K, 900 K, 1000 K, and 1100 K for the $\Sigma7(132)/[1\bar{1}1]$ GB. The horizontal, red, dash-dotted line indicates the value of the bulk diffusivity at the indicated temperature.

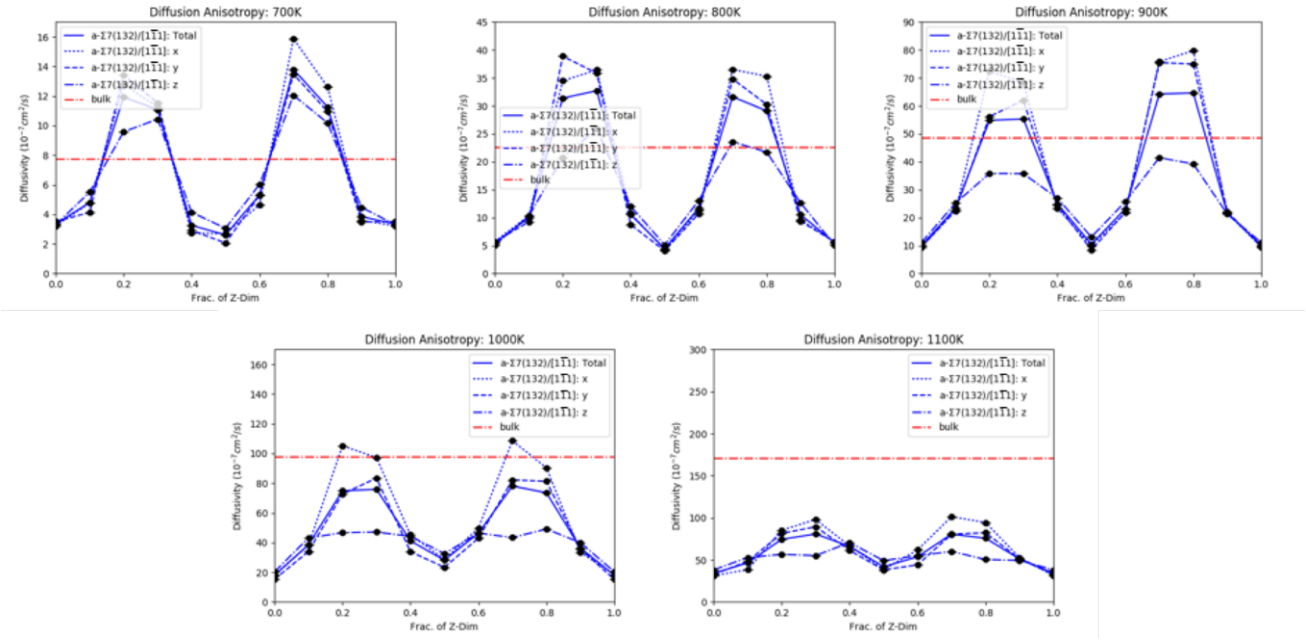


**Figure C.59** Total diffusivities and direction-specific diffusivities calculated at 700 K, 800 K, 900 K, 1000 K, and 1100 K for the a-Σ7(132)/[1$\bar{1}$1] GB. The horizontal, red, dash-dotted line indicates the value of the bulk diffusivity at the indicated temperature.

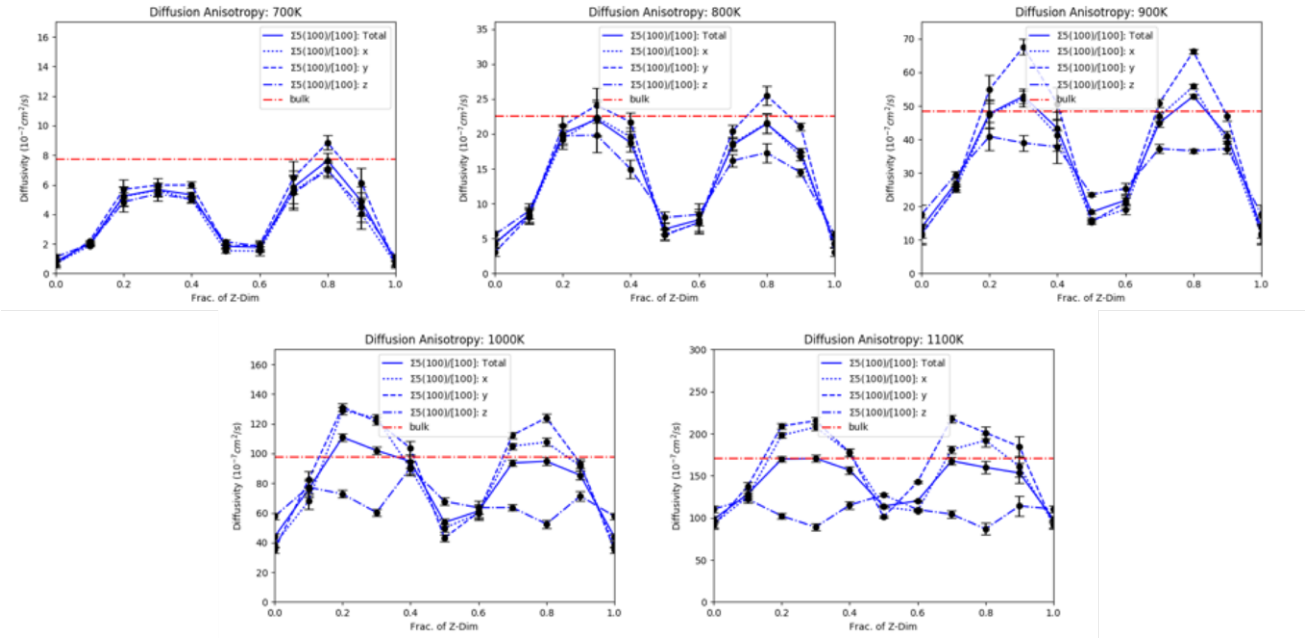


**Figure C.60** Total diffusivities and direction-specific diffusivities calculated at 700 K, 800 K, 900 K, 1000 K, and 1100 K for the $\Sigma 5(100)/[100]$ GB. The horizontal, red, dash-dotted line indicates the value of the bulk diffusivity at the indicated temperature.

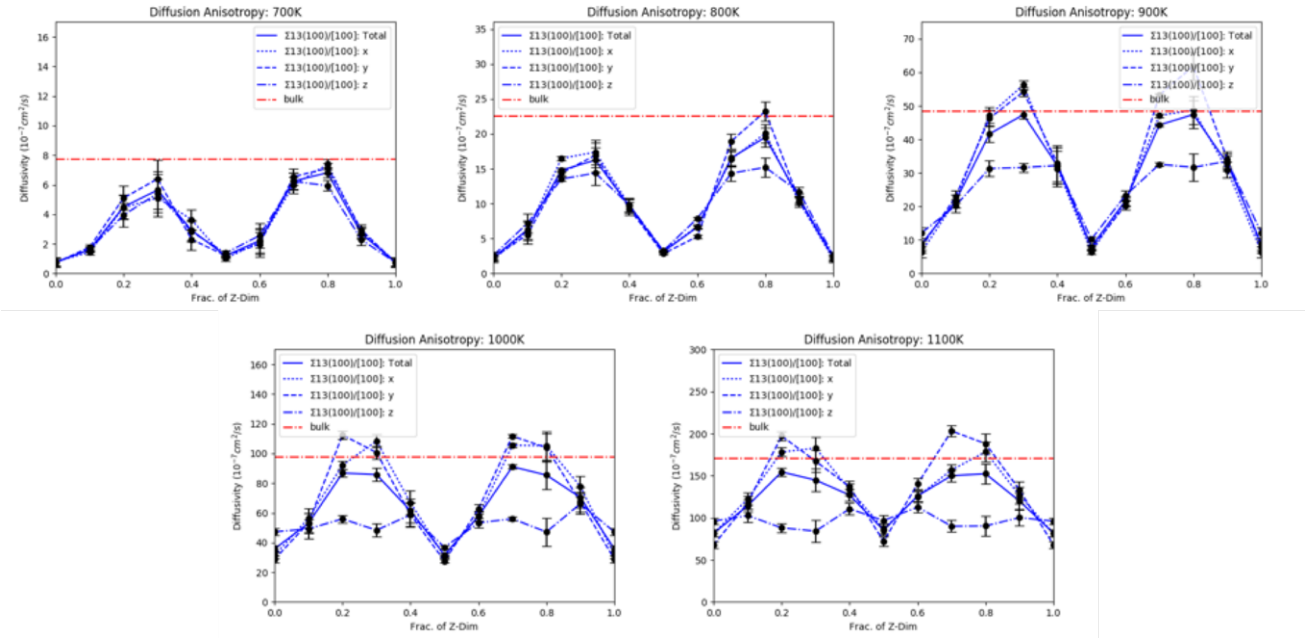


**Figure C.61** Total diffusivities and direction-specific diffusivities calculated at 700 K, 800 K, 900 K, 1000 K, and 1100 K for the Σ13(100)/[100] GB. The horizontal, red, dash-dotted line indicates the value of the bulk diffusivity at the indicated temperature.

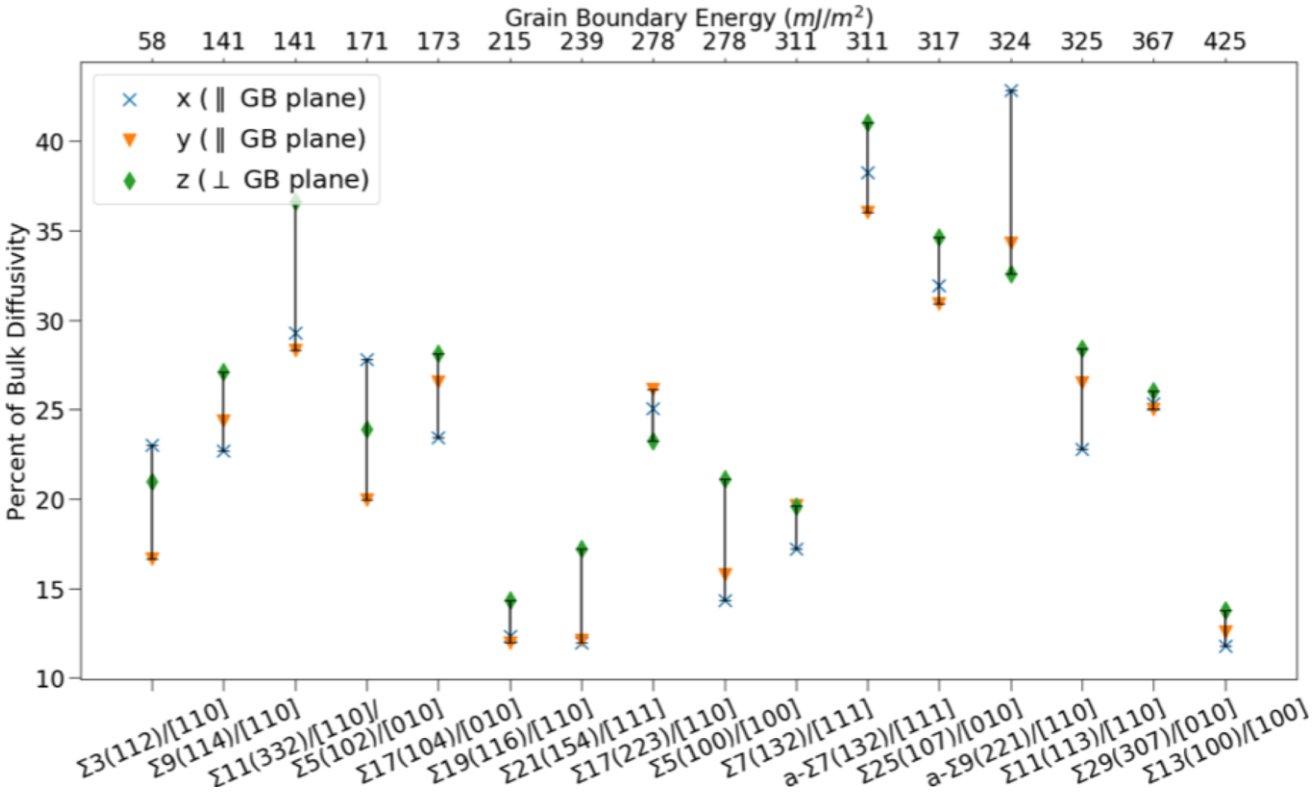


**Figure C.62** Anisotropic diffusivity per GB cell. Differences between the maximum and minimum diffusivities are indicated by the black, vertical lines, and are taken as a measure of anisotropy. Diffusivities in the x- and y-directions are indicated by blue x's and orange inverted triangles, respectively, while diffusivities in the z-direction is indicated by green diamonds. x- and y-directions are parallel to the GB plane; z-direction is normal to the GB plane.

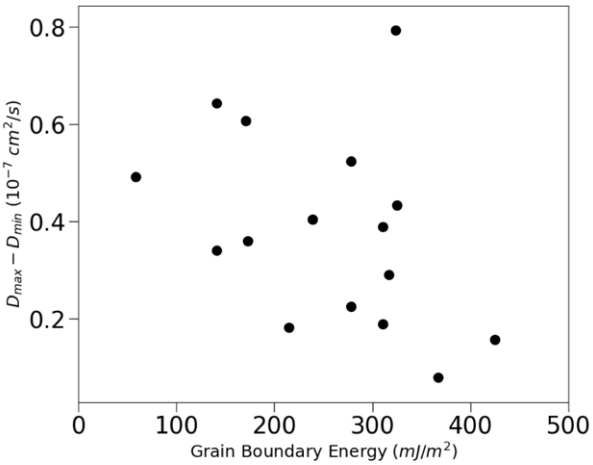


**Figure C.63** Diffusion anisotropy vs. GBE at 700 K. Diffusion anisotropy is defined as the difference between the maximum and minimum direction-specific diffusivity at each GB. The data yield a Pearson's correlation coefficient of r = -0.39.

## Bibliography


1. Chung, D.; Elgqvist, E.; Santhanagopalan, S., Automotive Lithium-ion Battery (LIB) Supply Chain and U.S. Competitiveness Considerations. U.S. Dept. of Energy, Clean Energy Manufacturing Analysis Center: 2015.
2. Batteries: 2019 Annual Progress Report. U.S. Dept. of Energy, Vehicle Technologies Office: 2019.
3. BU-205: Types of Lithium-ion. (accessed October 9, 2019).
4. Berg, E. J.; Villevieille, C.; Streich, D.; Trabesinger, S.; Novák, P., Rechargeable Batteries: Grasping for the Limits of Chemistry. *J. Electrochem. Soc.* **2015,** *162* (14), A2468-A2475.
5. Armand, M.; Tarascon, J. M., Building Better Batteries. *Nature* **2008,** *451*, 652-657.
6. Bruce, P. G.; Freunberger, S. A.; Hardwick, L. J.; Tarascon, J. M., Li-$O_2$ and Li-S Batteries with High Energy Storage. *Nat. Mater.* **2011,** *11* (1), 19-29.
7. Crabtree, G., The Joint Center for Energy Storage Research: A New Paradigm for Battery Research and Development. *AIP Conf. Proc.* **2015,** *1652* (1), 112-128.
8. van Noorden, R., The Rechargeable Revolution: A Better Battery. *Nature* 6 March 2014, pp 26-28.
9. Cox, P. A., *The Elements: Their Origin, Abundance, and Distribution*. Oxford University Press: Oxford, 1989.
10. Vanysek, P., Electrochemical Series. In *CRC Handbook of Chemistry and Physics*, 96 ed.; Haynes, W. M., Ed. CRC Press: Boca Raton, FL, 2015; p 79.
11. Huggins, R. A., *Advanced Batteries: Materials Science Aspects*. Springer: New York, 2009.
12. Bachman, J. C.; Muy, S.; Grimaud, A.; Chang, H. H.; Pour, N.; Lux, S. F.; Paschos, O.; Maglia, F.; Lupart, S.; Lamp, P.; Giordano, L.; Shao-Horn, Y., Inorganic Solid-State Electrolytes for Lithium Batteries: Mechanisms and Properties Governing Ion Conduction. *Chem. Rev.* **2016,** *116* (1), 140-162.
13. Kanno, R.; Hata, T.; Kawamoto, Y.; Irie, M., Synthesis of a New Lithium Ionic Conductor, Thio-LISICON–Lithium Germanium Sulfide System. *Solid State Ionics* **2000,** *130*, 97-104.
14. Muramatsu, H.; Hayashi, A.; Ohtomo, T.; Hama, S.; Tatsumisago, M., Structural Change of $Li_2S$–$P_2S_5$ Sulfide Solid Electrolytes in the Atmosphere. *Solid State Ionics* **2011,** *182* (1), 116-119.
15. Arbi, K.; Mandal, S.; Rojo, J. M.; Sanz, J., Dependence of Ionic Conductivity on Composition of Fast Ionic Conductors $Li_{1+x}Ti_{2-x}Al_x(PO_4)_3$, $0 \leq x \leq 0.7$. A Parallel NMR and Electric Impedance Study. *Chem. Mater.* **2002,** *14*, 1091-1097.
16. Hartmann, P.; Leichtweiss, T.; Busche, M. R.; Schneider, M.; Reich, M.; Sann, J.; Adelhelm, P.; Janek, J., Degradation of NASICON-Type Materials in Contact with Lithium Metal: Formation of Mixed Conducting Interphases (MCI) on Solid Electrolytes. *J. Phys. Chem.*

*C* **2013,** *117* (41), 21064-21074.

17. Yao, X.; Huang, B.; Yin, J.; Peng, G.; Huang, Z.; Gao, C.; Liu, D.; Xu, X., All-Solid-State Lithium Batteries with Inorganic Solid Electrolytes: Review of Fundamental Science. *Chin. Phys. B* **2016,** *25* (1), 018802.
18. Bohnke, O., The Fast Lithium-Ion Conducting Oxides $Li_{3x}La_{2/3-x}TiO_3$ from Fundamentals to Application. *Solid State Ionics* **2008,** *179* (1-6), 9-15.
19. Geiger, C. A.; Alekseev, E.; Lazic, B.; Fisch, M.; Armbruster, T.; Langner, R.; Fechtelkord, M.; Kim, N.; Pettke, T.; Weppner, W., Crystal Chemistry and Stability of "$Li_7La_3Zr_2O_{12}$" Garnet: A Fast Lithium-Ion Conductor. *Inorg. Chem.* **2011,** *50* (3), 1089-1097.
20. Murugan, R.; Thangadurai, V.; Weppner, W., Fast Lithium Ion Conduction in Garnet-Type $Li_7La_3Zr_2O_{12}$. *Angew. Chem. Int. Ed.* **2007,** *46* (41), 7778-7781.
21. Allen, J. L.; Wolfenstine, J.; Rangasamy, E.; Sakamoto, J., Effect of Substitution (Ta, Al, Ga) on the Conductivity of $Li_7La_3Zr_2O_{12}$. *J. Power Sources* **2012,** *206*, 315-319.
22. Rangasamy, E.; Wolfenstine, J.; Sakamoto, J., The Role of Al and Li Concentration on the Formation of Cubic Garnet Solid Electrolyte of Nominal Composition $Li_7La_3Zr_2O_{12}$. *Solid State Ionics* **2012,** *206*, 28-32.
23. Thompson, T.; Sharafi, A.; Johannes, M. D.; Huq, A.; Allen, J. L.; Wolfenstine, J.; Sakamoto, J., A Tale of Two Sites: On Defining the Carrier Concentration in Garnet-Based Ionic Conductors for Advanced Li Batteries. *Adv. Energy Mater.* **2015,** *5* (11).
24. Thompson, T.; Wolfenstine, J.; Allen, J. L.; Johannes, M.; Huq, A.; David, I. N.; Sakamoto, J., Tetragonal vs. Cubic Phase Stability in Al – Free Ta Doped $Li_7La_3Zr_2O_{12}$ (LLZO). *J. Mater. Chem. A* **2014,** *2* (33), 13431-13436.
25. Brandt, K., Historical Development of Secondary Lithium Batteries. *Solid State Ionics* **1994,** *69*, 173-183.
26. Whittingham, M. S., History, Evolution, and Future Status of Energy Storage. *Proc. IEEE* **2012,** *100* (Special Centennial Issue), 1518-1534.
27. https://www.sionpower.com/. (accessed October 10, 2019).
28. Li, Z.; Huang, J.; Yann Liaw, B.; Metzler, V.; Zhang, J., A Review of Lithium Deposition in Lithium-Ion and Lithium Metal Secondary Batteries. *J. Power Sources* **2014,** *254*, 168-182.
29. Xu, W.; Wang, J.; Ding, F.; Chen, X.; Nasybulin, E.; Zhang, Y.; Zhang, J.-G., Lithium Metal Anodes for Rechargeable Batteries. *Energy Environ. Sci.* **2014,** *7* (2), 513-537.
30. Aurbach, D., Review of Selected Electrode–Solution Interactions which Determine the Performance of Li and Li Ion Batteries. *J. Power Sources* **2000,** *89*, 206–218.
31. Stark, J. K.; Ding, Y.; Kohl, P. A., Dendrite-Free Electrodeposition and Reoxidation of Lithium-Sodium Alloy for Metal-Anode Battery. *J. Electrochem. Soc.* **2011,** *158* (10), A1100-A1105.
32. Yu, S.; Park, H.; Siegel, D. J., Thermodynamic Assessment of Coating Materials for Solid-State Li, Na, and K Batteries. *ACS Appl. Mater. Interfaces* **2019,** *11* (40), 36607-36615.
33. Christensen, J.; Albertus, P.; Sanchez-Carrera, R. S.; Lohmann, T.; Kozinsky, B.; Liedtke, R.; Ahmed, J.; Kojic, A., A Critical Review of Li/Air Batteries. *J. Electrochem. Soc.* **2012,** *159* (2), A2076-A2081.
34. Tutusaus, O.; Mohtadi, R.; Arthur, T. S.; Mizuno, F.; Nelson, E. G.; Sevryugina, Y. V., An Efficient Halogen-Free Electrolyte for Use in Rechargeable Magnesium Batteries. *Angew. Chem. Int. Ed.* **2015,** *54* (27), 7900-7904.

35. Gu, P.; Zheng, M.; Zhao, Q.; Xiao, X.; Xue, H.; Pang, H., Rechargeable Zinc–Air Batteries: A Promising Way to Green Energy. *J. Mater. Chem. A* **2017,** *5* (17), 7651-7666.
36. Lee, J.-S.; Tai Kim, S.; Cao, R.; Choi, N.-S.; Liu, M.; Lee, K. T.; Cho, J., Metal-Air Batteries with High Energy Density: Li-Air versus Zn-Air. *Adv. Energy Mater.* **2011,** *1* (1), 34-50.
37. Fang, G.; Zhou, J.; Pan, A.; Liang, S., Recent Advances in Aqueous Zinc-Ion Batteries. *ACS Energy Lett.* **2018,** *3* (10), 2480-2501.
38. Han, S.-D.; Kim, S.; Li, D.; Petkov, V.; Yoo, H. D.; Phillips, P. J.; Wang, H.; Kim, J. J.; More, K. L.; Key, B.; Klie, R. F.; Cabana, J.; Stamenkovic, V. R.; Fister, T. T.; Markovic, N. M.; Burrell, A. K.; Tepavcevic, S.; Vaughey, J. T., Mechanism of Zn Insertion into Nanostructured δ-MnO2: A Nonaqueous Rechargeable Zn Metal Battery. *Chem. Mater.* **2017,** *29* (11), 4874-4884.
39. Diggle, J. W.; Despic, A. R.; Bockris, J. O. M., The Mechanism of the Dendritic Electrocrystallization of Zinc. *J. Electrochem. Soc.* **1969,** *116* (11), 1503-1514.
40. Fu, J.; Cano, Z. P.; Park, M. G.; Yu, A.; Fowler, M.; Chen, Z., Electrically Rechargeable Zinc-Air Batteries: Progress, Challenges, and Perspectives. *Adv. Mater.* **2017,** *29* (7), 1604685.
41. Li, Y.; Dai, H., Recent Advances in Zinc-Air Batteries. *Chem. Soc. Rev.* **2014,** *43* (15), 5257-5275.
42. Liu, Z.; Abedin, S. Z. E.; Endres, F., Electrodeposition of Zinc Films from Ionic Liquids and Ionic Liquid/Water Mixtures. *Electrochim. Acta* **2013,** *89*, 635-643.
43. Liu, Z.; Zein El Abedin, S.; Ghazvini, M. S.; Endres, F., Electrochemical Synthesis of Vertically Aligned Zinc Nanowires Using Track-Etched Polycarbonate Membranes As Templates. *Phys. Chem. Chem. Phys.* **2013,** *15* (27), 11362-11367.
44. Liu, Z.; Cui, T.; Pulletikurthi, G.; Lahiri, A.; Carstens, T.; Olschewski, M.; Endres, F., Dendrite-Free Nanocrystalline Zinc Electrodeposition from an Ionic Liquid Containing Nickel Triflate for Rechargeable Zn-Based Batteries. *Angew. Chem. Int. Ed.* **2016,** *55*, 2889 - 2893.
45. http://www.phinergy.com/. (accessed March 19. 2018).
46. Li, Q.; Bjerrum, N. J., Aluminum as Anode for Energy Storage and Conversion: A Review. *J. Power Sources* **2002,** *110*, 1–10.
47. Matsuda, Y.; Ouchi, Y.; Tamura, H., Anodic Polarization of Aluminum in Organic Electrolytes. *J. Appl. Electrochem.* **1974,** *4* (1), 53-56.
48. Licht, S.; Levitin, G.; Yarnitzky, C.; Tel-Vered, R., The Organic Phase for Aluminum Batteries. *Electrochem. Solid-State Lett.* **1999,** *2* (6), 262-264.
49. Endres, F., Ionic Liquids: Solvents for the Electrodeposition of Metals and Semiconductors. *ChemPhysChem* **2002,** *3* (2), 144-154.
50. Jiang, T.; Brym, M. J. C.; Dube, G.; Lasia, A.; Brisard, G. M., Electrodeposition of Aluminium from Ionic Liquids: Part I - Electrodeposition and Surface Morphology of Aluminium from Aluminium Chloride (AlCl3)-l-Ethyl-3-Methylimidazolium Chloride ( EMImCl) Ionic Liquids. *Surf. Coat. Technol.* **2006,** *201* (1-2), 1-9.
51. Jiang, T.; Brym, M. J. C.; Dube, G.; Lasia, A.; Brisard, G. M., Electrodeposition of Aluminium from Ionic Liquids: Part II - Studies on the Electrodeposition of Aluminum from Aluminum Chloride (AICl(3)) - Trimethylphenylammonium Chloride (TMPAC) Ionic Liquids. *Surf. Coat. Technol.* **2006,** *201* (1-2), 10-18.
52. Nakayama, Y.; Senda, Y.; Kawasaki, H.; Koshitani, N.; Hosoi, S.; Kudo, Y.; Morioka, H.; Nagamine, M., Sulfone-Based Electrolytes for Aluminium Rechargeable Batteries. *Phys. Chem. Chem. Phys.* **2015,** *17* (8), 5758-5766.

53. Chen, H.; Xu, H.; Zheng, B.; Wang, S.; Huang, T.; Guo, F.; Gao, W.; Gao, C., Oxide Film Efficiently Suppresses Dendrite Growth in Aluminum-Ion Battery. *ACS Appl. Mater. Interfaces* **2017,** *9* (27), 22628-22634.
54. Gaddum, L. W.; French, H. E., The Electrolysis of Grignard Solutions. *J. Am. Chem. Soc.* **1927,** *39* (82), 1295-1299.
55. Genders, J. D.; Pletcher, D., Studies Using Microelectrodes of the Mg(II)/Mg Couple in Tetrahydrofuran and Propylene Carbonate. *J. Electroanal. Chem.* **1986,** *199*, 93-100.
56. Lu, Z.; Schechter, A.; Moshkovich, M.; Aurbach, D., On the Electrochemical Behavior of Magnesium Electrodes in Polar Aprotic Electrolyte Solutions. *J. Electroanal. Chem.* **1999,** *466*, 203–217.
57. Gregory, T. D.; Hoffman, R. J.; Winterton, R. C., Nonaqueous Electrochemistry of Magnesium Applications to Energy Storage. *J. Electrochem. Soc.* **1990,** *137* (3), 775-780.
58. Aurbach, D.; Lu, Z.; Schechter, A.; Gofer, Y.; Gizbar, H.; Turgeman, R.; Cohen, Y.; Moshkovich, M.; Levi, E., Prototype Systems for Rechargeable Magnesium Batteries. *Nature* **2000,** *407*, 724-726.
59. Aurbach, D.; Weissman, I.; Gofer, Y.; Levi, E., Nonaqueous Magnesium Electrochemistry and its Application in Secondary Batteries. *Chem. Rev.* **2003,** *3* (1), 61-73.
60. Matsui, M., Study on Electrochemically Deposited Mg Metal. *J. Power Sources* **2011,** *196* (16), 7048-7055.
61. Ha, S. Y.; Lee, Y. W.; Woo, S. W.; Koo, B.; Kim, J. S.; Cho, J.; Lee, K. T.; Choi, N. S., Magnesium(II) Bis(Trifluoromethane Sulfonyl) Imide-Based Electrolytes with Wide Electrochemical Windows for Rechargeable Magnesium Batteries. *ACS Appl. Mater. Interfaces* **2014,** *6* (6), 4063-4073.
62. Jackle, M.; Gross, A., Microscopic Properties of Lithium, Sodium, and Magnesium Battery Anode Materials Related to Possible Dendrite Growth. *J. Chem. Phys.* **2014,** *141* (17), 174710.
63. Aurbach, D.; Cohen, Y.; Moshkovich, M., The Study of Reversible Magnesium Deposition by In Situ Scanning Tunneling Microscopy. *Electrochem. Solid-State Lett.* **2001,** *4* (8), A113-A116.
64. Jäckle, M.; Helmbrecht, K.; Smits, M.; Stottmeister, D.; Groß, A., Self-Diffusion Barriers: Possible Descriptors for Dendrite Growth in Batteries? *Energy Environ. Sci.* **2018,** *11* (12), 3400-3407.
65. Muldoon, J.; Bucur, C. B.; Oliver, A. G.; Sugimoto, T.; Matsui, M.; Kim, H. S.; Allred, G. D.; Zajicek, J.; Kotani, Y., Electrolyte Roadblocks to a Magnesium Rechargeable Battery. *Energy Environ. Sci.* **2012,** *5* (3), 5941-5950.
66. Yoo, H. D.; Shterenberg, I.; Gofer, Y.; Gershinsky, G.; Pour, N.; Aurbach, D., Mg Rechargeable Batteries: An On-Going Challenge. *Energy Environ. Sci.* **2013,** *6* (8), 2265-2279.
67. Davidson, R.; Verma, A.; Santos, D.; Hao, F.; Fincher, C.; Xiang, S.; Van Buskirk, J.; Xie, K.; Pharr, M.; Mukherjee, P. P.; Banerjee, S., Formation of Magnesium Dendrites during Electrodeposition. *ACS Energy Lett.* **2018,** *4* (2), 375-376.
68. Ellis, B. L.; Nazar, L. F., Sodium and Sodium-Ion Energy Storage Batteries. *Curr. Opin. Solid State Mater. Sci.* **2012,** *16* (4), 168-177.
69. Palomares, V.; Casas-Cabanas, M.; Castillo-Martínez, E.; Han, M. H.; Rojo, T., Update on Na-Based Battery Materials. A Growing Research Path. *Energy Environ. Sci.* **2013,** *6* (8), 2312-2337.

70. Adelhelm, P.; Hartmann, P.; Bender, C. L.; Busche, M.; Eufinger, C.; Janek, J., From Lithium to Sodium: Cell Chemistry of Room Temperature Sodium-Air and Sodium-Sulfur Batteries. *Beilstein J. Nanotechnol.* **2015,** *6*, 1016-1055.
71. Hartmann, P.; Bender, C. L.; Vracar, M.; Durr, A. K.; Garsuch, A.; Janek, J.; Adelhelm, P., A Rechargeable Room-Temperature Sodium Superoxide ($NaO_2$) Battery. *Nat. Mater.* **2013,** *12* (3), 228-232.
72. Wu, J.; Liu, J.; Lu, Z.; Lin, K.; Lyu, Y.-Q.; Li, B.; Ciucci, F.; Kim, J.-K., Non-Flammable Electrolyte for Dendrite-Free Sodium-Sulfur Battery. *Energy Storage Materials* **2019,** *23*, 8-16.
73. Choudhury, S.; Wei, S.; Ozhabes, Y.; Gunceler, D.; Zachman, M. J.; Tu, Z.; Shin, J. H.; Nath, P.; Agrawal, A.; Kourkoutis, L. F.; Arias, T. A.; Archer, L. A., Designing Solid-Liquid Interphases for Sodium Batteries. *Nat. Commun.* **2017,** *8* (1), 898, 1-10.
74. Gao, H.; Xin, S.; Xue, L.; Goodenough, J. B., Stabilizing a High-Energy-Density Rechargeable Sodium Battery with a Solid Electrolyte. *Chem* **2018,** *4* (4), 833-844.
75. Ye, H.; Wang, C.-Y.; Zuo, T.-T.; Wang, P.-F.; Yin, Y.-X.; Zheng, Z.-J.; Wang, P.; Cheng, J.; Cao, F.-F.; Guo, Y.-G., Realizing a Highly Stable Sodium Battery with Dendrite-Free Sodium Metal Composite Anodes and $O_3$-Type Cathodes. *Nano Energy* **2018,** *48*, 369-376.
76. Sun, B.; Li, P.; Zhang, J.; Wang, D.; Munroe, P.; Wang, C.; Notten, P. H. L.; Wang, G., Dendrite-Free Sodium-Metal Anodes for High-Energy Sodium-Metal Batteries. *Adv. Mater.* **2018**, 1801334.
77. Ye, L.; Liao, M.; Zhao, T.; Sun, H.; Zhao, Y.; Sun, X.; Wang, B.; Peng, H., A Sodiophilic Interphase-Mediated, Dendrite-Free Anode with Ultrahigh Specific Capacity for Sodium-Metal Batteries. *Angew. Chem. Int. Ed.* **2019,** *131*, 17210-17216.
78. Ren, X.; Lau, K. C.; Yu, M.; Bi, X.; Kreidler, E.; Curtiss, L. A.; Wu, Y., Understanding Side Reactions in K-$O_2$ Batteries for Improved Cycle Life. *ACS Appl. Mater. Interfaces* **2014,** *6* (21), 19299-19307.
79. Ren, X.; Wu, Y., A Low-Overpotential Potassium-Oxygen Battery Based on Potassium Superoxide. *J. Am. Chem. Soc.* **2013,** *135* (8), 2923-2926.
80. Zhao, Q.; Hu, Y.; Zhang, K.; Chen, J., Potassium-Sulfur Batteries: A New Member of Room-Temperature Rechargeable Metal-Sulfur Batteries. *Inorg. Chem.* **2014,** *53* (17), 9000-9005.
81. Xiao, N.; McCulloch, W. D.; Wu, Y., Reversible Dendrite-Free Potassium Plating and Stripping Electrochemistry for Potassium Secondary Batteries. *J. Am. Chem. Soc.* **2017,** *139* (28), 9475-9478.
82. Peled, E.; Meitav, A.; Brand, M., Calcium Thionyl Chloride High-Rate Reserve Cell. *J. Electrochem. Soc.* **1981,** *128* (9), 1936-1938.
83. Babai, M.; Pallivathikal, M., Comparison of the Behavior of the Li/$SOCl_2$ and Ca/$SOCI_2$ Systems at Elevated Temperatures. *J. Power Sources* **1989,** *28*, 325 - 334.
84. Wade, W. L.; Walker, C. W.; Binder, M., Performance of Calcium/Thionyl Chloride Cells Containing $Sr(AlCl_4)_2$ Electrolyte. *J. Power Sources* **1989,** *28*, 295 - 300.
85. Aurbach, D.; Skaletsky, R.; Gofer, Y., The Electrochemical Behavior of Calcium Electrodes in a Few Organic Electrolytes. *J. Electrochem. Soc.* **1991,** *138* (12), 3536-3545.
86. Ponrouch, A.; Frontera, C.; Barde, F.; Palacin, M. R., Towards a Calcium-Based Rechargeable Battery. *Nat. Mater.* **2016,** *15* (2), 169-172.
87. Wang, D.; Gao, X.; Chen, Y.; Jin, L.; Kuss, C.; Bruce, P. G., Plating and Stripping Calcium in an Organic Electrolyte. *Nat. Mater.* **2018,** *17* (1), 16-20.

88. Thangadurai, V.; Kaack, H.; Weppner, W. J. F., Novel Fast Lithium Ion Conduction in Garnet-Type $Li_5La_3M_2O_{12}$ (M = Nb, Ta). *J. Am. Ceram. Soc.* **2003,** *86* (3), 437-440.
89. Bernstein, N.; Johannes, M. D.; Hoang, K., Origin of the Structural Phase Transition in $Li_7La_3Zr_2O_{12}$. *Phys. Rev. Lett.* **2012,** *109* (20), 205702.
90. Thompson, T.; Yu, S.; Williams, L.; Schmidt, R. D.; Garcia-Mendez, R.; Wolfenstine, J.; Allen, J. L.; Kioupakis, E.; Siegel, D. J.; Sakamoto, J., Electrochemical Window of the Li-Ion Solid Electrolyte $Li_7La_3Zr_2O_{12}$. *ACS Energy Lett.* **2017,** *2* (2), 462-468.
91. Xie, H.; Alonso, J. A.; Li, Y.; Fernández-Díaz, M. T.; Goodenough, J. B., Lithium Distribution in Aluminum-Free Cubic $Li_7La_3Zr_2O_{12}$. *Chem. Mater.* **2011,** *23* (16), 3587-3589.
92. Awaka, J.; Kijima, N.; Hayakawa, H.; Akimoto, J., Synthesis and Structure Analysis of Tetragonal $Li_7La_3Zr_2O_{12}$ with the Garnet-Related Type Structure. *J. Solid State Chem.* **2009,** *182* (8), 2046-2052.
93. Logéat, A.; Köhler, T.; Eisele, U.; Stiaszny, B.; Harzer, A.; Tovar, M.; Senyshyn, A.; Ehrenberg, H.; Kozinsky, B., From Order to Disorder: The Structure of Lithium-Conducting Garnets $Li_{7-x}La_3Ta_xZr_{2-x}O_{12}$ (x=0–2). *Solid State Ionics* **2012,** *206*, 33-38.
94. Cussen, E. J., Structure and Ionic Conductivity in Lithium Garnets. *J. Mater. Chem.* **2010,** *20* (25), 5167-5173.
95. O'Callaghan, M. P.; Lynham, D. R.; Cussen, E. J.; Chen, G. Z., Structure and Ionic-Transport Properties of Lithium-Containing Garnets $Li_3Ln_3Te_2O_{12}$ (Ln = Y, Pr, Nd, Sm-Lu). *Chem. Mater.* **2006,** *18*, 4681-4689.
96. Xu, M.; Park, M. S.; Lee, J. M.; Kim, T. Y.; Park, Y. S.; Ma, E., Mechanisms of $Li^+$ Transport in Garnet-Type Cubic $Li_{3+x}La_3M_2O_{12}$(M= Te, Nb, Zr). *Phys. Rev. B* **2012,** *85* (5), 052301.
97. Gamburg, Y. D.; Zangari, G., *Theory and Practice of Metal Electrodeposition*. 2011; p 1-378.
98. Liu, X. W.; Li, W. W.; Yu, H. Q., Cathodic Catalysts in Bioelectrochemical Systems for Energy Recovery from Wastewater. *Chem. Soc. Rev.* **2014,** *43* (22), 7718-7745.
99. Sharafi, A.; Kazyak, E.; Davis, A. L.; Yu, S.; Thompson, T.; Siegel, D. J.; Dasgupta, N. P.; Sakamoto, J., Surface Chemistry Mechanism of Ultra-Low Interfacial Resistance in the Solid-State Electrolyte $Li_7La_3Zr_2O_{12}$. *Chem. Mater.* **2017,** *29* (18), 7961-7968.
100. Sharafi, A.; Yu, S.; Naguib, M.; Lee, M.; Ma, C.; Meyer, H. M.; Nanda, J.; Chi, M.; Siegel, D. J.; Sakamoto, J., Impact of Air Exposure and Surface Chemistry on Li– $Li_7La_3Zr_2O_{12}$ Interfacial Resistance. *J. Mater. Chem. A* **2017,** *5*, 13475–13487.
101. Hirai, T.; Yoshimatsu, I.; Yamaki, J.-i., Influence of Electrolyte on Lithium Cycling Efficiency with Pressurized Electrode Stack. *J. Electrochem. Soc.* **1994,** *141* (3), 611-614.
102. Monroe, C.; Newman, J., The Impact of Elastic Deformation on Deposition Kinetics at Lithium/Polymer Interfaces. *J. Electrochem. Soc.* **2005,** *152* (2), A396-A404.
103. Cheng, E. J.; Sharafi, A.; Sakamoto, J., Intergranular Li Metal Propagation through Polycrystalline $Li_{6.25}Al_{0.25}La_3Zr_2O_{12}$ Ceramic Electrolyte. *Electrochim. Acta* **2017,** *223*, 85-91.
104. Ishiguro, K.; Nakata, Y.; Matsui, M.; Uechi, I.; Takeda, Y.; Yamamoto, O.; Imanishi, N., Stability of Nb-Doped Cubic $Li_7La_3Zr_2O_{12}$ with Lithium Metal. *J. Electrochem. Soc.* **2013,** *160* (10), A1690-A1693.
105. Ishiguro, K.; Nemori, H.; Sunahiro, S.; Nakata, Y.; Sudo, R.; Matsui, M.; Takeda, Y.; Yamamoto, O.; Imanishi, N., Ta-Doped $Li_7La_3Zr_2O_{12}$ for Water-Stable Lithium Electrode of Lithium-Air Batteries. *J. Electrochem. Soc.* **2014,** *161* (5), A668-A674.

106. Nagao, M.; Hayashi, A.; Tatsumisago, M.; Kanetsuku, T.; Tsuda, T.; Kuwabata, S., In Situ SEM Study of a Lithium Deposition and Dissolution Mechanism in a Bulk-Type Solid-State Cell with a $Li_2S$-$P_2S_5$ Solid Electrolyte. *Phys. Chem. Chem. Phys.* **2013,** *15* (42), 18600-6.
107. Porz, L.; Swamy, T.; Sheldon, B. W.; Rettenwander, D.; Frömling, T.; Thaman, H. L.; Berendts, S.; Uecker, R.; Carter, W. C.; Chiang, Y.-M., Mechanism of Lithium Metal Penetration through Inorganic Solid Electrolytes. *Adv. Energy Mater.* **2017,** *7* (20), 1701003.
108. Ren, Y.; Shen, Y.; Lin, Y.; Nan, C.-W., Direct Observation of Lithium Dendrites inside Garnet-Type Lithium-Ion Solid Electrolyte. *Electrochem. Commun.* **2015,** *57*, 27-30.
109. Sudo, R.; Nakata, Y.; Ishiguro, K.; Matsui, M.; Hirano, A.; Takeda, Y.; Yamamoto, O.; Imanishi, N., Interface Behavior Between Garnet-Type Lithium-Conducting Solid Electrolyte and Lithium Metal. *Solid State Ionics* **2014,** *262*, 151-154.
110. Wu, B.; Wang, S.; Lochala, J.; Desrochers, D.; Liu, B.; Zhang, W.; Yang, J.; Xiao, J., The Role of the Solid Electrolyte Interphase Layer in Preventing Li Dendrite Growth in Solid-State Batteries. *Energy Environ. Sci.* **2018,** *11* (7), 1803-1810.
111. Wolfenstine, J.; Allen, J. L.; Sakamoto, J.; Siegel, D. J.; Choe, H., Mechanical Behavior of Li-Ion-Conducting Crystalline Oxide-Based Solid Electrolytes: A Brief Review. *Ionics* **2018,** *24* (5), 1271-1276.
112. David, I. N.; Thompson, T.; Wolfenstine, J.; Allen, J. L.; Sakamoto, J.; Viyas, B., Microstructure and Li-Ion Conductivity of Hot-Pressed Cubic $Li_7La_3Zr_2O_{12}$. *J. Am. Ceram. Soc.* **2015,** *98* (4), 1209-1214.
113. Sharafi, A.; Haslam, C. G.; Kerns, R. D.; Wolfenstine, J.; Sakamoto, J., Controlling and Correlating the Effect of Grain Size with the Mechanical and Electrochemical Properties of $Li_7La_3Zr_2O_{12}$ Solid-State Electrolyte. *J. Mater. Chem. A* **2017,** *5* (40), 21491-21504.
114. Hummelshoj, J. S.; Luntz, A. C.; Norskov, J. K., Theoretical Evidence for Low Kinetic Overpotentials in Li-$O_2$ Electrochemistry. *J. Chem. Phys.* **2013,** *138* (3), 034703.
115. Hohenberg, P.; Kohn, W., Inhomogeneous Electron Gas. *Phys. Rev.* **1964,** *136* (3B), B864-B871.
116. Kohn, W.; Sham, L. J., Self-Consistent Equations Including Exchange and Correlation Effects. *Phys. Rev.* **1965,** *140* (4A), A1133-A1138.
117. Perdew, J. P.; Zunger, A., Self-Interaction Correction to Density-Functional Approximations for Many-Electron Systems. *Phys. Rev. B* **1981,** *23* (10), 5048-5079.
118. Ceperley, D. M.; Alder, B. J., Ground State of the Electron Gas by a Stochastic Method. *Phys. Rev. Lett.* **1980,** *45* (7), 566-569.
119. Perdew, J. P.; Burke, K., Comparison Shopping for a Gradient-Corrected Density Functional. *Int. J. Quantum Chem.* **1996,** *57*, 309-319.
120. Perdew, J. P.; Burke, K.; Ernzerhof, M., Generalized Gradient Approximation Made Simple. *Phys. Rev. Lett.* **1996,** *77* (18), 3865-3868.
121. Kresse, G.; Furthmuller, J., Efficiency of *ab-initio* Total Energy Calculations for Metals and Semiconductors using a Plane-Wave Basis Set. *Comput. Mater. Sci.* **1996,** *6*, 15-50.
122. Kresse, G.; Furthmuller, J., Efficient Iterative Schemes for *ab initio* Total-Energy Calculations using a Plane-Wave Basis Set. *Phys. Rev. B* **1996,** *54* (16), 11169-11185.
123. Kresse, G.; Hafner, J., *Ab-Initio* Molecular-Dynamics for Liquid-Metals. *Phys. Rev. B* **1993,** *47* (1), 558-561.
124. Blöchl, P. E., Projector Augmented-Wave Method. *Phys. Rev. B* **1994,** *50* (24), 17953-17979.

125. Kresse, G.; Joubert, D., From Ultrasoft Pseudopotentials to the Projector Augmented-Wave Method. *Phys. Rev. B* **1999,** *59* (3), 1758-1775.
126. Pack, J. D.; Monkhorst, H. J., "Special Points for Brillouin-Zone Integrations"—A Reply. *Phys. Rev. B* **1977,** *16* (4), 1748-1749.
127. Allen, M. P.; Tildesley, D. J., *Computer Simulation of Liquids*. Oxford University Press: Oxford, 1987.
128. Chang, H.; Lim, C., Zinc Deposition During Charging Nickel/Zinc Batteries. *J. Power Sources* **1997,** *66*, 115-119.
129. Erdey-Gruz, T.; Volmer, M., The Theory of Hydrogen Overvoltage. *Z. Phys. Chem.* **1930,** *150* (3/4), 203-213.
130. Sahari, A.; Azizi, A.; Schmerber, G.; Dinia, A., Nucleation, Growth, and Morphological Properties of Electrodeposited Nickel Films from Different Baths. *Surf. Rev. Lett.* **2008,** *15* (6), 717-725.
131. Stephens, R. M.; Willis, M.; Alkire, R. C., Additive-Assisted Nucleation and Growth by Electrodeposition II. Mathematical Model and Comparison with Experimental Data. *J. Electrochem. Soc.* **2009,** *156* (10), D385-D394.
132. Sun, M. H.; Liao, H. G.; Niu, K. Y.; Zheng, H. M., Structural and Morphological Evolution of Lead Dendrites During Electrochemical Migration. *Sci. Rep.* **2013,** *3*, 1-6.
133. Willis, M.; Alkire, R., Additive-Assisted Nucleation and Growth by Electrodeposition I. Experimental Studies with Copper Seed Arrays on Gold Films. *J. Electrochem. Soc.* **2009,** *156* (10), D377-D384.
134. Ferrante, F.; Prestianni, A.; Cortese, R.; Schimmenti, R.; Duca, D., Density Functional Theory Investigation on the Nucleation of Homo and Heteronuclear Metal Clusters on Defective Graphene. *J. Phys. Chem. C* **2016,** *120* (22), 12022-12031.
135. Prestianni, A.; Ferrante, F.; Sulman, E. M.; Duca, D., Density Functional Theory Investigation on the Nucleation and Growth of Small Palladium Clusters on a Hyper-Cross-Linked Polystyrene Matrix. *J. Phys. Chem. C* **2014,** *118* (36), 21006-21013.
136. Saidi, W. A., Density Functional Theory Study of Nucleation and Growth of Pt Nanoparticles on $MoS_2$(001) Surface. *Cryst. Growth Des.* **2015,** *15* (2), 642-652.
137. Balluffi, R. W.; Allen, S. M.; Carter, W. C.; Kemper, R. A., *Kinetics of Materials*. Wiley-Interscience: Hoboken, N.J., 2005; p. 645.
138. Toschev, S.; Markov, I., Transient Nucleation in Electrodeposition of Mercury. *J. Cryst. Growth* **1968,** *3-4*, 436-440.
139. Murnaghan, F. D., The Compressibility of Media under Extreme Pressures. *Proc. Natl. Acad. Sci. U.S.A.* **1944,** *30*, 244-247.
140. Ledbetter, H. M., Elastic Properties of Zinc - Compilation and a Review. *J. Phys. Chem. Ref. Data* **1977,** *6* (4), 1181-1203.
141. Fiorentini, V.; Methfessel, M., Extracting Convergent Surface Energies from Slab Calculations. *J. Phys.: Condens. Matter* **1996,** *8*, 6525–6529.
142. Kittel, C., *Introduction to Solid State Physics*. 8th ed.; Wiley: Hoboken, NJ, 2005.
143. Simmons, G.; Wang, H., *Single Crystal Elastic Constants and Calculated Aggregate Properties: A Handbook*. M.I.T. Press: Cambridge, Mass., 1971.
144. Haas, P.; Tran, F.; Blaha, P., Calculation of the Lattice Constant of Solids with Semilocal Functionals. *Phys. Rev. B* **2009,** *79* (8), 085104.

145. Wedig, U.; Jansen, M.; Paulus, B.; Rosciszewski, K.; Sony, P., Structural and Electronic Properties of Mg, Zn, and Cd from Hartree-Fock and Density Functional Calculations Including Hybrid Functionals. *Phys. Rev. B* **2007,** *75* (20), 205123.
146. Anderson, M. S.; Swenson, C. A.; Peterson, D. T., Experimental Equations of State for Calcium, Strontium, and Barium Metals to 20-kbar from 4-K to 295-K. *Phys. Rev. B* **1990,** *41* (6), 3329-3338.
147. Kohn, W.; Mattsson, A. E., Edge Electron Gas. *Phys. Rev. Lett.* **1998,** *81* (16), 3487-3490.
148. Mattsson, A. E.; Kohn, W., An Energy Functional for Surfaces. *J. Chem. Phys.* **2001,** *115* (8), 3441-3443.
149. Mattsson, A. E.; Armiento, R.; Schultz, P. A.; Mattsson, T. R., Nonequivalence of the Generalized Gradient Approximations PBE and PW91. *Phys. Rev. B* **2006,** *73* (19), 195123.
150. Mattsson, T. R.; Mattsson, A. E., Calculating the Vacancy Formation Energy in Metals: Pt, Pd, and Mo. *Phys. Rev. B* **2002,** *66* (21), 214110.
151. Zucker, R. V.; Chatain, D.; Dahmen, U.; Hagège, S.; Carter, W. C., New Software Tools for the Calculation and Display of Isolated and Attached Interfacial-Energy Minimizing Particle Shapes. *J. Mater. Sci.* **2012,** *47* (24), 8290-8302.
152. Tyson, W. R.; Miller, W. A., Surface Free Energies of Solid Metals: Estimation from Liquid Surface Tension Measurements. *Surf. Sci.* **1977,** *62*, 267-276.
153. de Boer, F. R.; Boom, R.; Mattens, W. C. M.; Miedema, A. R.; Niessen, A. K., *Cohesion in Metals: Transition Metal Alloys*. North-Holland: Amsterdam, 1988.
154. Miedema, A. R., Surface Energies of Solid Metals. *Z. Metall.* **1978,** *69* (5), 287-292.
155. Miedema, A. R.; Boom, R., Surface-Tension and Electron-Density of Pure Liquid-Metals. *Z. Metall.* **1978,** *69* (3), 183-190.
156. Hayun, S.; Tran, T.; Ushakov, S. V.; Thron, A. M.; van Benthem, K.; Navrotsky, A.; Castro, R. H. R., Experimental Methodologies for Assessing the Surface Energy of Highly Hygroscopic Materials: The Case of Nanocrystalline Magnesia. *J. Phys. Chem. C* **2011,** *115* (48), 23929-23935.
157. Smith, J. G.; Naruse, J.; Hiramatsu, H.; Siegel, D. J., Theoretical Limiting Potentials in $Mg/O_2$ Batteries. *Chem. Mater.* **2016,** *28* (5), 1390-1401.
158. Feldbauer, G.; Wolloch, M.; Bedolla, P. O.; Mohn, P.; Redinger, J.; Vernes, A., Adhesion and Material Transfer Between Contacting Al and TiN Surfaces from First Principles. *Phys. Rev. B* **2015,** *91* (16), 165413.
159. Tran, R.; Xu, Z. H.; Radhakrishnan, B.; Winston, D.; Sun, W. H.; Persson, K. A.; Ong, S. P., Surface Energies of Elemental Crystals. *Sci. Data* **2016,** *3*, 1-10.
160. Wang, J.; Wang, S.-Q., Surface Energy and Work Function of FCC and BCC Crystals: Density Functional Study. *Surf. Sci.* **2014,** *630*, 216-224.
161. Fu, J.; Zhang, C.; Zhao, J., Gupta Potential for Alkaline Earth Metals: Calcium and Strontium. *Comput. Mater. Sci.* **2014,** *85*, 142-146.
162. Tyson, W. R., Surface Energies of Solid Metals. *Can. Metall. Q.* **1975,** *14* (4), 307-314.
163. Durand, W. J.; Peterson, A. A.; Studt, F.; Abild-Pedersen, F.; Norskov, J. K., Structure Effects on the Energetics of the Electrochemical Reduction of $CO_2$ by Copper Surfaces. *Surf. Sci.* **2011,** *605* (15-16), 1354-1359.
164. Ingram, D. B.; Linic, S., First-Principles Analysis of the Activity of Transition and Noble Metals in the Direct Utilization of Hydrocarbon Fuels at Solid Oxide Fuel Cell Operating Conditions. *J. Electrochem. Soc.* **2009,** *156* (12), B1457-B1465.

165. Norskov, J. K.; Rossmeisl, J.; Logadottir, A.; Lindquist, L.; Kitchin, J. R.; Bligaard, T.; Jonsson, H., Origin of the Overpotential for Oxygen Reduction at a Fuel-Cell Cathode. *J. Phys. Chem. B* **2004,** *108*, 17886-17892.
166. Man, I. C.; Su, H.-Y.; Calle-Vallejo, F.; Hansen, H. A.; Martínez, J. I.; Inoglu, N. G.; Kitchin, J.; Jaramillo, T. F.; Nørskov, J. K.; Rossmeisl, J., Universality in Oxygen Evolution Electrocatalysis on Oxide Surfaces. *ChemCatChem* **2011,** *3* (7), 1159-1165.
167. Rossmeisl, J.; Qu, Z. W.; Zhu, H.; Kroes, G. J.; Nørskov, J. K., Electrolysis of Water on Oxide Surfaces. *J. Electroanal. Chem.* **2007,** *607* (1-2), 83-89.
168. Mukherjee, J.; Linic, S., First-Principles Investigations of Electrochemical Oxidation of Hydrogen at Solid Oxide Fuel Cell Operating Conditions. *J. Electrochem. Soc.* **2007,** *154* (9), B919-B924.
169. Peterson, A. A.; Abild-Pedersen, F.; Studt, F.; Rossmeisl, J.; Norskov, J. K., How Copper Catalyzes the Electroreduction of Carbon Dioxide into Hydrocarbon Fuels. *Energy Environ. Sci.* **2010,** *3* (9), 1311-1315.
170. Viswanathan, V.; Hansen, H. A.; Rossmeisl, J.; Nørskov, J. K., Universality in Oxygen Reduction Electrocatalysis on Metal Surfaces. *ACS Catal.* **2012,** *2* (8), 1654-1660.
171. Tang, J.-J.; Yang, X.-B.; OuYang, L.; Zhu, M.; Zhao, Y.-J., A Systematic First-Principles Study of Surface Energies, Surface Relaxation and Friedel Oscillation of Magnesium Surfaces. *J. Phys. D: Appl. Phys.* **2014,** *47* (11), 115305.
172. Girishkumar, G.; McCloskey, B.; Luntz, A. C.; Swanson, S.; Wilcke, W., Lithium−Air Battery: Promise and Challenges. *J. Phys. Chem. Lett.* **2010,** *1* (14), 2193-2203.
173. Hummelshoj, J. S.; Blomqvist, J.; Datta, S.; Vegge, T.; Rossmeisl, J.; Thygesen, K. S.; Luntz, A. C.; Jacobsen, K. W.; Norskov, J. K., Communications: Elementary Oxygen Electrode Reactions in the Aprotic Li-Air Battery. *J. Chem. Phys.* **2010,** *132* (7), 071101.
174. Siahrostami, S.; Tripkovic, V.; Lundgaard, K. T.; Jensen, K. E.; Hansen, H. A.; Hummelshoj, J. S.; Myrdal, J. S.; Vegge, T.; Norskov, J. K.; Rossmeisl, J., First Principles Investigation of Zinc-Anode Dissolution in Zinc-Air Batteries. *Phys. Chem. Chem. Phys.* **2013,** *15* (17), 6416-6421.
175. Viswanathan, V.; Norskov, J. K.; Speidel, A.; Scheffler, R.; Gowda, S.; Luntz, A. C., Li-$O_2$ Kinetic Overpotentials: Tafel Plots from Experiment and First-Principles Theory. *J. Phys. Chem. Lett.* **2013,** *4* (4), 556-560.
176. Viswanathan, V.; Thygesen, K. S.; Hummelshoj, J. S.; Norskov, J. K.; Girishkumar, G.; McCloskey, B. D.; Luntz, A. C., Electrical Conductivity in $Li_2O_2$ and Its Role in Determining Capacity Limitations in Non-Aqueous Li-$O_2$ Batteries. *J. Chem. Phys.* **2011,** *135* (21), 214704.
177. Lee, B.; Seo, D.-H.; Lim, H.-D.; Park, I.; Park, K.-Y.; Kim, J.; Kang, K., First-Principles Study of the Reaction Mechanism in Sodium–Oxygen Batteries. *Chem. Mater.* **2014,** *26* (2), 1048-1055.
178. Mo, Y.; Ong, S. P.; Ceder, G., First-Principles Study of the Oxygen Evolution Reaction of Lithium Peroxide in the Lithium-Air Battery. *Phys. Rev. B* **2011,** *84* (20), 205446.
179. Chen, L. D.; Norskov, J. K.; Luntz, A. C., Al-Air Batteries: Fundamental Thermodynamic Limitations from First-Principles Theory. *J. Phys. Chem. Lett.* **2015,** *6* (1), 175-179.
180. Chen, L. D.; Nørskov, J. K.; Luntz, A. C., Theoretical Limits to the Anode Potential in Aqueous Mg–Air Batteries. *J. Phys. Chem. C* **2015,** *119* (34), 19660-19667.
181. Kazemiabnavi, S., Continuum-Scale Modeling of Rechargeable Batteries. **2019**.

182. Barai, P.; Higa, K.; Srinivasan, V., Lithium Dendrite Growth Mechanisms in Polymer Electrolytes and Prevention Strategies. *Phys. Chem. Chem. Phys.* **2017,** *19* (31), 20493-20505.
183. Barai, P.; Higa, K.; Srinivasan, V., Impact of External Pressure and Electrolyte Transport Properties on Lithium Dendrite Growth. *J. Electrochem. Soc.* **2018,** *165* (11), A2654-A2666.
184. Byer, C. M.; Li, B.; Cao, B.; Ramesh, K. T., Microcompression of Single-Crystal Magnesium. *Scr. Mater.* **2010,** *62* (8), 536-539.
185. Greer, J. R.; De Hosson, J. T. M., Plasticity in Small-Sized Metallic Systems: Intrinsic Versus Extrinsic Size Effect. *Prog. Mater. Sci.* **2011,** *56* (6), 654-724.
186. Greer, J. R.; Nix, W. D., Size Dependence of Mechanical Properties of Gold at the Sub-Micron Scale. *Appl. Phys. A* **2005,** *80* (8), 1625-1629.
187. Greer, J. R.; Nix, W. D., Nanoscale Gold Pillars Strengthened through Dislocation Starvation. *Phys. Rev. B* **2006,** *73* (24), 245410.
188. Kim, J.-Y.; Greer, J. R., Tensile and Compressive Behavior of Gold and Molybdenum Single Crystals at the Nano-Scale. *Acta Mater.* **2009,** *57* (17), 5245-5253.
189. Xu, C.; Ahmad, Z.; Aryanfar, A.; Viswanathan, V.; Greer, J. R., Enhanced Strength and Temperature Dependence of Mechanical Properties of Li at Small Scales and its Implications for Li Metal Anodes. *Proc. Natl. Acad. Sci. U.S.A.* **2017,** *114* (1), 57-61.
190. Yu, Q.; Shan, Z. W.; Li, J.; Huang, X.; Xiao, L.; Sun, J.; Ma, E., Strong Crystal Size Effect on Deformation Twinning. *Nature* **2010,** *463* (7279), 335-338.
191. Li, G.; Monroe, C. W., Dendrite Nucleation in Lithium-Conductive Ceramics. *Phys. Chem. Chem. Phys.* **2019,** *21* (36), 20354-20359.
192. Herbert, E. G.; Dudney, N. J.; Rochow, M.; Thole, V.; Hackney, S. A., On the Mechanisms of Stress Relaxation and Intensification at the Lithium/Solid-State Electrolyte Interface. *J. Mater. Res.* **2019,** *34* (21), 3593-3616.
193. LePage, W. S.; Chen, Y.; Kazyak, E.; Chen, K.-H.; Sanchez, A. J.; Poli, A.; Arruda, E. M.; Thouless, M. D.; Dasgupta, N. P., Lithium Mechanics: Roles of Strain Rate and Temperature and Implications for Lithium Metal Batteries. *J. Electrochem. Soc.* **2019,** *166* (2), A89-A97.
194. Masias, A.; Felten, N.; Garcia-Mendez, R.; Wolfenstine, J.; Sakamoto, J., Elastic, Plastic, and Creep Mechanical Properties of Lithium Metal. *J. Mater. Sci.* **2018,** *54* (3), 2585-2600.
195. Yu, S.; Siegel, D. J., Grain Boundary Softening: A Potential Mechanism for Lithium Metal Penetration through Stiff Solid Electrolytes. *ACS Appl. Mater. Interfaces* **2018,** *10* (44), 38151-38158.
196. Wang, Y.; Wang, J. J.; Zhang, H.; Manga, V. R.; Shang, S. L.; Chen, L. Q.; Liu, Z. K., A First-Principles Approach to Finite Temperature Elastic Constants. *J. Phys. Condens. Matter.* **2010,** *22* (22), 225404.
197. Fine, M. E.; Brown, L. D.; Marcus, H. L., Elastic Constants Versus Melting Temperature in Metals. *Scr. Metall.* **1984,** *18* (9), 951-956.
198. Wills, J. M.; Eriksson, O.; Soderlind, P.; Boring, A. M., Trends of the Elastic Constants of Cubic Transition Metals. *Phys. Rev. Lett.* **1992,** *68* (18), 2802-2805.
199. Boyer, L. L.; Kaxiras, E.; Mehl, M. J.; Feldman, J. L.; Broughton, J. Q., Application of Magic Strains to Predict New Ordered Phases: A Five-Fold Coordinated Crystal Structure for Silicon. In *Ordering and Disordering in Alloys*, Yavari, A. R., Ed. Springer Netherlands: Dordrecht, 1992; pp 506-513.
200. Mehl, M. J.; Osburn, J. E.; Papaconstantopoulos, D. A.; Klein, B. M., Structural Properties of Ordered High-Melting-Temperature Intermetallic Alloys from First-Principles

Total-Energy Calculations. *Phys. Rev. B: Condens. Matter Mater. Phys.* **1990,** *41* (15), 10311-10323.
201. Osburn, J. E.; Mehl, M. J.; Klein, B. M., First-Principles Calculation of the Elastic Moduli of $Ni_3Al$. *Phys. Rev. B: Condens. Matter Mater. Phys.* **1991,** *43* (2), 1805-1807.
202. Kresse, G.; Hafner, J., Norm-Conserving and Ultrasoft Pseudopotentials for First-Row and Transition Element. *J. Phys.: Condens. Matter* **1994,** *6*, 8245-8257.
203. Methfessel, M.; Paxton, A. T., High-Precision Sampling for Brillouin-Zone Integration in Metals. *Phys. Rev. B* **1989,** *40* (6), 3616-3621.
204. de Jong, M.; Chen, W.; Angsten, T.; Jain, A.; Notestine, R.; Gamst, A.; Sluiter, M.; Ande, C. K.; van der Zwaag, S.; Plata, J. J.; Toher, C.; Curtarolo, S.; Ceder, G.; Persson, K. A.; Asta, M., Data from: Charting the Complete Elastic Properties of Inorganic Crystalline Compounds. In *Charting the Complete Elastic Properties of Inorganic Crystalline Compounds*, Repository, D. D., Ed. Dryad: Dryad, 2015.
205. de Jong, M.; Chen, W.; Angsten, T.; Jain, A.; Notestine, R.; Gamst, A.; Sluiter, M.; Krishna Ande, C.; van der Zwaag, S.; Plata, J. J.; Toher, C.; Curtarolo, S.; Ceder, G.; Persson, K. A.; Asta, M., Charting the Complete Elastic Properties of Inorganic Crystalline Compounds. *Sci. Data* **2015,** *2*, 150009.
206. Le Page, Y.; Saxe, P., Symmetry-General Least-Squares Extraction of Elastic Data for Strained Materials from *ab initio* Calculations of Stress. *Phys. Rev. B* **2002,** *65* (10), 104104.
207. Nye, J. F., *Physical Properties of Crystals: Their Representation by Tensors and Matrices*. Oxford University Press: Oxford, 1957.
208. Hill, R., The Elastic Behaviour of a Crystalline Aggregate. *Proc. Phys. Soc., London, Sect. A* **1952,** *65* (5), 349-354.
209. Ranganathan, S. I.; Ostoja-Starzewski, M., Universal Elastic Anisotropy Index. *Phys. Rev. Lett.* **2008,** *101* (5), 055504.
210. Marmier, A.; Lethbridge, Z. A. D.; Walton, R. I.; Smith, C. W.; Parker, S. C.; Evans, K. E., ElAM: A Computer Program for the Analysis and Representation of Anisotropic Elastic Properties. *Comput. Phys. Commun.* **2010,** *181* (12), 2102-2115.
211. Togo, A.; Chaput, L.; Tanaka, I.; Hug, G., First-Principles Phonon Calculations of Thermal Expansion in $Ti_3SiC_2$,$Ti_3AlC_2$, and $Ti_3GeC_2$. *Phys. Rev. B* **2010,** *81* (17), 174301.
212. Togo, A.; Oba, F.; Tanaka, I., First-Principles Calculations of the Ferroelastic Transition Between Rutile-Type and $CaCl_2$-Type $SiO_2$ at High Pressures. *Phys. Rev. B* **2008,** *78* (13), 134106.
213. Born, M.; Huang, K., *Dynamical Theory of Crystal Lattices*. Oxford University Press: Oxford, 1954.
214. Jain, A.; Ong, S. P.; Hautier, G.; Chen, W.; Richards, W. D.; Dacek, S.; Cholia, S.; Gunter, D.; Skinner, D.; Ceder, G.; Persson, K. A., Commentary: The Materials Project: A Materials Genome Approach to Accelerating Materials Innovation. *APL Mater.* **2013,** *1* (1), 011002.
215. Varshni, Y. P., Temperature Dependence of the Elastic Constants. *Phys. Rev. B* **1970,** *2* (10), 3952-3958.
216. Balsara, N. P.; Singh, M.; Eitouni, H. B.; Gomez, E. D. High Elastic Modulus Polymer Electrolytes. 2013.
217. Satterfield, M. B.; Majsztrik, P. W.; Ota, H.; Benziger, J. B.; Bocarsly, A. B., Mechanical Properties of Nafion and Titania/Nafion Composite Membranes for Polymer Electrolyte Membrane Fuel Cells. *J. Polym. Sci., Part B: Polym. Phys.* **2006,** *44*, 2327-2345.

218. Deng, Z.; Wang, Z.; Chu, I.-H.; Luo, J.; Ong, S. P., Elastic Properties of Alkali Superionic Conductor Electrolytes from First Principles Calculations. *J. Electrochem. Soc.* **2016,** *163* (2), A67-A74.
219. Sakuda, A.; Hayashi, A.; Tatsumisago, M., Sulfide Solid Electrolyte with Favorable Mechanical Property for All-Solid-State Lithium Battery. *Sci. Rep.* **2013,** *3* (1), 1-5.
220. Yang, Y.; Wu, Q.; Cui, Y.; Chen, Y.; Shi, S.; Wang, R. Z.; Yan, H., Elastic Properties, Defect Thermodynamics, Electrochemical Window, Phase Stability, and Li(+) Mobility of $Li_3PS_4$: Insights from First-Principles Calculations. *ACS Appl. Mater. Interfaces* **2016,** *8* (38), 25229-25242.
221. Herbert, E. G.; Tenhaeff, W. E.; Dudney, N. J.; Pharr, G. M., Mechanical Characterization of LiPON Films Using Nanoindentation. *Thin Solid Films* **2011,** *520*, 413-418.
222. Kim, K.; Siegel, D. J., Correlating Lattice Distortions, Ion Migration Barriers, and Stability in Solid Electrolytes. *J. Mater. Chem. A* **2019,** *7* (7), 3216-3227.
223. Wolfenstine, J.; Allen, J. L.; Sakamoto, J.; Siegel, D. J.; Choe, H., Mechanical Behavior of Li-Ion-Conducting Crystalline Oxide-Based Solid Electrolytes: A Brief Review. *Ionics* **2018,** *24*, 1271-1276.
224. Yu, S.; Schmidt, R. D.; Garcia-Mendez, R.; Herbert, E.; Dudney, N. J.; Wolfenstine, J. B.; Sakamoto, J.; Siegel, D. J., Elastic Properties of the Solid Electrolyte $Li_7La_3Zr_2O_{12}$ (LLZO). *Chem. Mater.* **2016,** *28* (1), 197-206.
225. Turley, J.; Sines, G., The Anisotropy of Young's Modulus, Shear Modulus and Poisson's Ratio in Cubic Materials. *J. Phys. D: Appl. Phys.* **1971,** *4*, 264-271.
226. Dawson, J. A.; Canepa, P.; Famprikis, T.; Masquelier, C.; Islam, M. S., Atomic-Scale Influence of Grain Boundaries on Li-Ion Conduction in Solid Electrolytes for All-Solid-State Batteries. *J. Am. Chem. Soc.* **2018,** *140* (1), 362-368.
227. Gao, X.; Fisher, C. A. J.; Kimura, T.; Ikuhara, Y. H.; Kuwabara, A.; Moriwake, H.; Oki, H.; Tojigamori, T.; Kohama, K.; Ikuhara, Y., Domain Boundary Structures in Lanthanum Lithium Titanates. *J. Mater. Chem. A* **2014,** *2* (3), 843-852.
228. Moriwake, H.; Gao, X.; Kuwabara, A.; Fisher, C. A. J.; Kimura, T.; Ikuhara, Y. H.; Kohama, K.; Tojigamori, T.; Ikuhara, Y., Domain Boundaries and their Influence on Li Migration in Solid-State Electrolyte (La,Li)$TiO_3$. *J. Power Sources* **2015,** *276*, 203-207.
229. Inaguma, Y.; Liquan, C.; Itoh, M.; Nakamura, T.; Uchida, T.; Ikuta, H.; Wakihara, M., High Ionic Conductivity in Lithium Lanthanum Titanate. *Solid State Commun.* **1993,** *86* (10), 689-693.
230. Yashima, M.; Itoh, M.; Inaguma, Y.; Morii, Y., Crystal Structure and Diffusion Path in the Gast Lithium-Ion Conductor $La_{0.62}Li_{0.16}TiO_3$. *J. Am. Chem. Soc.* **2005,** *127* (10), 3491-3495.
231. Cheng, L.; Chen, W.; Kunz, M.; Persson, K.; Tamura, N.; Chen, G.; Doeff, M., Effect of Surface Microstructure on Electrochemical Performance of Garnet Solid Electrolytes. *ACS Appl. Mater. Interfaces* **2015,** *7* (3), 2073-2081.
232. Ohta, S.; Kihira, Y.; Asaoka, T., Grain Boundary Analysis of the Garnet-Like Oxides $Li_{7+X-Y}La_{3-X}A_XZr_{2-Y}Nb_YO_{12}$ (A = Sr or Ca). *Frontiers in Energy Research* **2016,** *4*, 1-6.
233. El Shinawi, H.; Janek, J., Stabilization of Cubic Lithium-Stuffed Garnets of the Type "$Li_7La_3Zr_2O_{12}$" by addition of gallium. *J. Power Sources* **2013,** *225*, 13-19.
234. Tenhaeff, W. E.; Rangasamy, E.; Wang, Y.; Sokolov, A. P.; Wolfenstine, J.; Sakamoto, J.; Dudney, N. J., Resolving the Grain Boundary and Lattice Impedance of Hot-Pressed $Li_7La_3Zr_2O_{12}$ Garnet Electrolytes. *ChemElectroChem* **2014,** *1* (2), 375-378.

235. Li, Y.; Wang, Z.; Li, C.; Cao, Y.; Guo, X., Densification and Ionic-Conduction Improvement of Lithium Garnet Solid Electrolytes by Flowing Oxygen Sintering. *J. Power Sources* **2014,** *248*, 642-646.
236. Ohta, S.; Seki, J.; Yagi, Y.; Kihira, Y.; Tani, T.; Asaoka, T., Co-Sinterable Lithium Garnet-Type Oxide Electrolyte with Cathode for All-Solid-State Lithium Ion Battery. *J. Power Sources* **2014,** *265*, 40-44.
237. Gao, D.; Wu, R.; Chen, P.; Hong, T.; Cheng, J., Microwave Assisted Reactive Sintering for Al Doped $Li_7La_3Zr_2O_{12}$ Lithium Ion Solid State Electrolyte. *Mater. Res. Express* **2020,** *6* (12), 125539.
238. Xu, B.; Duan, H.; Xia, W.; Guo, Y.; Kang, H.; Li, H.; Liu, H., Multistep Sintering to Synthesize Fast Lithium Garnets. *J. Power Sources* **2016,** *302*, 291-297.
239. Yu, S.; Siegel, D. J., Grain Boundary Contributions to Li-Ion Transport in the Solid Electrolyte $Li_7La_3Zr_2O_{12}$ (LLZO). *Chem. Mater.* **2017,** *29* (22), 9639-9647.
240. Shiiba, H.; Zettsu, N.; Yamashita, M.; Onodera, H.; Jalem, R.; Nakayama, M.; Teshima, K., Molecular Dynamics Studies on the Lithium Ion Conduction Behaviors Depending on Tilted Grain Boundaries with Various Symmetries in Garnet-Type $Li_7La_3Zr_2O_{12}$. *J. Phys. Chem. C* **2018,** *122* (38), 21755-21762.
241. Chaudhari, P.; Matthews, J. W., Coincidence Twist Boundaries between Crystals of MgO Smoke. *Appl. Phys. Lett.* **1970,** *17* (3), 115-117.
242. Chaudhari, P.; Matthews, J. W., Coincidence Twist Boundaries between Crystalline Smoke Particles. *J. Appl. Phys.* **1971,** *42* (8), 3063-3066.
243. Adams, S.; Rao, R. P., High Power Lithium Ion Battery Materials by Computational Design. *Phys. Status Solidi A* **2011,** *208* (8), 1746-1753.
244. Adams, S.; Rao, R. P., Ion Transport and Phase Transition in $Li_{7-x}La_3(Zr_{2-x}M_x)O_{12}$ (M = $Ta^{5+}$, $Nb^{5+}$, x = 0, 0.25). *J. Mater. Chem.* **2012,** *22* (4), 1426-1434.
245. Rao, R. P.; Gu, W.; Sharma, N.; Peterson, V. K.; Avdeev, M.; Adams, S., In Situ Neutron Diffraction Monitoring of $Li_7La_3Zr_2O_{12}$ Formation: Toward a Rational Synthesis of Garnet Solid Electrolytes. *Chem. Mater.* **2015,** *27* (8), 2903-2910.
246. Yow, Z. F.; Oh, Y. L.; Gu, W.; Rao, R. P.; Adams, S., Effect of $Li^+/H^+$ Exchange in Water Treated Ta-Doped $Li_7La_3Zr_2O_{12}$. *Solid State Ionics* **2016,** *292*, 122-129.
247. Plimpton, S., Fast Parallel Algorithms for Short-Range Molecular Dynamics. *J. Comput. Phys.* **1995,** *117*, 1-19.
248. Rittner, J. D.; Seidman, D. N., <110> Symmetric Tilt Grain-Boundary Structures in FCC Metals with Low Stacking-Fault Energies. *Phys. Rev. B* **1996,** *54* (10), 6999-7015.
249. Tschopp, M. A.; McDowell, D. L., Structural Unit and Faceting Description of Σ3 Asymmetric Tilt Grain Boundaries. *J. Mater. Sci.* **2007,** *42* (18), 7806-7811.
250. Tschopp, M. A.; McDowell, D. L., Structures and Energies of Σ3 Asymmetric Tilt Grain Boundaries in Copper and Aluminium. *Philos. Mag.* **2007,** *87* (22), 3147-3173.
251. Tschopp, M. A.; McDowell, D. L., Asymmetric Tilt Grain Boundary Structure and Energy in Copper and Aluminium. *Philos. Mag.* **2007,** *87* (25), 3871-3892.
252. Tschopp, M. A.; Solanki, K. N.; Gao, F.; Sun, X.; Khaleel, M. A.; Horstemeyer, M. F., Probing Grain Boundary Sink Strength at the Nanoscale: Energetics and Length Scales of Vacancy and Interstitial Absorption by Grain Boundaries in α-Fe. *Phys. Rev. B* **2012,** *85* (6), 064108.

253. Keblinski, P.; Phillpot, S. R.; Wolf, D.; Gleiter, H., Thermodynamic Criterion for the Stability of Amorphous Intergranular Films in Covalent Materials. *Phys. Rev. Lett.* **1996,** *77* (14), 2965-2968.
254. Tschopp, M. A.; Solanki, K. N.; Gao, F.; Sun, X.; Khaleel, M. A.; Horstemeyer, M. F., Probing Grain Boundary Sink Strength at the Nanoscale: Energetics and Length Scales of Vacancy and Interstitial Absorption by Grain Boundaries in α-Fe. *Phys. Rev. B* **2012,** *85* (6), 064108.
255. Terentyev, D.; He, X.; Serra, A.; Kuriplach, J., Structure and Strength of〈110〉Tilt Grain Boundaries in BCC Fe: An Stomistic Study. *Comput. Mater. Sci.* **2010,** *49* (2), 419-429.
256. Readey, D. W.; Jech, R. E., Energies and Grooving Kinetics of [001] Tilt Boundaries in Nickel Oxide. *J. Am. Ceram. Soc.* **1968,** *51* (4), 201-208.
257. Read, W. T.; Shockley, W., Dislocation Models of Crystal Grain Boundaries. *Phys. Rev.* **1950,** *78* (3), 275-289.
258. McCarthy, K. A.; Chalmers, B., Energies of Grain Boundaries in Silver Chloride Crystals. *Canadian Journal of Physics* **1958,** *36*, 1645-1651.
259. Moment, R. L.; Gordon, R. B., Energy of Grain Boundaries in Halite. *J. Am. Ceram. Soc.* **1964,** *47* (11), 570-573.
260. Kingery, W. D., Plausible Concepts Necessary and Sufficient for Interpretation of Ceramic Grain-Boundary Phenomena: I, Grain-Boundary Characteristics, Structure, and Electrostatic Potential. *J. Am. Ceram. Soc.* **1974,** *57* (1), 1-8.
261. Saylor, D. M.; El Dasher, B. S.; Adams, B. L.; Rohrer, G. S., Measuring the Five-Parameter Grain-Boundary Distribution from Observations of Planar Sections. *Metall. Mater. Trans. A* **2004,** *35A*, 1981-1989.
262. Saylor, D. M.; El Dasher, B. S.; Pang, Y.; Miller, H. M.; Wynblatt, P.; Rollett, A. D.; Rohrer, G. S., Habits of Grains in Dense Polycrystalline Solids. *J. Am. Ceram. Soc.* **2004,** *87* (4), 724-726.
263. Saylor, D. M.; El Dasher, B. S.; Rollett, A. D.; Rohrer, G. S., Distribution of Grain Boundaries in Aluminum as a Function of Five Macroscopic Parameters. *Acta Mater.* **2004,** *52* (12), 3649-3655.
264. Saylor, D. M.; El Dasher, B. S.; Sano, T.; Rohrer, G. S., Distribution of Grain Boundaries in $SrTiO_3$ as Function of Five Macroscopic Parameters. *J. Am. Ceram. Soc.* **2004,** *87* (4), 670-676.
265. Saylor, D. M.; Morawiec, A.; Rohrer, G. S., Distribution of Grain Boundaries in Magnesia as a Function of Five Macroscopic Parameters. *Acta Mater.* **2003,** *51* (13), 3663-3674.
266. Saylor, D. M.; Morawiec, A.; Rohrer, G. S., The Relative Free Energies of Grain Boundaries in Magnesia as a Function of Five Macroscopic Parameters. *Acta Mater.* **2003,** *51* (13), 3675-3686.
267. Saylor, D. M.; Rohrer, G. S., Determining Crystal Habits from Observations of Planar Sections. *J. Am. Ceram. Soc.* **2002,** *85* (11), 2799-2804.
268. von Alfthan, S.; Haynes, P. D.; Kaski, K.; Sutton, A. P., Are the Structures of Twist Grain Boundaries in Silicon Ordered at 0 K? *Phys. Rev. Lett.* **2006,** *96* (5), 055505.
269. Dawson, J. A.; Canepa, P.; Clarke, M. J.; Famprikis, T.; Ghosh, D.; Islam, M. S., Toward Understanding the Different Influences of Grain Boundaries on Ion Transport in Sulfide and Oxide Solid Electrolytes. *Chem. Mater.* **2019,** *31* (14), 5296-5304.

270. de Klerk, N. J. J.; Wagemaker, M., Diffusion Mechanism of the Sodium-Ion Solid Electrolyte $Na_3PS_4$ and Potential Improvements of Halogen Doping. *Chem. Mater.* **2016,** *28* (9), 3122-3130.
271. Constable, F. H., The Mechanism of Catalytic Decomposition. *Proc. R. Soc. London, Ser. A* **1925,** *108*, 355-378.
272. Linert, W.; Jameson, R. F., The Isokinetic Relationship. *Chem. Soc. Rev.* **1989,** *18*, 477-505.
273. Meyer, W.; Neldel, H., Concerning the Relationship Between the Energy Constant Epsilon and the Quantum Constant Alpha in the Conduction-Temperature Formula in Oxydising Semi-Conductors. *Phys. Z.* **1937,** *38*, 1014-1019.
274. Liu, L.; Guo, Q. X., Isokinetic Relationship, Isoequilibrium Relationship, and Enthalpy-Entropy Compensation. *Chem. Rev.* **2001,** *101* (3), 673-695.
275. Yelon, A.; Movaghar, B.; Crandall, R. S., Multi-Excitation Entropy: Its Role in Thermodynamics and Kinetics. *Rep. Prog. Phys.* **2006,** *69* (4), 1145-1194.
276. Steltenpohl, A.; Memmel, N., Self-Diffusion on Pd(111). *Surf. Sci.* **2000,** *454-456*, 558-561.
277. Almond, D. P.; West, A. R., Entropy Effects in Ionic Conductivity. *Solid State Ionics* **1986,** *18 & 19*, 1105-1109.
278. Bejina, F.; Jaoul, O., Silicon Diffusion in Silicate Minerals. *Earth Planet. Sci. Lett.* **1997,** *153*, 229-238.
279. Berenov, A. V.; MacManus-Driscoll, J. L.; Kilner, J. A., Observation of the Compensation Law During Oxygen Diffusion in Perovskite Materials. *Int. J. Inorg. Mater.* **2001,** *3*, 1109-1111.
280. Kreuer, K. D., Aspects of the Formation and Mobility of Protonic Charge Carriers and the Stability of Perovskite-Type Oxides. *Solid State Ionics* **1999,** *125*, 285-302.
281. Juma, A.; Wafula, H.; Wendler, E.; Dittrich, T., Meyer-Neldel rule for Cu (I) Diffusion in $In_2S_3$ Layers. *J. Appl. Phys.* **2014,** *115* (5), 053703.
282. Iwaoka, H.; Arita, M.; Horita, Z., Hydrogen Diffusion in Ultrafine-Grained Palladium: Roles of Dislocations and Grain Boundaries. *Acta Mater.* **2016,** *107*, 168-177.
283. Diederichsen, K. M.; Buss, H. G.; McCloskey, B. D., The Compensation Effect in the Vogel–Tammann–Fulcher (VTF) Equation for Polymer-Based Electrolytes. *Macromolecules* **2017,** *50* (10), 3831-3840.
284. Gottstein, G.; Shvindlerman, L. S., The Compensation Effect in Thermally Activated Interface Processes. *Interface Sci.* **1998,** *6*, 265-276.
285. Sursaeva, V. G.; Protasova, S.; Straumal, B. B., Meyer-Neldel Rule for the Kinetic Properties of Grain and Interphase Boundaries. *Defect and Diffusion Forum* **2001,** *192-193*, 15-26.
286. Tilley, R. J. D., *Defects in Solids*. John Wiley and Sons: Hoboken, N.J., 2008.
287. Miara, L. J.; Ong, S. P.; Mo, Y.; Richards, W. D.; Park, Y.; Lee, J.-M.; Lee, H. S.; Ceder, G., Effect of Rb and Ta Doping on the Ionic Conductivity and Stability of the Garnet $Li_{7+2x-y}(La_{3-x}Rb_x)(Zr_{2-y}Ta_y)O_{12}$ ($0 \leq x \leq 0.375$, $0 \leq y \leq 1$) Superionic Conductor: A First Principles Investigation. *Chem. Mater.* **2013,** *25* (15), 3048-3055.
288. Moffat, T. P.; Yang, H., Patterned Metal Electrodeposition Using an Alkanethiolate Mask. *J. Electrochem. Soc.* **1995,** *142*, L220-L222.

289. Madey, T. E.; Chen, W.; Wang, H.; Kaghazchi, P.; Jacob, T., Nanoscale Surface Chemistry over Faceted Substrates: Structure, Reactivity and Nanotemplates. *Chem. Soc. Rev.* **2008,** *37* (10), 2310-2327.
290. Energy Information Administration, Monthly Energy Review July 2020, Table 2.1.
291. Iermakova, D. I.; Dugas, R.; Palacín, M. R.; Ponrouch, A., On the Comparative Stability of Li and Na Metal Anode Interfaces in Conventional Alkyl Carbonate Electrolytes. *J. Electrochem. Soc.* **2015,** *162* (13), A7060-A7066.
292. Qian, J.; Henderson, W. A.; Xu, W.; Bhattacharya, P.; Engelhard, M.; Borodin, O.; Zhang, J. G., High Rate and Stable Cycling of Lithium Metal Anode. *Nat. Commun.* **2015,** *6*, 6362.
293. Komaba, S.; Hasegawa, T.; Dahbi, M.; Kubota, K., Potassium Intercalation into Graphite to Realize High-Voltage/High-Power Potassium-Ion Batteries and Potassium-Ion Capacitors. *Electrochem. Commun.* **2015,** *60*, 172-175.
294. Wu, Y., Cyclic Voltammograms for K Metal Anodes. Email correspondence ed.; Nagy, K. S., Ed. 2017.
295. Orikasa, Y.; Masese, T.; Koyama, Y.; Mori, T.; Hattori, M.; Yamamoto, K.; Okado, T.; Huang, Z. D.; Minato, T.; Tassel, C.; Kim, J.; Kobayashi, Y.; Abe, T.; Kageyama, H.; Uchimoto, Y., High Energy Density Rechargeable Magnesium Battery using Earth-Abundant and Non-Toxic Elements. *Sci. Rep.* **2014,** *4*, 5622.
296. See, K. A.; Chapman, K. W.; Zhu, L.; Wiaderek, K. M.; Borkiewicz, O. J.; Barile, C. J.; Chupas, P. J.; Gewirth, A. A., The Interplay of Al and Mg Speciation in Advanced Mg Battery Electrolyte Solutions. *J. Am. Chem. Soc.* **2016,** *138* (1), 328-337.
297. Aurbach, D.; Schechter, A.; Moshkovich, M.; Cohen, M. L., On the Mechanisms of Reversible Magnesium Deposition Processes. *J. Electrochem. Soc.* **2001,** *148* (9), A1004-A1014.
298. Yagi, S.; Tanaka, A.; Ichitsubo, T.; Matsubara, E., Electrochemical Stability of Metal Electrodes for Reversible Magnesium Deposition/Dissolution in Tetrahydrofuran Dissolving Ethylmagnesium Chloride. *ECS Electrochem. Lett.* **2012,** *1*(2), D11-D14.
299. Shao, Y.; Liu, T.; Li, G.; Gu, M.; Nie, Z.; Engelhard, M.; Xiao, J.; Lv, D.; Wang, C.; Zhang, J. G.; Liu, J., Coordination Chemistry in Magnesium Battery Electrolytes: How Ligands Affect Their Performance. *Sci. Rep.* **2013,** *3*, 3130.
300. Aurbach, D.; Gofer, Y.; Lu, Z.; Schechter, A.; Chusid, O.; Gizbar, H.; Cohen, Y.; Ashkenazi, V.; Moshkovich, M.; Turgeman, R.; Levi, E., A Short Review on the Comparison Between Li Battery Systems and Rechargeable Magnesium Battery Technology. *J. Power Sources* **2001,** *97-98*, 28-32.
301. Barile, C. J.; Barile, E. C.; Zavadil, K. R.; Nuzzo, R. G.; Gewirth, A. A., Electrolytic Conditioning of a Magnesium Aluminum Chloride Complex for Reversible Magnesium Deposition. *J. Phys. Chem. C* **2014,** *118* (48), 27623-27630.
302. Mizrahi, O.; Amir, N.; Pollak, E.; Chusid, O.; Marks, V.; Gottlieb, H.; Larush, L.; Zinigrad, E.; Aurbach, D., Electrolyte Solutions with a Wide Electrochemical Window for Rechargeable Magnesium Batteries. *J. Electrochem. Soc.* **2008,** *155* (2), A103-A109.
303. Viestfrid, Y.; Levi, M. D.; Gofer, Y.; Aurbach, D., Microelectrode Studies of Reversible Mg Deposition in THF Solutions Containing Complexes of Alkylaluminum Chlorides and Dialkylmagnesium. *J. Electroanal. Chem.* **2005,** *576* (2), 183-195.
304. Aurbach, D.; Suresh, G. S.; Levi, E.; Mitelman, A.; Mizrahi, O.; Chusid, O.; Brunelli, M., Progress in Rechargeable Magnesium Battery Technology. *Adv. Mater.* **2007,** *19* (23), 4260-4267.

305. Pour, N.; Gofer, Y.; Major, D. T.; Aurbach, D., Structural Analysis of Electrolyte Solutions for Rechargeable Mg Batteries by Stereoscopic Means and DFT Calculations. *J. Am. Chem. Soc.* **2011,** *133* (16), 6270-6278.
306. Doe, R. E.; Han, R.; Hwang, J.; Gmitter, A. J.; Shterenberg, I.; Yoo, H. D.; Pour, N.; Aurbach, D., Novel, Electrolyte Solutions Comprising Fully Inorganic Salts with High Anodic Stability for Rechargeable Magnesium Batteries. *Chem. Commun. (Cambridge, U.K.)* **2014,** *50* (2), 243-245.
307. Hall, J. J., Electronic Effects in the Elastic Constants of n-Type Silicon. *Phys. Rev.* **1967,** *161* (3), 756-761.
308. Jain, A. L., Pressure Dependence of the Elastic Shear Constants of Li. *Phys. Rev.* **1961,** *123* (4), 1234-1238.
309. Nash, H. C.; Smith, C. S., Single-Crystal Elastic Constants of Lithium. *J. Phys. Chem. Solids* **1958,** *9*, 113-118.
310. Schmunk, R. E.; Smith, C. S., Pressure Derivatives of the Elastic Constants of Aluminum and Magnesium. *J. Phys. Chem. Solids* **1959,** *9*, 100-112.
311. Slotwinski, T.; Trivisonno, J., Temperature Dependence of the Elastic Constants of Single Crystal Lithium. *J. Phys. Chem. Solids* **1968,** *30*, 1276-1279.
312. Stassis, C.; Zaretsky, J.; Misemer, D. K.; Skriver, H. L.; Harmon, B. N.; Nicklow, R. M., Lattice Dynamics of FCC Ca. *Phys. Rev. B* **1983,** *27* (6), 3303-3307.
313. Tallon, J. L.; Wolfenden, A., Temperature Dependence of the Elastic Constants of Aluminum. *J. Phys. Chem. Solids* **1979,** *40*, 831-837.
314. Barrett, C. S., X-Ray Study of the Alkali Metals at Low Temperatures. *Acta Crystallogr.* **1956,** *9*, 671-677.
315. Batchelder, D. N.; Simmons, R. O., Lattice Constants and Thermal Expansivities of Silicon and of Calcium Fluoride between 6° and 322°K. *J. Chem. Phys.* **1964,** *41* (8), 2324-2329.
316. Beg, M. M.; Nielsen, M., Temperature Dependence of Lattice Dynamics of Lithium 7. *Phys. Rev. B* **1976,** *14* (10), 4266-4273.
317. Busk, R. S., Effect of Temperature on the Lattice Parameters. *J. Met.* **1952**, 207-208.
318. Jette, E. R.; Foote, F., Precision Determination of Lattice Constants. *J. Chem. Phys.* **1935,** *3* (10), 605-616.
319. King, H. W., Temperature-Dependent Allotropic Stuctures of the Elements. *Bull. Alloy Phase Diagrams* **1982,** *3* (2), 276.
320. Kresch, M.; Lucas, M.; Delaire, O.; Lin, J. Y. Y.; Fultz, B., Phonons in Aluminum at High Temperatures Studied by Inelastic Neutron Scattering. *Phys. Rev. B* **2008,** *77* (2), 024301.
321. Nuss, J.; Wedig, U.; Kirfel, A.; Jansen, M., The Structural Anomaly of Zinc: Evolution of Lattice Constants and Parameters of Thermal Motion in the Temperature Range of 40 to 500 K. *Z. Anorg. Allg. Chem.* **2010,** *636* (2), 309-313.
322. Okada, Y.; Tokumaru, Y., Precise Determination of Lattice Parameter and Thermal Expansion Coefficient of Silicon Between 300 and 1500 K. *J. Appl. Phys.* **1984,** *56* (2), 314-320.
323. Pugh, S. F., XCII. Relations Between the Elastic Moduli and the Plastic Properties of Polycrystalline Pure Metals. *Philos. Mag.* **2009,** *45* (367), 823-843.